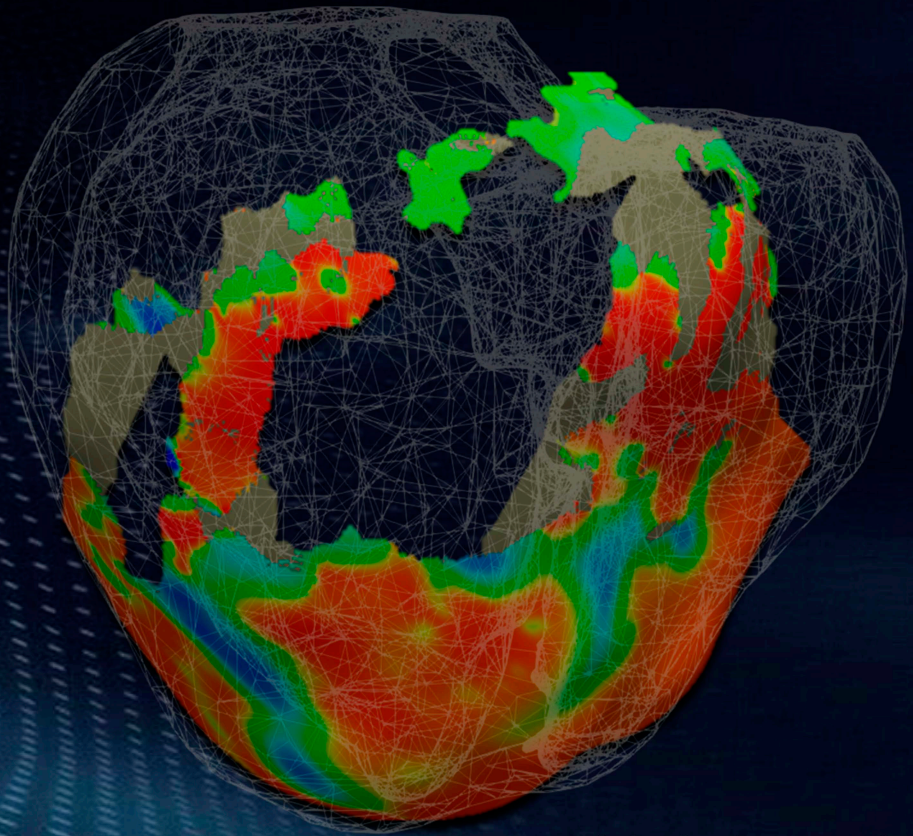# Computational Modelling of the Human Heart and Multiscale Simulation of its Electrophysiological Activity aimed at the Treatment of Cardiac Arrhythmias related to Ischaemia and Infarction

DOCTORAL THESIS

Author
Alejandro Daniel López Pérez

Supervisors
Prof. José María Ferrero De Loma-Osorio
Dr. Rafael Sebastián Aguilar

Computational Modelling of the Human Heart and Multiscale Simulation of its Electrophysiological Activity aimed at the Treatment of Cardiac Arrhythmias related to Ischaemia and Infarction

DOCTORAL THESIS

Alejandro Daniel López Pérez

Supervisors:
Prof. José María Ferrero De-Loma Osorio
Dr. Rafael Sebastián Aguilar

UNIVERSITAT
POLITÈCNICA
DE VALÈNCIA

July 2019
Valencia, Spain

Alejandro Daniel López Pérez

Doctoral thesis:

Computational Modelling of the Human Heart and Multiscale Simulation of its Electrophysiological Activity aimed at the Treatment of Cardiac Arrhythmias related to Ischaemia and Infarction

Universitat Politècnica de València, Valencia, Spain

PROGRAMA DE DOCTORADO EN TECNOLOGÍAS PARA LA SALUD Y EL BIENESTAR

Doctoral thesis submitted to the Department of Electronic Engineering in fulfilment of the requirements for the degree of Doctor of Philosophy at the Universitat Politècnica de València, Valencia, Spain.

This doctoral thesis was carried out at the *Centro de Investigación e Innovación en Bioingeniería* (Ci2B) from the Univesitat Politècnica de València (Valencia, Spain), in close collaboration with the *Computational Multiscale Simulation Lab* (CoMMLab) from the Universitat de València Estudi General.

Funding information

Author:
Alejandro Daniel López Pérez

Supervisors:

Prof. José María Ferrero De Loma-Osorio
Universitat Politècnica de València, Valencia, Spain

Dr. Rafael Sebastián Aguilar
Universitat de València Estudi General, Valencia, Spain

External Evaluators:

Dr. Esther Pueyo Paules
Centro de Investigación Biomédica en Red en Bioingeniería, Biomateriales y Biomedicina (CIBER-BBN), Spain

Dr. Jesús Carro Fernández
Universidad San Jorge, Zaragoza, Spain

Dr. Pablo Laguna Lasaosa
Universidad de Zaragoza, Zaragoza, Spain

Reading Committee:

Dr. Pablo Laguna Lasaosa
Universidad de Zaragoza, Zaragoza, Spain

Dr. Lucía Romero Pérez
Universitat Politècnica de València, Valencia, Spain

Dr. Pablo Lamata De La Orden
King's College London, London, United Kingdom

ABSTRACT

Abstract

Cardiovascular diseases represent the main cause of morbidity and mortality worldwide, causing around 18 million deaths every year. Among these diseases, the most common one is the ischaemic heart disease, usually referred to as *myocardial infarction* (MI). After surviving to a MI, a considerable number of patients develop life-threatening *ventricular tachycardias* (VT) during the chronic stage of the MI, that is, weeks, months or even years after the initial acute phase. This particular type of VT is typically sustained by reentry through slow *conducting channels* (CC), which are filaments of surviving myocardium that cross the non-conducting fibrotic *infarct scar*. When anti-arrhythmic drugs are unable to prevent recurrent VT episodes, *radiofrequency ablation* (RFA), a minimally invasive procedure performed by catheterization in the electrophysiology (EP) laboratory, is commonly used to interrupt the electrical conduction through the CCs responsible for the VT permanently. However, besides being invasive, risky and time-consuming, in the cases of VTs related to chronic MI, up to 50% of patients continue suffering from recurrent VT episodes after the RFA procedure. Therefore, there exists a need to develop novel pre-procedural strategies to improve RFA planning and, thereby, increase this relatively low success rate.

In the last decade, the field of *computational cardiac EP* has demonstrated the potential of 3D cardiac models to perform reliable *in-silico* (using computational simulation) studies, useful for both patient risk stratification and therapy planning. Hence, in this thesis, we have developed a full pipeline based on non-invasive clinical data for constructing personalized image-based 3D models of infarcted ventricles and torso in order to perform pre-procedural personalized *in-silico* EP studies aimed at RFA planning in cases of reentrant VTs related to chronic MI.

First, we conducted an exhaustive review of the literature associated with the existing 3D cardiac models in order to gain a deep knowledge about their main features and the methods used for their construction, with special focus on those models oriented to simulation of cardiac EP. Later, using a clinical dataset of a chronically infarcted patient with a history of infarct-related VT, we designed and implemented a number of strategies and methodologies to (1) build patient-specific 3D computational models of infarcted ventricles that can be used to perform simulations of cardiac EP at the organ level, including the infarct scar and

the surrounding region known as *border zone* (BZ); (2) construct 3D torso models that enable to compute the simulated ECG; and (3) carry out pre-procedural personalized *in-silico* EP studies, trying to replicate the actual EP studies conducted in the EP laboratory prior to the ablation. The goal of these methodologies is to allow locating the CCs into the 3D ventricular model in order to help in defining the optimal ablation targets for the RFA procedure.

Lastly, as a proof-of-concept, we performed a retrospective simulation case study, in which we were able to induce an infarct-related reentrant VT using different modelling configurations for the BZ. We validated our results by reproducing with a reasonable accuracy the patient's ECG during VT, as well as in sinus rhythm from the endocardial activation maps invasively recorded via electroanatomical mapping systems in this latter case. This allowed us to find the location and analyse the features of the CC responsible for the clinical VT. Importantly, such *in-silico* EP study might have been conducted prior to the RFA procedure, since our approach is completely based on non-invasive clinical data acquired before the real intervention.

These results confirm the feasibility of performing useful pre-procedural personalized *in-silico* EP studies, as well as the potential of the proposed approach to become a helpful tool for RFA planning in cases of infarct-related reentrant VTs in the future. Nevertheless, the developed methodology requires further improvements and validation by means of simulation studies including large cohorts of patients. Moreover, there still exist several challenging issues hampering the incorporation of simulation-based strategies into the current clinical workflow, such as the lack of robust methods for the full automated generation of personalized 3D cardiac models from medical imaging datasets, or the high computational burden and long computing times associated with the simulations required to faithfully reproduce the cardiac EP at the organ and torso level. Anyhow, the current rapid advance of numerical methods and computing architectures is expected to overcome these drawbacks in the near future, thus enabling the use of approaches based on computational cardiac EP for risk stratification and therapy planning in the clinical environments.

Resumen

Las enfermedades cardiovasculares constituyen la principal causa de morbilidad y mortalidad a nivel mundial, causando en torno a 18 millones de muertes cada año. De entre ellas, la más común es la enfermedad isquémica cardíaca, habitualmente denominada como *infarto de miocardio* (IM). Tras superar un IM, un considerable número de pacientes desarrollan *taquicardias ventriculares* (TV) potencialmente mortales durante la fase crónica del IM, es decir, semanas, meses o incluso años después la fase aguda inicial. Este tipo concreto de TV normalmente se origina por una reentrada a través de canales de conducción (CC), filamentos de miocardio superviviente que atraviesan la *cicatriz del infarto* fibrosa y no conductora. Cuando los fármacos anti-arrítmicos resultan incapaces de evitar episodios recurrentes de TV, la *ablación por radiofrecuencia* (ARF), un procedimiento mínimamente invasivo realizado mediante cateterismo en el laboratorio de electrofisiología (EF), se usa habitualmente para interrumpir de manera permanente la propagación eléctrica a través de los CCs responsables de la TV. Sin embargo, además de ser invasivo, arriesgado y requerir mucho tiempo, en casos de TVs relacionadas con IM crónico, hasta un 50% de los pacientes continúa padeciendo episodios recurrentes de TV tras el procedimiento de ARF. Por tanto, existe la necesidad de desarrollar nuevas estrategias pre-procedimiento para mejorar la planificación de la ARF y, de ese modo, aumentar esta tasa de éxito relativamente baja.

En la última década, el campo de la *EF cardíaca computacional* ha demostrado el potencial de los modelos cardíacos 3D para realizar estudios *in-silico* (mediante simulación computacional) fiables, de utilidad tanto para la estratificación del riesgo como para la planificación de terapias. Así pues, en esta tesis hemos desarrollado toda una metodología, basada en datos clínicos no invasivos, para construir modelos 3D basados en imagen de ventrículos infartados y torso para realizar estudios *in-silico* de EF personalizados y pre-procedimiento destinados a la planificación de ARF en casos de TVs reentrantes relacionadas con IM crónico.

En primer lugar, realizamos una revisión exhaustiva de la literatura referente a los modelos cardiacos 3D existentes, con el fin de obtener un profundo conocimiento de sus principales características y los métodos usados en su construcción, con especial atención sobre los modelos orientados a simulación de EF cardíaca. Posteriormente, usando datos clínicos de un paciente con historial de TV relacionada con infarto, diseñamos e implementamos una serie de estrategias y metodologías para (1) generar

modelos computacionales 3D específicos de paciente de ventrículos infartados que puedan usarse para realizar simulaciones de EF cardíaca a nivel de órgano, incluyendo la cicatriz del infarto y la región circundante conocida como *zona de borde* (ZB); (2) construir modelos 3D de torso que permitan la obtención del ECG simulado; y (3) llevar a cabo estudios *in-silico* de EF personalizados y pre-procedimiento, tratando de replicar los verdaderos estudios de EF realizados en el laboratorio de EF antes de la ablación. La finalidad de estas metodologías es la de localizar los CCs en el modelo ventricular 3D para ayudar a definir los objetivos de ablación óptimos para el procedimiento de ARF.

Por último, a modo de prueba de concepto, realizamos el estudio retrospectivo por simulación de un caso, en el que logramos inducir la TV reentrante relacionada con el infarto usando diferentes configuraciones de modelado para la ZB. Validamos nuestros resultados mediante la reproducción, con una precisión razonable, del ECG del paciente en TV, así como en ritmo sinusal a partir de los mapas de activación endocárdica obtenidos invasivamente mediante sistemas de mapeado electroana-tómico en este último caso. Esto permitió encontrar la ubicación y analizar las características del CC responsable de la TV clínica. Cabe destacar que dicho estudio *in-silico* de EF podría haberse efectuado antes del procedimiento de ARF, puesto que nuestro planteamiento está completamente basado en datos clínicos no invasivos adquiridos antes de la intervención real.

Estos resultados confirman la viabilidad de la realización de estudios *in-silico* de EF personalizados y pre-procedimiento de utilidad, así como el potencial del abordaje propuesto para llegar a ser en un futuro una herramienta de apoyo para la planificación de la ARF en casos de TVs reentrantes relacionadas con infarto. No obstante, la metodología propuesta requiere de notables mejoras y validación por medio de estudios de simulación con grandes cohortes de pacientes. Por otra parte, aún existen varios retos que dificultan la incorporación de las estrategias basadas en simulación a la práctica clínica actual, tales como la falta de métodos robustos para la generación automatizada de modelos cardíacos 3D personalizados a partir de datos de imagen médica, o la elevada carga computacional y los largos tiempos de computación asociados a las simulaciones necesarias para reproducir fielmente la EF cardíaca a nivel de órgano y torso. Sin embargo, se espera que el actual rápido avance de los métodos numéricos y las arquitecturas de computación permita superar estos inconvenientes en un futuro próximo, habilitando así el uso de las estrategias basadas en la EF cardíaca computacional para estratificación de riesgos y planificación de terapias en los entornos clínicos.

Resum

Les malalties cardiovasculars constitueixen la principal causa de morbiditat i mortalitat a nivell mundial, causant entorn a 18 milions de morts cada any. De elles, la més comuna és la malaltia isquèmica cardíaca, habitualment denominada *infart de miocardi* (IM). Després de superar un IM, un considerable nombre de pacients desenvolupen *taquicàrdies ventriculars* (TV) potencialment mortals durant la fase crònica de l'IM, és a dir, setmanes, mesos i fins i tot anys després de la fase aguda inicial. Aquest tipus concret de TV normalment s'origina per una reentrada a través dels *canals de conducció* (CC), filaments de miocardi supervivent que travessen la *cicatriu de l'infart* fibrosa i no conductora. Quan els fàrmacs anti-arítmics resulten incapaços d'evitar episodis recurrents de TV, l'*ablació per radiofreqüència* (ARF), un procediment mínimament invasiu realitzat mitjançant cateterisme en el laboratori de electrofisiologia (EF), s'usa habitualment per a interrompre de manera permanent la propagació elèctrica a través dels CCs responsables de la TV. No obstant això, a més de ser invasiu, arriscat i requerir molt de temps, en casos de TVs relacionades amb IM crònic fins a un 50% dels pacients continua patint episodis recurrents de TV després del procediment d'ARF. Per tant, existeix la necessitat de desenvolupar noves estratègies pre-procediment per a millorar la planificació de l'ARF i, d'aquesta manera, augmentar la taxa d'èxit, que es relativament baixa.

En l'última dècada, el camp de la *EF cardíaca computacional* ha demostrat el potencial dels models cardíacs 3D per a realitzar estudis *in-silico* (mitjançant simulació computacional) fiables i d'utilitat tant per a l'estratificació del risc, com per a la planificació de teràpies. Així doncs, en aquesta tesi hem desenvolupat tota una metodologia, basada en dades clíniques no invasius, per a construir models 3D basats en imatge de ventricles infartats i tors per a realitzar estudis *in-silico* de EF personalitzats i pre-procediment destinats a la planificació d'ARF en casos de TVs reentrants relacionades amb IM crònic.

En primer lloc, realitzem una revisió exhaustiva de la literatura referent als models cardíacs 3D existents, amb la finalitat d'obtindre un profund coneixement de les seues principals característiques i els mètodes usats en la seua construcció, amb especial atenció sobre els models orientats a simulació de EF cardíaca. Posteriorment, usant dades clíniques d'un pacient amb historial de TV relacionada amb infart, dissenyem i implementem una sèrie d'estratègies i metodologies per a (1) generar models computacionals 3D específics de pacient de ventricles infartats capaços de

realitzar simulacions de EF cardíaca a nivell d'òrgan, incloent la cicatriu de l'infart i la regió circumdant coneguda com a *zona de vora* (ZV); (2) construir models 3D de tors que permeten l'obtenció del ECG simulat; i (3) dur a terme estudis *in-silico* de EF personalitzats i pre-procediment, tractant de replicar els vertaders estudis de EF realitzats en el laboratori de EF abans de l'ablació. La finalitat d'aquestes metodologies és la de localitzar els CCs en el model ventricular 3D per a ajudar a definir els objectius d'ablació òptims per al procediment d'ARF.

Finalment, a manera de prova de concepte, realitzem l'estudi retrospectiu per simulació d'un cas, en el qual aconseguim induir la TV reentrant relacionada amb l'infart usant diferents configuracions de modelatge per a la ZV. Validem els nostres resultats mitjançant la reproducció, amb una precisió raonable, del ECG del pacient en TV, així com en ritme sinusal a partir dels mapes d'activació endocardíac obtinguts invasivament mitjançant sistemes de mapatge electro-anatòmic en aquest últim cas. Això va permetre trobar la ubicació i analitzar les característiques del CC responsable de la TV clínica. Cal destacar que aquest estudi *in-silico* de EF podria haver-se efectuat abans del procediment d'ARF, ja que el nostre plantejament està completament basat en dades clíniques no invasius adquirits abans de la intervenció real.

Aquests resultats confirmen la viabilitat de la realització d'estudis *in-silico* de EF personalitzats i pre-procediment d'utilitat, així com el potencial de l'abordatge proposat per a arribar a ser en un futur una eina de suport per a la planificació de l'ARF en casos de TVs reentrants relacionades amb infart. No obstant això, la metodologia proposada requereix de notables millores i validació per mitjà d'estudis de simulació amb grans cohorts de pacients. D'altra banda, encara existeixen diversos reptes que dificulten la incorporació de les estratègies basades en simulació a la pràctica clínica actual, tals com la falta de mètodes robustos per a la generació automatitzada de models cardíacs 3D personalitzats a partir de dades d'imatge mèdica, o l'elevada càrrega computacional i els llargs temps de computació associats a les simulacions necessàries per a reproduir fidelment la EF cardíaca a nivell d'òrgan i tors. No obstant això, s'espera que l'actual ràpid avanç dels mètodes numèrics i les arquitectures de computació permeta superar aquests inconvenients en un futur pròxim, habilitant així l'ús de les estratègies basades en la EF cardíaca computacional per a estratificació de riscos i planificació de teràpies en els entorns clínics.

INDEX

Table of Contents

List of Figures

Chapter 1. Introduction

Chapter 3. Three-Dimensional Cardiac Computational Modelling

Chapter 4. Clinical Data

Chapter 5. Three-Dimensional Computational Models of Infarcted Ventricles and Torso

Chapter 6. Electrophysiological Modelling

Chapter 7. Personalized Electrophysiological Study using Computational Simulation

List of Tables

List of Videos

Video playlists

Sinus activation. Videos corresponding to the simulations of CARTO®-derived sinus activation.

https://www.youtube.com/playlist?list=PL98EKQIbetNobrKiaro9H3KI2FjcGpT7j

Positive VT induction. Videos of all those simulations that resulted in a positive VT induction.

https://www.youtube.com/playlist?list=PL98EKQIbetNq4MdEMpVkOd6bx0TQNYDXZ

Negative VT induction. Videos of eight different simulations that resulted in a negative VT induction.

https://www.youtube.com/playlist?list=PL98EKQIbetNpgBP8NT9CpQ2WmhqOPhSeR

Single videos

Video S1. Stabilization of myocyte-fibroblast couplings on model *#3* (noER+20fib).

https://youtu.be/f8_QJSOsqQ4

Video S2. Positive VT induction on model *#6* (ER+10fib) from pacing site *epi#1*.

https://youtu.be/1LepgvOTBJI

Video S3. Positive VT induction on model *#7* (ER+20fib) from pacing site *endo#1*.

https://youtu.be/qshQTkZPE0k

Video S4. Positive VT induction on model *#6* (ER+10fib) from pacing site *epi#1*, with CVsBZ-50%.

https://youtu.be/13Td_t8MWOE

Video S5. Negative VT induction on model *#6* (ER+10fib) from pacing site *epi#1*, with CVsBZ-75%.

https://youtu.be/HMMrHHb3YqM

Video S6. Positive VT induction on model *#4* (noER+30fib) from pacing site *epi#1*.

https://youtu.be/nJAsVjX_67A

Video S7. Negative VT induction on model *#8* (ER+30fib) from pacing site *epi#1*.

https://youtu.be/DDr1Ag_XSSE

Video S8. Negative VT induction on model *#8* (ER+30fib) from pacing site *endo#1*.

https://youtu.be/mxE9i4ANqXg

Video S9. Negative VT induction on model *#6* (ER+10fib) from pacing site *epi#2*.
https://youtu.be/m11Z1QdmHNU

Video S10. Negative VT induction on model *#5* (ER+00fib) from pacing site *epi#2*.
https://youtu.be/XWC9MMWigh0

Video S11. Negative VT induction on model *#3* (noER+20fib) from pacing site *epi#1*.
https://youtu.be/iMUctH2WiRM

Video S12. Negative VT induction on model *#6* (ER+10fib) from pacing site *endo#1*.
https://youtu.be/lV_hen97G8M

Video S13. Negative VT induction on model *#5* (ER+00fib) from pacing site *endo#1*, due to bidirectional functional propagation block.
https://youtu.be/xtdoWtn-DGs

Video S14. Positive VT induction on model *#5* (ER+00fib) from pacing site *epi#1*.
https://youtu.be/u8NAd3TvQ0g

NOMENCLATURE

Acronyms

2D	Bi-dimensional
3D	Three-dimensional
AHA	American Heart Association
AP	Action potential
APD	Action potential duration
AV	Atrioventricular (node)
BCL	Basic cycle length
bpm	(Heart) beats per minute
BSPM	Body surface potentials maps
BZ	Border zone
CAD	Computer-aided design
CC	Conducting channel
CCS	Cardiac conduction system
CI	Coupling interval
CL	Cycle length
CRT	Cardiac resynchronisation therapy
CT	Computed tomography
CV	Conduction velocity
DE-MRI	Delayed enhancement-magnetic resonance imaging
DTI	Diffusion tensor imaging
DT-MRI	Diffusion tensor-magnetic resonance imaging
EAM	Electroanatomical map/mapping
ECG	Electrocardiogram
EM	Electromechanical
EP	Electrophysiology or electrophysiological
FEM	Finite element method
GPU	Graphical processing unit
GUI	Graphic user interface
HH	Hodgkin and Huxley

HPC	High-performance computing
LBBB	Left bundle branch block
LV	Left ventricle
MRI	Magnetic resonance imaging
MS-CT	Multi slice-computed tomography
ODE	Ordinary differential equation
PCA	Principal components analysis
PDE	Partial differential equation
PDM	Point distribution model
PES	Programmed electrical stimulation
PMJ	Purkinje-myocardium junction
RFA	Radiofrequency ablation
ROI	Region-of-interest
RV	Right ventricle
SA	Sinoatrial (node)
SD	Standard deviation
VT	Ventricular tachycardia
VV	Interventricular

Abbreviations

CVsBZ-25%	CVs in the BZ reduced to 25% with respect to healthy myocardium
CVsBZ-50%	CVs in the BZ reduced to 50% with respect to healthy myocardium
CVsBZ-75%	CVs in the BZ reduced to 75% with respect to healthy myocardium
ER+00fib	Electrical remodelling and 0% fibrosis in the BZ
ER+10fib	Electrical remodelling and 10% fibrosis in the BZ
ER+20fib	Electrical remodelling and 20% fibrosis in the BZ
ER+30fib	Electrical remodelling and 30% fibrosis in the BZ
noER+00fib	No electrical remodelling and 0% fibrosis in the BZ
noER+10fib	No electrical remodelling and 10% fibrosis in the BZ
noER+20fib	No electrical remodelling and 20% fibrosis in the BZ
noER+30fib	No electrical remodelling and 30% fibrosis in the BZ

Computational Modelling of the Human Heart and Multiscale Simulation of its Electrophysiological Activity aimed at the Treatment of Cardiac Arrhythmias related to Ischaemia and Infarction

Chapter 1

Introduction

The first chapter of this doctoral thesis makes a brief introduction of a number of basic concepts that are closely related to the fundamentals of this work. Those concepts must be properly introduced, since we will be referring to them across the entire document. However, it is important to note that this chapter does not include a description of the state-of-the-art in cardiac computational modelling, as such analysis will be presented in Chapter 3.

1.1. The heart

The heart is a vital organ that, as shown in Figure 1.1, is located within the rib cage, in the middle of chest, slightly shifted to the left side, surrounded by the lungs and leaned on the diaphragm. The main function of the heart is to pump the blood in order to ensure the blood distribution across the whole organism and, consequently, the oxygen and nutrients supply provided by the bloodstream to all the organs and tissues that comprise the human body.
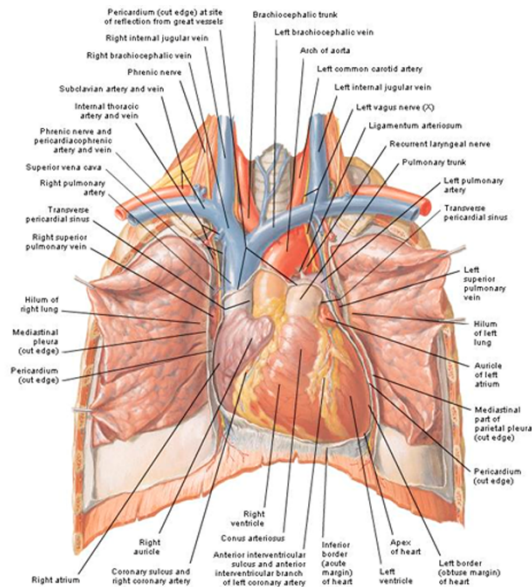
Figure 1.1. Illustration of the anatomical position of the heart within the human body, showing an anterior view with spread lungs in order to expose the heart.

As observed in Figure 1.2, the heart is composed of four chambers or cavities: the atria, which are the two superior cavities separated by the interatrial septum, and the ventricles, the two inferior chambers separated by the interventricular septum. The atria are the cavities that receive the blood from outside the heart, while the ventricles are the chambers that pump the blood from the heart to the rest of the organism. At the right side of the heart, the right atrium receives the deoxygenated blood from the rest of the body through the superior and inferior cava veins. Next, the blood passes to the right ventricle (RV) across the tricuspid valve and, then, the RV pumps the blood through the pulmonary artery, crossing the pulmonary valve, towards the lungs. At the left side, oxygenated blood coming from the lungs fills the right atrium through the pulmonary veins. After that, the blood crosses the mitral valve down to the left ventricle (LV), from where the blood is pumped through the aorta artery, after crossing the aortic valve, aiming to be distributed all over the organism, thereby irrigating organs and tissues.
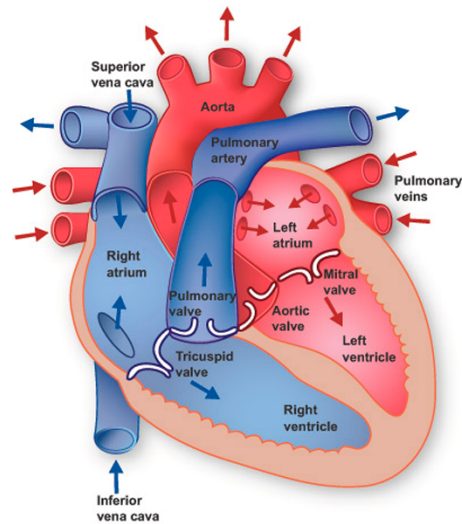
Figure 1.2. Representation of the anatomical structure of the human heart, showing a coronal cross-section of the organ including the main vessels. Image taken from the website of the *Texas Heart Institute*:
www.texasheart.org/heart-health/heart-information-center/topics/heart-anatomy/

The external surface of the heart is named *epicardium*, while the internal surface of each of the four cardiac chambers is known as *endocardium*. Figure 1.3 shows the highly complex anatomical structure of the endocardial surfaces of both ventricles in the human heart. Such complexity is caused by the presence of two different types of structures emerging from the ventricular endocardia: *papillary muscles* and *endocardial trabeculations*. The papillary muscles are tissue prolongations joining the ventricular walls to the leaflets of the atrio-ventricular valves (tricuspid and mitral valves) by means of fibrous filaments known as *chordae tendineae*. The endocardial trabeculations, or *trabeculae carneae*, are other kind of tissue prolongations that are thinner than papillary muscles. They also start from the ventricular wall, from which they can join another trabeculation or merge again with the wall at another site, even crossing to the opposite side of the cardiac cavity, thus giving rise to the complex tissue network that is appreciated in Figure 1.3.
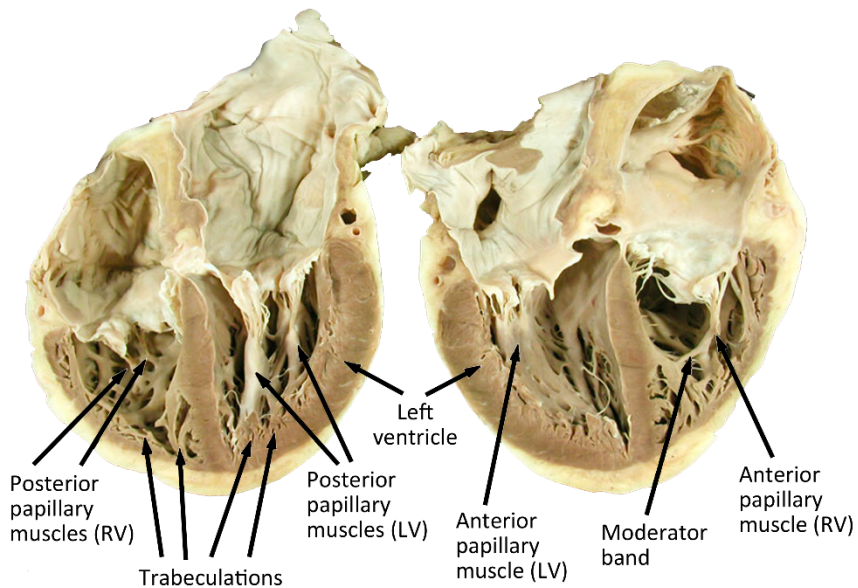
Figure 1.3. Dissection of an explanted human heart. Anterior (*right*) and posterior (*left*) views of a coronal cross-section, exhibiting the highly complex anatomical structure of the endocardial surfaces of ventricles. Image adapted from the *Atlas of Human Cardiac Anatomy, The Visible Heart Lab, University of Minnesota*:
www.vhlab.umn.edu/atlas/sectioned/Heart0005-4chamber-vent.jpg

1.1.1. Cardiac tissue structure

The heart is a muscular organ and, therefore, it is mostly composed of a specialized muscular tissue known as cardiac muscle or *myocardium*. As the skeletal muscle, the myocardium is mainly formed by striated muscle fibres named *cardiomyocytes* or just *myocytes*, although they present several important differences with respect to the skeletal muscle fibres. However, despite myocytes comprised most of the myocardial tissue volume, it is also populated by other cell types, such as *fibroblasts*. Ventricular myocytes are elongated cells that normally have a single nucleus, showing an approximately prism-like shape (see Figure 1.4[b]), with an average length of about 100-150 μm and a width usually ranging from 11 to 20 μm (Beuckelmann et al., 1992; Forbes and Sperelakis, 1984). To form the ventricular myocardium, such cardiac cells are arranged longitudinally so that the main axis of each myocyte is nearly parallel to the axis of its neighbouring cells, as shown in Figure 1.4. Moreover,

the ventricular myocytes are linked to each other through the *gap junctions*, specialized proteins that connect the intracellular spaces of neighbour cells, which are mainly concentrated at the so-called *intercalated discs*, the terminal ends of myocytes.
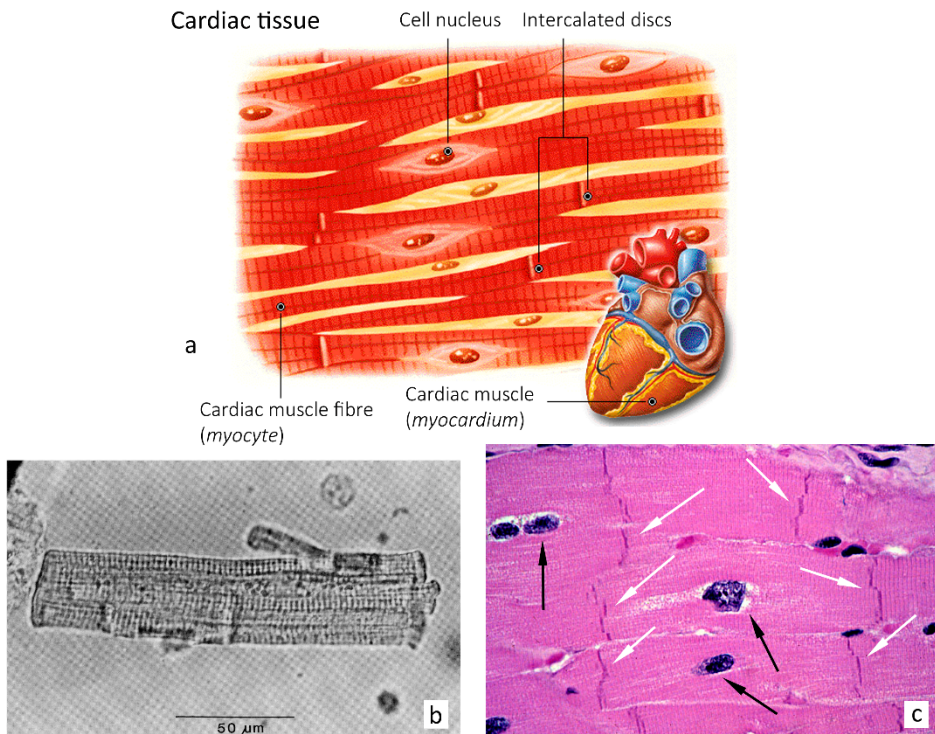
Figure 1.4. (*a*) Illustration representing the structure of the human cardiac muscle. (*b*) Microscopic image of an isolated human ventricular myocyte. Reproduced from (Beuckelmann *et al.*, 1992). (*c*) Microscopic photograph of a stained sample of cardiac muscle, exhibiting myocytes nuclei (*black arrows*) and intercalated discs (*white arrows*). Image adapted from the *Histology Learning System of Boston University*:
www.bu.edu/histology/p/06303ooa.htm

In the late 60's, Streeter *et al.* thoroughly studied the organization of the ventricular myocytes that compose the LV myocardium in a number of canine hearts (Streeter et al., 1969). They observed well-defined and regular patterns, revealing the rotation of the orientation of the cardiac muscle fibres across the ventricular walls, as a function of the transmural distance from endocardium to epicardium, and also along the longitudinal axis of ventricles, as a function of

the height relative to the apex-base axis. Furthermore, the authors characterized those patterns by defining a fibre angle, α, measured with respect to a local coordinates system referred to the epicardial surface, as represented in Figure 1.5. The *rotational anisotropy* of the cardiac fibre orientation observed by Streeter *et al.* was later confirmed both in dogs (LeGrice et al., 1995) and in other large mammals, including humans (Rohmer et al., 2007). Those structural patterns of the ventricular myocardial architecture, together with the characteristic shape of ventricular myocytes, have a great influence on heart function, since the contraction of the cardiac muscle is mainly caused by the shrinkage or shortening of myocytes along their longitudinal axes.
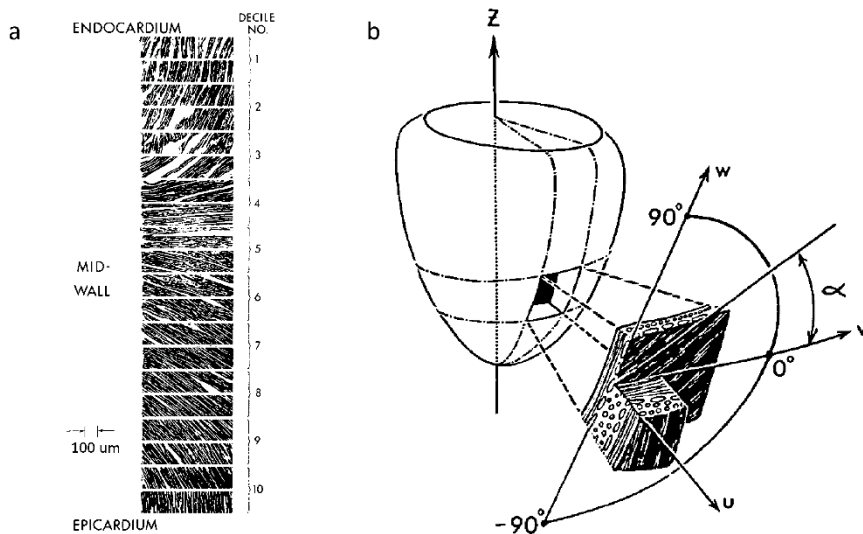
Figure 1.5. Study on the cardiac fibres architecture in canine LV by Streeter *et al.* (*a*) Representation of a sequence of microscopic photographs from successive ventricular tissue sections taken from the endocardium to the epicardium, exhibiting the rotation of the cardiac fibre orientation as a function of wall depth. Tissue sections are parallel to the epicardial surface. (*b*) Illustration representing the characterization of the LV myocardial architecture by means of the fibre angle, α, defined with respect to the local orthogonal axes u, v, w referred to the epicardial surface. Images adapted from (Streeter *et al.*, 1969)

1.1.2. Cardiac conduction system

From the standpoint of the engineering, the heart may be described as an electromechanical pump, since its mechanical function as a blood pump is triggered by a previous electrical excitation. Under physiological conditions, such excitation begins at the primary pacemaker of the heart, the sinoatrial (SA) node, later reaches secondary pacemaker, the atrioventricular (AV) node, and lastly propagates across the ventricles through a network of specialized myocytes. Those structures, the two pacemakers along with the ventricular network, compose the so-called *cardiac conduction system* (CCS). As observed in Figure 1.6, the SA node is located within the myocardial wall of the right atrium near the entrance of the superior vena cava, while the AV node lies at the lower back portion of the interatrial septum. Both nodes are formed by a group of specialized cardiomyocytes that are capable of generating electrical impulses spontaneously and rhythmically with no need of external stimulation, thereby developing the cardiac pacemaker function. Nevertheless, as a primary pacemaker, the AV node is the main responsible to determine the cardiac rhythm under physiological conditions.
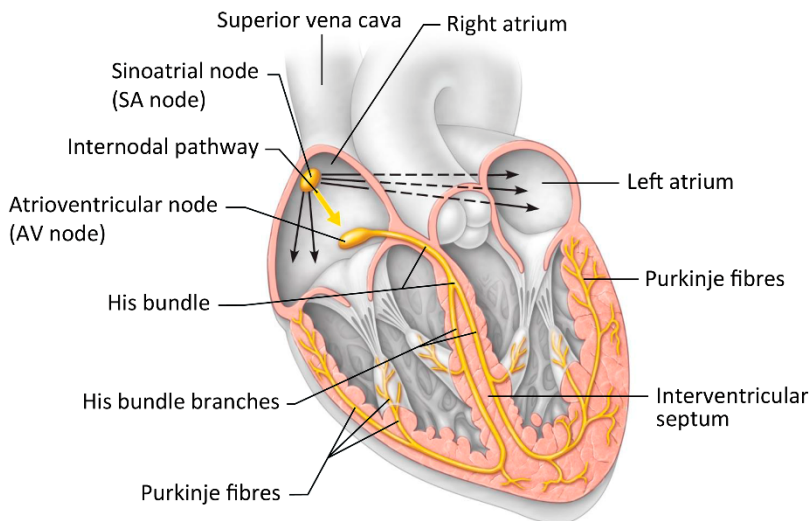
Figure 1.6. Cardiac conduction system. Illustration of a coronal cross-section of the human heart, showing a representation of the structure of the cardiac conduction system (CCS). Image adapted from *Cardiovascular system – the heart, Pearson Education, Inc.*: https://slideplayer.com/slide/8916387/

The ventricles and the atria are electrically isolated between them, as they are physically separated by a non-conducting fibrous annulus. However, besides its secondary pacemaker function, the AV node also enables the electrical connection between atria and ventricles. Under physiological conditions, the electrical impulses delivered by the SA node spread across the atrial walls and, when they reach the AV node, it transmits those impulses to the ventricles through the ventricular network, thus ensuring a synchronized contraction pattern such that the atria contract first and the ventricles contract later in order to pump the blood efficiently.

The ventricular network of the CCS is composed of a particular kind of myocytes known as *Purkinje cells*, which are highly specialized for a fast electrical conduction, significantly faster than in normal ventricular myocytes. Such network starts at the AV node, giving rise to the *His bundle* at the upper part of the interventricular septum. As shown in Figure 1.6, the His bundle divides into two branches, respectively known as left and right bundle branch, which run through the septum at subendocardial level towards the ventricles' apex. In each ventricle, the corresponding bundle branch divides into a few main ramifications, which in turn keep dividing and anastomosing to form a complex network confined in subendocardial layers termed *Purkinje network*. This *His-Purkinje system* is electrically isolated from the surrounding tissue all along its path, except for the terminal ends of Purkinje fibres, named *Purkinje-myocardium junctions* (PMJ). Those numerous points, scattered all over the endocardium of both ventricles, are the sites where the electrical impulse coming from the AV node and rapidly transmitted through the His-Purkinje system is injected into the ventricular myocardium in order to trigger the activation that propagates across the entire ventricles. Such a synchronized electrical activation leads to a highly coordinated ventricular contraction, thus ensuring an effective mechanical performance of the heart as a blood pump.

1.2. Cardiac electrophysiology

Electrophysiology (EP) is the branch of physiology that studies the electrical properties of cells and the electrical behaviour of biological tissues,

which is basically related to the ionic currents (i.e., fluxes of ions) that flow between neighbouring cells. As introduced in the section above, the heart behaves as an electromechanical pump and, hence, its electrical activity is an important matter of study. Therefore, the cardiac EP is the branch of EP that focuses on the study of the electrical behaviour of cardiac cells and tissues. However, the clinical cardiac EP, commonly referred to as cardiac EP or just as EP in the clinical environment, is the subspeciality of cardiology that deals with the study, diagnosis and treatment of the electrical cardiac disorders leading to pathological alterations of the heart rhythm.
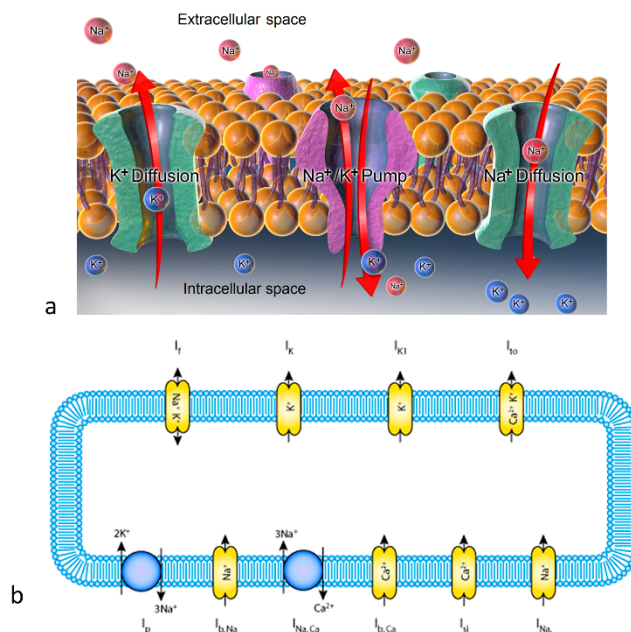
Figure 1.7. (*a*) Illustration of the myocyte cell membrane, showing a representation of transmembrane ion channels of sodium (Na^+) and potassium (K^+) and of Na^+/K^+ pump. Image taken from *Wikiwand*: www.wikiwand.com/en/Resting_potential. (*b*) Schematic diagram showing the main ion channels, pumps and exchangers embedded in the cell membrane of myocytes. Image taken from *Physiome Project* website: models.physiomepro ject.org/exposure/91d93b61d7da56b6baf1f0c4d88ecd77/difrancesco_noble_1985.cellml/view

Regarding the electrical behaviour of cardiac cells, the cardiomyocytes that compose the contractile myocardium present at rest a considerable electric potential difference between the intra- and extracellular medium, leading to a considerably negative membrane *resting potential* of around –90 mV when the

cell is electrically quiescent. Nevertheless, as represented in Figure 1.7, embedded in the cell membrane of myocytes there are a large amount of specialized proteins that, under certain conditions, enable the transference of specific ion species between the intra- and extracellular medium, mainly sodium (Na^+), potassium (K^+), calcium (Ca^{2+}) and chloride (Cl^-) ions. Those transmembrane structures are the main responsible for the active electrical behaviour of cardiomyocytes, which basically are of three different types: *ion channels*, *pumps* and *exchangers* (see Figure 1.7).
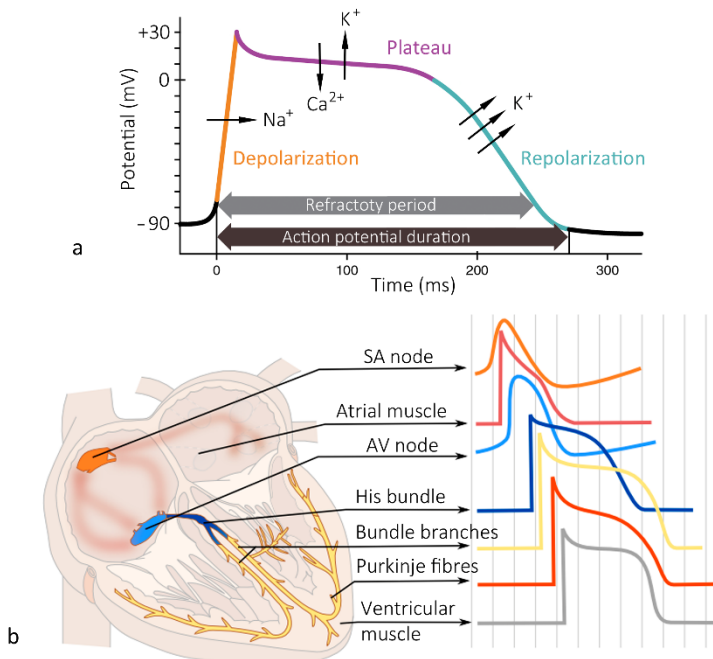
Figure 1.8. (*a*) Action potential (AP) of a cardiomyocyte, showing the main ion currents responsible for each AP phase. Adapted from *Anatomy & Physiology (chapter 19)*, *Rice University*: cnx.org/contents/FPtK1zmh@6.27:MCgS6S0t@3/Cardiac-Muscle-and-Electrical-Activity. (*b*) APs exhibiting distinct features depending on the associated type of cardiac cell. Image adapted from the online *Textbook of Cardiology*:
   www.textbookofcardiology.org/wiki/Cardiac_Arrhythmias

When a cardiomyocyte in resting state is properly stimulated, it reacts by triggering an action potential (AP), which consists on temporal but significant changes in the myocyte membrane potential. As shown in Figure 1.8[a], first the myocyte depolarizes, that is, its membrane potential experiences a sharp

change by which it becomes positive. This is known as the *upstroke* or *depolarization phase* of the cardiac AP, which is caused by the activation (opening) of the fast Na$^+$ channels leading to a massive and very quick intake of Na$^+$ ions, thereby making the electric potential of intracellular medium exceed that of the extracellular space. After that, there is a rapid inactivation of Na$^+$ channels giving rise to the *plateau phase*, in which the membrane potential temporally remains positive and approximately constant due to the balance between the intake of Ca^{2+} ions and the efflux of K$^+$ ions moving through their respective ion channels. Once the Ca^{2+} channels inactivate (close), the *repolarization phase* starts, since the K$^+$ efflux continues and even increases because of the activation of more K$^+$ channels, thus progressively reducing the membrane potential until reaching again the strongly negative resting potential. Thus, the distinct ion channels, which allow the passive diffusion of specific ions through the cell membrane, are the main responsible for the myocyte AP, while the ion pumps and exchangers are active transporters acting continuously in order to restore and maintain the adequate ion concentrations in the intracellular medium. Indeed, with the exception of pacemaker cells from SA and AV nodes (see Figure 1.8[b]) and Purkinje cells, in absence of stimulation the myocyte membrane potential remains nearly constant at the resting potential value due to the perfect balance between inward and outward ion currents.

As can be appreciated in Figure 1.8[b], the distinct types of cardiac cells exhibit APs with different features, mainly differing in their AP duration (APD) and morphology as a result of different expression levels of specific ion channels in the cell membrane of each myocyte type. Note that the myocytes from SA and AV nodes, in addition to lacking a plateau phase, show a non-constant resting potential that progressively increases. This diastolic depolarization is the automatic mechanism that allows such cells to act as pacemakers, since their resting potential continue increasing until making those specialized myocytes depolarize and trigger an AP spontaneously after a certain time despite the absence of external stimulation. Purkinje cells can also trigger an AP sponta-neously, although requiring a longer period without stimulation compared to pacemaker cells.

With respect to the electrical behaviour of cardiac tissue, the AP of a myocyte is able to propagate to the neighbouring ones, such that an AP in a ventricular myocyte, for instance, can propagate across the whole ventricular myocardium leading to a syncytium-like behaviour (functional syncytium). This electrical propagation is mediated by the gap junctions, which are transmembrane proteins that are shared by adjacent myocytes, such that their intracellular mediums are interconnected through these special channel proteins. Thereby, the changes in the intracellular ion concentrations associated with the myocyte AP, also affect the neighbouring myocytes, making them to develop an AP as well. However, the gap junctions are mostly concentrated in the intercalated discs located in the terminal ends of myocytes (see Figure 1.4). Consequently, the electrical propagation between adjacent myocytes and, hence, across the myocardial tissue, is up to three times faster along the longitudinal axis of myocytes than in the transverse directions (Clerc, 1976). Therefore, the electrical propagation in the myocardium is highly anisotropic due to the myocardial tissue architecture.

1.2.1. Action potential and myocyte contraction

The mechanical behaviour of myocytes is mediated by the increase in the intracellular Ca^{2+} concentration during the AP plateau phase, which triggers the physiological mechanisms leading to myocyte contraction. Importantly, the influx of Ca^{2+} from the extracellular space is insufficient to cause an effective myocyte contraction. However, such Ca^{2+} intake triggers in turn a mechanism named *calcium-induced calcium release*. This mechanism consists of an important release of Ca^{2+} ions into the myocyte cytoplasm from the *sarcoplasmic reticulum*, which is an intracellular structure that basically acts as a calcium store. By means of this intracellular calcium release, the Ca^{2+} cytoplasmic concentration finally manages to rise up to the level required to trigger the mechanisms of myocyte contraction. Thus, the mechanical contraction of myocytes is caused by a previous electrical excitation, since the intracellular calcium release triggering the contraction mechanisms is associated with the depolarization of the myocyte membrane potential.

1.3. **Myocardial infarction**

Coronary arteries are the vessels that provide the blood supply to the cardiac muscle. *Coronary artery disease* occurs when any of those arteries is partially or completely obstructed, so that the blood flow within the myocardium decreases critically or even stops. This extremely serious circumstance makes a part of the cardiac muscle go into acute ischaemia due to the oxygen and nutrients deprivation as a consequence of the loss of blood supply. This cause-effect relationship is the reason why the coronary artery disease is also termed *ischaemic heart disease* or *ischaemic cardiomyopathy*.
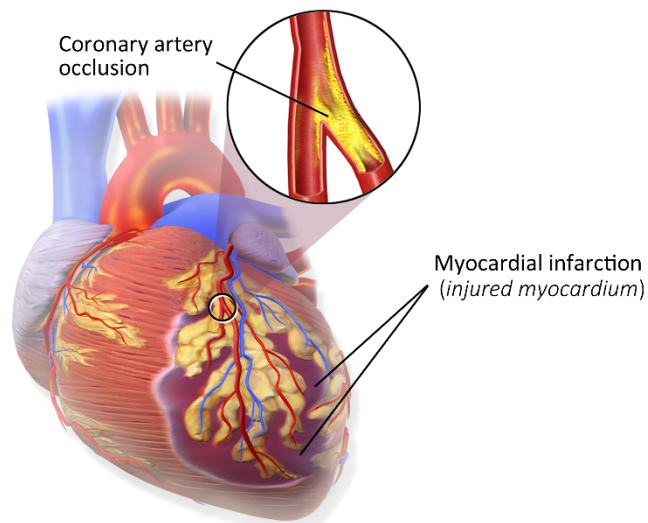
Figure 1.9. Illustration of a myocardial infarction, showing the injured myocardium (highlighted in *purple*) as a consequence of the occlusion of a coronary artery caused by the formation of atherosclerotic plaques. Image adapted from *Wikipedia*:
https://en.wikipedia.org/wiki/Myocardial_infarction

The most common reasons leading to coronary artery occlusion are related to atherosclerosis, which basically consists of cholesterol deposition within the artery lumen forming atherosclerotic plaques. Regardless the cause of the coronary artery blockage, when myocardial ischaemia persists for several minutes, it leads to an irreversible damage in the cardiac muscle known as *myocardial infarction* (MI), as illustrated in Figure 1.9. Indeed, the concept of MI is formally defined as myocardial cell death (i.e., myocytes necrosis) caused by a prolonged situation of myocardial ischaemia (Thygesen et al., 2019).

Cardiomyocytes begin to die a few minutes after the onset of the blood supply deprivation and may continue dying during several hours (Thygesen et al., 2007). The extent of the myocardial damage mainly depends on three factors: (1) the exact location of the coronary artery occlusion, which determines the extension of tissue deprived of blood supply, (2) the severity of that occlusion (partial or complete) and (3) the time elapsed between the obstruction and reperfusion of the coronary artery, that is, the duration of the ischaemic event.

1.3.1. Myocardial infarction healing

After the acute myocardial ischaemia phase, the inflammatory response derived from the tissue damage triggers a healing process that aims to "repair" the injured myocardium. That MI healing process comprises various successive phases that evolve across several weeks (Arai, 2015; Daskalopoulos et al., 2012; Liehn et al., 2011). Therefore, a MI may be classified as acute, healing or healed as a function of the time elapsed from the obstruction of the coronary artery (Arai, 2015; Thygesen et al., 2007). Very basically, the final goal of the MI healing process is to replace the dead myocytes in the infarcted area by collagen fibres (replacement fibrosis), giving rise to the formation of a dense fibrotic core commonly known as *infarct scar*, which is unable to contract and develop electrical activity. Although it may vary depending on the extent of the injured area, among other factors (age, gender, race, genetics, etc.), in humans the MI healing process is expected to be completed in 5 to 6 weeks (Ertl and Frantz, 2005; Thygesen et al., 2007). After that time, the formation of the fibrotic infarct scar is supposed to be finished, such that the MI is already in its healed stage, also commonly referred to as *chronic MI*.

However, the tissue remodelling resulting from the MI healing process is not homogeneous. Surrounding the central fibrotic core, there exists a region that constitutes the transition between the infarct scar and the intact (healthy) myocardium named the *border zone* (BZ), also termed *grey zone* or *peri-infarct zone*. The BZ is composed of viable and still working myocardial tissue, although it exhibits an altered behaviour compared to the healthy myocardium. This

transition region is characterized by the presence of both EP and structural remodelling, since the electrical conduction properties and the composition of the myocardium in the BZ exhibit significant differences with respect to the healthy ventricular tissue. Concerning the EP properties, the AP of the surviving cardiomyocytes that populate the BZ are known to differ from the AP of healthy ventricular myocytes (Mendonca Costa et al., 2018). At the structural level, experimental studies have revealed the presence of fibrotic tissue infiltrated within the BZ, thus giving rise to an anomalous and heterogeneous myocardial composition in that region (de Jong et al., 2011; Rutherford et al., 2012; Seidel et al., 2016). Moreover, a slowing-down of the propagation of electrical wavefronts across the BZ has also been reported, probably as a consequence of the combination of electrical and structural remodelling (de Bakker et al., 1993; Nguyen et al., 2014).

1.4. Cardiac arrhythmias

Cardiac arrhythmias are disorders of the electrical behaviour of the heart leading to abnormal rhythms of cardiac contraction, which can be slower or faster compared to the physiological rates, or simply irregular. Those arrhythmias characterized by an atypically slow cardiac rhythm are named *bradyarrhythmias* or *bradycardias*, which give rise to heart rates below 60 beats per minute (bpm). When the cardiac rhythm is too fast, typically above 100 bpm, such arrhythmias are termed *tachyarrhythmias* or *tachycardias*. On the other hand, *fibrillation* is an irregular and extremely rapid heart rhythm (more than 300 bpm) that leads to an uncoordinated cardiac contraction, thus causing a poor mechanical performance of the heart as a blood pump.
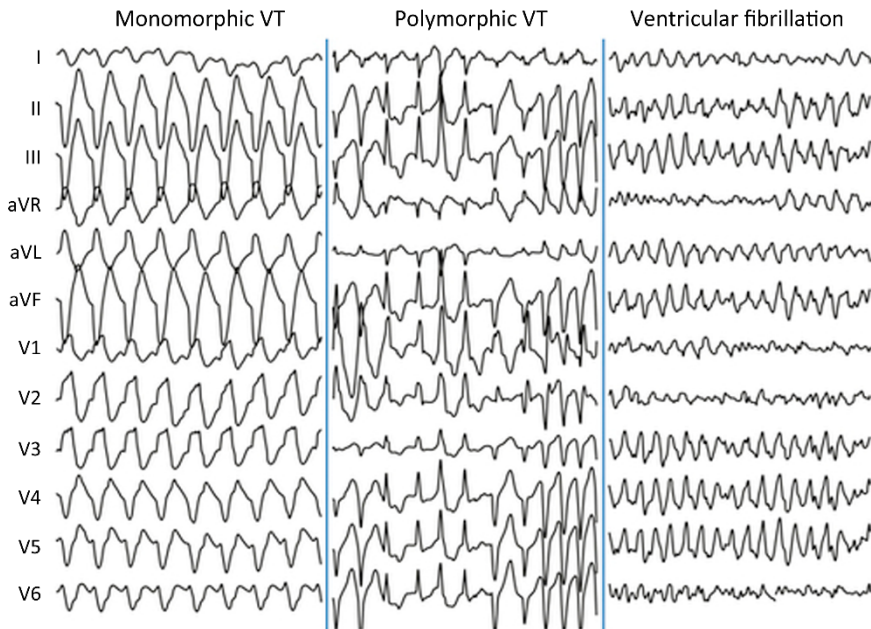
Figure 1.10. Electrocardiographic signals corresponding to the 12-lead ECG, revealing the electrical activity in the heart during monomorphic VT (*left*), polymorphic VT (*centre*) and ventricular fibrillation (*right*). Image adapted from (Issa *et al.*, 2012)

The atria and the ventricles can suffer from cardiac arrhythmias separately, which are respectively known as *supraventricular* and *ventricular arrhythmias*. Therefore, a *ventricular tachycardia* (VT) is an atypically fast heart rate, although not necessarily irregular, originated by an abnormal activation of the ventricles that leads to an accelerated contraction rhythm. Indeed, VTs may be *monomorphic* or *polymorphic*, depending on whether the ventricular contraction is rapid and regular, or irregular as a consequence of a disorganized electrical activity in the ventricles. As shown in Figure 1.10, the collection of electrocardiographic signals registered on the body surface usually referred to as *electrocardiogram* (ECG), reveals how the patterns of electrical activity in the heart become increasingly disorganized when monomorphic VT, polymorphic VT and ventricular fibrillation are respectively compared. Monomorphic VTs show a regular morphological pattern, while the ECG signals associated with polymorphic VTs and ventricular fibrillations exhibit a morphology that is continuously changing as a result of an unorganized or even chaotic electrical activity in the ventricles.

1.4.1. Mechanisms of cardiac arrhythmias

The most common mechanisms leading to cardiac arrhythmias may be subdivided into *focal activity* due to abnormalities in the formation of the electrical impulses in the heart, such as *abnormal automacity* or *triggered activity*, and conduction disturbances giving rise to the phenomenon usually known as *reentry* (Antzelevitch and Burashnikov, 2011; Tse, 2016).

Tachycardias induced by abnormal automaticity occur when cardiac cells different from the ones forming the two heart pacemakers (SA and AV nodes) begin to depolarize spontaneously, giving rise to the so-called *ectopic beats*. The propagation of such ectopic beats (also termed *extrasystoles*) across the cardiac tissue interfere with the normal electrical activity of the heart triggered from the CCS, thus leading to cardiac rhythm disorders. In the case of triggered activity, the cardiac cells exhibit an altered EP behaviour, such that they depolarize again during or immediately after the repolarization phase of a previous AP, giving rise to the so-called *early* and *delayed afterdepolarizations*, respectively.

Reentry-mediated tachycardias, commonly referred to as *reentrant tachycardias*, arise from the presence of an obstacle, either anatomical or functional, that blocks the electrical propagation, or of regions exhibiting significant conduction delays. Under certain conditions, those conduction anomalies may give rise to the formation of circus-like electrical pathways, known as *reentrant pathways* or *circuits*, through which the activation wavefront can propagate repetitively, again and again, in an electrical loop around the propagation obstacle that leads to an accelerated cardiac rhythm.

1.4.2. Ventricular tachycardia related to chronic MI

Several types of VT are specifically associated with each phase of the MI healing process, as well as with the acute myocardial ischemia (Janse and Wit, 1989; Kaplinsky et al., 1981). Nevertheless, in this work we will focus on the *reentrant monomorphic VT*, which is a VT type whose mechanisms are typically related to the presence of a chronic (or healed) MI in the ventricular

myocardium (Aliot et al., 2009; de Bakker et al., 1988; Issa et al., 2012; Lazzara and Scherlag, 2003).
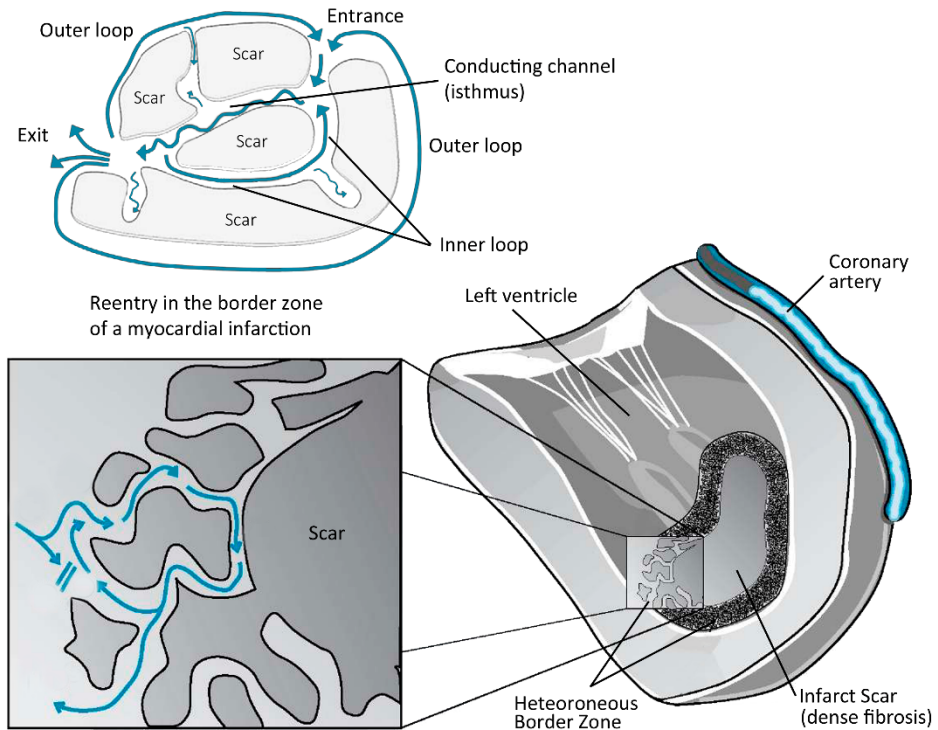
Figure 1.11. Mechanism of reentrant VTs related to chronic MI. Illustration showing the mechanisms leading to VT caused by reentry through the CCs that usually appear within the BZ due to its heterogeneous tissue composition. Images adapted from (Benito and Josephson, 2012) and what-when-how.com/acp-medicine/ ventricular-arrhythmias-part-1/

In the presence of a chronic MI, the dense fibrotic infarct scar represents an anatomical/structural propagation obstacle. Furthermore, the geometry of an infarct scar can be highly irregular, which is usually intermingled with the viable (i.e., conducting) but remodelled myocardial tissue corresponding to the BZ. Several studies have described the BZ as a region of slowed conduction that is structurally heterogeneous, composed of surviving but electrically remodelled myocytes infiltrated with fibrotic patches and bundles extending from the core of compact fibrosis (infarct scar), thus resulting in a highly arrhythmogenic tissue (de Bakker et al., 1993; Nguyen et al., 2014; Rohr, 2012; Rutherford et al., 2012). Such a complex structure makes the infarcted region (including both infarct scar

and BZ) highly prone to the formation of filaments or corridors of conducting tissue completely surrounded by non-excitable tissue (conduction obstacle). Frequently, those viable tissue strands crossing the infarct scar have two or more terminal ends that communicate between them different sites of the conducting myocardium that surrounds the infarcted area (see Figure 1.11). In such a case, these filaments electrically connect distant points of the conducting myocardium, forming the so-called *isthmuses* or *conducting channels* (CC). Hence, as illustrated in Figure 1.11, those CCs constitute electrical circuits that are potentially capable of supporting reentrant activities leading to VTs (Aliot et al., 2009; Benito and Josephson, 2012; de Bakker et al., 1988; de Chillou et al., 2002).

Therefore, several weeks after suffering from an acute ischaemic event causing a MI, when the healing process is already completed, and even months or years later (Issa et al., 2012), a significant number of patients develop life-threatening VTs triggered by reentry through the CCs, as a consequence of the highly arrhythmogenic nature of remodelled and heterogeneous tissue that surrounds the non-conducting infarct scar, that is, the BZ. On the other hand, that kind of infarct-related reentrant VTs usually gives rise to a rapid but stable and well-organized electrical activity in the ventricles, since the activation wavefront travels repetitively following the same reentrant pathway supported by the CC responsible for the VT. Hence, such VTs are commonly identified as monomorphic VTs due to the stable and regular patterns observed in the morphology of the resulting ECG signals (see Figure 1.10) (Aliot et al., 2009; Issa et al., 2012).

1.5. Radiofrequency ablation

The first clinical approach to treat most of cardiac arrhythmias relies on the administration of anti-arrhythmic drugs (Al-Khatib et al., 2018; Katritsis et al., 2017). Nonetheless, frequently those cardiac disorders cannot be properly controlled only by medication, since such drugs are in some cases unable to prevent recurrent arrhythmic episodes or are not well tolerated by the patient. In such cases, radiofrequency ablation (RFA) is a common alternative procedure

useful in the management of several types of both supraventricular (Calkins et al., 2012; Katritsis et al., 2017) and ventricular arrhythmias (Al-Khatib et al., 2018; Aliot et al., 2009).
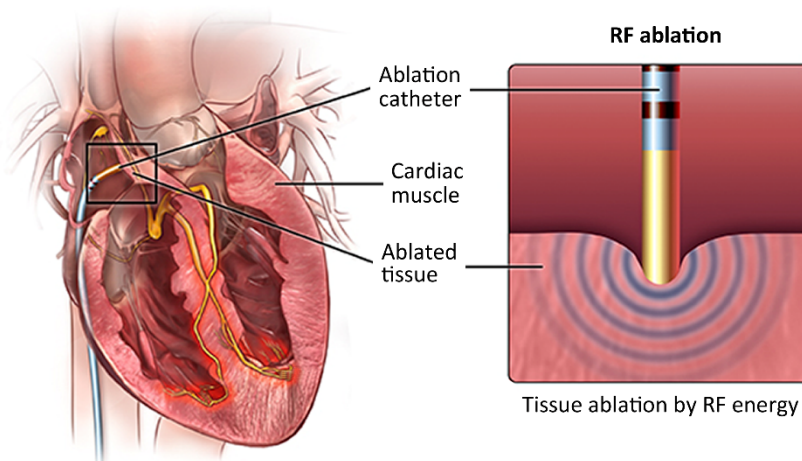
Figure 1.12. Illustration of a RFA ablation procedure, showing the access of cardiac cavities via catheterization (*left*) and the myocardial tissue ablation by the application of radiofrequency (RF) energy through the ablation catheter. Image adapted from the website of *The University of Chicago Medicine*: www.uchicagomedicine.org/conditions-services/heart-vascular/arrhythmias/treatments/ablation-therapy

RFA is a minimally invasive procedure performed by catheterization, which aims to electrically isolate regions triggering ectopic activity or to interrupt reentry circuits, in the case of reentrant arrhythmias. Using an ablation catheter (specific for ablation), the myocardial tissue is cauterized by applying radiofrequency energy (see Figure 1.12), such that the ablated tissue remains unable to propagate the electrical activity after the procedure (Morady, 1999). In the case of reentrant VTs related to chronic MI, the main objective of the RFA procedures is to interrupt or isolate the CCs that act as structural substrates for the reentry pathways (Aliot et al., 2009; Baldinger et al., 2016). Therefore, the CCs responsible for the infarct-related VTs are the RFA targets, aiming to permanently block the propagation through the reentrant circuits (Al-Khatib et al., 2018; Berruezo et al., 2015; Stevenson et al., 1993).

1.6. Electroanatomical mapping

Before any RFA procedure aiming for eliminating a cardiac arrhythmia, usually in the same session indeed, the electrophysiologists perform an intracardiac (i.e., invasive) EP study by means of diagnostic catheters, which are used to explore the cardiac cavities by recording the electrical activity of the myocardial tissue. The main goal of such EP study is to locate the origin of a focal activity or the location of a reentrant circuit based on the features the registered electrograms (EGM), that is, the electrical signals registered directly from the myocardium by the electrodes placed at the catheter tip (Arora and Kadish, 1996).
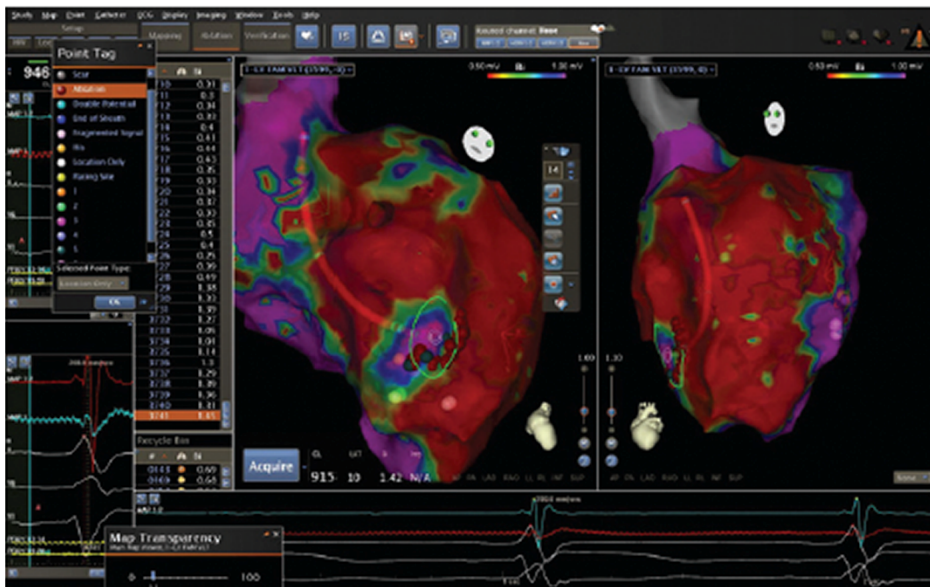
Figure 1.13. CARTO® 3 System. Screenshot of the console of CARTO® software, showing from two different perspectives the 3D surface representing the geometry of the LV endocardium, together with the EGM signals recorded by the intracavitary catheters. The 3D surface is rendered with transparency to allow the visualization of the catheter position, also displaying a colour-code corresponding to the peak-to-peak amplitude of the bipolar EGMs registered at each point in order to generate the electroanatomical map (EAM) of the LV.

The electroanatomical mapping (EAM) systems are advanced technological solutions that appeared in the late 90's (Ben-Haim et al., 1996; Gepstein et al., 1997), which nowadays are commonly employed in the EP laboratory to guide RFA procedures aimed at treating both atrial (Calkins et al., 2012) and ventricular arrhythmias (Aliot et al., 2009; Priori et al., 2015). Those EAM systems, such as CARTO® 3 (Biosense Webster, Diamond Bar, CA, USA)[1], Rhythmia HDx™ (Boston Scientific, Marlborough, MA, USA)[2] or EnSite Precision™ (Abbott, Chicago, Illinois, USA)[3], have the ability to display the recorded EP data onto three-dimensional (3D) surfaces that represent the geometry of the mapped cardiac chambers, as observed in Figure 1.13. Such 3D surfaces are reconstructed thanks to the accurate tracking of the catheter position in every moment, which is performed by means of systems based on electromagnetic fields, rather than the traditional approach based on fluoroscopy (Ben-Haim et al., 1996; Gepstein et al., 1997). Therefore, EAM systems enable a seamless and really useful integration of the EP data recorded by the catheter with the spatial information related to the 3D cardiac geometry. Every registered EGM is linked to a particular point of the reconstructed 3D surfaces, thus generating the so-called *electroanatomical maps* (EAMs) by displaying the measured EP data mapped onto the 3D representations of the cardiac cavities (see Figure 1.13). Furthermore, these systems allow an important reduction of the radiation exposure due to fluoroscopy, both for the patient and for the health personnel performing the EP study.

In the case of infarct-related VTs, EAM systems are considered as a really helpful tool to identify the precise location of CCs as RFA targets (Al-Khatib et al., 2018; Aliot et al., 2009), based on the abnormal features of the EGM registered from the infarcted region (Bogun et al., 2005; Gardner et al., 1985) in combination with its accurate position represented on the 3D reconstruction of the mapped cardiac chambers.

---

[1] CARTO® 3 System: www.biosensewebster.com/products/carto-3.aspx
[2] Rhythmia HDx™ Mapping System: www.bostonscientific.com/en-US/products/capital-equipment--mapping-and-navigation/rhythmia-mapping-system.html
[3] EnSite Precision™ Cardiac Mapping System: www.cardiovascular.abbott/int/en/hcp/products/electrophysiology/ensite-precision-cardiac-mapping-system.html

1.7. Three-dimensional cardiac imaging

Currently, 3D imaging modalities, such as computed tomography (CT) or magnetic resonance imaging (MRI), are widely used in clinical cardiology for the assessment of both cardiac structure and function (Constantine et al., 2004; Hundley et al., 2010; Sheth et al., 2015). However, due its position and orientation within the thorax, the heart is not aligned with the orthogonal axes of the human body: axial, sagittal and coronal planes. Therefore, the 3D images aimed at exploring the heart are usually reformatted (or directly acquired when possible) into the specific cardiac planes represented in Figure 1.14: *short-axis*, *long-axis* or two-chamber view, and *four-chamber view*, which correspond to the axial, sagittal and coronal planes of the heart, respectively.
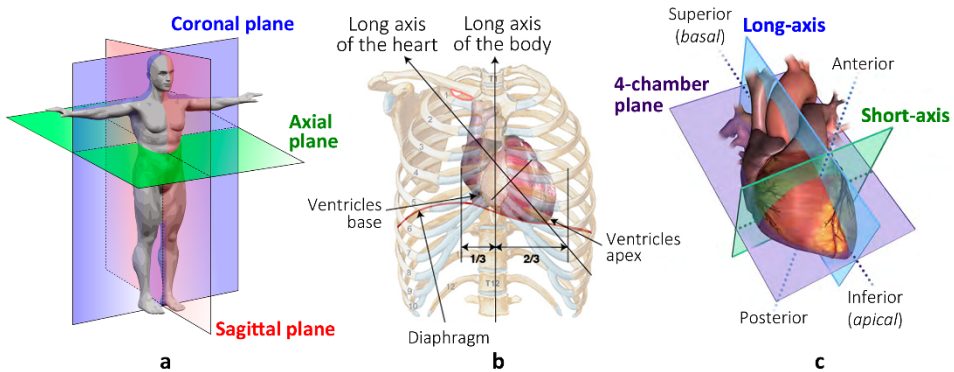
Figure 1.14. (*a*) Representation of the three orthogonal planes of the human body: axial, sagittal and coronal. (*b*) Illustration showing the orientation of the longitudinal axis of the heart with respect to the longitudinal axis of the body. (*c*) Definition of the three orthogonal planes of the human heart: short-axis (*axial*), long-axis or two-chamber plane (*sagittal*) and four-chamber plane (*coronal*).

In the context of MI and their related VTs, the use of various modalities of 3D cardiac imaging also represents a common tool for diagnosis and therapy planning in the current clinical workflow (Baritussio et al., 2018; Mahida et al., 2017). Those 3D imaging datasets allow the cardiologists to evaluate non-invasively the myocardial ischaemic injury, as well as the contractility and mechanical performance of the infarcted ventricles.

Delayed enhancement-MRI (DE-MRI), also termed late gadolinium enhancement (LGE), is a MRI modality that enables assessing *in-vivo* and non-invasively the precise location and extension of the damaged tissue (including the infarct scar and BZ) due to the hyper-enhancement of the infarcted region in the images (see Figure 1.15) caused by a gadolinium-based contrast agent (Doltra et al., 2013; Fieno et al., 2000; Kim et al., 1999a). In fact, cardiac DE-MRI is currently considered as the gold-standard test for *in-vivo* assessment of fibrotic scars and myocardial viability after MI in clinical settings (Jamiel et al., 2017; Mahida et al., 2017; Patel et al., 2017). In combination with the contrast agent, this MRI modality provides a substrate characterization in the different stages of the MI, from the acute ischaemia to chronic MI, that has shown close correlation with histopathological analyses (Amado et al., 2004; Fieno et al., 2000; Kim et al., 1999a; Wagner et al., 2003).
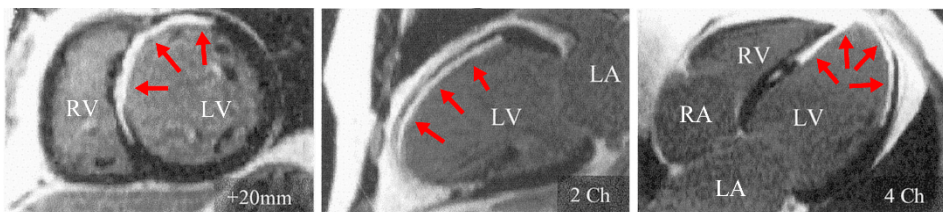
Figure 1.15. Slices from a cardiac DE-MRI dataset, oriented in the three cardiac planes: short-axis (*left*), long-axis or two-chamber view (*centre*) and four-chamber plane (*right*). *Red arrows* indicate the hyper-enhanced regions in the images resulting from the presence of the gadolinium-based contrast agent within the infarcted myocardium. LV: left ventricle; RV: right ventricle; LA: left atrium; RA: right atrium.

Chapter 2

Motivation and Objectives

In this second chapter, we begin by outlining the background and the motivation that promoted the conception and the implementation of this thesis. After that, we describe the objectives pursued by this thesis, both the main general aim and the specific goals that must be fulfilled in order to reach the main objective. Lastly, we present a description of the structure of this document aiming to give an overview of how this thesis has been organized.

2.1. Motivation

Despite the medical and technological advances, cardiovascular disease represents the leading cause of both mortality and morbidity in the world, being responsible for nearly 18 million deaths annually worldwide (WHO, 2018). A large number of deaths related to cardiac malfunction result from rapid tachycardias developed on the structurally diseased (remodelled) ventricular myocardium, such as ventricular fibrillation, which usually leads to sudden

cardiac death (Priori et al., 2001, 2015). Moreover, the morbidity associated with cardiac electrical disorders (i.e., cardiac arrhythmias) constitute a major burden on the health care system worldwide. Only in Europe the annual health care direct costs derived from cardiovascular disease is estimated to be of €111 billion, increasing up to €210 billion when the overall impact on European economy is considered (Wilkins et al., 2017). Novel electrical therapies have rapidly proven to be cost effective and have become part of the international recommendations. However, the large amount of disparate data that may be currently considered by the electrophysiologists is overwhelming and, therefore, remain very difficult to integrate in order to be fruitfully used for patients' stratification and therapies' optimization. Hence, the high economical and epidemiologic burden associated with cardiovascular disease worldwide demands new methodologies and technology-based tools able to improve patient management and therapy planning.

Among cardiovascular diseases, the ischaemic heart disease (or coronary artery disease) is the most common one (Abubakar et al., 2015; Nowbar et al., 2014). After surviving to an episode of acute myocardial infarction (MI) due to a coronary artery occlusion, a considerable number of patients develop potentially lethal ventricular tachycardias (VT) during the chronic stage of the MI, that is, weeks, months or even years after the acute ischaemic event (Issa et al., 2012). Those VTs related to chronic MI are usually triggered by reentry (reentrant VTs), as a consequence of the highly arrhythmogenic nature of the heterogeneous and remodelled tissue composing the border zone (BZ) that surrounds the infarct scar (Aliot et al., 2009; de Bakker et al., 1988, 1993; Lazzara and Scherlag, 2003; Nguyen et al., 2014). Such infarct-related reentrant VTs are typically linked to well-defined reentrant circuits mediated by slow conducting channels (CC), formed by strands of surviving myocytes that traverse the non-conducting infarct scar, thus leading to monomorphic VTs (Aliot et al., 2009; de Bakker et al., 1988; Issa et al., 2012).

In those cases in which the anti-arrhythmic medication fails to prevent recurrent VT episodes, radiofrequency ablation (RFA) is commonly used in order to interrupt permanently the electrical conduction across the CCs acting as structural substrates for the reentrant circuit associated with the VT, thus

avoiding the reentrant activity responsible for the infarct-related VT (Baldinger et al., 2016; Berruezo et al., 2015; de Chillou et al., 2002; Stevenson et al., 1993; Wilber, 2008).

Currently, cardiac delayed enhancement-MRI (DE-MRI) is widely used to explore the infarcted myocardium prior to the RFA procedures, since it provides a helpful and non-invasive characterization of the VT substrate, even allowing to differentiate between the infarct scar and the viable myocardial tissue corresponding to the BZ. Indeed, the potential usefulness of the pre-procedural substrate characterization and CCs delineation based on DE-MRI for planning and guiding ablation procedures aimed at infarct-related VTs has already been assessed in numerous studies (Andreu et al., 2011, 2015, 2017; Ashikaga et al., 2007; Fernández-Armenta et al., 2013; Perez-David et al., 2011; Soto-Iglesias et al., 2016; Wijnmaalen et al., 2011; Yamashita et al., 2016).

Following the usual approach, the patients suffering from recurrent infarct-related VTs are normally subject to an invasive electrophysiological (EP) study performed via catheterization immediately before the RFA procedure. During those EP studies, the interventional electrophysiologists try to induce the clinical VT previously undergone by the patient, by means of pacing protocols applied at selected sites of the ventricular myocardium. A positive induction of a monomorphic VT is considered as an evidence of the presence of a reentrant pathway responsible for the VT, likely mediated by a CC associated with the chronically infarcted myocardium (Pedersen et al., 2014; Priori et al., 2015). Then, the specialists usually compare the morphology of the ECG resulting from the induced VT with the ECG registered during the clinical VT episodes in order to discern whether both VTs match or, on the contrary, they are different VTs. In the case of positive correlation, the physicians aim to locate and ablate the CCs linked to the clinical VT in order to block the propagation through the reentrant circuit, thereby avoiding the reentry and, consequently, the recurrent VT onset.

The electroanatomical mapping (EAM) systems are nowadays of great help in locating the critical CCs and defining the optimal ablation targets, because of their ability to integrate in an intuitive 3D representation the EP data

and the geometrical information registered by the diagnostic catheters during the EP study. They are especially helpful when the clinical VTs are unmappable due to non-inducibility (pacing protocols fail to induce the VT) or hemodynamic instability, since the EAM maps allow to correlate every registered electrogram (EGM) to a particular point onto the 3D representation of the mapped cardiac cavity, including those EGMs showing abnormal features typically associated with the CCs (Aliot et al., 2009; Marchlinski et al., 2000; Priori et al., 2015). Nevertheless, these EP studies are invasive, risky and very time-consuming. Moreover, despite the use of EAM systems, they show a relatively low success rate, since up to 50% of patients experience recurrent VT episodes after the RFA procedure, consequently needing for one or more successive re-interventions (Aliot et al., 2009; Baldinger et al., 2016; Gerstenfeld, 2013; Yokokawa et al., 2013).

In contrast to the invasive EP studies guided by EAM systems, an alternative non-invasive approach for the pre-procedural exploration of the target substrate, aiming for planning RFA procedures, is the use of personalized image-based 3D computational cardiac models able to perform accurate simulations of the EP behaviour of the heart. As a result of the intensive research in the field of *computational cardiac EP*, in the last decade these simulation-based strategies have exhibited the potential to carry out reliable *in-silico* EP studies, which might be of great help in gaining insights into the mechanisms underlying to a wide variety of cardiac disorders (Arevalo et al., 2016; Krueger et al., 2013a; Lopez-Perez et al., 2015; Smith et al., 2011; Trayanova et al., 2012, 2017; Trayanova and Boyle, 2013; Vigmond et al., 2009). Hence, these non-invasive approaches could potentially improve the understanding and prediction capability of a number of pathological conditions related to cardiac EP and, therefore, aid in developing better strategies for the diagnosis, therapy planning and management of numerous cardiac diseases.

Nonetheless, despite the considerable potential shown by those *in-silico* approaches, a number of important questions related to the necessary level of detail required by the computational cardiac models remain unanswered. Such issues concern the degree of anatomical and structural detail at organ and tissue level, respectively, as well as the biophysical faithfulness of the cardiac EP

modelling strategies. In the particular case of chronic MI, for instance, the influence on the mechanisms related to the onset and sustenance of reentrant VTs, derived from the specific manner in which the microscopic structural and functional tissue remodelling in the infarct BZ are included in the macroscopic 3D models, still has to be fully investigated. In fact, the personalization and modelling of certain key components of the computational cardiac models are still challenging, as it is the case of the critical region of the infarct BZ (Mendonca Costa et al., 2018). On the other hand, the degree of model personalization necessary for accurate simulation of patient-specific VT episodes also remains a matter of debate. The question concerning the requirement of only personalized cardiac anatomy or, on the contrary, the additional need of incorporating functional personalization related to patient-specific cardiac EP, must also be clarified as an essential feature for the construction of 3D cardiac computational models aiming for therapy planning based on personalized *in-silico* EP studies.

2.2. Objectives

The main general objective of this doctoral thesis is to develop a full pipeline, exclusively based on non-invasive clinical data, to generate patient-specific 3D computational models of infarcted ventricles and torso able to perform personalized *in-silico* EP studies. Such studies must include computational simulation of cardiac EP at both organ (ventricles) and torso level in order to obtain the simulated ECGs, since their results must be compared to the non-invasive standard clinical recordings of the patient (i.e., the patient's real ECG) aiming to replicate the decision-making process commonly followed by the specialists in the EP laboratory based on comparing the ECGs from clinical and induced VTs. The final goal is to develop a non-invasive strategy based on computational simulation capable of aiding electrophysiologists in the planning of RFA procedures aimed at reentrant VTs related to chronic MI, by means of pre-procedural (i.e., prospective) personalized *in-silico* EP studies.

2.2.1. Specific objectives

To achieve the main general objective of this thesis, we divided that major goal into the specific (partial) objectives listed below.

- Comprehensive review of the existing bibliography related to the development of 3D cardiac computational models aimed at biophysical simulation, not restricted to, but specially focused on, the simulation of cardiac EP. This task was planned as the first specific objective of this thesis aiming to gain a deep knowledge about all the methods used and the features included in the 3D cardiac models previously developed for biophysical simulation, thereby serving as a guide to ensure a proper development of the subsequent stages of this thesis.

- Definition of the non-invasive clinical datasets required to construct patient-specific 3D models of infarcted ventricles and torso.

- Design and implementation of an approach to generate personalized and detailed 3D models of infarcted ventricles able to perform simulations of cardiac EP.

  - Definition and implementation of a methodology to obtain 3D reconstructions of patient-specific ventricles anatomy from clinical DE-MRI datasets.

  - Definition and implementation of a methodology to obtain 3D reconstructions of patient-specific infarction geometry from clinical DE-MRI datasets, including the infarct scar and the BZ.

  - Definition and implementation of a methodology to incorporate the cardiac fibres orientation into the 3D ventricular model.

- Development and implementation of a novel image-based approach to include personalized patterns of structural remodelling within the region of the BZ.

- Development and implementation of a methodology to interpret the EP data invasively registered via CARTO® 3 System and to integrate them with the constructed 3D ventricular models, only for testing and validating purposes.

- Design and implementation of a strategy to generate personalized 3D models of the torso from clinical imaging datasets.

- Design and implementation of a strategy to model and reproduce, by using computational simulation, the EP behaviour of the following cardiac tissues in simulations at the organ level.

    - Healthy ventricular myocardium.

    - Dense fibrotic tissue, corresponding to the infarct scar.

    - Heterogeneous tissue corresponding to the BZ, defining several modelling approaches including different degrees of both electrical and structural remodelling.

- Design and implementation of a methodology to compute the simulated ECGs using the built 3D torso models.

- Definition of a simulation pipeline to assess the VT inducibility by means of personalized *in-silico* EP studies, making use of the 3D models of infarcted ventricles and torso previously developed.

- Performance of a simulation case study aiming to assess the feasibility and the ability of the proposed approach to:

    - Reproduce the patient's cardiac EP during sinus rhythm, including the ECG, as a first validation step for the developed approach.

- Replicate the infarct-related clinical VTs suffered by the patient, including the ECG, in order to test the predictive capability and accuracy of the developed approach.

- Locate the CCs responsible for the clinical VTs to help in the definition of the optimal ablation targets prior to the actual RFA procedure, in order to assess the potential usefulness in therapy planning of the developed approach.

- Additionally, this simulation case study will allow evaluating the arrhythmogenic impact of the different modelling approaches proposed for the BZ.

2.3. Structure of the thesis

In this final section of this second chapter, we give an overview of the structure of this doctoral thesis, briefly describing the content of each of their main sections. This thesis document is composed of nine chapters, which are organized as follows.

Chapter 1 – Introduction briefly addressed a number of concepts that compose the fundamentals of this thesis. Those concepts had to be clearly introduced, since we will be referring to them throughout the entire thesis document.

Chapter 2 – Motivation and Objectives has exposed the rationale that promoted the development of this thesis, as well as the main goals that are expected to achieve.

Chapter 3 – Three-dimensional Cardiac Computational Modelling presents a thorough review on the field of 3D cardiac models aimed at biophysical simulation, describing the evolution through the last decades of the features and methods associated with such models, with a special focus on their application to computational cardiac EP. It also presents a comprehensive table of 3D cardiac models, including detailed information about the features and methods related to each of the 60 models that we revised exhaustively.

Chapter 4 – Clinical Data describes the clinical dataset that we used in this thesis, together with the main methods that we employed in order to pre-process those data.

Chapter 5 – Three-dimensional Computational Models of Infarcted Ventricles and Torso presents a detailed description of the pipeline that we designed aiming to build patient-specific 3D models of infarcted ventricles and torso from clinical imaging datasets.

Chapter 6 – Electrophysiological Modelling is devoted to describe the EP models, along with all the assumptions and strategies that we used to reproduce the human cardiac EP at both organ (ventricles) and body level by computational simulation.

Chapter 7 – Personalized Electrophysiological Study using Computational Simulation provides a detailed description of the simulation pipeline proposed in this thesis to perform personalized EP studies by computational simulation, aiming for therapy planning in cases of infarct-related VTs. It also presents the results obtained from the simulation case study that we conducted in order to test the developed approach and, furthermore, a preliminary discussion about those results.

Chapter 8 – Discussion presents a comprehensive critical discussion that addresses all the concerns raised in this thesis and compares it to the related literature. That chapter deals with the numerous methods used and decisions made in order to construct the 3D models and simulate the cardiac EP, as well as with the results obtained from the computational simulations performed, along with the conclusions derived from them.

Finally, *Chapter 9 – Conclusions and Perspectives* exposes the main overall conclusions derived from the final results of this doctoral thesis, as well as a brief reflection on the future perspectives of the image-based simulation approach proposed, including the major improvements that it requires.

Chapter 3

Three-Dimensional Cardiac Computational Modelling

This chapter is based on a review article entitled "*Three-dimensional cardiac computational modelling: methods, features and applications*" (Lopez-Perez et al., 2015), which was written by the author and both supervisors of this doctoral thesis and published in 2015 in the journal *BioMedical Engineering OnLine*, a peer-reviewed journal indexed in the JCR (journal citation reports). That publication was the result of the fulfilment of the task planned as the first objective for this thesis (see Chapter 2), which was a comprehensive analysis of the current *state-of-the-art* on three-dimensional (3D) cardiac computational modelling, as well as a thorough study of the evolution of such field of research from its beginning.

3.1. Introduction

This chapter presents a review of the methods used to construct 3D cardiac computational models, from their earliest developments (about fifty years ago) until today, also discussing their advantages and applicability to different areas. Since reviewing the entire literature related to the development of 3D cardiac computational models would be an insurmountable task, we conducted a systematic review based on an extensive bibliographic search, from which we finally chose 60 cardiac models. We consider that those 60 models are a representative set of examples that are suitable to outline the evolution of 3D cardiac computational modelling from its dawn. Therefore, we thoroughly analysed those representative models to explore the evolution of methods used to develop 3D cardiac models over the last decades.

As a main result of this review work, we produced a detailed summary table (see Table 3.2 at the end of this chapter) that lists in chronological order the 60 reviewed 3D cardiac computational models, which were developed and published over the last fifty years. This table provides information about the main features and specific methods used in the different stages of the development process of each reviewed model, also describing their information sources and online availability.

This chapter is organised as follows. First, we give a very brief overview of the current state of the art of 3D cardiac computational modelling. Then, we outline the evolution of 3D cardiac models from the '*early era*' to the present days, focusing on the methods used for the computational reconstruction of cardiac anatomy. Later, we address the different stages of the development process of 3D cardiac models (3D reconstruction of cardiac anatomy, meshing, etc.), reviewing the available methods to construct models and to include certain heart features (fibre orientation, cardiac conduction system, ischaemic scars, etc.) in those computational models aimed at biophysical simulation, with especial attention to cardiac electrophysiology (EP). The next section briefly describes the available personalization approaches in 3D cardiac computational modelling. After that, we address some uses of 3D cardiac models by presenting examples related to several specific applications, focusing on cardiac EP

simulation and model-based image segmentation. Finally, this chapter exposes the table of 3D cardiac computational models, summarizing the key features of the 60 models the we thoroughly reviewed (Table 3.2).

3.2. Overview

Some decades ago, the early 3D cardiac computational models only enabled to perform very simple computational simulations of cardiac EP or cardiac mechanics analysis. Nevertheless, at present the combination of 3D computational models and biophysical simulation can help to interpret jointly a variety of experimental data, thus contributing to the understanding, diagnosis and treatment of complex diseases such as cardiac arrhythmias. For this reason, 3D cardiac computational modelling, sometimes also referred to as computational cardiology, is currently a rising field of research.

Nowadays, 3D cardiac models are becoming increasingly complex and are being used in several areas, such as cardiac image segmentation, statistical modelling of cardiac anatomy, patient risk stratification or surgical planning. In fact, some model-based methods are already being tested in clinical environments for diverse applications: diagnosis based on automated 3D cardiac image analysis, therapy planning and guidance in procedures such as radiofrequency ablation (RFA), etc. Furthermore, the great progress of medical imaging technologies over the last decades has allowed the evolution from generic 3D cardiac models to detailed patient-specific models, which are capable of faithfully representing the anatomy and different cardiac features of a given alive subject.

In conclusion, the integration of advanced 3D cardiac computational models into clinical environments is becoming more feasible due to the evolution of computing resources and the intensive research in fields such as computational simulation of cardiac EP and mechanics or model-based cardiac image analysis.

3.3. Evolution of 3D models of cardiac anatomy

The first step in the development process of a 3D cardiac model is the computational reconstruction of the heart anatomy by generating a 3D cardiac geometry. In this section, we present a brief survey of the evolution of 3D cardiac models, focusing on the methods used to build the computational reconstruction of cardiac anatomy, and highlighting the achieved level of anatomical detail.
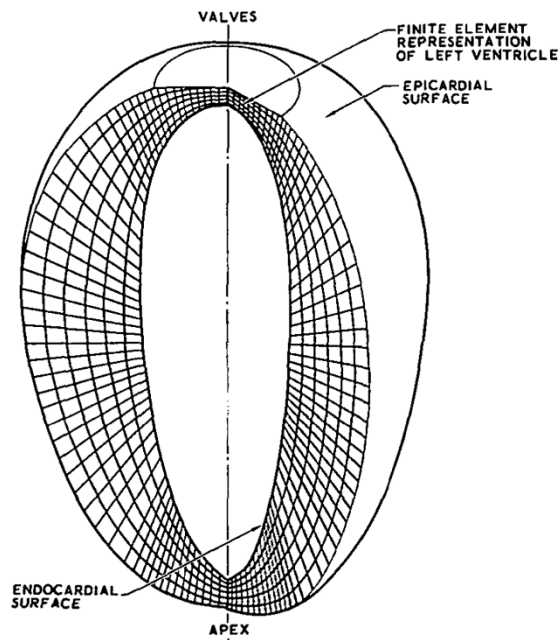
Figure 3.1. LV model based on ellipsoids of revolution truncated at the base, showing the subdivision of the ventricular wall into 198 hexahedral finite-elements. Reproduced from (Janz and Grimm, 1972)

3.3.1. Generic models

The early 3D computational models of cardiac anatomy were simplistic models based on geometric shapes. As shown in Figure 3.1, most of them only included the left ventricle (LV), represented by two concentric ellipsoids truncated at the base level to roughly approximate the shape of the LV (Colli

Franzone et al., 1998; Ghista and Sandler, 1969; Janz and Grimm, 1972; Koushanpour and Collings, 1966; Van den Broek and Van den Broek, 1980). However, this approach is still in use for specific applications in which the anatomical realism is not crucial for the purpose of the model (Kerckhoffs et al., 2003; Sermesant et al., 2006b).
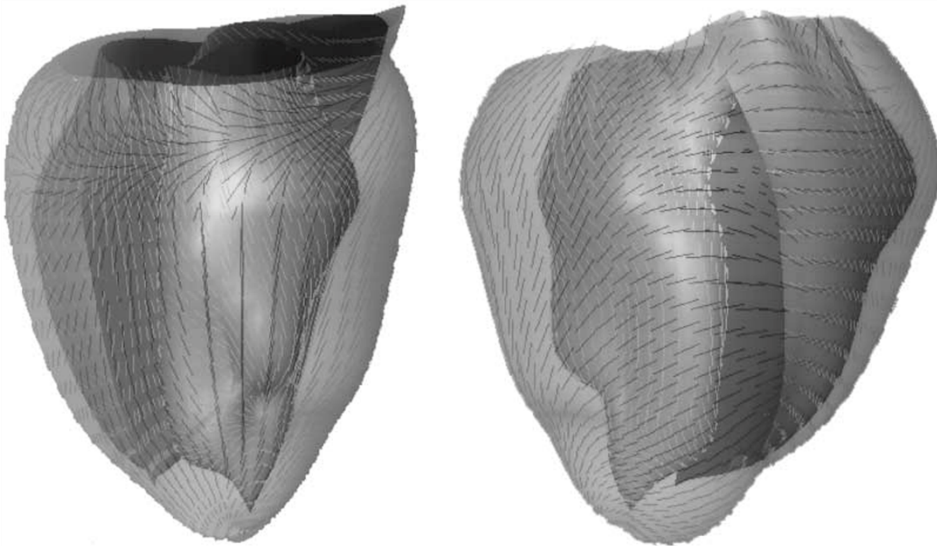
Figure 3.2. Rabbit bi-ventricular model from University of California San Diego. Anterior (*left*) and postero-lateral (*right*) views of the fitted 3D finite-element mesh of the model showing interpolated fibres displayed on epicardial and endocardial surfaces. Adapted from (Vetter and McCulloch, 1998)

Later, anatomical models appeared aiming to represent cardiac anatomy in a more realistic fashion, although still with a low level of anatomical detail due to the poor quality of the data used to build them. They were usually constructed by manual drawing from histo-anatomical slices (Horan et al., 1978; Miller and Geselowitz, 1978; Okajima et al., 1968; Vetter and McCulloch, 1998) or from measurements taken on explanted hearts (Nielsen et al., 1991; Stevens et al., 2003), or by segmenting pictures of histo-anatomical slices (Aoki et al., 1987; Freudenberg et al., 2000; Thakor and Eisenman, 1989; Trunk et al., 2007). Among these anatomical models, the most representative ones are two bi-ventricular models highly referenced in the literature and very reused in later works. They are the rabbit model from University of California San Diego (Vetter

and McCulloch, 1998) (see Figure 3.2) and the canine model from University of Auckland (Nielsen et al., 1991). Their main contribution was the inclusion of realistic cardiac fibre orientation obtained from experimental measurements.

The development of computer-aided design (CAD) tools enabled the construction of 3D cardiac models without any direct source of anatomical information (Bodin and Kuz'min, 2006; Harrild and Henriquez, 2000; Ruiz-Villa et al., 2009; Siregar et al., 1998). Their developers just took from the literature measurements of some anatomical details, such as chambers volumes or wall thickness, in order to virtually generate the model geometry. Figure 3.3 shows an example of a whole-heart CAD model (Siregar et al., 1998).
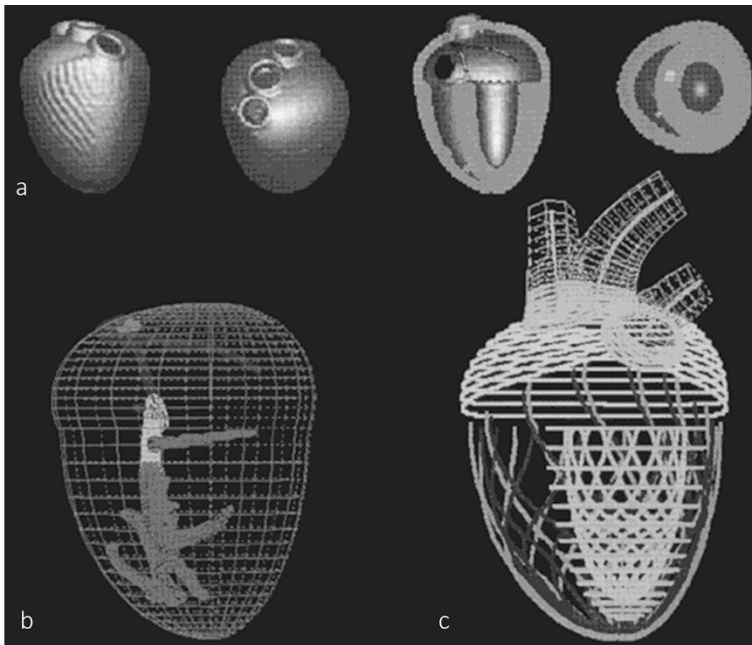
Figure 3.3. Whole-heart CAD model. (*a*) Different views of the volume rendering of the 3D cardiac model. (*b*) Wireframe representation showing the cardiac conduction system (CCS) included in the 3D model. (*c*) Wireframe representation showing the main cardiac vessels (aorta, pulmonary trunk and superior vena cava). Reproduced from (Siregar et al., 1998)

Atrial 3D models began proliferating later than ventricular ones for several reasons, such as the challenges associated with its 3D reconstruction due to the high complexity and inter-subject variability of atrial anatomy. Figure 3.4

shows the first 3D cardiac computational model of human atria developed in 2000 (Harrild and Henriquez, 2000). Probably, the higher lethality of ventricular disorders compared to atrial ones could be another important reason for this delay in the appearance of atrial models aimed at biophysical simulation. It seems logical to think that early 3D cardiac modellers preferred to devote their efforts to studies related to the most clinically relevant issues. Nevertheless, all kinds of model described above are present among reviewed 3D atrial models: geometric models (Blanc et al., 2001), CAD models (Harrild and Henriquez, 2000; Ruiz-Villa et al., 2009) and anatomical models from histo-anatomical slices (Seemann et al., 2006; Zemlin et al., 2001; Zhao et al., 2013).
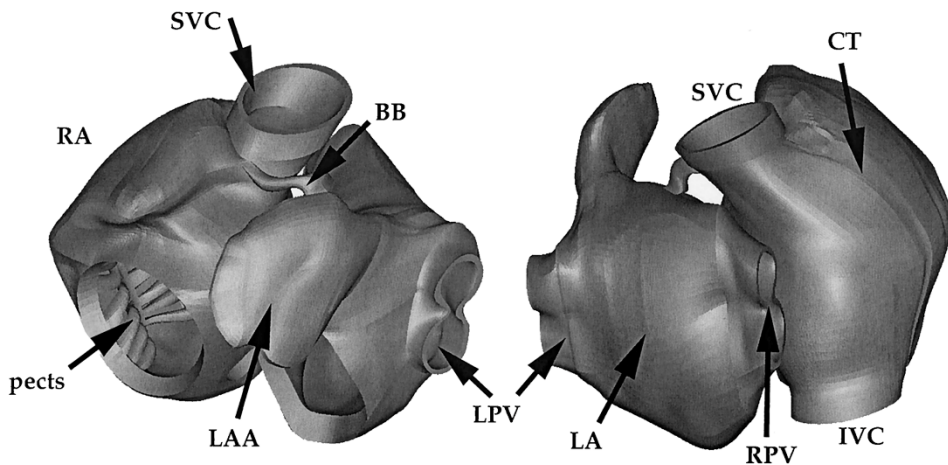
Figure 3.4. Anterior (*left*) and posterior (*right*) views of a CAD model corresponding to the first 3D cardiac computational model of human atria. RA: right atrium. LA: left atrium. pects: pectinate muscles. SVC: superior vena cava. IVC: inferior vena cava. LPV: left pulmonary vein. RPV: right pulmonary vein. BB: Bachmann's bundle. CT: crista terminalis. Reproduced from (Harrild and Henriquez, 2000)

3.3.2. Medical image-based models

The evolution of medical imaging technologies introduced the possibility of building realistic 3D cardiac models from either *in-vivo* or *ex-vivo* images, as demonstrated by early works (Creswell et al., 1992) and (Lorange and Gulrajani, 1993), respectively. Medical image-based 3D cardiac models have proliferated over the last two decades, due to the advance and consolidation of techniques

such as magnetic resonance imaging (MRI) (Arevalo et al., 2008; Gurev et al., 2011; Heidenreich et al., 2010a; Helm et al., 2005; Plotkowiak et al., 2008; Virag et al., 2002; Winslow et al., 2000) and computed tomography (CT) (Aslanidi et al., 2013; Deng et al., 2012), what led to the rise of 3D cardiac computational modelling. As will be discussed below, the development of new imaging modalities capable of providing structural and functional information of cardiac tissue was also a major breakthrough in 3D cardiac computational modelling.
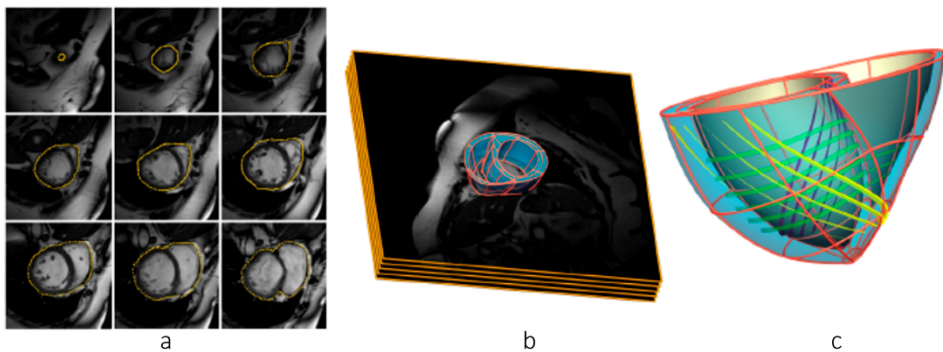
Figure 3.5. Patient-specific bi-ventricular model. (*a*) Set of *in-vivo* cardiac MRI slices showing manually segmented epicardial contour. (*b*) 3D cardiac model overlaid on the MRI stack. (*c*) Finite-element mesh with tri-cubic Hermite elements showing lines corresponding to the main direction of cardiac fibre orientation at epicardial (*yellow*), mid-wall (*green*) and endocardial (*purple*) level. Reproduced from (Niederer et al., 2009)

The increasing availability of *in-vivo* cardiac images, together with the rising trend towards personalized medicine, led to the appearance of *patient-specific* models. They represent the cardiac anatomy of a specific human subject derived from *in-vivo* images, usually MRI (Appleton et al., 2006; Haddad et al., 2005; Niederer et al., 2009) or CT (Romero et al., 2010; Yang et al., 2006). Figure 3.5 shows a patient-specific bi-ventricular model built from *in-vivo* MRI (Niederer et al., 2009). Building this kind of model requires imaging techniques synchronised with the ECG and breathing in order to overcome the noise and motion artefacts due to the cardiac cycle and breathing movements. Such techniques have also enabled building dynamic models, which include the intra-subject anatomical variations of the heart due to the cardiac cycle (Appleton et al., 2006; Haddad et al., 2005).

Cardiac atlases also appeared thanks to the increasing availability of *in-vivo* images. This kind of cardiac models are assembled by averaging several 3D cardiac image datasets from a population of subjects, thus generating a mean 3D cardiac image or shape (for further details about cardiac atlases see section 3.6.1). For instance, Lorenzo-Valdés *et al.* developed a bi-ventricular cardiac atlas from 14 manually segmented cine-MRI images (Lorenzo-Valdés et al., 2002) and Ordas *et al.* constructed a whole-heart atlas using *in-vivo* multislice-CT (MS-CT) images from 100 human subjects (Ordas et al., 2007) (see Figure 3.6).
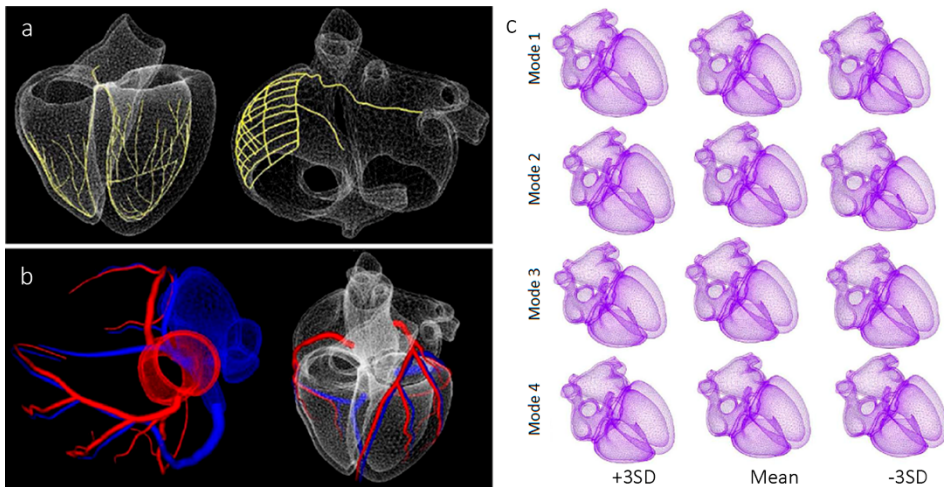
Figure 3.6. Whole-heart cardiac atlas constructed using MS-CT images from 100 human subjects. (*a*) Wireframe representation of the atlas showing the representation of the CCS included in the model at ventricular (*left*) and atrial level (*right*). (*b*) Wireframe representation showing the model of the main coronary vessels included in the cardiac atlas. (*c*) The four principal modes of variation of the whole-heart atlas. Adapted from (Ordas et al., 2007)

There are a few highly-detailed bi-ventricular models that deserve a special mention. All these models were built from very high-resolution *ex-vivo* MRI datasets (~25 μm per slice) from small mammalian hearts (rat, rabbit, etc.), showing an outstanding level of anatomical detail, including papillary muscles, endocardial trabeculations and even intra-myocardial vessels. Some of them also include detailed information at the tissue level provided by histological sections with specific staining (Burton et al., 2006; Plank et al., 2009). Figure 3.7 shows an example of a highly detailed rabbit bi-ventricular model (Bishop et al., 2010).
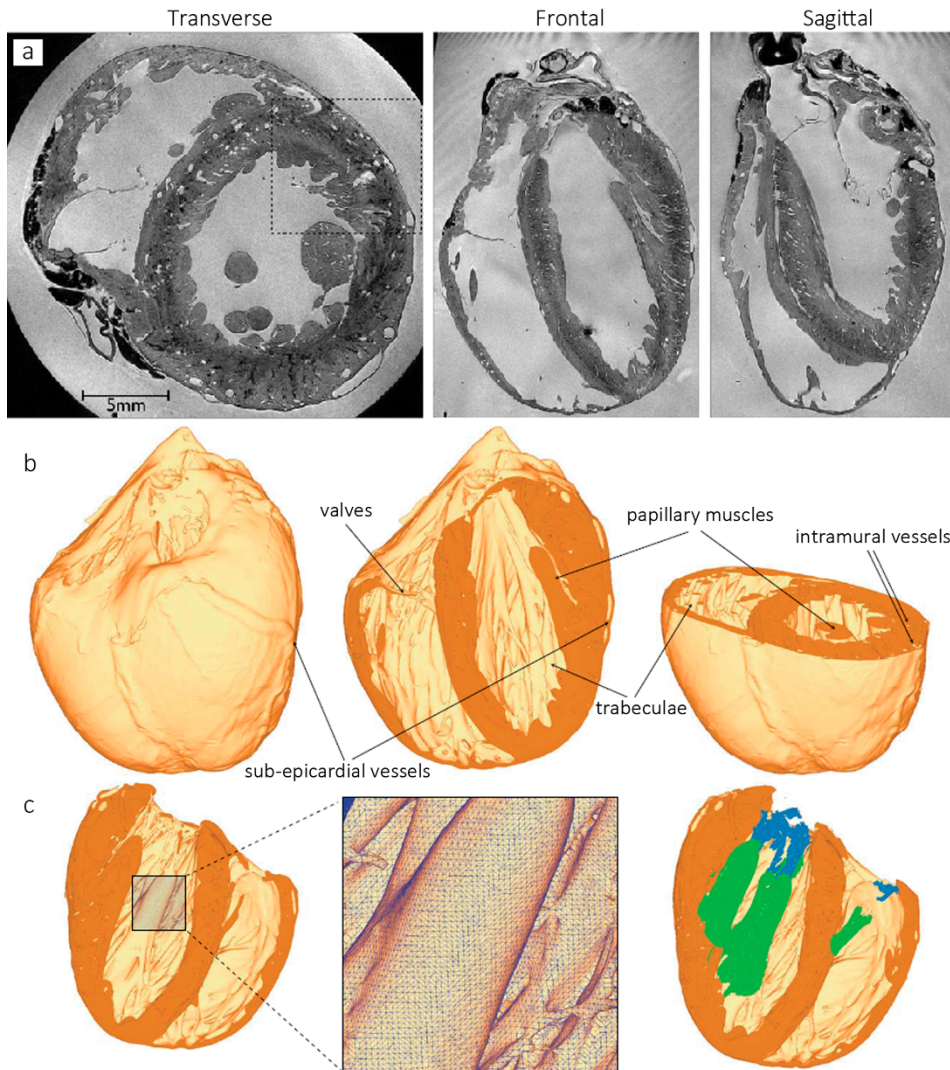
Figure 3.7. Highly detailed rabbit bi-ventricular model. (*a*) Sample of slices in different cardiac planes of very high-resolution *ex-vivo* MRI. (*b*) 3D rendering of the model, showing its high level of anatomical detail. (*c*) Detail of the tetrahedral finite-element mesh, showing the papillary muscles *(green)* and even the chordae tendineae *(blue)*. Adapted from (Bishop et al., 2010)
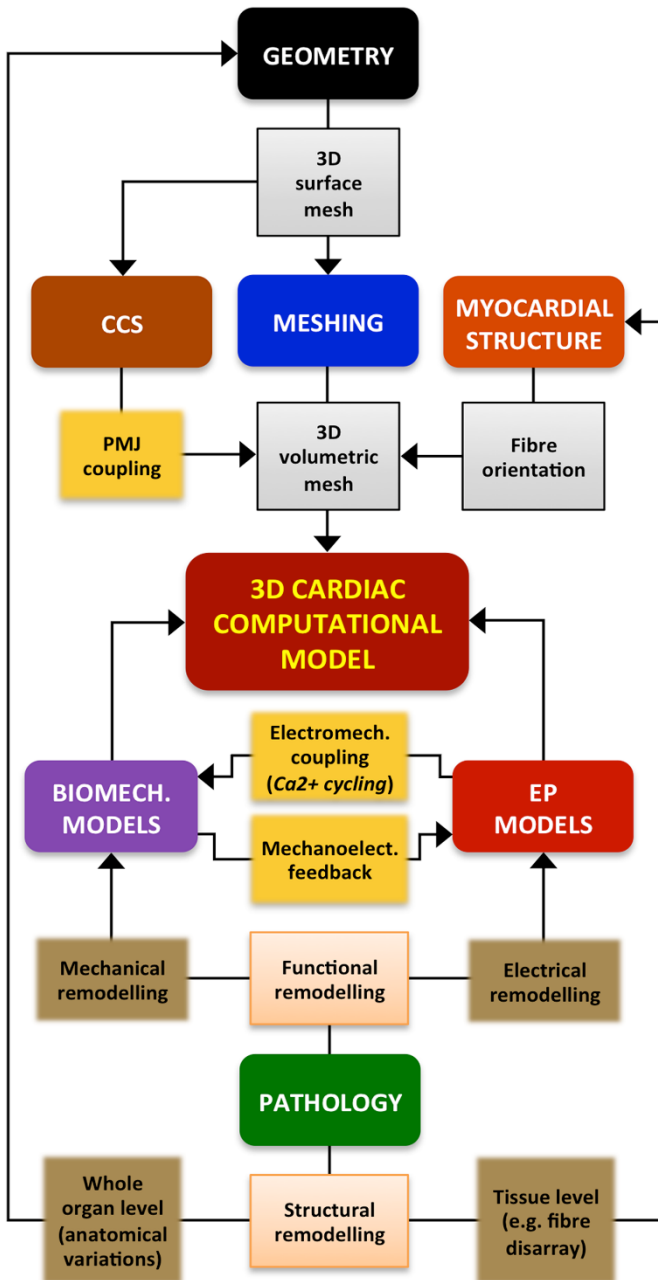
Figure 3.8. Schematic representation of the pipeline to build a 3D cardiac computational. This flowchart shows the main stages in the construction process of a 3D cardiac model aimed at biophysical simulation: 3D cardiac geometry generation, meshing, CCS generation, myocardial structure generation, biophysical modelling (cardiac EP and biomechanics) and cardiac pathology modelling. Lines and arrows depict the relationships between different stages by means of partial results (*grey boxes*) and coupling steps (*yellow boxes*). For pathology modelling, the diagram shows different types (*light orange boxes*) and subtypes (*brown boxes*) of cardiac pathology that can be included in a cardiac computational model, as well as the stage of the development process in which each kind of pathology should be consider. Reproduced from (Lopez-Perez et al., 2015)

3.4. Elements of a 3D cardiac computational model

In addition to the 3D geometry representing the cardiac anatomy, either fully or partially, every 3D cardiac computational model may also include many other elements: specific properties related to the cardiac tissue architecture, pathologies affecting the myocardial structure, biophysical models representing the EP or mechanical behaviour of the heart, etc.

In this section, we review all the components needed to build a complete 3D computational model of the heart aimed at biophysical simulation, paying special attention to cardiac EP. We also discuss which of those elements are necessary depending on the final purpose of the model, as well as the different existing approaches to incorporate them into the model. We assess the challenges associated with each step of the building process of a model, from the processing of raw clinical or biological data to the final application, including image segmentation, incorporation of cardiac substructures or volume meshing, among others.

3.4.1. Geometry

As shown in Figure 3.8, the generation of a 3D cardiac geometry, usually represented by a 3D surface mesh, is the very first step in the construction process of any 3D cardiac computational model. The geometry of the heart is a key feature playing an important role in its electrical and mechanical behaviour, so 3D cardiac models must represent it accurately and realistically.

In general, the geometry of 3D models usually represents one or several cardiac chambers (LV, bi-ventricular, atrial or whole-heart models). It can also include other anatomical structures, such as the great cardiac vessels, including outflow and/or inflow tracts (Ecabert et al., 2008, 2011; Trunk et al., 2007), the fibrous annulus of atrioventricular valves (Schulte et al., 2001; Wenk et al., 2010), part of the coronary tree, or some endocardial details such as papillary muscles and trabeculae carneae for ventricles or *crista terminalis*, pectinate muscles and fossa ovalis for atria (Ruiz-Villa et al., 2009; Seemann et al., 2006;

Zhao et al., 2013). However, it is important to note that the anatomical realism and accuracy required by a particular 3D cardiac model strongly depends on the intended final application, as well as its extension, in terms of cardiac chambers and structures included in the model. A study conducted by Bishop *et al.* concluded that the presence of trabeculations in a bi-ventricular model for EP simulation provides shortcut paths for excitation causing regional differences in electrical activation patterns after pacing compared to anatomically non-detailed models (Bishop et al., 2010). Nevertheless, the structurally simplified models (without endocardial details or vessels) are well suited for a large range of 3D cardiac modelling applications aimed at EP simulation (Bishop et al., 2010).
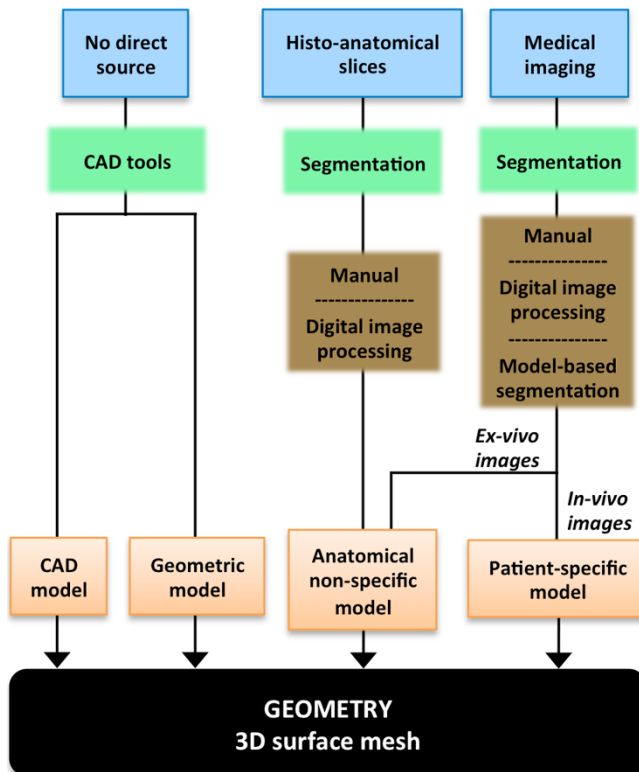
Figure 3.9. 3D cardiac geometry generation stage in the development process of 3D cardiac computational models. Diagram depicting the main alternatives to generate the 3D surface mesh that represents the cardiac geometry, showing the sources of anatomical information (*blue boxes*) and the methods (*green boxes*) used for this task, including their possible options (*brown boxes*), as well as the kind of model (*orange boxes*) obtained by means of each method. Adapted from (Lopez-Perez et al., 2015)

The level of anatomical detail achieved by a certain 3D cardiac model also depends on the source of anatomical information and the methodology used to build it, as shown in Figure 3.9. Geometric or CAD models, which are built from population-based data just considering some measurements of cardiac chambers volume or wall thickness, usually show an "idealized" geometry that coarsely represent an actual cardiac anatomy (Siregar et al., 1998; Van den Broek and Van den Broek, 1980). They are normally used when no direct source of anatomical information is available or when the simplicity of the geometry is preferred to the anatomical realism for the purpose of the model (Blanc et al., 2001; Kerckhoffs et al., 2003; Sermesant et al., 2006b).

Histo-anatomical slices are a good source of anatomical data to construct 3D cardiac models, as they can provide highly detailed information at both anatomical (Zhao et al., 2013) and histological level (Burton et al., 2006; Plank et al., 2009). However, there is usually a large gap between adjacent slices, thus leading to the loss of a great amount of information out of plane (Aoki et al., 1987; Horan et al., 1978; Miller and Geselowitz, 1978), although it can be mitigated by means of interpolation techniques.

As shown in Figure 3.9, medical image-based cardiac models can include patient-specific details obtained from clinical imaging data or population-based properties collected from *ex-vivo* datasets. Regarding *in-vivo* images, the main drawback comes from the fact that clinical imaging protocols usually provide sparse datasets with large gaps between slices. Most of clinical cardiac MRI sequences are acquired with a slice gap typically ranging from 8 to 10 mm, what often leads to the use of interpolation schemes in order to get smooth surfaces representing the cardiac anatomy (Appleton et al., 2006; Frangi et al., 2002; Schulte et al., 2001). However, *in-vivo* cardiac images can be currently acquired with much higher spatial resolution due the advance of imaging techniques in last decades. When high-resolution cardiac images are available, modellers have to deal with the segmentation of large stacks of tomographic slices, especially for very high-resolution *ex-vivo* datasets (Aslanidi et al., 2013; Bishop et al., 2010; Deng et al., 2012; Plotkowiak et al., 2008) or cardiac atlases, whose construction involves segmenting numerous *in-vivo* datasets (Hoogendoorn et al., 2013; Ordas et al., 2007). Manual segmentation is a very time-consuming

and tedious task, besides requiring expertise, whereas automatic segmentation of cardiac images is still challenging, especially for *in-vivo* datasets. Nonetheless, clinical imaging techniques (mainly MRI and CT) are today the source of anatomical information most commonly used to generate the geometry of 3D cardiac computational models.

Ex-vivo cardiac images can provide much higher spatial resolution than *in-vivo* datasets for several reasons: absence of motion artefacts, removal of surrounding tissue before the scan and lack of the limitations imposed by alive subjects (either human or non-human) regarding the acquisition time and the ionizing radiation dose, in the case of CT modalities. It allows highly detailed reconstructions of cardiac geometry, including structures very difficult to observe in *in-vivo* images, such as Bachmann's bundle or pectinate muscles in the atria and endocardial trabeculations in the ventricles (Arevalo et al., 2008; Plank et al., 2009) or leaflets of the cardiac valves and the chordae tendineae (Bishop et al., 2010). Recently, *ex-vivo* micro-CT with iodine staining allowed reconstructing structures such as the atrioventricular node and atrial preferential conducting bundles (Aslanidi et al., 2013). Among all reviewed works, the segmentation of *ex-vivo* images was usually performed by bi-dimensional (2D) semi-automatic approaches (slice by slice) combining classical image processing methods, such as region growing (Arevalo et al., 2008; Deng et al., 2012), snakes (Helm et al., 2005; Winslow et al., 2000) or level sets (Gurev et al., 2011; Plotkowiak et al., 2008). However, manual correction was needed in most cases after the automatic segmentation step (Arevalo et al., 2008; Deng et al., 2012; Gurev et al., 2011; Helm et al., 2005). For those models based on very high-resolution *ex-vivo* MRI, 2D semi-automatic segmentation was also applied based on thresholding and morphological operators (Burton et al., 2006) or complex pipelines using level sets (Bishop et al., 2010; Plank et al., 2009; Vadakkumpadan et al., 2009), although requiring a lower level of manual interaction in these cases.

In-vivo images can provide both anatomical and functional patient-specific information, thus enabling the characterization of cardiac motion (Hoogendoorn et al., 2013; Perperidis et al., 2005). The reviewed patient-specific *models* based on *in-vivo* MRI were mostly assembled by manual

segmentation (Haddad et al., 2005; Niederer et al., 2009). Images provided by certain MRI modalities, such as cine-MRI, can be segmented by 2D automatic approaches combining morphological operators and snakes (Appleton et al., 2006). 2D semi-automatic approaches based on snakes/level sets (Yang et al., 2006) and even 3D automatic methods (Romero et al., 2010) were applied to *in-vivo* MS-CT. Some cardiac atlases were also assembled from manually segmented MRI (Frangi et al., 2002; Lötjönen et al., 2004). Nevertheless, to facilitate the segmentation of large datasets, more complex approaches have been applied to assemble cardiac atlases such as, fitting of deformable models based on geometrical shapes followed by manual correction (Lorenz and von Berg, 2006), adaption of an initial mesh by piecewise affine transformation (Ecabert et al., 2008) or non-rigid registration with a previously manually segmented image (Hoogendoorn et al., 2013; Ordas et al., 2007; Perperidis et al., 2005).

In conclusion, high-resolution *ex-vivo* datasets enable considerably more detailed reconstructions of cardiac anatomy than *in-vivo* images. However, in addition to the explantation of the heart, the organ must undergo a whole process of tissue preparation (fixation, chambers filling, etc.) before the acquisition of *ex-vivo* cardiac datasets, either *ex-vivo* images or histological slices. This process could alter several features of cardiac structures, such as shape, size, volume, etc., especially in the case of histological sections due to the deformation caused by the slicing process (Burton et al., 2014; Gibb et al., 2012; Mansoori et al., 2007). Therefore, even though it is undoubtedly a good approximation, currently it remains unclear to what extent an *ex-vivo* derived geometry is relevant to the *in-vivo* function of the heart, as posed in (Creswell et al., 1992). To our knowledge, there is no literature addressing this issue thoroughly, so it is something to take into consideration when a 3D cardiac model based on *ex-vivo* images is used to perform computational simulation studies with potential clinical relevance.

Cardiac models may also include the coronary tree, which is often virtually generated from the anatomical knowledge, manually segmented from pictures of histo-anatomical slices (Trunk et al., 2007) or fitted from a previous model (Lorenz and von Berg, 2006). The full coronary tree can be segmented

from very high-resolution *ex-vivo* MRI (Bishop et al., 2010; Burton et al., 2006; Vadakkumpadan et al., 2009). The main coronary arteries can be reconstructed from *in-vivo* MRI using complex segmentation pipelines (Haddad et al., 2005). However, high-resolution MS-CT has become the most common modality for *in-vivo* assessment of the structure of coronary tree, since it allows segmenting part of the patient-specific cardiac vascular network (Hoogendoorn et al., 2013; Ordas et al., 2007). There are some applications in which the coronary tree might have a central role in the model, such as cardiac resynchronization therapy (CRT), where the implanted leads are spatially restricted to the lumen of some specific vessels (Niederer et al., 2012; Weese et al., 2013). Other authors have also studied the role played by blood vessels within the heart, and the changes in fibre orientation around them, in stabilizing arrhythmias, reporting changes in wavefront curvature around the blood vessels (Gibb et al., 2009).

3.4.2. Meshing

Despite 3D cardiac models with simplified geometries still play an important role for certain applications, mainly focused on mechanistic enquiry, current trends are moving towards complex and anatomically realistic patient-specific models. In any case, to enable the mathematical resolution of complex biophysical problems by means of numerical methods, the volume of both anatomically simple and detailed cardiac models must be discretized, being represented by a number of discrete 3D elements as a result of a meshing process. Figure 3.10 gives an overview of the most common meshing options for 3D cardiac computational models aimed at biophysical simulation. As shown, the geometry of cardiac models is usually represented by discrete 3D surface meshes resulting from the geometry generation stage, which later act as inputs for a volumetric mesh generator software (e.g. TetGen, NetGen, Tarantula). Among the existing spatial discretization techniques related to advanced numerical analysis, the finite-element method (FEM) is the most extended approach in 3D cardiac modelling for EP and mechanical simulation. A usual alternative to FEM method relies on grid-based meshes (finite-difference grid method), which can operate directly from a segmented image stack in order to discretize the volume (Plank et al., 2009) (see Figure 3.10).
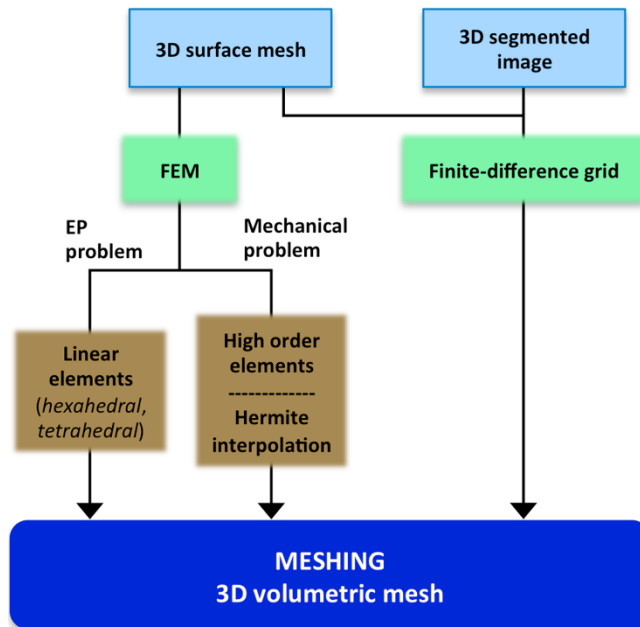
Figure 3.10. Meshing stage in the development process of 3D cardiac computational models. Diagram describing the most common methods (*green boxes*) and options (*brown boxes*) to build the 3D volumetric mesh of a cardiac model, using the 3D surface mesh or the 3D segmented image resulting from the cardiac geometry generation as a starting point for the meshing process. Reproduced from (Lopez-Perez et al., 2015)

For cardiac EP simulations, the most common meshing approach relies on unstructured volumetric FEM meshes consisting of linear elements, normally tetrahedral (Bishop et al., 2010) or hexahedral elements or even combinations thereof (Prassl et al., 2009). Note that, for the same number of nodes (i.e., the vertices of discrete FEM elements), tetrahedral-based meshes usually require a much larger number of elements than hexahedral meshes. Thus, the use of hexahedral elements is desirable to decrease the number of degrees of freedom of FEM models, even at the cost of a slightly poorer representation of subtle details of cardiac anatomy (Dux-Santoy et al., 2011; Heidenreich et al., 2010a). Moreover, the incorporation of fine anatomical structures (Purkinje tree, trabeculations, vascularization, etc.) to faithfully represent the cardiac anatomy also increases the number of degrees of freedom in 3D cardiac models.

On the other hand, the nature of the cardiac EP processes to be simulated imposes strong restrictions on the features of discrete 3D elements of FEM

meshes, in order to ensure the numerical stability of the solution. The main reason is related to the depolarization phase of the action potential (AP) of cardiomyocytes, which shows a very fast upstroke that produces a step-like wavefront over a small spatial extent (ten Tusscher and Panfilov, 2006a). Therefore, when complex biophysical models are used for EP simulations, the equations must be solved with constraints in the range of 0.05-0.005 ms for time step (*dt*) and of 0.1-0.5 mm for spatial discretization (*ds*), that is, for the average edge size of discrete 3D mesh elements (Niederer et al., 2011; Plank et al., 2008). In the case of simplified or phenomenological cardiac EP models, such as the Eikonal approach, spatial and temporal discretization is less demanding (in the order of *ds* = 0.5 mm and *dt* = 1 ms), resulting in much faster computation times (see section 3.4.5 for more details about different approaches for cardiac EP modelling).

Another extended computational representation of cardiac anatomy for mechanical problems is based on cubic Hermite elements, producing a smooth representation of the geometry that is well-suited to simulate large deformation mechanics by means of FEM methods (Lamata et al., 2011). Although that approach fails to faithfully represent the subtle anatomical details present in the heart, it provides a higher numerical accuracy for mechanical simulations than linear interpolation schemes in models based on tetrahedral or hexahedral elements (Pathmanathan et al., 2009). Indeed, models aimed at electromechanical simulations usually include two coupled FEM volumetric meshes: one consisting of linear elements aiming to solve the electrical component and another based on higher order elements (Kerckhoffs et al., 2003) or Hermite interpolation functions (Gurev et al., 2011) for the mechanical problem.

3.4.3. Myocardial structure

Cardiac myocytes (cardiomyocytes) are elongated cells arranged in a laminar sheet organization to form the ventricular myocardium (Anderson et al., 2009; LeGrice et al., 1995). The direction of the longitudinal axis of cardiac myocytes, known as *fibre orientation*, strongly determines the patterns of

activation and spreading of the electrical activity in the myocardium, since the electrical propagation is 3 to 4 times faster along this axis than in the transverse directions (Clerc, 1976). Furthermore, myocardial contraction is mainly caused by a shrinkage of myocytes along its longitudinal axis, so fibre orientation has also a great influence on the mechanical behaviour of cardiac tissue. Hence, cardiac fibre orientation is a necessary element in models aimed at realistic EP and mechanical computational simulations. Cardiac fibre orientation may be included in 3D cardiac models by setting the direction of the longitudinal axis as a property of every element of the 3D volumetric mesh resulting from the meshing stage (see Figure 3.8). Thereby, one can define the preferential direction in which the electrical excitation or mechanical deformation at any node of the volume mesh will propagate to its neighbours. This sort of cardiac fibre definition is known as axisymmetric (transversely isotropic), since the transverse and normal sheet (transmural direction) fibre directions are considered to have the same diffusion coefficients.
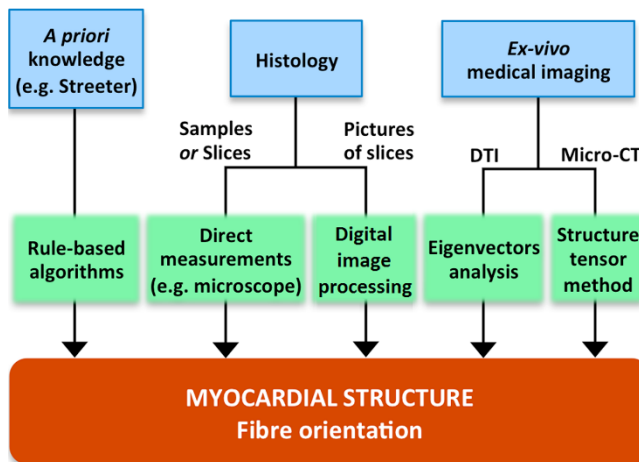
Figure 3.11. Myocardial structure generation stage in the development process of 3D cardiac computational models. Diagram showing the main sources of structural information at tissue level (*blue boxes*) and the methods (*green boxes*) used to obtain the cardiac fibre orientation to be included in a certain 3D cardiac model. Reproduced from (Lopez-Perez et al., 2015)

Figure 3.11 shows a schematic summary of the most common methods to obtain or estimate the cardiac fibre orientation within myocardial tissue, in order to map this information into 3D cardiac models. The most usual approach

relies on rule-based algorithms, which estimate the fibre orientation associated with each element of the volumetric mesh of cardiac models from pre-established patterns (Colli Franzone et al., 1998; Kerckhoffs et al., 2003; Ordas et al., 2007; Romero et al., 2010). Most of those rule-based methods are derived from Streeter's findings, who thoroughly studied and characterized the myocardial tissue structure in canine ventricles (Streeter et al., 1969). Fibre orientation can also be obtained from measurements taken on explanted hearts (Deng et al., 2012; Nielsen et al., 1991), by analysing histological sections under microscope (Vetter and McCulloch, 1998) or by digital processing of volume images assembled from high-resolution pictures of very thin histological slices by means of the structure tensor method (Burton et al., 2006; Zhao et al., 2013).

Diffusion tensor-MRI (DT-MRI), also called diffusion tensor imaging (DTI), is a MRI modality capable of tracking the diffusion of water molecules within the biological tissues. For cardiac DTI, it is well known that the direction of the primary eigenvector associated with each voxel of the acquired images matches the longitudinal axis of cardiac myocytes (Holmes et al., 2000; Hsu et al., 1998; Scollan et al., 1998). This information can be mapped into the volumetric mesh of 3D cardiac models to incorporate the cardiac fibre orientation (Arevalo et al., 2008; Gurev et al., 2011; Plank et al., 2009; Sermesant et al., 2003). *Ex-vivo* cardiac DTI also provide anatomical information, thus avoiding the need to merge different image modalities in order to construct 3D cardiac models including fibre orientation (Heidenreich et al., 2010a; Helm et al., 2005). Peyrat *et al.* generated a statistical atlas characterizing the variability of cardiac fibre orientation using *ex-vivo* DTI from nine canine hearts (Peyrat et al., 2007). In later works, Toussaint *et al.* developed an approach to estimate the patient-specific cardiac fibre orientation of the LV from a sparse set of 2D slices of *in-vivo* DTI (Toussaint et al., 2010, 2013) by making use of the aforementioned statistical atlas of cardiac fibres (Peyrat et al., 2007). However, despite recent promising advances in this direction (McGill et al., 2015b, 2015a; Nguyen et al., 2016; Stoeck et al., 2017), currently *in-vivo* cardiac DTI is not capable of providing full patient-specific fibre orientation of whole hearts due to its high sensitivity to motion artefacts.

Ex-vivo micro-CT with iodine staining is another image modality recently used to assess cardiac fibre orientation in certain critical regions of atrial tissue by means of the structure tensor method (Aslanidi et al., 2013). Nevertheless, *in-vivo* micro-CT is not feasible because of the high dose of ionizing radiation required by such technique.
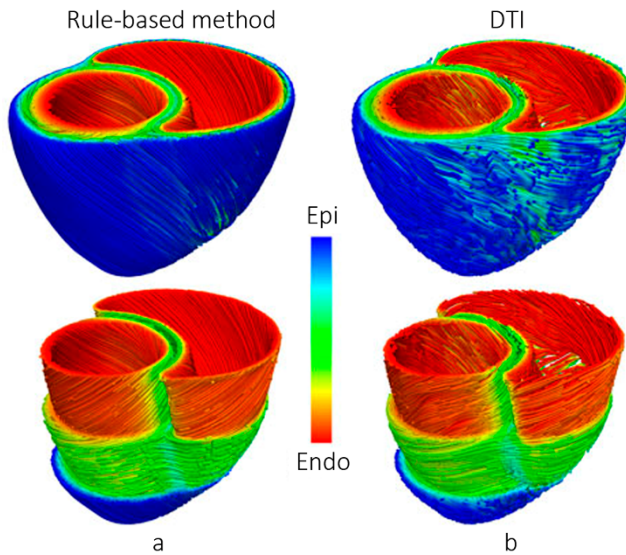
Figure 3.12. Different methods to include cardiac fibre orientation in a 3D bi-ventricular model. Comparison between (*a*) a rule-based method (Laplace-Dirichlet) and (*b*) DTI-based estimation of the myocardial fibre orientation for a 3D model of canine ventricles. Adapted from (Bayer et al., 2012)

A few studies have compared the performance of rule-based methods to that of DTI-derived fibre orientation in the setting of EP simulations. Employing a unique 3D cardiac model (i.e., the same geometry in both cases), Bishop *et al.* showed that global electrical activation patterns simulated using a rule-based linear approach were very similar to those obtained with fibre orientation based on *ex-vivo* DTI, thus demonstrating the reliability of the former method for EP studies (Bishop et al., 2009). As shown in Figure 3.12, in a similar study Bayer *et al.* compared a novel rule-based method (Laplace-Dirichlet algorithm) to DTI-derived fibre orientation (Bayer et al., 2012), reaching analogous conclusions with respect to (Bishop et al., 2009).

In conclusion, currently there is no *in-vivo* technique capable of providing full patient-specific cardiac fibre orientation of the whole heart. However, rule-based algorithms derived from prior knowledge of myocardial structure, such as Streeter's data (Streeter et al., 1969), have demonstrated to be a suitable approach for cardiac EP simulation studies.

3.4.4. Cardiac conduction system

The electrical activation of ventricles is initially triggered by the so-called *cardiac conduction system* (CCS). Along with the two primary pacemakers of the heart, the sinus and the atrioventricular (AV) nodes, the CCS consists of a heterogeneous and complex 3D network that combines subendocardial and free-running fibres formed by specialized myocytes. Under physiological conditions, the CCS ensures a paced and coordinated activation of the ventricular myocardium, making the heart to develop an efficient performance as blood pump (Dobrzynski et al., 2013). The *His-Purkinje system*, corresponding to the ventricular network of the CCS, is highly specialized for a rapid propagation of the AP with conduction velocities (CV) in the range of 2-4 m/s. Their fibres are isolated from surrounding myocardium by connective tissue sheaths all along the network, with the exception of terminal ends, thus allowing the AP propagation to the ventricular working myocardium at those connecting points called *Purkinje-myocardium junctions* (PMJs) (Tranum-Jensen et al., 1991). The location of those PMJs plays a key role, since they are the sources of the early electrical activations that subsequently lead to the activation of the whole ventricles (Dobrzynski et al., 2013).

Figure 3.13 shows the main steps and alternatives to generate CCS models aiming to be coupled to 3D cardiac models, as shown in Figure 3.8. Some 3D cardiac models include the CCS at functional level, that is, excluding its anatomical structure, by considering altered endocardial properties that emulate faster activations (Chinchapatnam et al., 2009) or by defining on the endocardial surfaces a number of discrete early activation points, usually obtained from the literature (e.g. from (Durrer et al., 1970)) or from electrical recordings (Pollard and Barr, 1991). Simplified models that aim to mimic the CCS

structure can be constructed using different techniques, such as manual delineation of CCS networks on the endocardial surfaces of cardiac models (Romero et al., 2010) or fractal tree-like representations (Abboud et al., 1991). More complex algorithms to generate anatomical models of the CCS are based on numerous rules seeking to characterize its main structural features (Sebastian et al., 2013). Such rules are normally extracted from histological studies in explanted hearts from different mammalian species (rat, rabbit, dog, lamb, etc.).
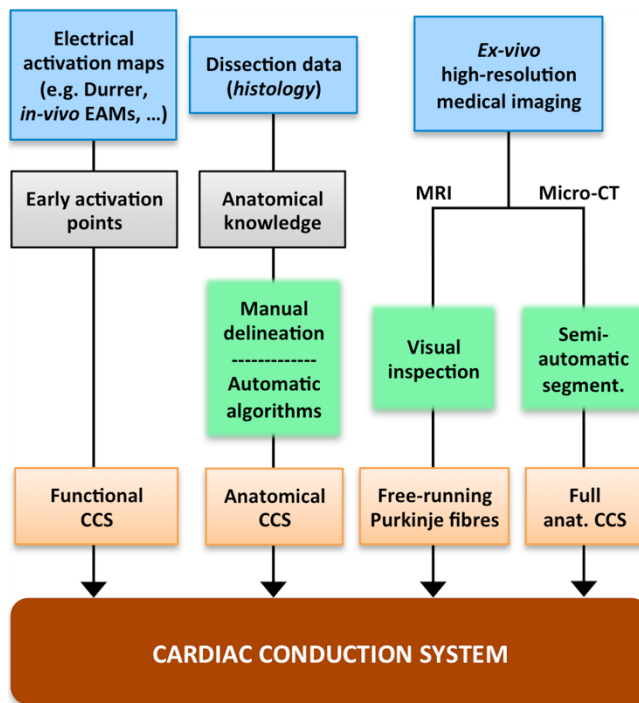
Figure 3.13. CCS generation stage in the development process of 3D cardiac computational models. Diagram outlining several ways to generate CCS models to be coupled to 3D cardiac models. It shows the information sources (*blues boxes*), the partial results obtained (*grey boxes*) and the methods (*green boxes*) used to generate different kinds of CCS models (*orange boxes*). Reproduced from (Lopez-Perez et al., 2015)

It is possible to visualize the CCS structure using *ex-vivo* microscopic images with specific markers, such as staining or connexin antibodies (e.g. (Garcia-Bustos et al., 2017, 2019)). Very high-resolution *ex-vivo* MRI has allowed locating a number of free-running Purkinje fibres by visual inspection (Bordas et

al., 2011; Vadakkumpadan et al., 2009) and recently *ex-vivo* micro-CT with iodine staining has enabled an image-based semi-automatic reconstruction of the full CCS (Stephenson et al., 2012), all in small mammalian hearts. More recently, Stephenson *et al.* presented the first complete 3D representation of the human CCS structure, also generated from contrast-enhanced *ex-vivo* micro-CT (Stephenson et al., 2017). However, reconstructing the CCS by means of *in-vivo* imaging techniques is not feasible, since the microscopic dimensions of its structures are smaller than the maximum spatial resolution of current clinical imaging systems.

Importantly, as shown in Figure 3.8, the electric connection between the CCS models and 3D cardiac anatomy requires specific computational models for PMJ coupling, due to the highly specialized inhomogeneous connection with the ventricular working myocardium at those terminal points of the CCS. Those models try to reproduce the propagation delay at PMJs in healthy and pathological conditions, adding transitional regions or resistor elements to couple both cell types (Azzouzi et al., 2011; Berenfeld and Jalife, 1998; Boyle et al., 2010; Dux-Santoy et al., 2013). The determination of the location and density of PMJs remains highly challenging, so computational studies can provide insights into this important matter in both normal and arrhythmic scenarios (Behradfar et al., 2014). Nevertheless, some recent studies have proposed novel methods to estimate the location of PMJs clusters from *in-vivo* electroanatomical maps (EAMs) aiming to generate anatomical CCS models that attempt to functionally emulate the patient's CCS (Barber et al., 2017; Cardenes et al., 2014; Palamara et al., 2014, 2015).

Aside from the CCS structure, 3D cardiac models oriented to biophysical simulation must include specific AP models specially developed to capture the particular EP behaviour of Purkinje cells (DiFrancesco and Noble, 1985; Stewart et al., 2009). The most recently developed Purkinje AP models include the Ca^{2+} subsystem spatial organization and receptors distribution, which are unique to Purkinje cells (Li and Rudy, 2011; Passini et al., 2017), thus allowing a more accurate modelling of ventricular arrhythmias related to CCS and of interaction with drugs. A number of EP computational studies have already integrated realistic CCS models, both in structural and EP sense, to analyse its role in non-

physiological scenarios, such as during ventricular arrhythmias (Behradfar et al., 2014; Boyle et al., 2010), ventricular pacing (Romero et al., 2010) or in response to the administration of antiarrhythmic drugs (Dux-Santoy et al., 2011; Trovato et al., 2017).

3.4.5. Electrophysiology

After modelling the 3D cardiac anatomy and defining the myocardial structure, those models aimed at computational simulation of cardiac EP require mathematical models that simulate the EP behaviour of myocardium. Figure 3.14 briefly summarizes the main methods and options used to simulate the electrical behaviour of the heart by means of EP models. In the 70s and the 80s, these models usually had the form of *cellular automatas* (Miller and Geselowitz, 1978; Moe et al., 1964), but this kind of rule-based paradigm was progressively substituted by equation-based approaches. As shown in Figure 3.14, the latter models consist of two main components: the cellular-level equations, corresponding to AP models aiming to reproduce the electrical behaviour of a single cardiac cell (e.g., a ventricular myocyte), and the tissue-level equations, which intend to simulate the interaction and propagation of the electrical activity between neighbouring cells.

Over the past decades, extensive patch-clamp experiments revealing the dynamic properties of specific transmembrane ionic channels of cardiac myocytes (Sakmann and Neher, 1984) provided data to formulate comprehensive mathematical descriptions of the ionic currents that underlie the AP of cardiac cells. Cellular-level equations of AP models are usually based on the well-known Hodgkin and Huxley (HH) formalism, originally established more than 60 years ago (Hodgkin and Huxley, 1952). According to that formalism, the cellular AP is described by a system of non-linear first order ordinary differential equations (ODEs) that models the kinetics of individual ionic channels, pumps and exchangers, as well as their electrical interactions (Fink et al., 2011). The HH formalism is still in use to mathematically formulate these ionic currents, although currently a new paradigm based on Markov-type models has also been adopted to build more biophysically realistic models of

ionic channels (Rudy and Silva, 2006). Currently, AP models are highly specific, including models for several animal species, a variety of pathophysiological disorders and different portions of human heart in normal or diseased conditions: ventricles (Grandi et al., 2010; O'Hara et al., 2011; ten Tusscher et al., 2004), atria (Courtemanche et al., 1998; Grandi et al., 2011; Maleckar et al., 2009; Nygren et al., 1998) and Purkinje cells (Sampson et al., 2010; Stewart et al., 2009) (see (Fink et al., 2011) and (Roberts et al., 2012) for a review on cardiac AP models).
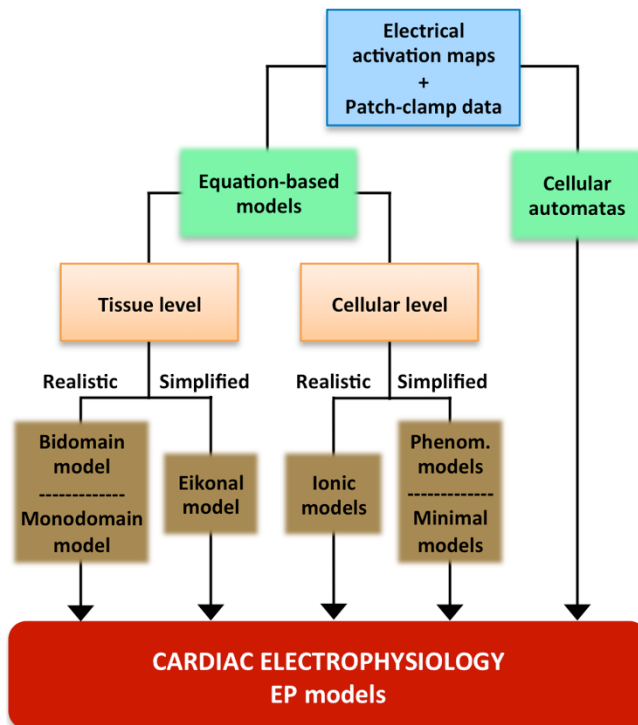
Figure 3.14. Cardiac electrophysiology modelling stage in the development process of 3D cardiac computational models aimed at EP simulation. Diagram summarizing very briefly the main methods (*green boxes*) and options (*brown boxes*) to model cardiac EP by means of mathematical models from experimental data (*blue box*) provided by electrical activation maps at tissue level and patch-clamp experiments at cellular level. Reproduced from (Lopez-Perez et al., 2015)

The ventricular myocardium is electrophysiologically inhomogeneous, as cardiac myocytes in different portions of the ventricles exhibit different ionic

currents affecting the features of their APs. EP heterogeneities in the ventricles include epicardial-endocardial (Liu et al., 1993), apico-basal (Szentadrassy et al., 2005) and left-right (Volders et al., 1999) differences in ionic channels and, hence, in APs. The most recent AP models of human ventricles include some of these regional variations, as in the case of the models by ten Tusscher *et al.* (ten Tusscher et al., 2004; ten Tusscher and Panfilov, 2006b) and O'Hara *et al.* (O'Hara et al., 2011), which state different formulations for endocardial, epicardial and mid-myocardial myocytes to include the so-called *transmural heterogeneity*. In spite of the lack of experimental evidence on the anatomical boundaries of these different regions within the heart, the transmural heterogeneity has been considered in some 3D models of human ventricles (Heidenreich et al., 2010a), as well as other regional EP differences, such as Bachmann's bundle, crista terminalis or pectinate muscles in atrial models (Ferrer et al., 2015b; Martinez-Mateu et al., 2018).

At the tissue level, myocardial cells are electrically coupled, so that, under physiological conditions, ionic currents flow from each myocyte to its neighbouring ones. Therefore, a tissue-level model, in which axial currents flow between cells through low-resistance *gap junctions*, must accompany the cellular models mentioned above. That model should consider the inherently anisotropic behaviour of the myocardium due to the cardiac fibre orientation, as well as the fact that such tissue consists of two different media separated by cell membranes, referred to as intracellular and extracellular domains. The mathematical homogenization of this concept resulted in the so-called *bidomain model*, which was developed in the late 70s (Miller and Geselowitz, 1978). It consists of two partial differential equations (PDEs), allowing to calculate extracellular and intracellular potentials, respectively. Since membrane potentials depend on transmembrane ionic currents, consequently tissue-level equations are coupled to cellular-level ones. Hence, the complete model (cell and tissue level) is formed by a system of two PDEs and a certain number of ODEs, which are highly non-linear. Those two PDEs include different conductivity tensors for intracellular and extracellular domains, both determined by cardiac fibre orientation. Assuming equal anisotropy ratios for both domains, that is, both tensors are related by a constant, the two PDEs become uncoupled, so that the bidomain formulation is reduced to the so-called

monodomain model (Roth, 1988). One of the PDEs is of the reaction-diffusion type and includes all the ionic current ODEs in its independent term. This system must be solved to compute transmembrane potentials, after which extracellular potentials are directly derived from the second PDE.

Those AP models that include a specific formulation for each individual transmembrane ionic channel are commonly known as *ionic models*. This kind of models usually have a large number of state variables and, consequently, of ODEs as well. The ionic AP model of human ventricles by O'Hara *et al.*, for instance, includes 48 state variables (O'Hara et al., 2011). The equation systems combining those ODEs (ionic AP model) with the PDEs (tissue-level model) pose a mathematically challenging problem that requires numerical methods to be solved (e.g. FEM method), thus turning into a highly demanding computational task. For those reasons, the implementation of EP simulations on 3D cardiac models necessarily requires high-performance computing (HPC) techniques.

Several alternatives have been proposed to overcome such limitation, though at the cost of losing realism in the mathematical description. The so-called *phenomenological models*, for instance, substitute the actual ionic current descriptions by simple mathematical equations to reduce the number of state variables. Historically, the first of these simplified models was developed in 1961 by FitzHugh (FitzHugh, 1961), which later was further improved and adapted to cardiac AP (Aliev and Panfilov, 1996; Mitchell and Schaeffer, 2003). However, there is no biophysical correlation between ionic currents and the mathematical terms of this kind of models, so that they are unable to simulate complex dynamic patterns of excitation and repolarization of cardiac tissue, such as rapid pacing or reentrant activities. The evolution of those purely phenomenological models resulted in the so-called *minimal models*, which try to gain some biophysical sense by associating each term to actual but simplified ionic currents (Bueno-Orovio et al., 2008; Fenton and Karma, 1998; Mitchell and Schaeffer, 2003). On the other hand, another simplification that affects the propagation part of the phenomenon is the so-called *Eikonal* approximation. It replaces the reaction-diffusion equation with an Eikonal equation, which is simpler and based on a Huygens approach (Colli Franzone et al., 1990; Keener, 1991). More recently, Relan *et al.* proposed a new strategy combining both

assumptions, that is, minimal plus Eikonal models (Relan et al., 2011). This approach gives rise to a hybrid framework that may combine models with different levels of detail, including detailed biophysical models, with a relatively low computational demand (Camara et al., 2011).

3.4.6. Electromechanical coupling

Although mentioned, modelling of cardiac mechanics lacks a specific section in this chapter, as it mainly focuses on 3D models for cardiac EP simulation. Very briefly, it involves the use of biomechanical models at organ level, using the equations of continuum mechanics to describe the organ deformation resulting from the active tension generated by the myocytes, and models of myocyte contraction at cellular level that include myofilaments models at subcellular level depicting the actin-myosin interactions and its calcium-based activation system (e.g. (Mullins and Bondarenko, 2013; Rice et al., 2008)) (see (Trayanova and Rice, 2011) for a review).

However, it is important to highlight that every 3D cardiac model aimed at electromechanical (EM) computational simulation must include the EM coupling, also known as *excitation-contraction coupling* (Jafri, 2012; Williams et al., 2010), as shown in Figure 3.8. The electrical activation of myocytes is the event that triggers their mechanical contraction by means of the Ca^{2+} cycling (i.e., the release and reuptake process of intracellular Ca^{2+}), which is the responsible for the initiation of actin-myosin interactions that ultimately lead to myocytes shortening (Pfeiffer et al., 2014).

On the other hand, cardiac models oriented to EM simulation may also include the *mechano-electric feedback* (see Figure 3.8). Acute changes in ventricular mechanics can affect the cardiac EP (Pfeiffer et al., 2014; Quinn et al., 2014) due to mechanisms such as stretch-activated ion channels (Craelius et al., 1988; Kohl et al., 1999) or mechanical modulation of cell calcium handling, even causing mechanically triggered arrhythmias (Kohl et al., 2005).

3.4.7. **Pathology**

An important number of diseases can cause structural remodelling at both tissue and whole heart level, as well as functional remodelling at tissue and cellular level affecting the electrical and mechanical performance of the heart. Therefore, 3D cardiac models aimed at studying the effects of such diseases by computational simulation should include both types of remodelling at the corresponding levels.

As shown in Figure 3.8, simulation-oriented models can include functional remodelling (electrical or mechanical) by adapting the biophysical models that reproduce the EP behaviour at cell or tissue level. In the case of EP models, it generally involves modifications in parameters associated with the equations of certain ionic currents to reflect the effects of the EP remodelling at cellular level, previously studied by voltage- or patch-clamp experiments, as for example done in (Cabo and Boyden, 2003). A similar approach is used for genetic mutations, whose effects on cardiac EP are usually introduced as changes in the conductance or kinetic parameters of those ionic currents directly affected by a particular mutation (Clancy and Rudy, 2001). At the tissue level, the most common approach to include the EP remodelling consists in modifying the conductivity parameters of the tissue-level model, thus altering the intensity of current flows between neighbouring cells and, consequently, the CVs. Left bundle branch block (LBBB), for example, may be considered as a functional alteration at the tissue level included in the Purkinje 3D cardiac model (Reumann et al., 2007). Functional remodelling can also affect the EM coupling. In heart failure, for instance, Ca^{2+} cycling is altered resulting in impaired contractility (Marks, 2013; Pfeiffer et al., 2014), what increases the risk of extrasystoles (ectopic beats) and arrhythmia due to mechano-electric feedback (Hansen et al., 1990; Wang et al., 1994). In this regard, Trayanova *et al.* have studied these arrhythmogenic mechanisms by computational simulation using 3D cardiac models (Trayanova et al., 2010).

Structural remodelling can affect cardiac anatomy at both organ and tissue level. As shown in Figure 3.8, the geometry of 3D models must include every pathological variation of cardiac anatomy at whole organ level caused by any disease, either affecting the volume, shape or wall thickness of any cardiac

chamber. There are examples of models showing left atrium dilation caused by sustained atrial fibrillation (Ruiz-Villa et al., 2009), right ventricle (RV) hypertrophy (Heidenreich et al., 2010a), hypertrophic and dilated cardiomyopathy in LV (Romero et al., 2010) or LV wall thinning due to chronic myocardial infarction (MI) (Wenk et al., 2010). At the tissue level, cardiac pathologies can also alter the myocardial structure (see Figure 3.8), which collaterally leads to functional disorders, since it alters the electrical propagation patterns and the mechanical performance of the myocardium. Several 3D models, for instance, include the cardiac fibre orientation disarray typically associated with infarcted myocardial regions (Wu et al., 2006), both from *ex-vivo* DTI (Arevalo et al., 2008; Vadakkumpadan et al., 2009) and from histological studies (Rutherford et al., 2012), aiming to assess by computational simulation the influence on the electrical propagation of such kind of structural remodelling at the tissue level.

Infarct scars, the chronic ischaemic injuries resulting from the replacement fibrosis associated with the MI healing process, may be included in 3D models to assess its influence on the EP and mechanical performance of the heart. These fibrotic lesions are usually segmented from *in-vivo* delayed enhancement-MRI (DE-MRI) (Arevalo et al., 2016; Ashikaga et al., 2013; Deng et al., 2018; Pashakhanloo et al., 2018; Prakosa et al., 2018) and, less frequently, from *ex-vivo* DTI based on the fractional anisotropy (Arevalo et al., 2008; Vadakkumpadan et al., 2009) and from anatomical MRI based on wall thinning (Wenk et al., 2010). Image-based reconstruction provides accurate information about the extension and location of ischaemic injuries within the geometry of a given 3D model, also allowing to differentiate between the infarct scar (fibrotic core) and the border zone (BZ), which is the remodelled but still working tissue surrounding the infarct scar. In addition, mathematical models used for biophysical simulations must consider the functional remodelling associated with the infarcted cardiac tissue. For EP simulations, infarcted cardiac models usually include EP remodelling in the BZ reflecting the slowed conduction (tissue level) and the changes in the AP (myocyte level) experimentally observed, as for instance done in (Arevalo et al., 2013; Ashikaga et al., 2013; Deng et al., 2016; Ringenberg et al., 2014).

Cardiac tissue can also undergo diffuse myocardial fibrosis, a kind of structural remodelling related to aging and also to a broad variety of cardiac and systemic diseases: hypertension, diabetes, dilated and hypertrophic cardiomyopathy, chronic renal insufficiency, atrial fibrillation, etc. The progress of diffuse fibrosis may lead to mechanical disorders, such as systolic and diastolic dysfunction (Martos et al., 2007), and turns the myocardium into a more arrhythmogenic substrate (Sridhar et al., 2017; ten Tusscher and Panfilov, 2007). Therefore, 3D models can include this kind of fibrosis in order to study its influence on the cardiac performance by computational simulation, e.g. in (McDowell et al., 2011).

3.4.8. Example of a 3D cardiac computational model

Figure 3.15 shows an example of a 3D bi-ventricular computational model oriented to cardiac EP simulation, which includes all components previously described in this chapter. The geometry of ventricles and that of the infarct scar are patient-specific, both segmented from the same *in-vivo* DE-MRI image stack. The cardiac geometry was manually delineated with a high level of anatomical detail, including papillary muscles and main endocardial trabeculations, as show in Figure 3.15[a]. The infarct scar was semi-automatically segmented using the standard deviation (SD) from remote method (Kim et al., 1999a), applying two distinct thresholds to differentiate the infarct scar from the BZ. The FEM volumetric mesh was built using voxels, that is, regular hexahedral elements with an edge length size of 0.4 mm, aiming to decrease the number of degrees of freedom in the computational model, yielding a mesh composed of 3.2 million elements (voxels) and 3.5 million nodes (element vertices).

The rest of the elements of this 3D cardiac model, including the CCS, cardiac fibre orientation and biophysical models of cardiac EP, are generic instead of patient-specific, as they derive from population data. Cardiac fibre orientation was computed for every volume mesh element by means of a rule-based algorithm (Sebastian et al., 2009) relying on Streeter's findings (Streeter et al., 1969). For the CCS, an automatic algorithm based on *a priori* anatomical

knowledge obtained from dissection data (Sebastian et al., 2013) was used to generate an anatomical model of the His-Purkinje network specific for this particular bi-ventricular model, which was later coupled to the endocardial surfaces of the volume mesh.
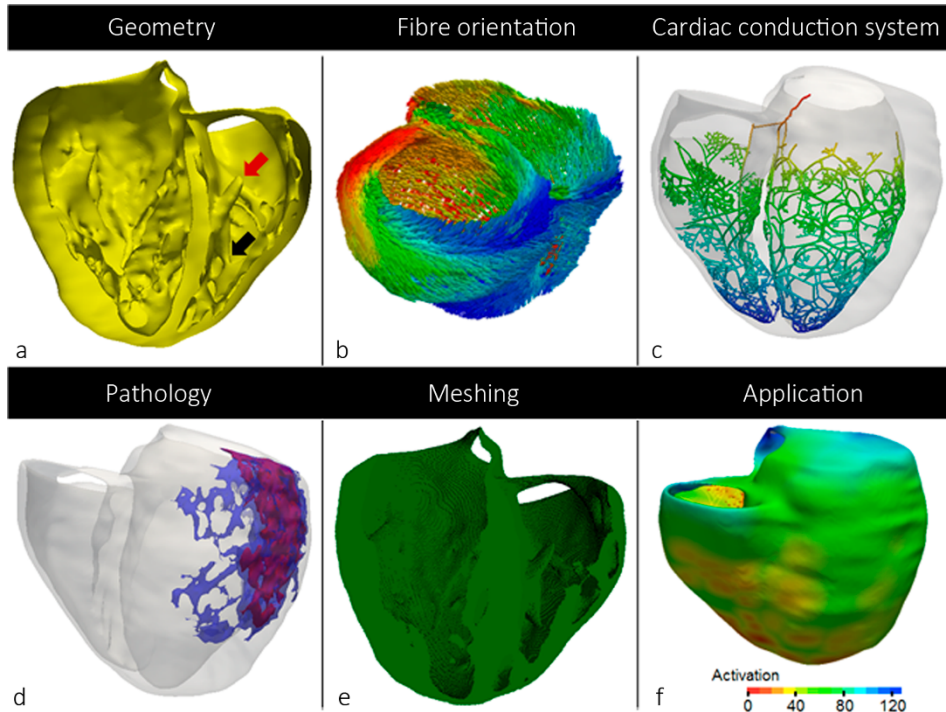
Figure 3.15. Example of a 3D bi-ventricular patient-specific computational model, showing its main elements and final application. (*a*) Geometry of human ventricles with highly-detailed endocardium, highlighting details such as septal papillary muscle (*red arrow*) and moderator band in the RV (*black arrow*). (*b*) Cardiac fibre orientation generated by a rule-based algorithm. (*c*) Anatomical CCS model coupled to endocardial surfaces. (*d*) Myocardial infarction showing the infarct scar (*red*) and the BZ (*blue*). (*e*) FEM volume mesh composed of regular hexahedral elements. (*f*) Biophysical computational simulation of cardiac EP, showing an activation map of the ventricles after delivering a single stimulus at the His bundle. Reproduced from (Lopez-Perez et al., 2015)

Concerning the final application of this 3D bi-ventricular model, a specific FEM solver called ELVIRA (Heidenreich et al., 2010b) was employed to perform computational simulations of cardiac EP with a time step (dt) of 0.02 ms. Regarding the biophysical models, the monodomian approach (Roth, 1988) was

used to simulate the electrical propagation at the tissue level. Two different ionic models were chosen to simulate the APs of cardiac cells: a model of human Purkinje cells for the CCS (Stewart et al., 2009) and a model of human ventricular myocyte that includes the transmural heterogeneity, that is, with different AP features for endo-, mid- and epicardial cells (ten Tusscher and Panfilov, 2006a). Furthermore, the functional remodelling associated with MI was considered at the tissue level. The conductivities modulating the CVs were reduced aiming to emulate the slowed conduction in the BZ, while they were set to zero within the infarct scar to completely cancel the propagation across that region.

3.5. Personalization of 3D cardiac computational models

Patient-specific cardiac modelling can pave a new avenue of possibilities in cardiology, since it is able to integrate anatomical and functional information from a certain patient provided by different types of medical studies, tools and technologies in an intuitive and easily comprehensible fashion. This might help physicians to jointly assess a variety of data derived from multiple diagnostic techniques, including different imaging modalities, ECG recordings, invasive electrical recordings, such as electrograms (EGM) or EAMs, etc. It could be very helpful in risk stratification, therapy planning, surgical guidance or follow-up, for instance. However, currently only a few cardiac features can be completely personalized. Hence, this section is devoted to briefly outline the personalization approaches that are currently available in 3D cardiac computational modelling. Table 3.1 summarizes those current personalization possibilities for 3D cardiac models.

The anatomy can be personalized for a specific subject by building a patient-specific model from *in-vivo* images, including the patient's pathological variations of cardiac anatomy. Some types of structural remodelling at the tissue level may also be personalized, such as the location and extension of infarct scars, which can be accurately reproduced from *in-vivo* images (e.g. DE-MRI as used in (Ashikaga et al., 2013; Ringenberg et al., 2014; Ukwatta et al., 2016)) or

from EAMs recorded during RFA procedures. T1 mapping is an emerging MRI modality able to quantitatively assess the level of diffuse fibrosis *in-vivo* (Dass et al., 2012; Mewton et al., 2011). This novel technique might allow including the patient-specific level of diffuse fibrosis in 3D cardiac models in a quantitative fashion.

Features		Technique	Invasiveness
Anatomy		Segmentation from *in-vivo* image	Non-invasive
Fibre orientation		Image-based estimation (*in-vivo* DTI)	Non-invasive
Cardiac conduction system		PMJs from EAMs	Invasive
Pathology Structural remodelling	*Anatomical variations*	Clinical image-based	Non-invasive
	Localised fibrosis	Image-based (e.g. DE-MRI)	Non-invasive
		EAMs	Invasive
	Diffuse fibrosis	Image-based (T1 mapping MRI)	Non-invasive
Electro-physiology	*Action potential*	EGMs (*estimation*)	Invasive
		ECG (*estimation*)	Non-invasive
	Heterogeneity	NO	
	Elect. remodelling	NO	
	Genetic mutations	NO	
	Conduction velocities	Global: ECG	Non-invasive
		Local: EAMs	Invasive
	APD restitution curve	EAMs	Invasive
	Extracellular ion concentrations	Blood test (electrolyte concentrations) (*time-variant*)	Invasive
	Activation pattern	ECG or BSPM	Non-invasive
		EAMs	Invasive
Cardiac mechanics	*Biomech. Model*	Dynamic image-based	Non-invasive
	Material properties	NO	
	Boundary conditions	Dynamic image-based	Non-invasive

Table 3.1. Current personalization possibilities in 3D cardiac computational modelling. This table shows the techniques that are currently available to personalize different features and components of 3D cardiac computational models aimed at biophysical simulation, specifying whether the technique is invasive or non-invasive. Reproduced from (Lopez-Perez et al., 2015)

The CCS and cardiac fibre orientation are two paramount elements of 3D simulation-oriented cardiac models that cannot be completely personalized yet.

Making use of highly dense EAMs it is possible to locate a set of early activation points on the endocardial ventricular surfaces, which are supposed to correlate to PMJs. Such information can be directly used as a functional CCS (Pop et al., 2011a) or to generate an anatomical CCS model by an inverse estimation of the patient's His-Purkinje network attempting to reproduce the patient-specific electrical activation pattern (Barber et al., 2017, 2018; Cardenes et al., 2014; Palamara et al., 2014). Nonetheless, currently there is no *in-vivo* imaging modality with sufficient spatial resolution to enable a detailed visualisation of the CCS structure. For fibre orientation, only sparse 2D DTI slices can be acquired *in-vivo*, allowing to estimate the patient's fibre orientation of the LV from a fibre atlas (Toussaint et al., 2010, 2013). However, it is worth mentioning that very recently there has been several promising advances in relation to *in-vivo* cardiac DTI (McGill et al., 2015b; Nguyen et al., 2016; Nielles-Vallespin et al., 2017; Stoeck et al., 2017).

Regarding cardiac EP, patch-clamp experiments are the only technique capable of providing detailed information about ionic currents, which requires the isolation of single cells from tissue samples. Then, the patient-specific transmembrane current dynamics cannot be measured and, hence, the mathematical models aiming to reproduce the AP at cellular level (e.g. ionic models) cannot be customized. Due to the same reason, there is no possibility to personalize the electrical remodelling derived from any disease, the effects on cardiac EP of a genetic mutation or the electrical heterogeneity between different regions, such as the transmural heterogeneity in ventricular myocardium. However, cardiac modellers do have the opportunity to choose the EP model at cellular level that best matches the patient's AP features from among a set of existing models, even accounting for the EP remodelling associated with certain genetic disorders such as Brugada syndrome, thus obtaining a *patient-group* customization instead of patient-specific (Britton et al., 2013; Krueger et al., 2013b, 2013a; Muszkiewicz et al., 2016). Moreover, a coarse overall customization of the AP model can be included based on the APD value estimated from EGM recordings (Chen et al., 2016; Western et al., 2015) or even from the ECG (Gillette et al., 2017, 2018). Making use of Eikonal models at the tissue level, a few works have estimated the patient-specific electrical activation patterns and wave propagation CVs in ventricular myocardium, either

globally from ECG or body surface potential maps (BSPM) or locally (as spatially varying parameters) via EAMs (Sermesant et al., 2008), even considering the uncertainty due to the sparsity and noise of clinical data (Konukoglu et al., 2011). In subsequent studies, such approach was improved in order to personalize the CVs and APD restitution curves for bi-ventricular models (Chen et al., 2016; Relan et al., 2011) from the patient's ECG and the isochrones provided by *in-vivo* non-contact endocardial LV mapping (Lambiase et al., 2004), which were utilized to estimate certain EP parameters for a simplified AP model (Mitchell and Schaeffer, 2003). At the tissue level, some specific electrical pathways can be located in a given patient by means of EAMs, such as the main inter-atrial connection (Krueger et al., 2013b, 2013a) or reentry channels responsible for infarct-related ventricular tachycardias (VT) (Fernández-Armenta et al., 2013; Perez-David et al., 2011). Finally, extracellular ion concentrations can be estimated and set into an AP model from the measurement of blood electrolyte concentrations, although they are highly time-variant (Krueger et al., 2013b, 2013a).

For cardiac mechanics, the most common personalization approach consists of adjusting some parameters of biomechanical models from the information obtained via segmented dynamic images: cine-MRI, tagged-MRI, dynamic-CT, ultrasound images, etc. Thereby, those parameters may be adapted aiming to make the 3D model reproduce the patient-specific cardiac motion as accurately as possible (Sermesant et al., 2008). Boundary conditions for mechanical simulations can be estimated from dynamic images as well.

3.6. Applications of 3D cardiac computational models

Currently, computational clinical cardiology is a rising field of research with a large number of potential applications. Cardiac image analysis, including segmentation, and computational simulation of cardiac biophysics are two well-established applications of 3D cardiac models. Cardiac EP simulation, for instance, is becoming a powerful tool to gain insight into multiple electrical cardiac disorders at both tissue and whole organ level. The main reason is that a wide variety of experiments cannot be conducted *in-vivo* due to unacceptable

risk to the patient, ethical reasons, lack of suitable techniques, inability to control all variables, etc. By contrast, 3D cardiac computational models enable to perform *in-silico* experiments making use of computational simulation in an easy and absolutely safe manner, with a complete absence of risk and keeping all variables under control. To give evidence of that, we present in this section numerous examples taken from the literature of several specific applications, mainly related to cardiac EP simulation and model-based image analysis, with the aim to exhibit the potential usefulness of 3D cardiac computational modelling into clinical environments as a powerful tool to aid in the prevention, diagnosis, treatment and follow-up of cardiac diseases.

3.6.1. Cardiac image segmentation

One of the most challenging tasks in the development of patient-specific models is the segmentation of *in-vivo* cardiac images. A broad variety of methods have been proposed (see (Petitjean and Dacher, 2011) for a review on cardiac MRI segmentation), although it seems that the recently appeared approaches based on deep learning techniques are currently outperforming all precedent ones (Bernard et al., 2018). However, among such precedents, one of the most advanced approaches proposed so far for the automation of this task relies on the paradigm of *model-based segmentation*. It has been widely applied to *in-vivo* cardiac image segmentation and analysis (Frangi et al., 2001) and requires the use of a reference model to act as a template.

Deformable models are always based on an initial mesh (template) that resembles the target objects (i.e., the cardiac structures to be segmented), which is used as an initialization for the segmentation process. This initial mesh can be built using any methodology: ellipsoid-based model (Sermesant et al., 2006b) (see Figure 3.16), image-based model (Schulte et al., 2001; Sermesant et al., 2003), assembled from dissection data (Sermesant et al., 2006a), etc. Briefly, the initial mesh is first placed, either manually or automatically, within the cardiac image stack to be segmented overlapping the cardiac anatomy. Then, it is deformed driven by the intensity levels of the cardiac image in an iterative

process, until reaching a certain optimum point with the ultimate goal of fitting the initial mesh to the patient-specific cardiac anatomy.
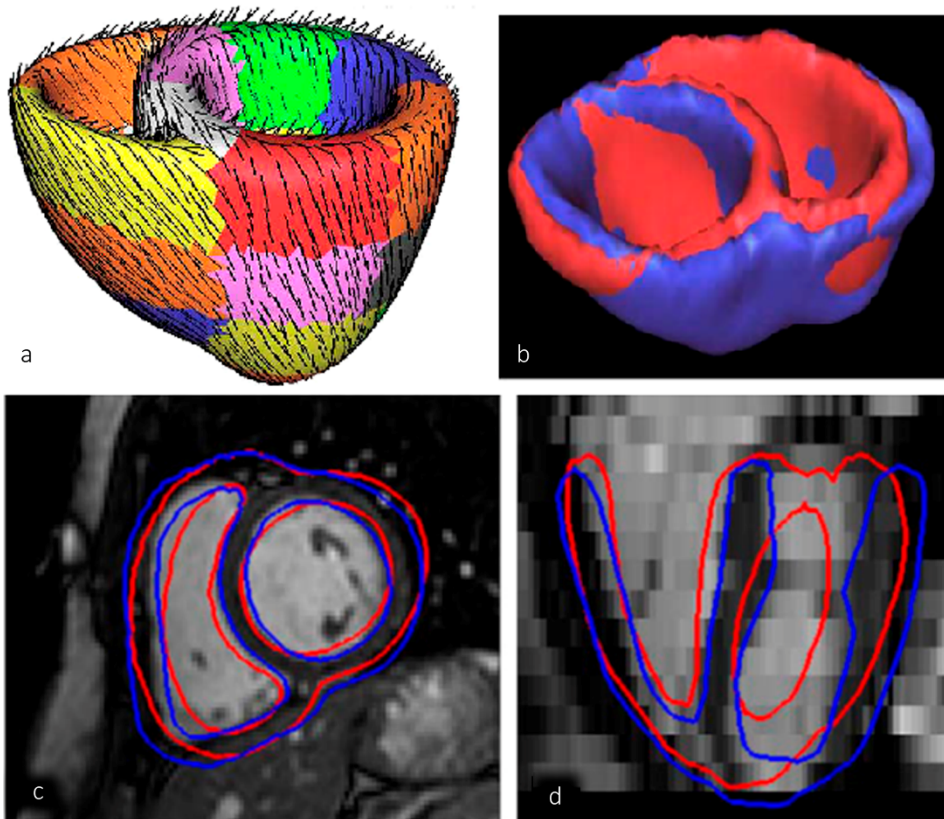
Figure 3.16. (*a*) Initial mesh (geometrical model based on ellipsoids) of a bi-ventricular deformable model for cardiac MRI segmentation, including cardiac fibre orientation (*black lines*) and AHA regions (*colour code*). (*b*) 3D surfaces of the model. MRI slices in the cardiac short-axis (*c*) and four-chambers plane (*d*), showing the contours before (*red*) and after (*blue*) the local deformation of the initial model mesh in order to match the patient-specific cardiac anatomy. Adapted from (Sermesant et al., 2006b)

The mean shape or image resulting from a *cardiac atlas* can also be used as a segmentation tool by deforming it to match the target image, usually by non-rigid registration (Lorenzo-Valdés et al., 2002). The so-called *statistical cardiac models* (or *statistical atlases*) appeared as an evolution of cardiac atlases. They are a wide range of models mainly represented by *statistical shape models* (Frangi et al., 2002; Hoogendoorn et al., 2013; Lötjönen et al., 2004;

Perperidis et al., 2005), although there are other types such as *active appearance models* (Mitchell et al., 2000, 2002) or *active shape models* (Ordas et al., 2003). These model-based segmentation approaches rely on *a priori* statistical knowledge about cardiac anatomy and certain features of cardiac images. This knowledge derives from the statistical characterization of the anatomical variations (and image features) included in the population used to construct the atlas, usually including both healthy volunteers (normal shaped hearts) and patients with different pathological variations of cardiac anatomy. Figure 3.17 shows the mean shape and the statistical characterization of a whole-heart statistical atlas (Hoogendoorn et al., 2013). The dimensionality of the resulting variance and co-variance matrix is usually limited using principal components analysis (PCA) (Ecabert et al., 2008; Frangi et al., 2002; Lötjönen et al., 2004; Perperidis et al., 2005). The prior anatomical knowledge derived from this process is used to enhance the accuracy of the segmentation or analysis of a specific image modality and to increase its robustness when certain information in the image is poor or missing (see (Young and Frangi, 2009) for a review). The *shape-constrained deformable model* developed by Ecabert *et al.* is a mixed approach (Ecabert et al., 2008), which includes prior anatomical knowledge provided by a point distribution model (PDM) derived from a cardiac atlas. Although the particular method can vary depending on the model type, normally the image information (e.g., intensity levels) drives the segmentation process, while prior anatomical knowledge is simultaneously used to constraint the fitting process. That is why a statistical model is unable to recognize those anatomical variations that were not learned from its training set. Therefore, the power of statistical atlases as segmentation tools strongly depends on the population chosen for the atlas development. In addition, atlases are modality-specific since they learn from the grey levels specifically associated with a particular imaging technique. Moreover, most of the statistical models include the endocardial surfaces of all cardiac chambers covered by the model, but only the epicardium of the LV (Ecabert et al., 2008; Frangi et al., 2002; Hoogendoorn et al., 2013). This is because of the high complexity and inter-subject variability of the anatomy of RV and atria what, together with the thinness of their walls, complicates the statistical characterization of those cardiac chambers. Finally,

the *Cardiac Atlas Project*[4] (Fonseca et al., 2011), led by the University of Auckland, must be highlighted within this epigraph. It provides a wide database of cardiac images available online aiming to promote a collaborative development of anatomical and functional statistical atlases for both healthy and pathological hearts.
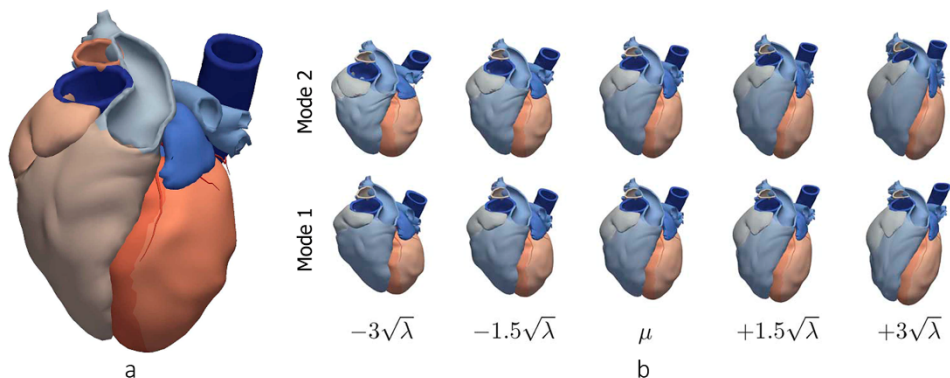
Figure 3.17. Whole-heart cardiac atlas constructed using *in-vivo* high-resolution MS-CT from 138 human subjects. (*a*) Mean shape of the whole-heart atlas. (*b*) First two modes of variation of the spatio-temporal whole-heart statistical atlas (μ represents the mean shape and $\sqrt{\lambda}$ is the standard deviation) at end-diastolic phase of cardiac cycle. Adapted from (Hoogendoorn et al., 2013)

3.6.2. Simulation of cardiac electrophysiology

3.6.2.1. Simulation of acute ischaemia

Significant changes affecting ionic currents and concentrations, AP features and tissue structure occur within the first 10-15 minutes after the occlusion of a coronary artery, corresponding to the phase of acute ischaemia. Those changes, along with the heterogeneous nature of them, predispose the ventricular myocardium to potentially lethal reentrant arrhythmias (Janse and Kleber, 1981). In the past decades, the mechanisms underlying the arrhythmogenicity associated with acute myocardial ischaemia have been theoretically studied using model-based computational simulation (Ferrero et al., 2014). The effects of acute ischaemia are of multiscale nature (Ferrero et al.,

---

[4] Cardiac Atlas Project. http://www.cardiacatlas.org/

1996, 2003; Romero et al., 2009; Shaw and Rudy, 1997; Tice et al., 2007; Trénor et al., 2007) and that is why 3D cardiac models have recently been used to study its effects at whole organ level by computational simulation of cardiac EP.

Heidenreich *et al.* used a 3D heterogeneous model of regionally ischaemic human ventricles to study the dynamics of ischaemic reentrant pathways by EP simulation (Heidenreich et al., 2012). This work predicted the appearance of figure-of-eight reentrant wavefronts crossing the central ischaemic zone, formed in the epicardial surface due to the prolonged refractory period of mid-myocardial layers. Moreover, this allowed to hypothesized that focal activity experimentally observed in the epicardium might be caused by reentrant wavefronts propagating in the mid-myocardium that re-emerge in the epicardial surface. Finally, the thin surviving layer (washout zone) present in the endocardial ischaemic BZ appears to protect the myocardium against the perpetuation of those reentrant wavefronts that cross the central ischaemic zone.

Three-dimensional cardiac models have also been used for simulations of global ischaemia in the context of cardiac defibrillation. Rodríguez *et al.* used a 3D model of rabbit ventricles to assess the effects of ischaemia on the lower and upper limits of vulnerability to reentry induced by electric shocks (Rodríguez et al., 2004). This study highlighted the importance of the transmural electrical events, the spatial extent of the shock-end excitation wavefronts and the slower recovery from shock-induced positive polarization in the mechanisms responsible for the limits of vulnerability.

3.6.2.2. Ablation of chronic myocardial infarction

When the acute phase of ischaemia ends, the healing process of the ischaemic tissue (now infarcted) begins and infarct-related ventricular arrhythmias can take place weeks, months or even years after the coronary occlusion (Lazzara and Scherlag, 1984). Therefore, computer simulations may be of great interest in the chronic period of myocardial infarction (MI) as a tool to aid clinicians during ablation interventions. Below we introduce some examples of EP simulation studies using 3D models of infarcted ventricles.

Vigmond *et al.* simulated reentrant mechanisms on a 3D image-based model of canine infarcted ventricles, including the infarct scar and BZ with electrical remodelling (Vigmond et al., 2009). Rantner *et al*. assessed the mechanisms of defibrillation efficacy using a model of rabbit infarcted ventricles (Rantner et al., 2012). Pop *et al.* tested the ability of computer simulations based on DTI images to predict the VT circuits previously measured in swine hearts by experimental EP studies (Pop et al., 2011a). Similarly, using 3D models of swine ventricles including electrically remodelled BZs and infarct scars, Ng *et al.* induced VTs in computational models with different configurations of the infarcted region, proving that both infarct scars and peri-infarct zones (the BZ) are needed for VT generation (Ng et al., 2012). They obtained similar reentrant circuits in both computational and experimental EP studies, showing that image-based modelling might be helpful in planning of RFA procedures. Indeed, several works have already tested the feasibility of 3D simulation based on *in-vivo* DE-MRI images to estimate ablation targets in human subjects undergoing infarct-related VTs (Arevalo et al., 2013; Ashikaga et al., 2013), emphasizing the effectiveness of this computational strategy. More recently, further retrospective studies with larger cohorts have demonstrated the potential usefulness of image-based computational simulation in risk stratification and therapy planning for infarcted patients with or without prior history of VT (Arevalo et al., 2016; Deng et al., 2016; Prakosa et al., 2018; Trayanova et al., 2017).

3.6.2.3. Cardiac resynchronisation therapy

CRT has become an established therapy to treat certain patients with heart failure suffering from conduction abnormalities, such as LBBB. Clinical trials evaluating CRT have demonstrated that a significant number of patients with heart failure and wide QRS do not respond to this therapy as positively as expected, especially patients with MI. A number of studies have used 3D cardiac models to provide insight into the complex mechanism that govern CRT efficacy by means of computational simulation, aiming to understand the pathophysio-logy of cardiac asynchrony to further improve CRT.

Reumann *et al.* designed a computational model, including different degrees of LBBB (0%, 20% and 40%), aiming to optimize the atrioventricular and interventricular (VV) delays, which are key parameters of CRT devices that require a tailored set-up (Reumann et al., 2007). Kerckchoffs *et al.* used an electromechanical model of canine heart to study the effect of the pacing site and infarct location (anterior, inferior, posterolateral or diffuse fibrosis) on regional mechanics and global haemodynamics (Kerckhoffs et al., 2007, 2009). They concluded that response to CRT was poorer in hearts with LBBB and large infarcted regions. Romero *et al.* assessed the effect of ventricular morphology (normal, dilated or hypertrophied) on the VV delay in order to obtain an optimal LV synchronization (Romero et al., 2010). The main conclusion was that the distance from the LV lead to the pacemaker and CCS, related to the thickness of the LV lateral wall, introduces a large delay that needs to be compensated by a pre-activation of the LV lead. Sermesant *et al.* developed a personalization strategy for anatomy and function aiming to predict the response to CRT *in-silico* (Sermesant et al., 2012). Personalized heart models reproduced acute effects of pacing on pressure development for several pacing conditions on two patients, achieving good agreement with invasive haemodynamic measurements. More recently, Okada *et al.* also built 3D personalized models of nine patients with heart failure and conduction blocks in order to reproduce the response to CRT by electromechanical simulation, showing the potential of such approach as a supporting tool for clinical decisions (Okada et al., 2017). Very recently, Carpio *et al.* carried out a simulation study using an image-based anatomically detailed ventricular model coupled to a CCS model, aiming to assess the efficacy of CRT depending on the placement of pacing leads (Carpio et al., 2019). Moreover, they simulated the ECG by means of a 3D torso model, taking the QRS shortening in response to CRT as a measure to quantify the therapy effectiveness. As shown, 3D cardiac computational models oriented at biophysical simulation are being widely used to study the mechanisms underlying the efficacy of CRT and even tested as a promising tool to help in the proper identification of candidates for CRT (Lee et al., 2018).

3.7. Conclusions

3D computational models of cardiac anatomy and function have significantly benefited from the revolution of medical imaging systems, as the advances on patient-specific modelling have enabled the use of 3D heart models reconstructed from clinical MRI or CT scans. A further development of techniques able to build 3D personalized cardiac models is expected to have a great impact on diagnosis, therapy planning and prevention of cardiac disorders. Current 3D cardiac models have achieved a remarkable structural and biophysical detail, providing a multi-parametric source of information that integrates multimodal images (*ex-vivo* and *in-vivo*), one-dimensional signals and biophysical data into a common spatio-temporal coordinate system, which is already helping to gain insights into several cardiac disorders, e.g., into mechanisms of arrhythmia in several diseased settings. The incorporation of critical cardiac structures, such as the CCS, cardiac fibre orientation and the coronary tree, will facilitate further biophysical modelling. The next step towards the translation of this approach into clinical environments are the automation and scalability of model-building procedures, allowing to easily process large-scale image databases. The evolution of the high-performance computing (HPC) technologies, such as graphical processing units (GPUs), are also expected to speed up the solving processes of biophysically detailed 3D simulations of cardiac function by means of affordable computing architectures, thus making the computational cardiac EP compatible with the clinical environment and its restricted time frames.

3.8. Table of 3D cardiac computational models

Table 3.2, built as a main result of this review work, is a large table specifically designed to give a complete summary about the reviewed models. In this table, all reviewed 3D cardiac computational models (60 models) appear sorted by chronological order in an attempt to outline the evolution of this kind of models over the last five decades.

Table 3.2 provides information about the data source and methods used to develop each one of the 60 reviewed 3D cardiac models, as well as their main features, final application and online availability. First column in Table 3.2, named '*Kind of model*', corresponds to a proposed classification based on the level of anatomical realism achieved by the model and the method used for the 3D reconstruction of cardiac anatomy. Second column, called '*Species (anatomy)*', specifies the animal species whose anatomy was modelled. Under the heading '*Model extension*', we detail the cardiac chambers and structures included in each model. Next two columns provide information about the source of the '*Anatomical information*' and the '*Segmentation method*' (for image-based models) used to build every model, respectively. The column labelled as '*Meshing*' shows the approach used to generate the 3D computational model from the reconstructed cardiac geometry and, if reported, some details such as the mesh resolution. '*Fibre orientation*' and '*CCS*' (cardiac conduction system) columns report whether or not these features are included in the model and, if so, the approach used to include them. '*Endocardium detail*' column gives information about the level of anatomical detail achieved in the reconstructed endocardial surfaces, in both ventricles and atria. Next column, named '*Other features*', collects miscellaneous information, such as the inclusion in the model of ischaemic scars, some kind of anatomical variation, labelling of interesting anatomical regions, etc. '*Model purpose*' column specifies the final application for which each model was originally developed. The last column, '*Online*', reports whether the model is available online, providing the link if so.

Note that the information related to most of the columns of Table 3.2 was previously addressed in a specific subsection of this chapter (see section 3.4), where we discuss why certain features or methods are needed or convenient for particular applications.

Additionally, Table 3.3 describes the meaning of all acronyms and abbreviations used to encode the information contained in Table 3.2.

MODEL	Kind of model	Species (anatomy)	Model extension	Anatomical information	Segmentation method	Meshing	Fibre orientation	CCS	Endo. detail	Other features	Model purpose	Online
Koushanpour & Collings, 1966	Geom	Rat, cat, turtle	LV	ExpM							MA	
Okajima et al., 1968	Anat	Human	BV	HS (3mm)	MD	vFEMh (3mm)		HPS, AK (Dog)			EP	
Ghista & Sandler, 1969	Geom	Human	LV	VLV							MA	
Janz & Grimm, 1972	Geom	Rat	LV, FAn	HS		vFEMh (198el)					MA	
Horan et al., 1978	Anat	Human	LV	HS(18)	MD	vFEMh (1675el,3.2mm)		AP, Dur			EP	
Miller & Geselowitz, 1978	Anat	Human	BV	HS (16,4.64mm)	MD	CA (4000,3.75mm)					EP	
Vinson et al., 1979	Anat	Human	LV	VLV	M	vFEMh (36el)					MA	
Van den Broek, 1980	Geom	Rabbit	LV	ExpM, ML			RBM				MA	
Aoki et al., 1987	Anat	Human	BV	pHS (7)	M	CA (50e3,1.5mm)		HPS, Dur			EP	
Thakor & Eisenman, 1989	Anat	Dog	BV	pHS (1.5mm)	M	vFEMh (1473el)		Purk, AK			EP	
Nielsen et al., 1991	Anat	Dog	BV	ExpM		vFEM-H (24el,41n)	DExp (SH)		Pap		MA, EP	AMDB
Creswell et al., 1992	IM	Dog	BV	iMRI (11,5mm)	M	vFEMh (x)						
Lorange & Gulrajani, 1993	IM	Human	WH	eCT (132)		CA (25e4,1mm)	Ventricles	HPS, 1120-PMJ			EP	
Colli Franzone et al., 1998	Geom		LV			vFEMh (x)	RBM	AP, Dur			EP	

Table 3.2. (part 1 of 5) Table of reviewed 3D cardiac computational models. It provides information about the main features included in each of the 60 reviewed models, as well as the methods used for its development.

MODEL	Kind of model	Species (anatomy)	Model extension	Anatomical information	Segmentation method	Meshing	Fibre orientation	CCS	Endo. detail	Other features	Model purpose	Online
Vetter & McCulloch, 1998	Anat	Rabbit	BV	HS (2-3mm)		vFEMx	DExp (SH)				EM	1
Siregar et al., 1998	CAD	Human	WH, GCV	ML		CA (x)	Lit	AVN, HPS, Dur			EP	
Yamaki et al., 1999	Anat	Human	WH			CA (50e3,1.5mm)		SAN, AVN, HPS, Dur		ISC	EP	
Freudenberg et al., 2000	Anat	Human	WH	pHS-VHP (1mm)	SA2D: CTS	CA (x)		SAN, AVN, HPS, AK(Human)	Pap		EP	
Harrild & Henriquez, 2000	CAD	Human	A	ML		vFEMh (25e4el,0.55mm)		Atr	Pec, FO		EP	
Winslow et al., 2000	IM	Rabbit	BV	eMRI (128,469 μm)	SA2D: SN	vFDG (x)	DTI(SH)				EP	
Blanc et al., 2001	Geom	Human	A	ML		sFEMt (250e3n,0.2mm)					EP	
Zemlin et al., 2001	Anat	Human	A	pHS-VHP (1mm)	SA2D: CTS	sFEMt (6e5el,0.28mm)	DExp(DH)	Atr	Pec, CT		EP	
Schulte et al., 2001	IM, PS, Def	Human	BV, FAn	iMRI (5mm)	M	sFEM-H					MBS	
Virag et al., 2002	IM, LD	Human	A	xMRI	M	sFEMt (50-400e3n)			FO		EP	
Lorenzo-Valdés et al., 2002	At	Human	BV, EpLV	14-iCine-MRI (8-10)	M						MBS-TCM	
Frangi et al., 2002	At + Stat	Human	BV, EpLV	14-iMRI (10mm)	M	sFEMt (x)					MBS	
Kerckhoffs et al., 2003	Geom		LV			EP - vFEMh (10e3el,11e3n,2mm) Mec-vFEMh (108el,3.2e3n)	RBM	AP (4), Dur			EM	

Table 3.2. (part 2 of 5) Table of reviewed 3D cardiac computational models. It provides information about the main features included in each of the 60 reviewed models, as well as the methods used for its development.

MODEL	Kind of model	Species (anatomy)	Model extension	Anatomical information	Segmentation method	Meshing	Fibre orientation	CCS	Endo. detail	Other features	Model purpose	Online
Stevens et al., 2003	Anat	Pig	BV	ExpM		vFEM-H (79el)	DExp (SH)				Mec	
Sermesant et al., 2003	IM, Def	Dog	BV	eDT-MRI	SA2D: CM	vFEMt (10e3el,2e3n)	DTI (DH)			LAR	MBS	
Lötjönen et al., 2004	At + Stat	Human	WH, EpV	25-iMRI (6-7mm)	M	sFEMt (x)			Pap		MBS	
Helm et al., 2005	IM	Dog	BV	eDT-MRI (0.8mm)	SA2D: SN	vFEM-H (24el)	DTI (SH)					
Haddad et al., 2005	IM, PS, Dyn	Human	WH, GCV, pCT	iMRI (2mm) iCine-MRI (7mm)	WH - M pCT - SA2D	sFEMt (x)				MCC		
Perperidis et al., 2005	At, Dyn	Human	BV, EpLV	26-iCine-MRI (10mm)	M + Reg	sFEMt (x)			Pap	MCC	other	
Bodin & Kuz'min, 2006	CAD	Human	WH, OEp, GCV	other		sFEMt (x)					EP	
Seemann et al., 2006	Anat	Human	A	pHS-VHP	SA2D: RG, SN	vFEMh (1.58e6el)		SAN, Atr	Pec, FO		EP	
Appleton et al., 2006	IM PS, Dyn	Human	BV	iCine-MRI (9)	A2D: CM, SN	CA (40e3)		HPS		MCC (20)	EP	
Yang et al., 2006	IM, PS	Human	WH, OE	iMS-CT (1mm)	SA2D: SN, LS							
Burton et al., 2006	IM, HD	Rabbit	BV, fCT	eMRI (24.4µm) pHS-St (10µm)	MRI-SA2D: CM pHS-A2D: CTS	vFEM	IM3D (SH)		Pap, TC	LT	EP	
Sermesant et al., 2006	Geom, Def	Human	BV			vFEMt (20e3el,4e3n)	DTI (DH)			LAR	Mec, MBS	
Lorenz & von Berg, 2006	At + Stat	Human	WH, EpLV, GCV, pCT	27-iMS-CT (0.5mm)	SA3D: Fit	sFEMt (x)					MBS	AMDB

Table 3.2. (part 3 of 5) Table of reviewed 3D cardiac computational models. It provides information about the main features included in each of the 60 reviewed models, as well as the methods used for its development.

MODEL	Kind of model	Species (anatomy)	Model extension	Anatomical information	Segmentation method	Meshing	Fibre orientation	CCS	Endo. detail	Other features	Model purpose	Online
Sermesant et al., 2006	1. Anat, Def,Dyn 2. IM, Def,Dyn	Dog	BV	1. ExpM 2. eDT-MRI(x)	SA2D: CM	vFEMt (40e3el,7e3n)	1. Lit (Dog) 2. DTI (DH)	AP, Dur		LAR	EP, Mec, MBS-TCM	
Trunk et al., 2007	Anat	Human	WH, GCV, pCT	pHS-VHP	M	Vox (1mm)					*other*	
Ordas et al., 2007	At	Human	WH, pCT	100-iMS-CT (2mm)	A3D: Reg	vFEMt (0.5mm)	RBM	Atr, HPS, AK(Human)		LAR, TH	EP	AMDB
Peyrat et al., 2007	At	Dog	WH	9-eMRI			DTI (SH)					2 AMDB
Arevalo et al., 2008	IM	Dog	WH	eMRI (0.8mm)	SA2D: CM, RG, LS	vFEMt (29e6el, 5e6n, 0.4mm)	DTI (SH)		Pap,TC	ISC	EP	
Plotkowiak et al., 2008	IM	Rabbit	BV	eMRI (24.4µm)	A2D: LS	vFEMt (3.7e6el,83e4n)			Pap		EP	
Ecabert et al., 2008	At + Def, Stat	Human	WH, EpLV, GCV	28-iMS-CT (0.67-3mm)	SA3D: Fit	sFEMt (14.7e3el, 7.3e3n,2.5-5mm)					MBS	AMDB
Ruiz-Villa et al., 2009	CAD	Human	A	ML		vFEMh (51e3el,1e5n)	Lit (Human)	Atr	Pec,FO	LAD	EP	
Niederer et al., 2009	IM, PS	Human	BV	iMRI (x)	M	vFEM-H (112el,183n)	Lit (Dog)				Mec	
Plank et al., 2009	IM, HD	1. Rabbit 2. Rat	BV	eMRI (24.4µm) pHS-St (10µm)	MRI - SA2D: LS,CM pHS-A3D: Reg(MRI)	1. vFEMt (24e6el, 4.3e6n,125µm)	1. RBM 2. DTI (SH)		Pap,TC	LAR	EP	
Vadakkumpadan et al., 2009	IM, HD	Rabbit	BV, fCT	eMRI (24.5µm)	SA2D: CM, RG, LS	vFEMx (31e6el,50µm)	DTI (SH)	Purk, hrMRI	Pap,TC	ISC	EP	
Heidenreich et al., 2010	IM	Human	BV	eDT-MRI (0.8mm)	M	vFEMh (1.3e6el, 1.4e6n,0.4mm)	DTI (SH)	HPS		RVD, TH	EP	

Table 3.2. (part 4 of 5) Table of reviewed 3D cardiac computational models. It provides information about the main features included in each of the 60 reviewed models, as well as the methods used for its development.

MODEL	Kind of model	Species (anatomy)	Model extension	Anatomical information	Segmentation method	Meshing	Fibre orientation	CCS	Endo. detail	Other features	Model purpose	Online
Romero et al., 2010	IM, PS	Human	BV	iMS-CT (x)	A3D: MBS	vFEMt (15-21e6el, 2.5-3.5e6n,>0.5mm)	RBM	Purk, Dur		LVH, LVD (3 models)	EP	
Bishop et al., 2010	IM, HD	Rabbit	BV, fCT, FAn	eMRI (24.4μm)	SA2D: LS	vFEMt (41.5e6el, 7e6n,125μm)	RBM		Pap, TC, CTen	LAR	EP	3
Wenk et al., 2010	IM	Sheep	LV, FAn	iMRI (x), pHD		vFEMh (x)	Lit (Dog)		Pap, CTen	ISC	Mec	
Gurev et al., 2011	IM	Dog, Human (3 models)	BV	eMRI (x)	SA2D: CM, RG, LS	EP - vFEMx (1.7e6el,1.4e6n) Mec - vFEM-H (172el,356n)	DTI (SH)	AP, Dur			EM	
Deng et al., 2012	IM	Human	WH	eCT (531, 0.33mm)	SA2D: CM, RG		DExp (SH)	SAN, Atr, AVN, HPS, AK(Human)	Pec, FO		EP	
Zhao et al., 2013	Anat, HD	Sheep	A	pHS (50μm)	SA2D: CM, RG	vFDG (0.1mm)	IM3D (SH)	SAN, Atr	Pec, CT		EP	
Aslanidi et al., 2013	IM, HD	Dog	A	eMicro-CT (36μm)	SA2D		eMicro-CT (SH)	AVN, Atr	Pec		EP	
Hoogendoorn et al., 2013	At + Stat, Dyn	Human	WH, EpLV, GCV, pCT	138-iMS-CT (2mm)	A3D: Reg	sFEMt (16e3n)				LAR, MCC (15)	MBS-TCM, other	4

Table 3.2. (part 5 of 5) Table of reviewed 3D cardiac computational models. It provides information about the main features included in each of the 60 reviewed models, as well as the methods used for its development.

AMDB: Anatomical Model Database. https://amdb.isd.kcl.ac.uk/
1: http://cmrg.ucsd.edu/
2: https://team.inria.fr/asclepios/data/
3: https://chaste.cs.ox.ac.uk/trac/browser/data/public

Kind of model	
Geom	Geometrical shape-based model (ellipsoid-based)
SAnat	Simple anatomical model
IM	Image-based model
PS	Patient-specific model
CAD	CAD model
Def	Deformable model
Stat	Statistical cardiac model
At	Cardiac atlas
Dyn	Dynamic model
HD	High level of anatomical detail
LD	Low level of anatomical detail
Model extension	
LV	Left ventricle model
BV	Bi-ventricle model
A	Bi-atrial model
WH	Whole heart model
GCV	Great cardiac vessels
pCT	Part of coronary tree
fCT	Full coronary tree
OE	Only endocardium
OEp	Only epicardium
EpLV	Only epicardium for LV
EpV	Only epicardium for ventricles
Fan	Fibrous annulus of atrio-ventricular valves
Anatomical information	
ExpM	Experimental measurements taken from explanted hearts
ML	Measurements taken from the literature
pHD	Pictures of heart dissections
HS (*n,mm*)	Histo-anatomical slices. *n*: number of slices. *mm*: slice thickness.
pHS (*n,mm*)	Pictures of histo-anatomical slices
pHS-St (*n,mm*)	Pictures of histo-anatomical slices with special staining
eMRI (*n,mm*)	*Ex-vivo* MRI
iMRI (*n,mm*)	*In-vivo* MRI
***N*-iMRI (*n,mm*)**	*In-vivo* MRI. *N*: population size (for atlases)
eCT (*n,mm*)	*Ex-vivo* CT
iCT (*n,mm*)	*In-vivo* CT
***N*-iCT (*n,mm*)**	*In-vivo* CT
VLV	*In-vivo* ventriculograhy of the LV (cine-angio-cardiography)

Table 3.3. (part 1 of 3) List of acronyms used to encode the information shown in the table of reviewed 3D cardiac computational models (Table 3.2).

Segmentation method	
MD	Manually drawn
M	Manual segmentation
SA2D	Semi-automatic 2D (slice by slice), with some manual interaction
A2D	Automatic 2D, without any manual interaction
SA3D	Semi-automatic 3D segmentation, with some manual interaction
A3D	Automatic 3D segmentation, without any manual interaction
CM	Classical image processing methods (*thresholing, edge detection, morphological op., etc.*)
CTS	Colour-thresholding segmentation
RG	Region growing
SN	Snakes
LS	Level sets
MBS	Model-based segmentation
Reg	Registration with a previously manually segmented image
Fit	Fitting an initial mesh to the target image
Meshing	
CA (*n,mm*)	Cellular automaton. *n*: number of cells. *mm*: spatial resolution.
sFEM-t (*el,n,mm*)	Surface finite element mesh with triangular elements. *el*: number of elements. *n*: number of nodes. *mm*: spatial resolution
vFEM-h (*el,n,mm*)	Volumetric finite element mesh with hexahedral elements
vFEM-t (*el,n,mm*)	Volumetric finite element mesh with tetrahedral elements
sFEM-H (*el,n,mm*)	Surface finite el. mesh based on cubic Hermite basis functions
vFEM-H (*el,n,mm*)	Volumetric finite el. mesh based on cubic Hermite basis functions
vFDG (*mm*)	Volumetric finite difference grid. *mm*: spatial resolution.
Vox (*mm*)	Voxels-based volumetric model (*not FEM*). *mm*: spatial resolution.
Fibre orientation	
RBM	By a rule-based method based on Streeter's findings
DTI	From *ex-vivo* DTI images
SH	From the same heart used for the anatomical reconstruction
DH	From a different heart than used for the anatomical reconstruction
DExp	From direct experimental measurements
Lit (*sp*)	Taken from the literature. *sp*: species
IM3D	From the volumetric image assembled from histological slices

Table 3.3. (part 2 of 3) List of acronyms used to encode the information shown in the table of reviewed 3D cardiac computational models (Table 3.2).

Cardiac conduction system	
AP (*n*)	CCS emulated by activation points on the endocardial surfaces. *n*: number of activations points
Dur	From the activation maps obtained by Durrer *et al.* 1970
HPS	His-Purkinje fibres
AVN	AV (atrioventricular) node
SAN	SN (sino-atrial) node
Purk	Only Purkinje fibres
AK (*sp*)	From the anatomical knowledge. *sp*: species
N-PMJ	Purkinje-muscle junctions. *N*: number of PMJs
Atr	Atrial conduction bundles: crista terminals, Bachmann's bundle and pectinate muscles
hrMRI	Free-running Purkinje fibres from high-resolution *ex-vivo* MRI
Endocardium detail	
Pap	Papillary muscles
TC	Trabeculae carnae
Pec	Pectinate muscles
CT	Crista terminalis
FO	Fossa ovalis
CTen	Chordae tendineae
Other features	
LAR	Labelling of anatomical regions
TH	Electrophysiological transmural heterogeneity in ventricular wall
RVH	RV hypertrophy
LVH	LV hypertrophy
LVD	LV dilation
LAD	Left atrium dilation
ISC	Infarct-derived ischemic scar in LV, including core and border zone
MCC (*n*)	Motion due to the cardiac cycle. *n*: number of phases
LT	Labelling of tissues (histological information)
Model purpose	
MA	Mechanical analysis
EP	Simulation of cardiac electrophysiology
EM	Simulation of cardiac electro-mechanics
Mec	Simulation of cardiac mechanics
MBS	Model-based segmentation
MBS-TCM	Model-based segmentation with tracking of cardiac motion

Table 3.3. (part 3 of 3) List of acronyms used to encode the information shown in the table of reviewed 3D cardiac computational models (Table 3.2).

Chapter 4

Clinical Data

In this chapter, we describe and discuss the clinical data that we used to develop our 3D computational models of patient-specific infarcted ventricles and torso aimed at the computational simulation of cardiac electrophysiology (EP).

4.1. Introduction

It is really important to highlight that the main restriction that we imposed on the design of our approach was that it should exclusively rely on non-invasive clinical data. Our final goal is to test the feasibility of performing reliable *in-silico* EP studies prior to radiofrequency ablation (RFA) procedures (i.e., prospective studies) by means of personalized 3D computational models of ventricles and torso. Thus, the use of data invasively recorded during the intervention to build such models would be a clear contradiction, as it would only allow retrospective studies with no usefulness for personalized therapy planning. That said, we did include data invasively registered via cardiac

catheterization in our work. However, such data were only used for validation purposes, aiming to test the performance of the built 3D computational models, as will be explained in detail in following chapters.

4.2. Clinical data

In this work, we used a set of anonymized clinical data from a 58-year-old male patient referred for RFA procedure aiming to terminate a monomorphic ventricular tachycardia (VT) related to a large chronic myocardial infarction (MI), which was located at the posterior wall of the left ventricle (LV). It is important to highlight the fact that the patient suffered the acute episode of myocardial ischaemia causing the MI 11 years before the clinical VT episode related to the MI. Hence, there was no doubt about the chronicity of the MI, which evidently was in its chronic (or healed) stage.
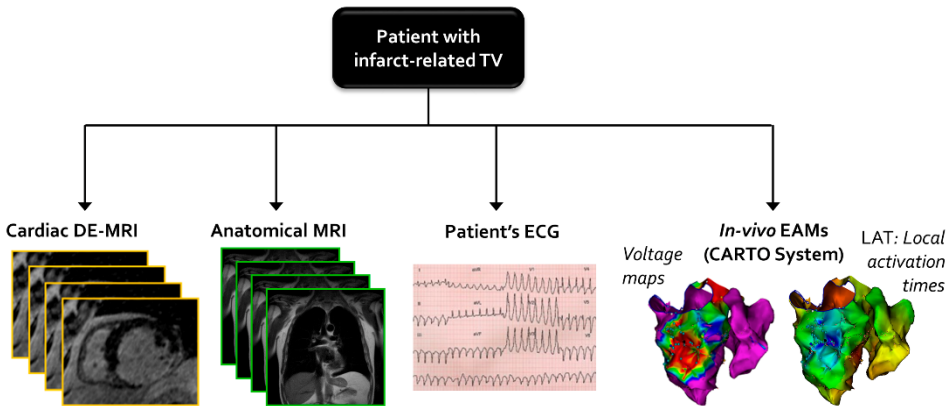
Figure 4.1. Schematic representation of the clinical dataset used in this work.

As shown in Figure 4.1, the clinical dataset used for this study included: (1) clinical high-resolution cardiac DE-MRI, (2) whole-torso anatomical MRI, (3) electroanatomical maps (EAM) invasively recorded via CARTO® 3 System (Biosense Webster, Inc., Diamond Bar, CA, USA) (Gepstein et al., 1997) and (4) 12-lead ECG signals registered during the RFA procedure both in sinus rhythm and during VT episodes induced by pacing protocols. In addition, some clinical ECG recordings were provided, both in sinus rhythm and during clinical VT (see

Figure 4.2). It must be highlighted that all those data were not specifically generated for research purposes, but they were collected in a clinical environment as part of its daily routine.
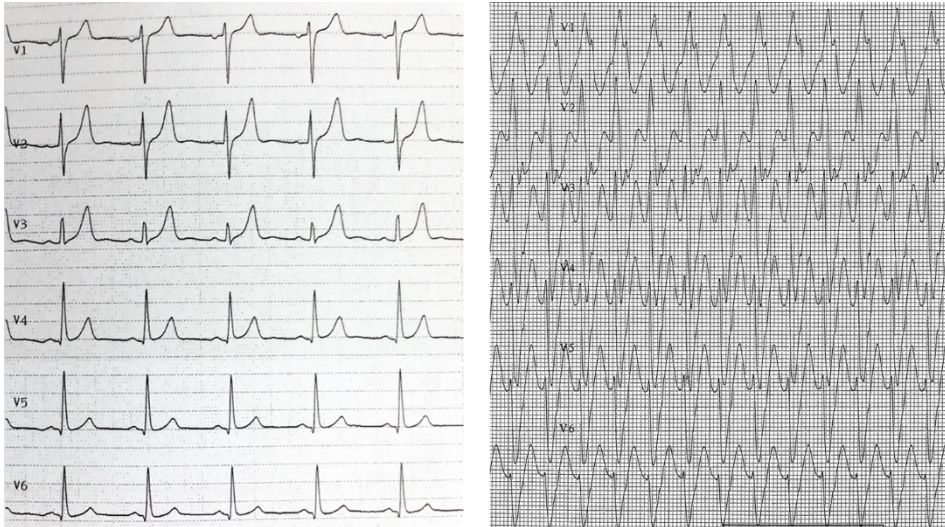
Figure 4.2. Fragments of scanned clinical ECG recordings showing the signals from precordial leads both in sinus rhythm (*left*) and during the clinical VT episode (*right*).

4.3. Cardiac DE-MRI

Regarding cardiac imaging techniques, delayed enhancement-MRI (DE-MRI) is an image modality that enables *in-vivo* evaluation of the tissue damaged by an ischaemic episode leading to MI, that is, the infarct scar and border zone (BZ). This visualization is possible due to the hyperenhancement of the infarcted region in the images caused by the gadolinium-based contrast agent (Doltra et al., 2013; Fieno et al., 2000; Kim et al., 1999a). In fact, it is currently considered as the gold-standard test for *in-vivo* assessment of infarct scar and myocardial viability after MI in clinical settings (Jamiel et al., 2017; Mahida et al., 2017; Patel et al., 2017). Cardiac DE-MRI provides substrate characterization after MI that has shown close correlation with histopathological analyses (Amado et al., 2004; Fieno et al., 2000; Kim et al., 1999a; Wagner et al., 2003), which even allows differentiating between the infarct scar and the BZ. Furthermore, the usefulness

of MRI-based substrate characterization and conducting channels (CC) delineation for planning and guiding ablation procedures aimed at infarct-related VTs has been tested in numerous studies (Andreu et al., 2011, 2015, 2017; Ashikaga et al., 2007; Fernández-Armenta et al., 2013; Perez-David et al., 2011; Soto-Iglesias et al., 2016; Wijnmaalen et al., 2011; Yamashita et al., 2016).
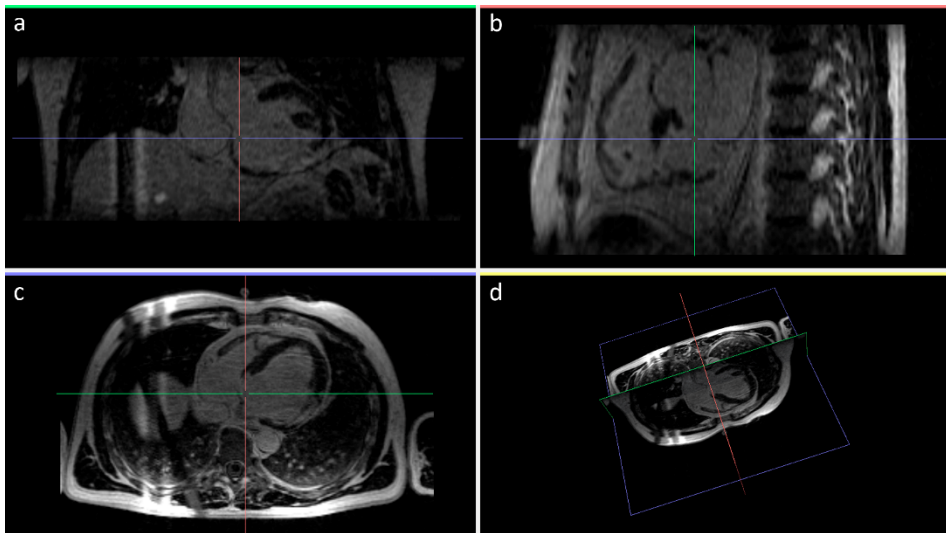
Figure 4.3. Cardiac DE-MRI stack. Views of DE-MRI slices in standard planes: (*a*) coronal, (*b*) sagittal and (*c*) axial planes and (*d*) 3D view of orthogonal standard planes.

In our particular case, a few days before the RFA procedure aimed at eliminating the clinical VT suffered by the patient, the cardiac DE-MRI was acquired in the standard axial plane by a MRI scanner Magnetom Avanto 1.5T[5] (Siemens Healthineers, Erlangen, Germany) using a phased-array body surface coil, about 15 minutes after the administration of the gadolinium-based contrast MultiHance (gadobenate dimeglumine, 529 mg/ml) (Bracco Diagnostics Inc., Monroe Township, New Jersey, USA). The acquisition was synchronized with both ECG (ECG-gated) and breathing (navigator-gated), imaging the heart at the end-diastolic phase of cardiac cycle, with a trigger time delay of 685 ms for a nominal R-R interval of 928 ms along the acquisition. The DE-MRI stack

---

[5] MRI scanner Siemens Avanto 1.5T (Siemens Healthineers, Erlagen, Germany)
www.siemens-healthineers.com/magnetic-resonance-imaging/0-35-to-1-5t-mri-scanner/magnetom-avanto

comprised 96 slices of 256×256 pixels encompassing the whole heart (ventricles and atria) with a pixel size of 1.4×1.4 mm in plane, a slice thickness of 1.4 mm and no gap between adjacent slices, thus resulting in an isotropic voxel of 1.4 mm^3.

4.3.1. Myocardial viability assessment

The assessment of myocardial viability performed in the clinic based on the DE-MRI revealed that the MI extended over 7 out of the 17 segments of the left ventricle (LV) model of the American Heart Association (AHA). Myocardial regions that appear affected in the DE-MRI were basal and medial segments of both inferoseptal (segments 3 and 9) and inferolateral walls (segments 5 and 11) and all segments (basal, mid and apical) of inferior wall (segments 4, 10 and 15), which correlates with the occlusion of the right coronary artery (Ortiz-Pérez et al., 2008).

4.4. Whole-torso anatomical MRI

Cardiac DE-MRI images acquired in clinical environments do not usually cover the whole torso, as they focus on the cardiac chambers. In addition to the ventricular model, we needed to develop a 3D model of the torso in order to perform computational simulations of cardiac EP at whole body level, that is, to compute simulated ECGs. Thus, we were also provided with an anatomical MRI covering the entire torso, from the neck to the waist (see Figure 4.4). That whole-torso MRI was acquired in the coronal plane, with a slice thickness of 10 mm. This is much coarser than the resolution of the cardiac DE-MRI stack, although it is within the usual range of spatial resolution for clinical anatomical MRI scans. Such anatomical MRI stack comprised 16 slices of 320×320 pixels with an in-plane resolution of 1.25×1.25 mm. Therefore, the volume dataset was composed of irregular voxels sizing 10×1.25×1.25 mm, thereby resulting in a resolution in coronal slices (Figure 4.4[a]) much finer than in axial (Figure 4.4[b]) and sagittal (Figure 4.4[c]) planes.
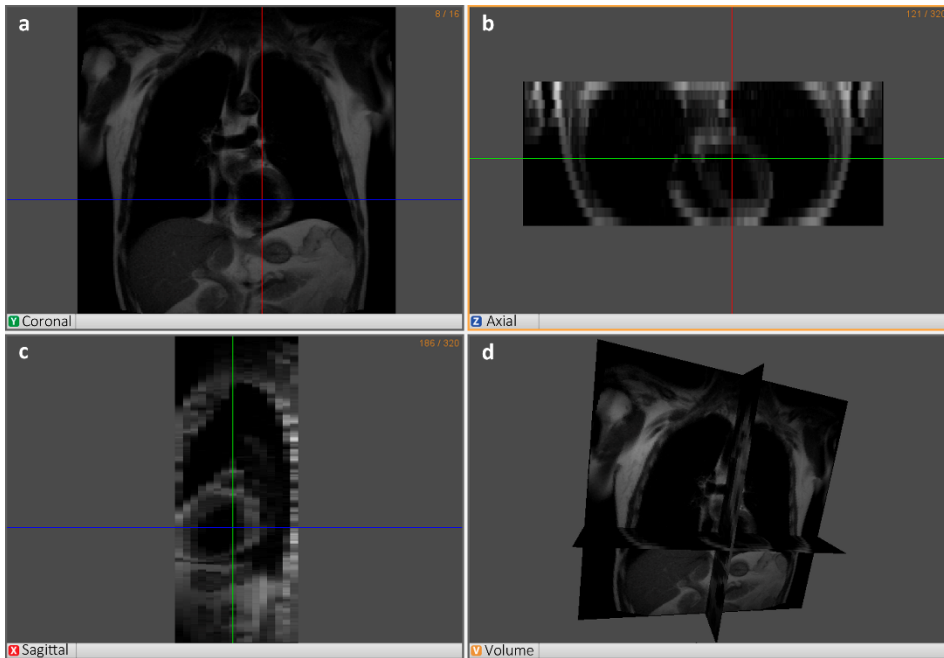
Figure 4.4. Whole-torso anatomical MRI. Views of MRI slices in standard planes: (*a*) coronal, (*b*) axial and (*c*) sagittal planes and (*d*) 3D view of orthogonal standard planes.

4.5. Electroanatomical maps

Since their appearance in the late 90's (Ben-Haim et al., 1996; Gepstein et al., 1997), electroanatomical mapping (EAM) systems have become a useful tool to guide RFA procedures, being increasingly used in interventions aimed at assessing both atrial (Calkins et al., 2012) and ventricular arrhythmias (Aliot et al., 2009; Priori et al., 2015). During the EP studies performed via catheterization, these systems create in real-time 3D maps of every assessed cardiac chamber, which integrates all EP information recorded by the sensors and electrodes placed at catheter tip. In the case of infarct-related VTs, EAM systems are considered as a helpful tool to identify CCs as RFA targets based on the abnormal features of the electrograms (EGM) in such regions (Bogun et al., 2005; Gardner et al., 1985), especially when clinical VT is unmappable due to haemodynamic instability or non-inducibility in the EP laboratory (Al-Khatib et al., 2018; Aliot et al., 2009; Marchlinski et al., 2000; Priori et al., 2015).

In our case, *in-vivo* EP data were invasively recorded by CARTO® 3 System using the *NaviStar® ThermoCool®* catheter (Biosense Webster, Inc., Diamond Bar, CA, USA) including a 3.5-mm open-irrigated tip, which can act as diagnostic and ablation catheter (Abdelwahab and Sapp, 2007). In Figure 4.5, one can observe the holes at catheter tip for saline irrigation during RFA. That catheter has a tip electrode and three additional ring electrodes referred to as M1 (tip electrode), M2, M3 and M4 from more distal (closer to the tip) to more proximal (farther from the tip), respectively. Thus, it records four unipolar EGMs and two bipolar (M1-M2 and M3-M4). As shown in Figure 4.5, those four electrodes are not equidistant, since the M2-M3 spacing is 5 mm while M1-M2 and M3-M4 spacing is 2 mm, respectively. Moreover, the catheter tip includes a pressure sensor to ensure a proper contact between the catheter and the myocardial wall during the mapping process.

Figure 4.5. Picture of the *NaviStar® ThermoCool®* catheter (Biosense Webster, Inc., Diamond Bar, CA, USA), showing its 3.5-mm open-irrigated tip with holes for saline irrigation during ablation and its four electrodes: M1, M2, M3 and M4.
Image adapted from: www.biosensewebster.com/emea/

For each studied cardiac chamber, CARTO® 3 System generates a triangle-based 3D surface mesh representing the geometry of the mapped anatomical surface (see Figure 4.6). Those meshes include every measurement point (hereinafter referred to as *CARTO® points*) as a vertex of the corresponding mesh. Besides recorded signals (bipolar and unipolar EGM signals and 12-lead ECG), additional data is associated with each CARTO® point, such as local activation time (LAT) annotation in ms, peak-to-peak voltage amplitude values for bipolar (BiP) and unipolar (UniP) signals measured in mV from distal EGMs (M1-M2 and M1, respectively), electrodes position (*x*, *y*, *z* coordinates) and contact pressure in grams.
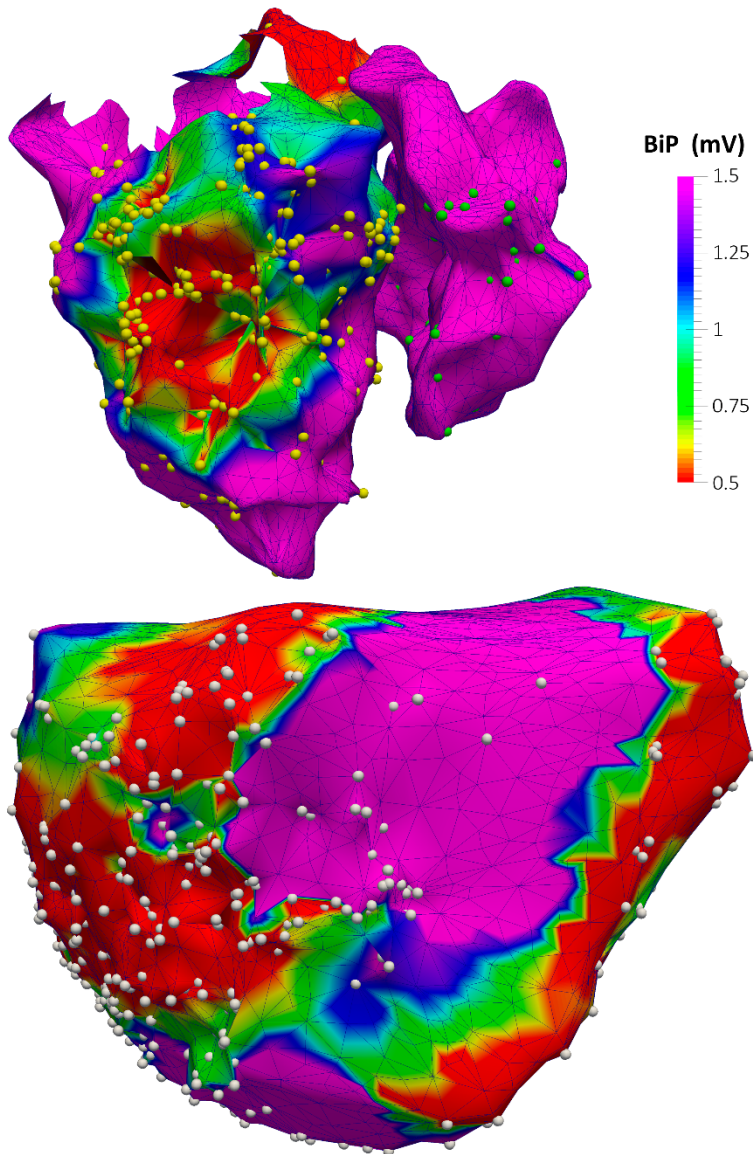
Figure 4.6. Posterior view of the 3D triangle-based surfaces extracted from CARTO® data files and converted into VTK file format, representing LV and RV endocardial surfaces (*top*) and ventricular epicardium (*bottom*). All CARTO® points recorded during the EP study are displayed as coloured spheres on the corresponding 3D surface: *yellow* for LV endocardium, *green* for RV endocardium and *white* for epicardium. Colour code displayed on the surfaces represents BiP (peak-to-peak bipolar potentials in mV) measured from distal bipolar EGM (M1-M2). Regions with BiP values under 0.5 mV are considered as non-excitable tissue corresponding to dense fibrotic scars, whereas values in the range 0.5-1.5 mV are considered to be part of the BZ.

In this case, the EAMs generated during the EP study contained 847 CARTO® points in total: 315 points from LV endocardium, 78 points from right ventricle (RV) endocardium and 454 points from epicardium. Those EAMs were acquired in sinus rhythm, including for every CARTO® point 18 different signals (12-lead ECG, four unipolar EGMs and two bipolar EGMs) that were recorded during 2.5 seconds at a sampling rate of 1 kHz. Regarding epicardial mapping, it was performed by accessing pericardial space through percutaneous (non-surgical) transthoracic subxiphoid approach by means of puncture using an epidural needle (Brugada et al., 2003; Sosa and Scanavacca, 2005; Tedrow and Stevenson, 2009; Yamada, 2014), following the access procedure originally described by Sosa *et al.* (Sosa et al., 1996, 2000). In Figure 4.6, one can observe that the most densely mapped regions (high concentration of CARTO® points) are located on the posterior wall of the LV, at both endocardial and epicardial level, matching the cardiac segments affected by the MI according to the myocardial viability assessment based on the DE-MRI (see section 4.3.1). This is because the main goal of the EP study conducted immediately prior to the RFA procedure was to detect CCs of viable tissue crossing the infarct scar as ablation targets, since they usually act as structural substrates for the reentrant pathways responsible for monomorphic VTs (Baldinger et al., 2016; Berruezo et al., 2015; de Chillou et al., 2002).

We implemented a tailored code in MATLAB® (The MathWorks Inc., Natick, MA, USA) to automate the process of reading the huge amount of data files generated by CARTO® 3 System during the EP study (more than 40,000 plain text ASCII files in our case) and to extract the information from them, including surface meshes and all data associated with every CARTO® point. Our code converts all surface meshes from CARTO® format into VTK file format (The Visualization Toolkit)[6] and encapsulates all signals and additional data in custom data structures to store them in a few MAT files, which is the file format for binary data container native to MATLAB®.

---

[6] The Visualization Toolkit (VTK). www.vtk.org

We also created a MATLAB® GUI (graphic user interface) to visualize all the data linked to each CARTO® point, as well as all the registered signals (both ECG and EGMs) and the location of the assessed point on the surface mesh representing the mapped cardiac surface (see Figure 4.7).
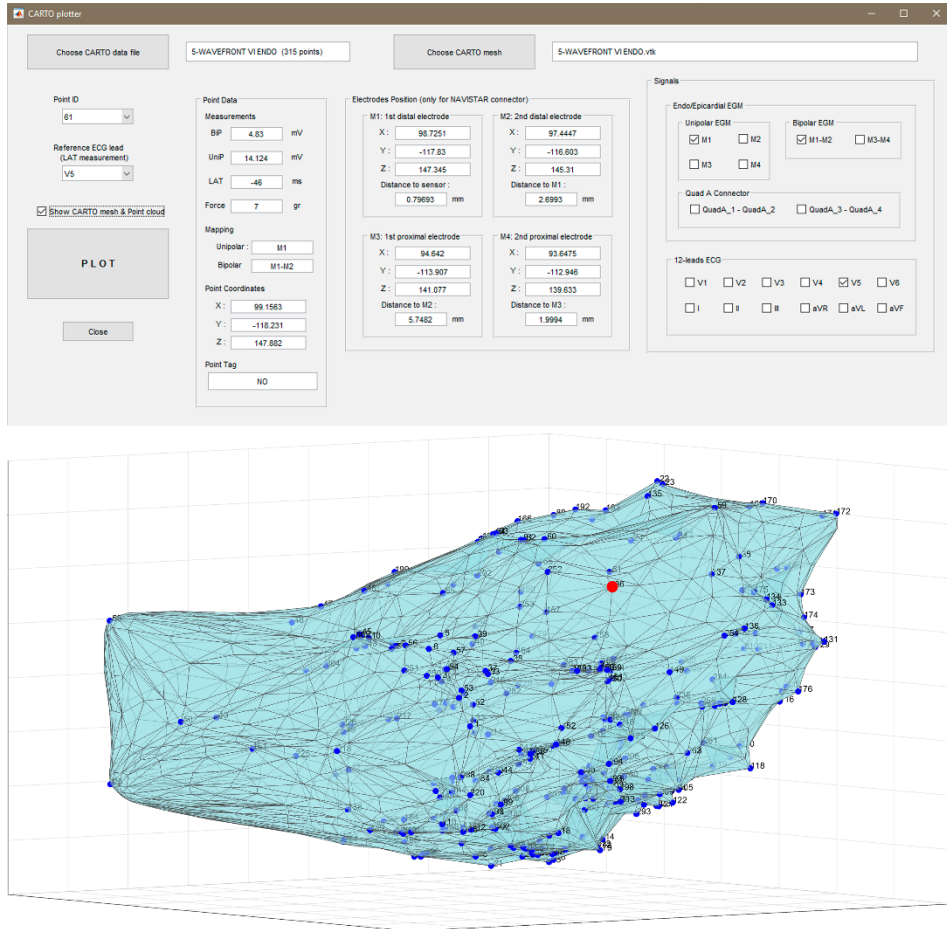
Figure 4.7. (*Top*) Custom MATLAB® GUI created to visualize all signals (ECG and EGM) and additional information associated with each CARTO® point. (*Bottom*) MATLAB® rendering of the 3D CARTO® surface representing the geometry of the LV endocardium with the assessed point highlighted in *red* and the rest of CARTO® points displayed in *blue*.

4.5.1. Post-processing of CARTO® data

LAT annotations provided by CARTO® 3 System represent the time difference between two distinct events: (1) the detection by the catheter electrodes of the arrival of an activation wavefront spreading through the myocardium and (2) a stable reference point defined on a certain ECG signal. Therefore, a negative LAT value means that the local activation happens before the event associated with the reference point (see Figure 4.8[a], for instance), while a positive value means that it happens after, usually corresponding to the so-called *late potentials* (see Figure 4.8[b]). In this case, the electrophysiologists chose the peak of the R wave in the precordial lead V5 as a reference point. Importantly, all signals (both ECG and EGMs) related to each CARTO® point were recorded during 2.5 seconds, with 2 seconds recorded just before the reference point (R-wave peak in V5 signal) and 0.5 seconds after that.

During the EP study, LAT annotations were automatically determined by the *Confidense*™ module of CARTO® 3 System. To ensure the accuracy of the EP data as much as possible, we carefully checked all those annotations one by one, correcting them when necessary. First, we removed all points with peak-to-peak amplitude under 0.5 mV in distal bipolar EGM (M1-M2), as they are considered as non-excitable tissue corresponding to the dense fibrotic scar (Marchlinski et al., 2000; Soejima et al., 2002) where LAT annotations make no sense since local activation is assumed not to happen (see Figure 4.8[d]). For healthy EGMs (see Figure 4.8[a], for instance), we used a custom MATLAB® code to automatically place a new LAT annotation on the deflection of distal bipolar signal (M1-M2) closest to the point of maximum negative slope in distal unipolar signal (M1) (Paul et al., 1990; Spach et al., 1979; Stevenson and Soejima, 2005). Those new annotations showed good agreement with LAT annotations determined by *Confidense*™ module in most cases. However, such criterion is not reliable for points showing noisy and fractionated signals (see Figure 4.8[c]), typically located at the BZ surrounding the infarct scar (Aliot et al., 2009). In those cases, we replaced LAT annotations manually under the close supervision of a well-trained electrophysiologist, who also reviewed LAT annotations for healthy EGMs. That expert also suggested us to remove a number of points showing highly fragmented bipolar EGMs in order to reduce the uncertainty degree that
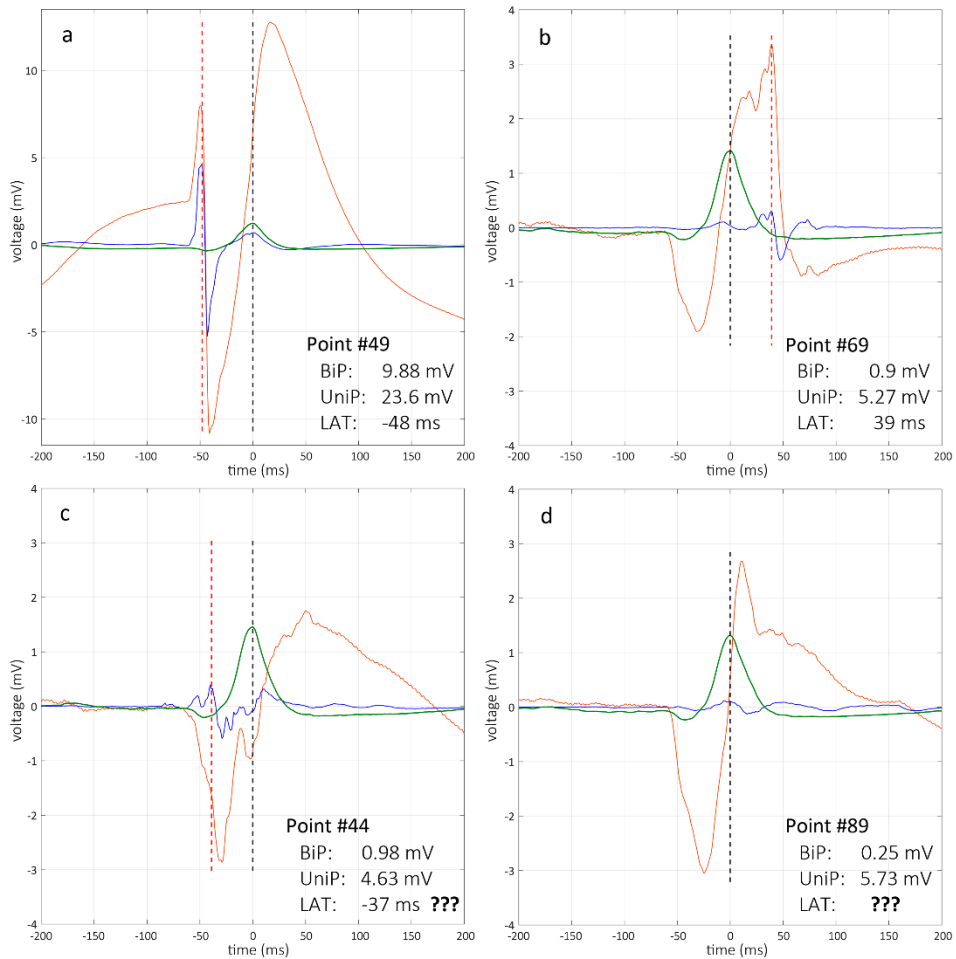
Figure 4.8. Examples of signals provided by CARTO® system, all of them recorded from LV endocardium and showing measured values for: BiP, UniP and LAT. The four graphs display the signals corresponding to the precordial lead V5 (*green*), distal unipolar EGM (M1) (*orange*) and distal bipolar EGM (M1-M2) (*blue*), showing 200 ms prior to R-wave peak in V5 lead (reference point for LAT measurement) and 200 ms after it. Dashed vertical lines represent the R-wave peak automatically detected by CARTO® system (*black*) and the estimated time for tissue activation (LAT annotation) after the checking process (*red*). (*a*) Example of healthy EGM, showing a typical high-amplitude biphasic bipolar EGM that happens notably before the QRS complex. (*b*) Example of late potential that normally correlates with regions of slowed conduction, in which tissue activation happens after the QRS complex. (*c*) Example of low-amplitude fractionated bipolar potential usually associated with regions of tortuous conduction due to the presence of interstitial or patchy fibrosis, for which LAT annotation may be unreliable. (*d*) Example of very low-amplitude bipolar potential typically related to non-excitable tissue (e.g., fibrotic scars), for which LAT annotation makes no sense.

is unavoidably linked to this kind of *in-vivo* data. Moreover, we discarded those points whose LAT value exhibited a poor coherence with their closest neighbours even after the checking process. After this thorough revision of LAT annotations, we only preserved 385 out of the 847 original CARTO® points: 84 for LV endocardium, 49 for RV endocardium and 252 for epicardium.

Finally, we shifted all LAT values to set the LAT of the earliest activated point (most negative LAT value) to 0 ms. That point, with a measured LAT value of -68 ms, was located on the septal region of the LV endocardium at mid-apical level, matching the onset region of the physiological activation sequence in human ventricles (Durrer et al., 1970; Opthof et al., 2017). The latest activated point, which as expected was located on the epicardial surface within the BZ near the scarred tissue, had a measured LAT value of 68 ms, that is, 136 ms after the activation onset. It means that local activation happened 68 ms after the R-wave peak in V5 lead. Evidently, myocardial regions with such a delayed activation do not contribute to the electrical activity manifested in the QRS complex of ECG signals (see Figure 4.8[b], for instance). Those activations normally correspond to late potentials, defined as isolated potentials occurring more than 10 ms after of the QRS complex, which are usually associated with the slowed conduction tissue composing the BZ and surrounding the infarct scar (Aliot et al., 2009).

Chapter 5

Three-Dimensional Computational Models of Infarcted Ventricles and Torso

---

In this chapter, we explain how we built our anatomically detailed patient-specific 3D ventricular model from the cardiac DE-MRI stack, including the 3D reconstruction of the heterogeneous remodelling related to the myocardial infarction (MI), considering the differentiation between the infarct scar and the surrounding border zone (BZ). We also describe how we mapped the CARTO® data onto the surface of the 3D ventricular model in order to integrate such information into the computational model. Furthermore, we address the construction of the 3D torso model aimed at computational simulation of cardiac electrophysiology (EP) at the body level, that is, to compute the simulated ECG.

Although presented here in a considerably further extended fashion, it must be noted that part of the content of this chapter was already included in a

research article entitled "*Personalized cardiac computational models: from clinical data to simulation of infarct-related ventricular tachycardia*", which was recently published in the indexed international journal *Frontiers in Physiology* in May 2019 (Lopez-Perez et al., 2019).

5.1. 3D patient-specific ventricular model

Briefly, we generated a 3D patient-specific bi-ventricular model (i.e., a 3D computational reconstruction of the patient's cardiac anatomy) by segmenting the desired cardiac structures on the DE-MRI slices, including the 3D geometry of the remodelling associated with the MI. The process to create such personalized 3D model from the images involved several steps, as it is explained in the sections below.

5.1.1. Pre-processing of the cardiac DE-MRI

Before segmenting the cardiac anatomy to create the 3D reconstruction of the ventricles, we performed a pre-processing of the DE-MRI stack aiming to ease the segmentation task. Firstly, we upsampled the image stack by linear interpolation to yield an isotropic resolution of 0.35 mm^3, from the coarser original resolution of 1.4 mm^3. After that, we rotated the DE-MRI stack from the standard axes (axial, sagittal and coronal) shown in Chapter 4 (see Figure 4.3) to the cardiac planes (short axis, long axis and four-chamber view), as observed in Figure 5.1. For that task, we used the software Gimias (Larrabide et al., 2009)[7], which allowed to define the cardiac orthogonal axes and perform the 3D multiplanar reconstruction of the DE-MRI stack. Next, we downsampled the reformatted dataset, but only along the short axis, so that the resulting image stack comprised 110 short-axis slices with slice thickness of 1.4 mm and in-plane resolution of 0.35×0.35 mm.

---

[7] Gimias. www.gimias.org/
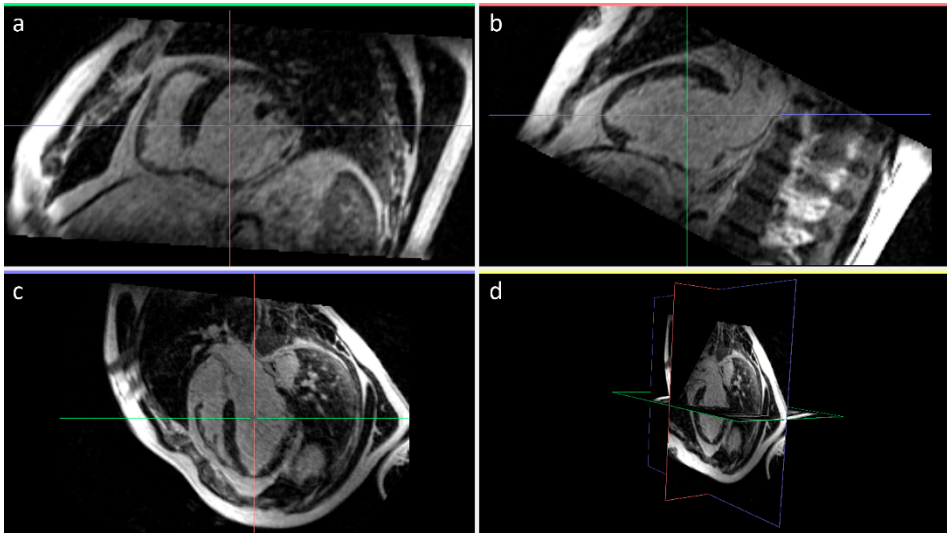
Figure 5.1. Cardiac DE-MRI stack rotated from standard to cardiac planes with Gimias. Different views of reformatted DE-MRI stack showing slices in the three orthogonal cardiac planes: (*a*) short axis, (*b*) long axis or two-chamber view, (*c*) four-chamber view and (*d*) 3D view of orthogonal cardiac planes.

5.1.2. 3D reconstruction of the ventricles

We imported the reformatted DE-MRI stack in DICOM format into the software Seg3D (Scientific Computing and Imaging Institute, University of Utah, USA) (Seg3D, 2013)[8] to perform highly detailed segmentation of whole ventricles by manually outlining the contours of epicardium and both endocardia, including papillary muscles and main trabeculations (see Figure 5.2). We mainly performed the manual segmentation on cardiac short-axis slices (Figure 5.2[a]), although we also used the other two cardiac planes (long axis [Figure 5.2[b]] and four-chamber view [Figure 5.2[c]]) to make corrections and refine certain regions not clearly visualized in short-axis view, such as mitral and aortic valves or the apices of both ventricles. As shown in Figure 5.2, we segmented the DE-MRI differentiating several cardiac structures: LV myocardium (including septum), RV myocardium and papillary muscles and main endocardial trabeculations for LV and RV. For both myocardia (LV and RV),

---

[8] Seg3D. www.sci.utah.edu/software/seg3d.html

we first outlined endocardial and epicardial surfaces on short-axis slices independently. Later, by means of logical operations, we created new ROIs (region-of-interest) just enclosing the myocardium of each ventricle, as they appear in Figure 5.2. It is important to remark that an expert in cardiac imaging checked and validated all segmentations in order to ensure the fidelity of the 3D reconstruction of the patient-specific anatomy.
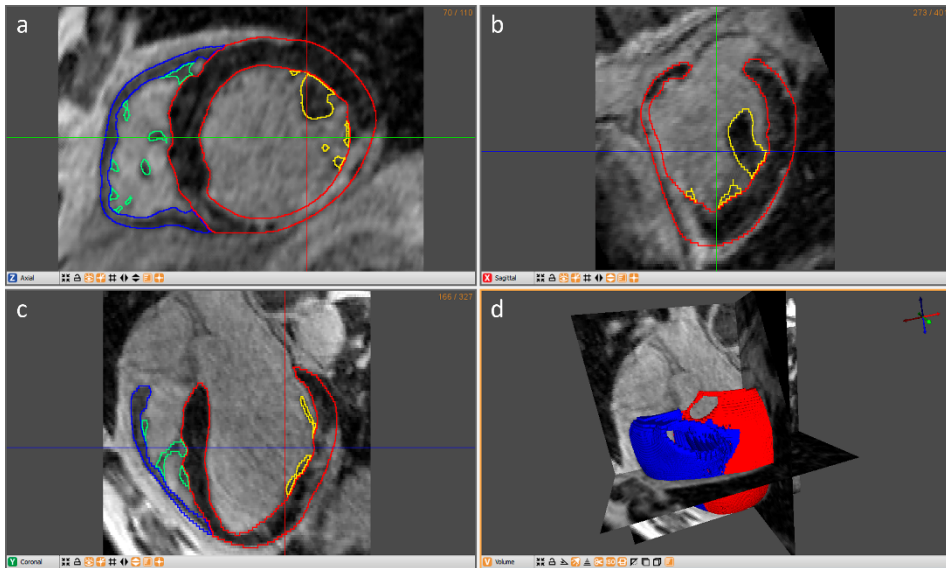
Figure 5.2. Manual segmentation process of cardiac DE-MRI slices performed with Seg3D. Contours highlighted in distinct colours show the different cardiac structures segmented independently: LV myocardium including the septum (*red*), RV myocardium (*blue*) and papillary muscles and endocardial trabeculations of LV (*yellow*) and RV (*green*). The four panels show segmented slices of the DE-MRI stack in different cardiac planes: (*a*) short axis, (*b*) long axis or two-chamber view, (*c*) four-chamber view and (*d*) rendering of the isosurfaces generated from segmentations (LV in *red* and RV in *blue*) displayed on an anterior 3D view of the orthogonal cardiac planes.

After the manual segmentation process, we merged all cardiac structures segmented separately to create a unique ROI enclosing the complete ventricular anatomy, including myocardia, papillary muscles and endocardial trabeculations of both ventricles. From this new ROI we generated a 3D isosurface still using Seg3D (see Figure 5.2[d]) and exported it as a triangular surface mesh in VTK format (see Figure 5.3[a]), thereby creating a raw version of the 3D surface model of the whole ventricles. Next, we edited the 3D surface model with

ParaView (Kitware Inc., New York, USA)[9] to perform a global smoothing in order to counteract the staircase effect resulting from the isosurface generation from a voxel-based data volume (see Figure 5.3). Then, we exported the smoothed version of the 3D surface model from ParaView in STL file format (StereoLithography) (3D Systems, Rock Hill, South Carolina, USA)[10]. Later, we edited the STL surface model with Blender (Blender Foundation, Amsterdam, The Netherlands)[11] aiming to check, refine and correct defects in the mesh at local level.

a   b
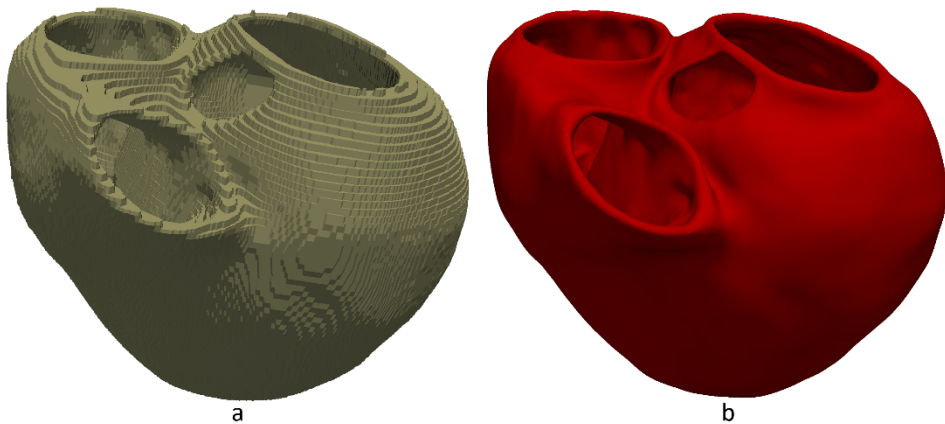
Figure 5.3. 3D surface model of ventricles generated from DE-MRI segmentation. Antero-basal view of the 3D surface model, showing four holes corresponding to the four cardiac valves: mitral and aortic for LV, and tricuspid and pulmonary for RV. (*a*) Raw 3D isosurface as it was generated by Seg3D, showing a notable staircase effect. (*b*) Final version of the 3D surface model after global smoothing with ParaView and local refinement with Blender.

As shown in Figure 5.3, our patient-specific model of the ventricles included the four heart valves: both atrioventricular vales, mitral (LV) and tricuspid (RV), and both semilunar valves, aortic (LV) and pulmonary (RV). In order to fully characterize our 3D model of the ventricles in an anatomical sense, we furthermore made some measurements from the segmented volume dataset. Cardiac cavity (blood pool) and myocardial tissue (cardiac muscle) respectively exhibited volumes of 176 ml and 163 ml for LV and of 77 ml and 53

---

[9] ParaView. www.paraview.org/

[10] 3D Systems. www.3dsystems.com/quickparts/learning-center/what-is-stl-file?smtNoRedir=1

[11] Blender. www.blender.org/

ml for RV. Thus, the volume of the entire myocardium (both ventricles) was 216 ml. Importantly, those volumes correspond to the end-diastolic phase of cardiac cycle, since it is the phase in which the DE-MRI was acquired.

5.1.2.1. Volume mesh generation

The final version of the 3D surface model (see Figure 5.3[b]) was edited using Gmsh software (Geuzaine and Remacle, 2009)[12] in order to convert it from STL into MESH file format[13]. Then, it served as an input for the software MeshGems-Hexa (Distene S.A.S., Bruyeres-le-Chatel, France)[14], which is a hexahedral volume mesh generator based on octree method (Schneiders, 2000). Among other parameters used to control the volumetric meshing process, we set a value of 0.4 mm as the desired element size (i.e., edge length). As a result, we obtained a hexahedra-based volume mesh comprised of 4 million nodes (vertices) and 3.71 million hexahedral elements.
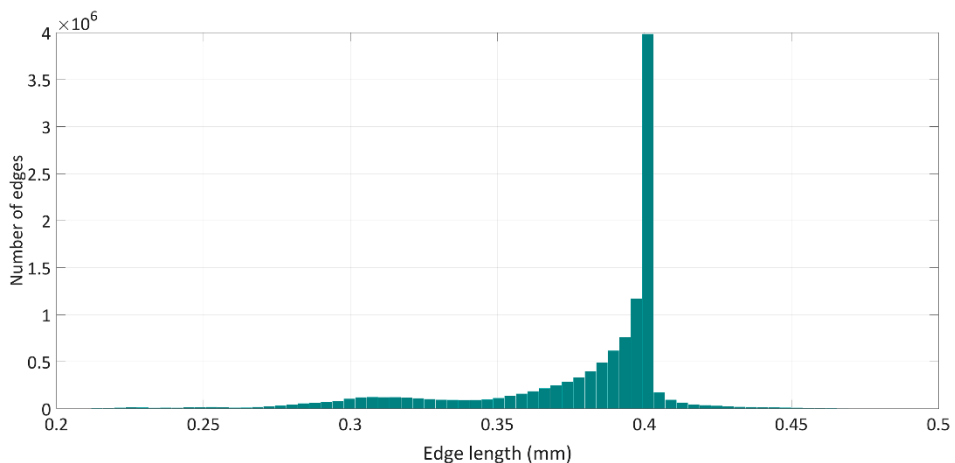
Figure 5.4. Histogram of edges length from the hexahedra-based volume mesh of the 3D ventricular model.

---

[12] Gmsh. gmsh.info/
[13] MEDIT: An interactive mesh visualization software. hal.inria.fr/inria-00069921/document
[14] MeshGems-Hexa: Volume Hexahedral Mesh Generation.
   www.meshgems.com/volume-meshing-meshgems-hexa.html

By means of a custom MATLAB® code, we translated the volume mesh from MESH into VTK file format and measured element edges length to assess the elements size dispersion. As shown in Figure 5.4, from over 11.72 million edges forming the volume mesh, most of them had a length of around 0.4 mm, yielding an average edge length of 0.38 mm. Note that the number of edges with a length below 0.4 mm, that is, smaller than the desired size, was much larger than the amount of greater ones. As deduced from the histogram of edges length (Figure 5.4), the mesh generation algorithm preferentially tended to split long edges creating shorter ones, thereby trying to avoid edges larger than the user defined value (0.4 mm). The explanation is that, in the vast majority of cases, those hexahedra located on (or adjacent to) the surface of the 3D ventricular model were compressed or split during the meshing process in order to fit the subtle details of the reconstructed cardiac anatomy, such as the endocardial trabeculations, what led to the shortening of the edges of such external elements. The result of such a fine fitting process can be appreciated in Figure 5.5, where the hexahedral volume mesh shows the high level of anatomical detail achieved by our 3D ventricular model, as well as their smooth surfaces accurately reproducing the complex anatomy of both endocardia.
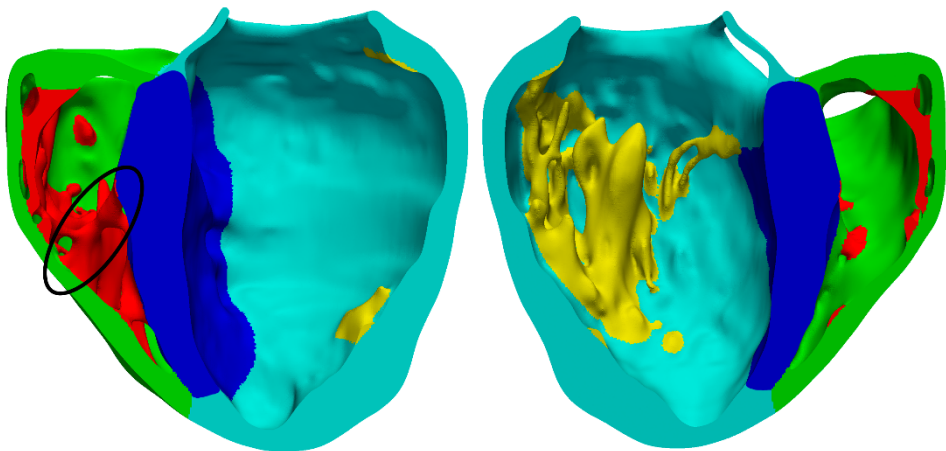
Figure 5.5. Hexahedra-based FEM volume mesh of the 3D patient-specific ventricular model. Anterior (*left*) and posterior (*right*) views of a coronal cross-section (four-chamber view) of the 3D ventricular model. Various cardiac regions are tagged with different colours: septum (*blue*), LV free wall (*cyan*), RV free wall (*green*) and papillary muscles and main endocardial trabeculations of LV (*yellow*) and RV (*red*). One can observe the high level of anatomical detail achieved for both endocardia, showing details such as the moderator band (*black ellipse*) bridging the septum and RV free wall.

Finally, we imported the volume mesh into ParaView to perform a mesh quality test (see Figure 5.6). We chose the scaled Jacobian as a quality metric, a parameter with values ranging from -1 to +1 that is very commonly used for the assessment of 3D unstructured FEM (finite-element method) meshes (Knupp, 2000, 2003). The scaled Jacobian measures the deformation degree of each volumetric element with respect to the ideal one, which is a perfect cube in the case of hexahedral meshes. In our volume model, all hexahedral elements showed positive values for scaled Jacobian, with more than 99% of them having values greater than 0.5, what guaranteed the suitability of the volume mesh for FEM solvers. This is because most of the hexahedra were nearly perfect cubes (scaled Jacobian close to +1), while only the most external elements were deformed to fit the shape of the original template, that is, the 3D surface model, as clearly appreciated in Figure 5.6.
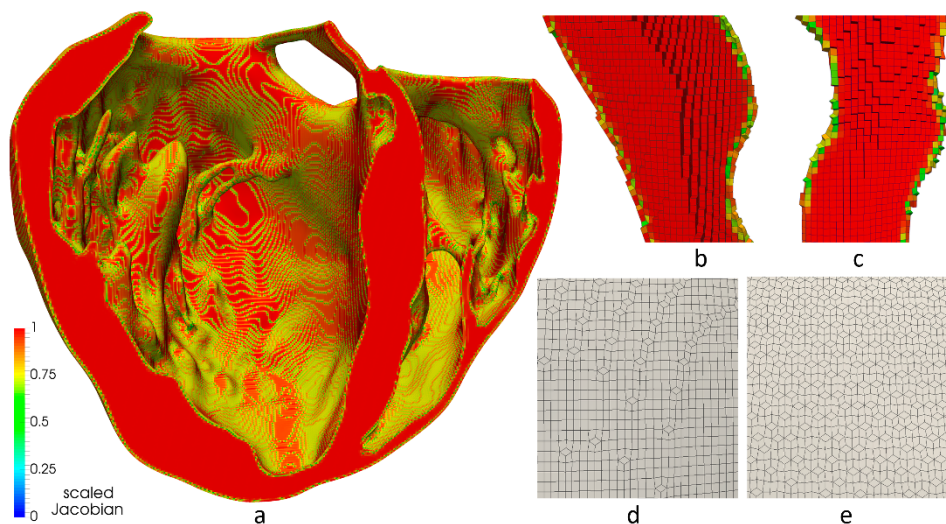
Figure 5.6. Hexahedra-based FEM volume mesh of the 3D ventricular model. (*a*) Posterior view of a coronal cross-section (four-chamber view) of the volume mesh showing papillary muscles and main trabeculations on the endocardia of both ventricles. As shown, there are elements with values of scaled Jacobian notably lesser than 1 only on endo- and epicardial surfaces. Blocks extracted from the LV free wall (*b*) and septum (*c*) show that only those hexahedra closest to the surfaces are deformed, whereas all hexahedral elements in the interior of ventricular walls are nearly perfect cubes with values for scaled Jacobian close to 1. Two detailed views on different regions of epicardial (*d*) and endocardial (*e*) surfaces of LV reveal the good adaptation of the external hexahedra to the fine cardiac anatomy represented by the 3D surface model.

5.1.3. 3D reconstruction of infarct scar and border zone

As explained in Chapter 1 (see section 1.4.2), VTs related to chronic MI usually result from the reentrant activity sustained through conducting channels (CC), whose substrate is commonly linked to the remodelled BZ intermingled with the fibrotic infarct scar (Aliot et al., 2009; de Bakker et al., 1988). Therefore, since our final goal was to reproduce the mechanisms associated with infarct-related VTs using computational simulation, our 3D ventricular model required the incorporation of 3D representations of the patient-specific geometry of the heterogeneous tissue remodelling derived from the MI, differentiating between the infarct scar, which is a dense fibrotic core, and the BZ, which is the remodelled but still functional tissue that surrounds the infarct scar.

We created such 3D representations of the infarct scar and BZ by segmenting the slices of the cardiac DE-MRI using a custom MATLAB® implementation of the so-called *standard deviation* (SD) *method*, a semi-automatic algorithm specifically developed for MI segmentation from DE-MRI images (Kim et al., 1999a). To apply the SD method, first we had to perform a manual pre-processing of every DE-MRI slice. As shown in Figure 5.7, within the region previously delineated as LV myocardium, we manually defined two new sub-regions on each short-axis slice of the DE-MRI stack. We traced (1) a region containing exclusively healthy tissue, usually referred to as *remote myocardium ROI* in the context of SD method, and (2) another one encompassing the infarcted myocardium along with some adjacent areas of normal tissue near the MI (*infarcted ROI*). Slice by slice, we computed the mean and SD values of the pixel intensity levels (i.e., grey levels) within the remote ROI. To classify the pixels belonging to the infarcted ROI of each short-axis slice based on grey levels, SD method defines thresholds by adding a certain number of times (N) the SD value above the mean value of the remote ROI of the same slice, so that thresholds are calculated as mean+N×SD. Then, applying those thresholds to the infarcted ROI of each slice, the algorithm automatically classified as dense fibrotic scar all pixels exceeding the threshold defined as mean+3×SD of the intensity levels of the remote ROI. Pixels with values between mean+2×SD and mean+3×SD were classified as BZ, while pixels under mean+2×SD were

considered as healthy tissue (Fieno et al., 2000; Kim et al., 1999a; Kolipaka et al., 2005; Perez-David et al., 2011; Yan, 2006).
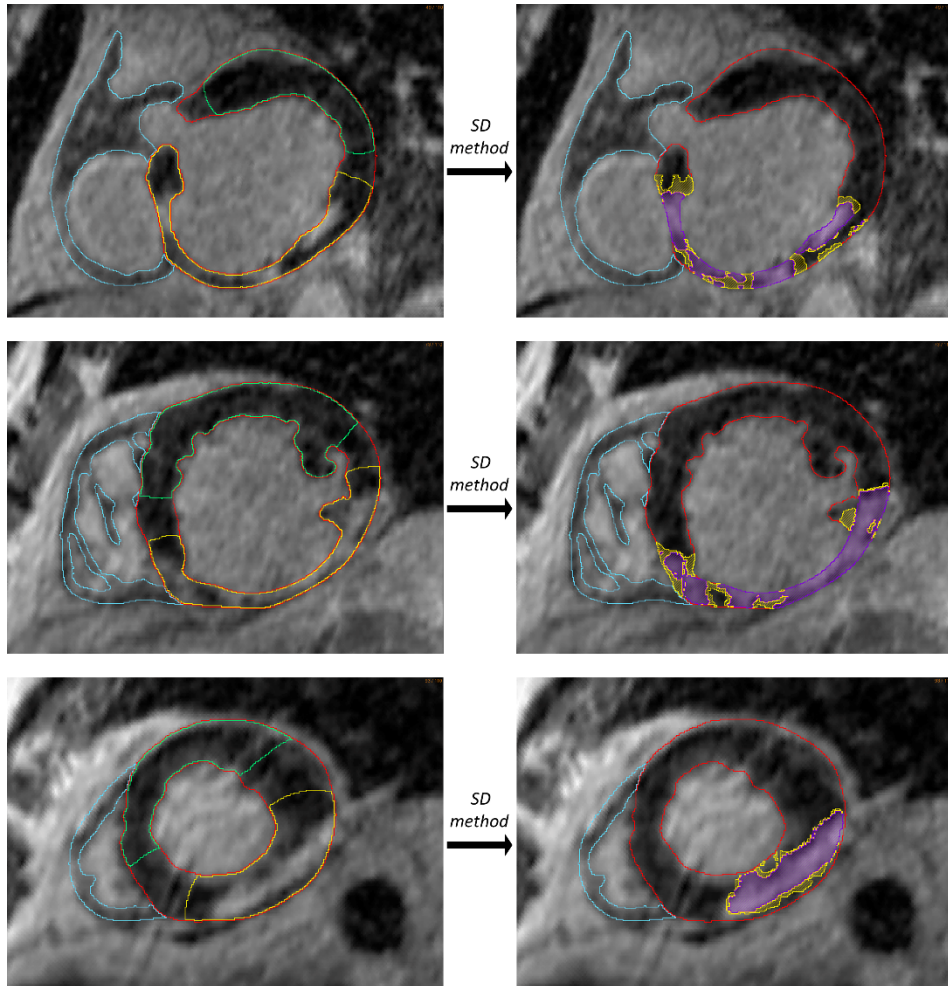
Figure 5.7. Segmentation process from DE-MRI slices of the heterogeneous remodelling related to the MI, including infarct scar and BZ. Each row shows examples of the two steps of segmentation process on short-axis DE-MRI slices at basal (*top*), mid-ventricular (*middle*) and apical (*bottom*) level of ventricles. *Left column* shows the first step that involves the manual definition of remote (*green*) and infarcted ROIs (*yellow*) within the LV myocardium ROI (*red*), also displaying the RV myocardium ROI (*cyan*). *Right column* shows the segmentation ROIs for infarct scar (*purple*) and BZ (*yellow*) resulting from the application, within the infarcted ROI, of the thresholds determined by SD method from the remote ROI of each slice.
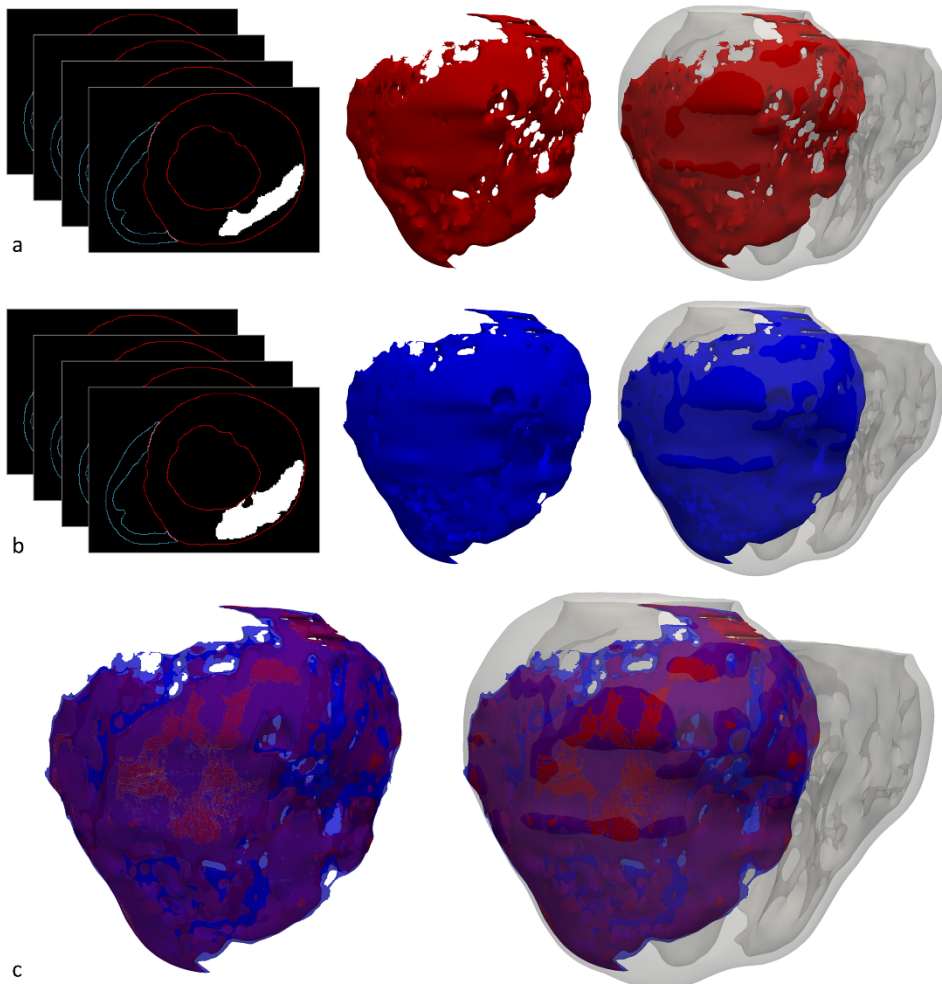
Figure 5.8. 3D representation of the heterogeneous remodelling associated with the MI reconstructed from DE-MRI images, including infarct scar and BZ. Top row (*a*) displays the 3D surface corresponding to the infarct scar (*red*), while the surface in the middle row (*b*) represents the whole ischaemic injury (*blue*), enclosing both the scar and the BZ. Both rows (*a* and *b*) show a representation of the volumetric binary masks created by the segmentation process (*left column*) and posterior views of the refined version of the 3D surfaces generated from those binary masks, both alone (*middle column*) and displayed into the 3D surface model of ventricles rendered with transparency (*right column*). Bottom row (*c*) shows the overlap of both 3D surfaces, representing the infarct scar (*red*) and the entire MI (*transparent blue*), respectively. The space enclosed by the whole MI surface and not covered by the infarct scar surface corresponds to the BZ, which surrounds the scar as can be appreciated.

As a result of this slice-wise semi-automatic segmentation process based on SD method, we obtained two different volumetric binary masks specifying those voxels of the DE-MRI that were classified as infarct scar and BZ, respectively. As shown in Figure 5.8, from both binary masks we generated two different isosurfaces enclosing the region representing the 3D geometry of the infarct scar and the whole MI (infarct scar and BZ together), respectively. For this task, we used the *isosurface* command, which is a MATLAB® built-in function. Those 3D surfaces, exported from MATLAB® in VTK format, were subject to a process of global smoothing (with ParaView software) and local refinement (with Blender software) similar to that described for the ventricular model in the section above.

Measurements taken from the segmented 3D dataset revealed that the entire MI extended over a volume of 40 ml, with 26 ml corresponding to the infarct scar and 14 ml to the BZ, thus comprising 16% and 8.5% of the volume of LV myocardium, respectively. Hence, the whole infarcted area, including infarct scar and BZ, encompassed 24.5% of the cardiac muscle composing the LV myocardium.

5.1.3.1. Mapping of the myocardial infarction into the 3D ventricular model

Finally, we mapped the infarct scar and BZ into the volume mesh of the 3D ventricular model using another custom MATLAB® code, which labelled every node and hexahedral element as infarct scar, BZ or healthy tissue, depending on its position relative to the 3D surfaces representing the scar and the whole MI. To do so, we implemented the even-odd rule, a well-known algorithm for inside-outside testing in the field of computer graphics. Applying such method, for each node of the volume mesh we assessed whether it lied inside or outside the two target surfaces. We considered as infarcted tissue (i.e., dense fibrosis) all nodes lying inside the scar surface, while those ones located between both surfaces, that is, outside the scar but inside the whole MI surface, were tagged as BZ. Lastly, we labelled as healthy tissue all the remaining nodes, that is, all those nodes lying outside the surface enclosing the whole MI. To
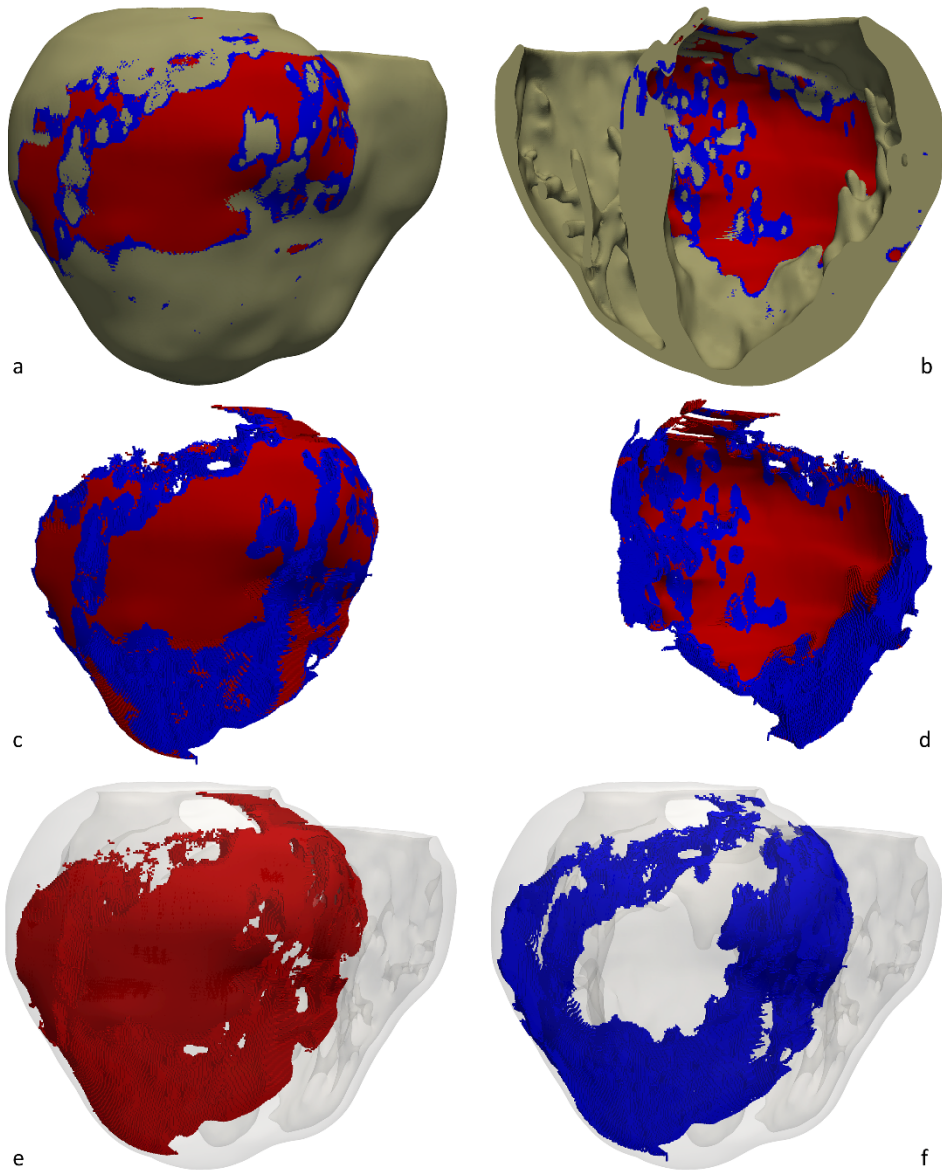
Figure 5.9. 3D patient-specific geometry of the heterogeneous remodelling associated with the MI, mapped into the hexahedral volume mesh of the 3D ventricular model. In all panels the infarct scar (dense fibrotic core) is represented in *red* and the BZ in *blue*. (*a*) Posterior view of the whole volume mesh and (*b*) anterior view of a coronal cross-section (four-chamber plane) showing the 3D distribution of infarct scar, BZ and healthy tissue (*beige*). (*c*) Posterior and (*d*) anterior views of those hexahedral elements labelled as infarct scar and BZ extracted from the 3D volume mesh. Posterior view of the hexahedral elements corresponding to the scar (*e*) and BZ (*f*) displayed into the 3D surface model of the ventricles rendered with transparency.

classify the hexahedral elements of the volume mesh, we followed the same approach by assessing the position of the centroid of every element. Figure 5.9 shows the result of this labelling process of the volume mesh for the 3D patient-specific geometry of the heterogeneous remodelling (infarct scar and BZ) associated with the MI. In Figure 5.9 it can be observed the high complexity of the 3D geometry of infarct scar and BZ, as well as the intermingling between both types of tissue and also between them and the healthy myocardium.

5.1.3.2. Structural remodelling in the border zone

Several studies have described the BZ as a region of slow conduction, composed of surviving but remodeled myocytes with infiltration of bundles of fibrosis extending from the core of compact fibrosis (infarct scar), all of which gives rise to a highly arrhythmogenic tissue (de Bakker et al., 1993; Nguyen et al., 2014; Rohr, 2012; Rutherford et al., 2012). Experimental observations based on histological sections have witnessed the presence of fibrosis infiltrated within the infarct BZ (de Bakker et al., 1988; Rutherford et al., 2012; Smith et al., 1991; Tschabrunn et al., 2016), mainly showing the appearance of patchy and interstitial fibrosis. Importantly, it is considered the most arrhythmogenic kind of fibrosis, as the presence of patchy fibrosis increases the susceptibility to unidirectional blocks due to source-sink mismatches resulting from sudden changes in the 3D geometry of excitable tissue. In addition, it slows down the conduction because of the propagation delays caused by the tortuous pathways that the activation wavefront is forced to take, also leading to electrogram (EGM) fragmentation due to the impaired activation of the myocardium infiltrated with fibrotic tissue (de Bakker et al., 2005; de Jong et al., 2011; Dhanjal et al., 2017; Nguyen et al., 2014).

Considering what is mentioned above regarding the structural remodelling in the BZ, we tried to reproduce the configuration of fibrosis in the BZ caused by the healing process of the MI based on the available clinical data, aiming to replicate it as patient-specific as possible. For this purpose, we implemented a MATLAB® code for mapping the grey intensity levels of the DE-MRI into the volume mesh of our 3D ventricular model, as shown in Figure 5.10.

First, we overlapped the volume dataset of DE-MRI onto the volume mesh. Since we generated the 3D ventricular model directly from the DE-MRI, that first task aiming to register both datasets did not require any transformation. Then, we just sought the DE-MRI voxel closest (in terms of Euclidean distance) to the centroid of each hexahedron to assign a grey level to every hexahedral element of the 3D ventricular model. Note that voxels of DE-MRI (isotropic voxels with edge length of 1.4 mm) are notably larger than volume mesh elements (hexahedra with average edge length of around 0.4 mm). Therefore, the intensity level associated with each DE-MRI voxel belonging to the ventricular myocardium was assigned to a cluster of volume elements that might comprise up to 64 hexahedra. This is the reason that explains the "stratified" appearance of the grey intensity levels along the LV long axis when displayed over the 3D ventricular model (see Figure 5.10).
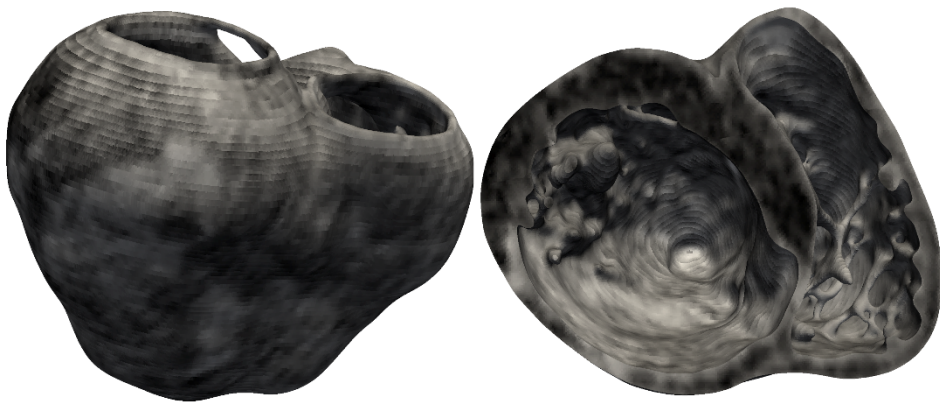
Figure 5.10. Grey intensity levels of the DE-MRI mapped into the hexahedral volume mesh of the 3D ventricular model, showing a postero-basal view of the whole model (*left*) and a basal view of a cross-section in the short-axis plane (*right*). The latter view shows the thinning (atrophy) of posterior, postero-lateral and postero-septal walls of the LV as a consequence of the healing process of the MI, as well as the concentration of high-intensity levels (closer to white) in those regions due to the accumulation of gadolinium-based contrast agent.

Finally, we generated different levels of fibrosis (10%, 20% and 30%) within the BZ based on the grey intensity levels mapped from the DE-MRI. Among the elements of volume mesh previously labelled as BZ, we defined as fibrotic those ones associated with the highest intensity levels, in an amount
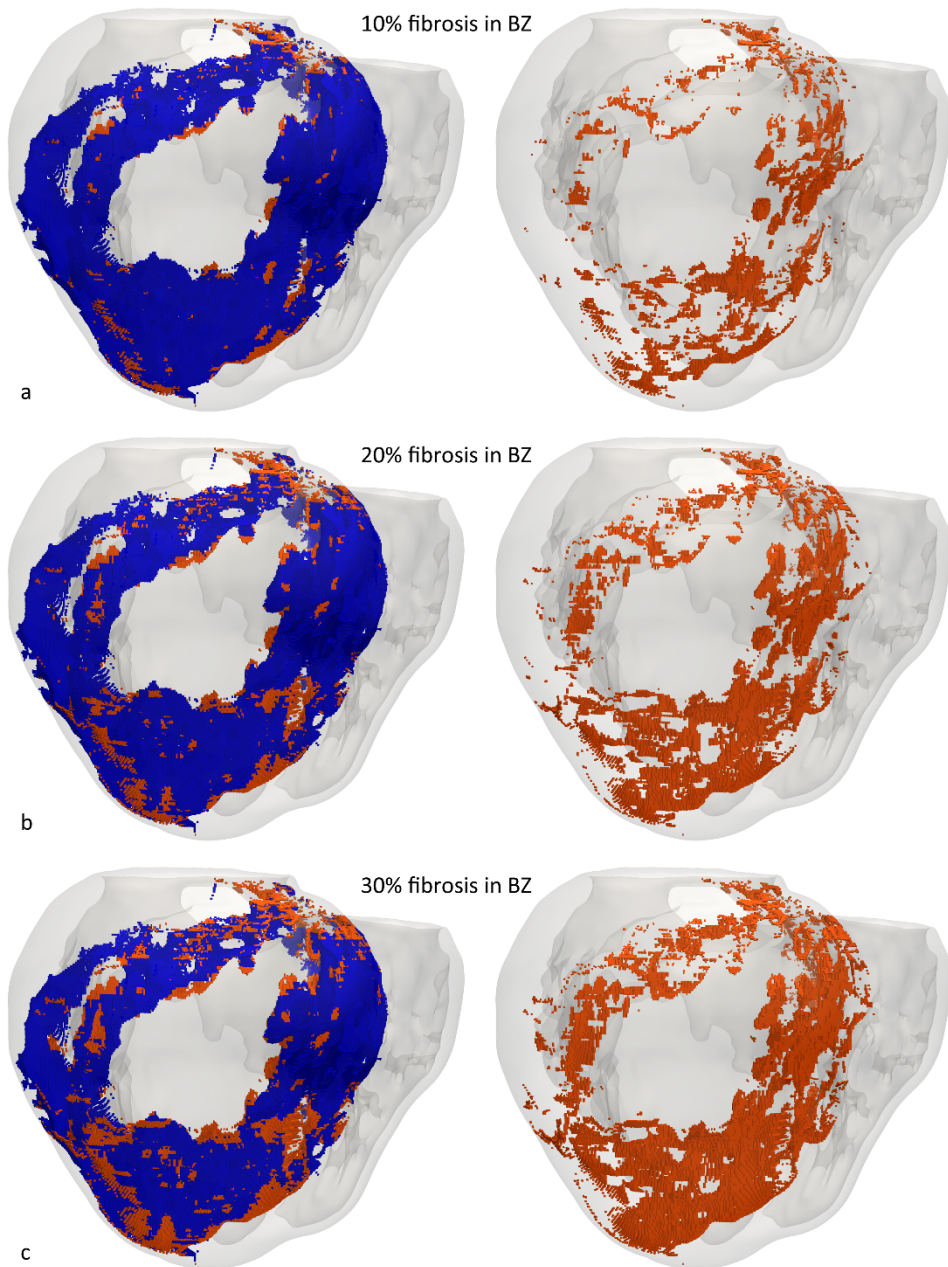
Figure 5.11. 3D fibrosis distributions resulting from the image-based incorporation of several degrees of structural remodelling within the BZ: (*a*) 10%, (*b*) 20% and (*c*) 30% fibrosis. All panels show a posterior view of the 3D surface model of ventricles (rendered with transparency) together with those hexahedral elements labelled as BZ (*blue*) and fibrosis (*orange*), extracted from the volume mesh of ventricular model. *Left column* shows both the BZ and fibrosis, while *right column* only shows fibrotic elements.

depending on the desired fibrosis level. In other words, we labelled as fibrotic a percentage of volume elements belonging to the BZ that matched the specified fibrosis density. For a fibrosis degree of 10%, for instance, among all hexahedral elements corresponding to the BZ, we considered as fibrotic the 10% of them matching those ones with the highest MRI-derived grey intensity levels.

As shown in Figure 5.11, our approach of image-based generation of different fibrosis levels within the BZ resulted in clusters (or patches) of fibrotic tissue. Hence, this strategy produced a distribution that may be classified as patchy fibrosis, usually defined as a mixture of bundles of myocardial and fibrotic tissue (de Jong et al., 2011), which is similar to those fibrosis patterns experimentally observed in the BZ of infarcted ventricles (de Bakker et al., 1988; Rutherford et al., 2012; Smith et al., 1991; Tschabrunn et al., 2016).

5.1.4. Labelling of the 3D ventricular model

After the meshing process generating the hexahedral volume mesh of the 3D ventricular model, we enriched the computational model by attaching to the mesh a set of useful labels and data. We performed such labelling process by means of another tailored MATLAB® code, which went through the whole 3D model adding several labels and data fields to every node and element (hexahedra) of the volume mesh. Labels attached to the mesh encode information about mesh quality metrics, such as the scaled Jacobian (Figure 5.6) or the aspect ratio between the shortest and the largest edge of each hexahedral element, specific cardiac regions (Figure 5.5), grey intensity levels mapped into the model from the DE-MRI (Figure 5.10) and normalized distance from the apex to the base of the ventricles (Figure 5.12[a]) as well as between endocardial and epicardial surface (Figure 5.12[b]). Other fields also provide essential information about cardiac tissue, such as the heterogeneous remodelling associated with the MI (infarct scar and BZ) (Figure 5.9), transmural EP heterogeneity of ventricular myocardium and the orientation of cardiac fibres, as will be described in Chapter 6 (see Figure 6.1 and, Figure 6.3 respectively). As explained in the corresponding sections above, the generation of each one of these labels and data fields required the implementation of a specific algorithm.
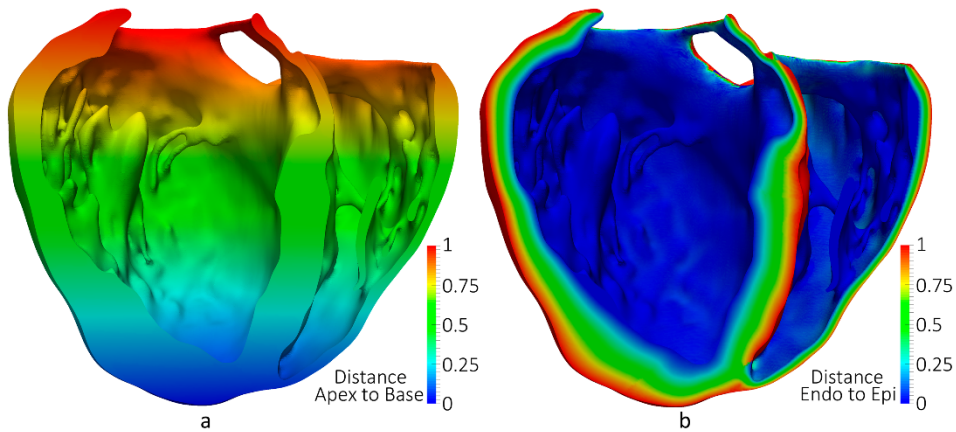
Figure 5.12. Labels attached to the volume mesh of the 3D computational model of ventricles. Posterior views of coronal cross-sections (four-chamber plane) of the 3D ventricular model with colour codes corresponding to the labels linked to mesh nodes providing information about the normalized distance (*a*) from the apex to the base of ventricles (i.e., the plane of mitral valve) and (*b*) from endocardial to epicardial surface. Note that, in the region of septum, we considered the LV side as the endocardial surface and the RV side as the epicardium.

5.1.5. CARTO® data integration

As already explained in Chapter 4 (see section 4.5), CARTO® 3 System generates surface meshes representing the 3D geometry of every mapped cardiac cavity, each of which contains all CARTO® measurement points recorded during the mapping process. In our case, there were three surfaces: LV endocardium, RV endocardium and epicardium (see Figure 4.6 in Chapter 4). However, the 3D position and orientation of such set of surfaces did not match the surfaces of the 3D ventricular model derived from the DE-MRI stack. Therefore, to align the three CARTO® meshes with our 3D patient-specific ventricular model, we needed to apply to those surfaces a rigid transformation (i.e., translation and rotation only, without scaling), which was determined by a MATLAB® implementation of the ICP (iterative closest point) algorithm (Besl and McKay, 1992). To compute the rigid transformation, we applied the ICP algorithm to the CARTO® surfaces for both endocardia (LV and RV) jointly, while the nodes (vertices) of the endocardial surfaces of the 3D ventricular model were considered as the target point cloud. Then, we applied to the CARTO®

surface representing the epicardium the same transformation computed for both endocardia to complete the registration between CARTO® surfaces and our 3D ventricular model, as observed in Figure 5.13.
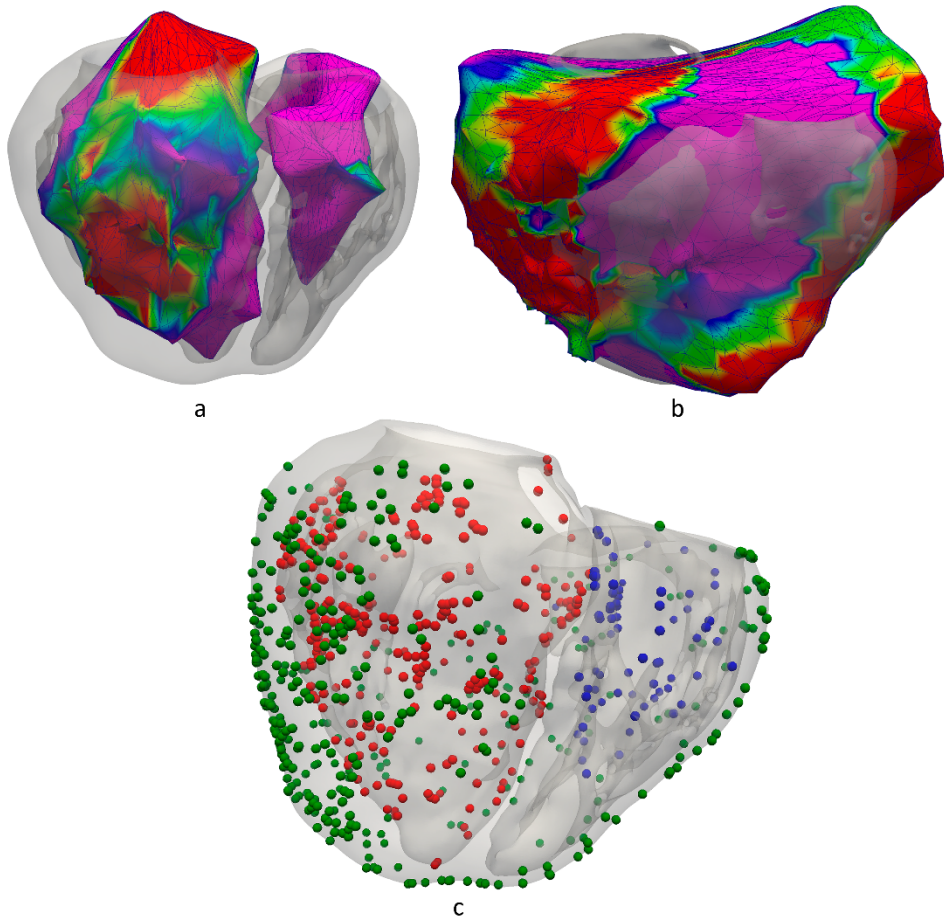
Figure 5.13. Registration process between CARTO® surface meshes and the 3D ventricular model. Posterior view of the 3D surface model of ventricles rendered with transparency, showing registered CARTO® surfaces for both (*a*) endocardia and (*b*) epicardium, as well as (*c*) checked CARTO® measurement points projected onto the 3D model, with spheres representing CARTO® points recorded from LV endocardium (*red*), RV endocardium (*blue*) and epicardium (*green*).

Finally, after the surfaces registration process, we projected all measurement points from each CARTO® mesh to the closest surface node of the 3D ventricular model, in terms of Euclidean distance. Importantly, we only projected onto the ventricular model those CARTO® points preserved after the checking process described in Chapter 4 (see section 4.5.1). Thereby, we got all checked CARTO® measurement points mapped onto the external surfaces of our 3D ventricular model, as displayed in Figure 5.13.

5.1.6. Candidates for conducting channels

As can be observed by visual inspection (see Figure 5.9), the 3D reconstruction from DE-MRI of the heterogeneous remodelling associated with the MI revealed the presence of an isthmus at epicardial level. It was completely surrounded by dense scar and mainly composed of BZ intermingled with some patches of healthy tissue. We can define such structure as a corridor or channel of surviving tissue that crosses the infarct scar with a trajectory that was approximately aligned with the apex-base direction, although with a slight inclination such that the upper side (the most basal extreme) was closer to the septum while the lower end (the most apical extreme) pointed towards the lateral wall of the LV. Regarding its size, the path of that isthmus had a length of 39 mm and it presented a quite regular width with an average of 7.5 mm, both measured on the epicardial surface. However, there was an intramural strangulation (also observable at epicardial level) located just at the lower side (apical end) of the isthmus, whose section width decreased to about 2 mm. Both shape and features of such structure match the definition of a CC, thus constituting a potential substrate for supporting reentrant VTs (de Bakker et al., 1988; Fernández-Armenta et al., 2013).

Furthermore, as appreciated in Figure 5.14[a], the integration of CARTO® data onto the 3D model showed good spatial correspondence between such epicardial isthmus and the location of a particular set of projected CARTO® points. Those points were tagged by the electrophysiologists, during the RFA procedure, as candidates to be part of a slow CC due to the characteristics of their bipolar EGMs (low voltage, fragmented and split signals, late and isolated

potentials, etc.) (Bogun et al., 2005; de Chillou et al., 2002). Figure 5.14[b] shows a section of such epicardial isthmus in the short-axis cardiac plane revealing its non-transmurality, since its structure never reaches the endocardial surface along its path, which is completely covered by scarred tissue at the endocardial side. On the other hand, in Figure 5.14[b] one can observe again the thinning (i.e., atrophy) of posterior, postero-lateral and postero-septal walls of the LV as a consequence of the healing process of the MI, matching the regions classified as infarct scar and BZ from the DE-MRI.

a   b
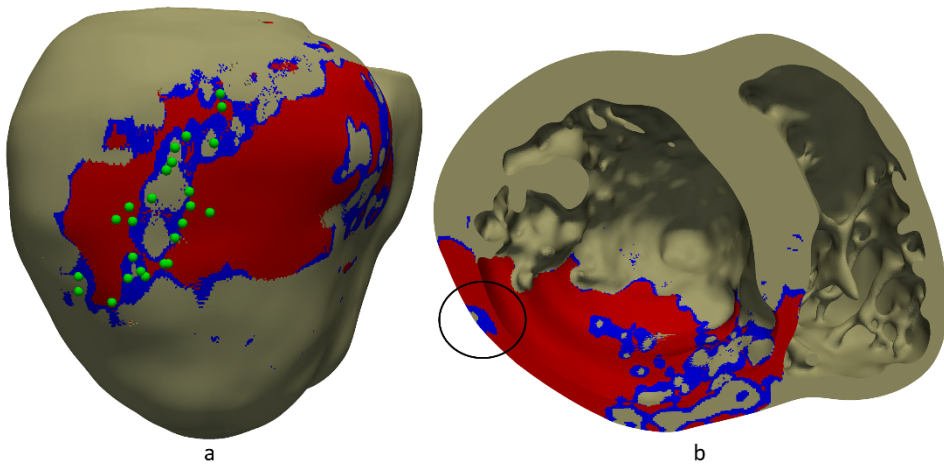
Figure 5.14. (*a*) Postero-lateral view of the 3D ventricular model showing a possible epicardial CC mainly composed of BZ (*blue*) intermingled with some patches of healthy tissue (*beige*) and completely surrounded by infarct scar (*red*). This epicardial isthmus closely matches the location of a set of projected CARTO® points (*green spheres*) tagged as candidates to be part of a CC according to the features of their EGMs. (*b*) Axial cross-section (short-axis plane) of the 3D ventricular model, showing a section of the structure candidate for epicardial CC (see *black circle*) that reveals its non-transmurality, as no point of its trajectory reaches the endocardial surface.

5.2. 3D torso model

In this section, we address the building process of the 3D torso model, including the reconstruction of the torso geometry from the whole-torso anatomical MRI and, subsequently, the generation of the FEM volume mesh.

5.2.1. 3D reconstruction of torso geometry

The whole-torso MRI stack was acquired in the coronal plane with a slice thickness of 10 mm, which is within the usual range for standard spatial resolution of clinical MRI scans, as commented in Chapter 4 (see section 4.3 for more details). From such anatomical MRI stack, we roughly segmented the main organs (lungs, liver, heart) and anatomical structures (bones, body contour, blood pools, great vessels) by manual delineation using the Seg3D software, as shown in Figure 5.15[a]. From those segmentations we also generated isosurfaces, as observed in Figure 5.15[b]. However, the low resolution of torso MRI hampered a detailed reconstruction of some important structures, so we decided to reuse a detailed torso model previously developed by other researchers from our group (Ferrer et al., 2015a). Thus, the idea was to fit the existing detailed torso model to our patient-specific image-based coarse torso. To carry out this task, first we placed a set of landmarks on the 3D surfaces representing the organs and anatomical structures included in both torso models. Then, we registered and fitted the surfaces of the detailed torso model to our image-based coarse torso (Figure 5.15[b]) by applying a linear transformation (translation, rotation and scaling) determined from the landmarks by means of a custom MATLAB® code based on Procrustes analysis (Goodall, 1991; Gower, 1975).

After the fitting process, we replaced the ventricles in the fitted detailed torso model by our patient-specific 3D ventricular model. Later, we edited the fitted surface meshes with Blender in order to remove some intersections between the ventricular model and surrounding organs. Therefore, all organs and anatomical structures included in the 3D torso model (torso contour, bones, lungs, liver and atria) resulted from the fitting process performed to adapt a previously constructed 3D model to the patient's anatomy, except for the ventricles and its blood pools, which corresponded to the patient-specific 3D ventricular model built from the DE-MRI stack.

a	b
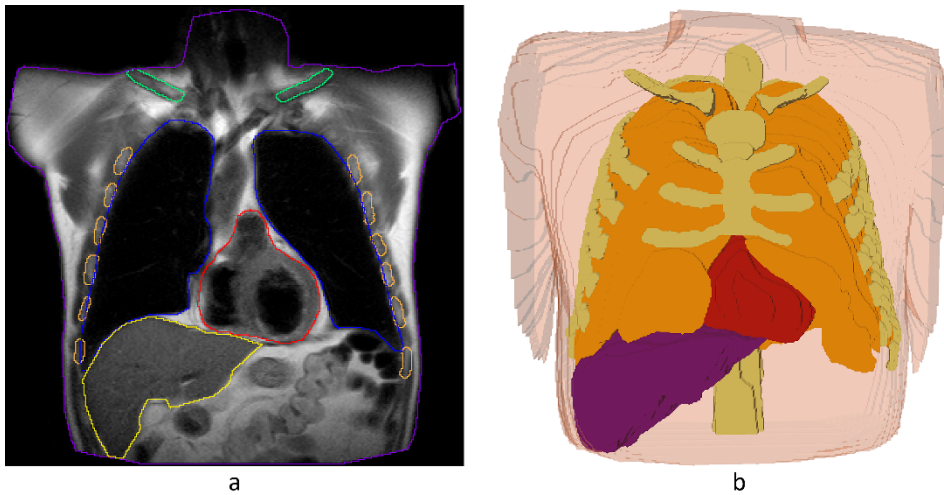
Figure 5.15. Generation process of the 3D torso model. (*a*) Slice of whole-torso anatomical MRI in coronal plane, showing manually delineated contours of several organs and anatomical structures: body contour (*purple*), collarbones (*green*), lungs (*blue*), ribs (*orange*), epicardium (*red*) and liver (*yellow*). (*b*) Raw isosurfaces (exported from Seg3D) resulting from the segmentation of low-resolution whole-torso MRI, showing bones, lungs, epicardium and liver within the body contour rendered with transparency.

5.2.2. Volume mesh generation

Once the surfaces of the detailed torso model were fitted to the patient's torso reconstruction, including the 3D surface of the patient-specific 3D ventricular model (see in Figure 5.16[b]), we used those surfaces as a template to generate a tetrahedra-based volume mesh (see in Figure 5.16[c]) by means of an open-source C++ library called TetGen (Si and Gärtner, 2005)[15]. As a result, we obtained a volume torso model consisting of 1.26 million nodes and 7.38 million tetrahedral elements.

Unlike the hexahedral mesh of the 3D ventricular model (see Figure 5.4), the tetrahedra-based volume mesh of the torso model presented an important dispersion of edges length. As shown in Figure 5.16[a], most of the edges in the

---

[15] TetGen. wias-berlin.de/software/index.jsp?id=TetGen&lang=1
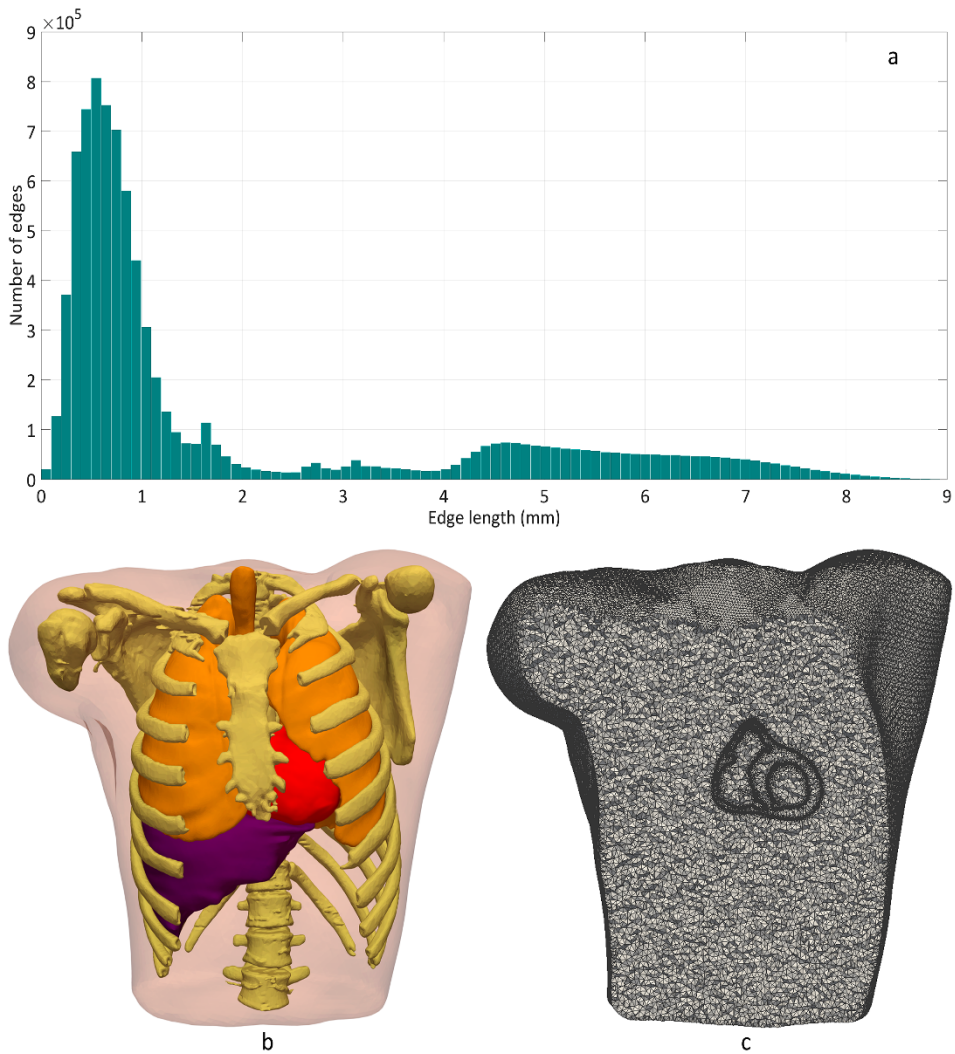
Figure 5.16. Volume mesh of the 3D torso model. (*a*) Histogram of edges length of tetrahedra-based volume mesh of torso model. (*b*) 3D surfaces defining the organs and tissues included in the existing detailed torso model after the fitting process to our imaged-based coarse torso. It includes body contour (rendered with transparency), bones, lungs, liver and ventricles (*in red*) corresponding to our 3D patient-specific model. It also includes atria and blood pools of the four cardiac chambers, although they are not visible in this view. (*c*) Cross-section in coronal plane of the volume mesh of 3D torso model, showing the edges of tetrahedral elements. Observe the refinement of tetrahedral elements in the region of ventricles, what results in edges in that region shorter than in the rest of the volume mesh.

tetrahedral mesh of the torso model have a length of around 0.55 mm, although they ranged from 0.1 to 9 mm. Such a wide range results from the refinement of the torso mesh in and around the region of the ventricles for the sake of accuracy of numerical solutions (see Figure 5.16[c]), whilst there is a coarsening of the elements far from the heart in order to reduce the computational burden. In fact, 2.72 million out of 7.38 million tetrahedra in the torso model correspond to the ventricular myocardium, which is a large amount considering the volume of ventricles relative to that of the whole torso. This was the result of imposing severe restrictions on elements size only in the region corresponding to the ventricular myocardium, defined by the 3D surface of the patient-specific ventricular model, in order to yield a spatial resolution (i.e., edges length of tetrahedral elements) in such region similar to that of the hexahedral mesh of our 3D model of ventricles. To do so, we used a set of input parameters for the meshing algorithm of TetGen that allow controlling the meshing process at both global and local level. As will be discussed in detail in Chapter 7 (see section 7.4), the problem of passive propagation of extracellular potentials, which only comprises the diffusion phenomenon without reaction component, does not require such a fine spatial resolution outside the heart as reaction-diffusion problem does within the ventricular myocardium (Prassl et al., 2009).

Chapter 6

Electrophysiological Modelling

This chapter addresses all the considerations and decisions that we made in order to biophysically model the electrophysiological (EP) behaviour at the different levels of biological organization: cell, tissue, organ and whole body. This is a necessary step aiming to perform multiscale computational simulations of cardiac EP making use of the 3D models of the ventricles (organ level) and torso (body level), whose building processes were described in Chapter 5.

Although presented here in a considerably further extended fashion, it must be noted that part of the content of this chapter was already included in a research article entitled "*Personalized cardiac computational models: from clinical data to simulation of infarct-related ventricular tachycardia*", which was recently published in the indexed international journal *Frontiers in Physiology* in May 2019 (Lopez-Perez et al., 2019).

6.1. Cellular level

As previously discussed in Chapter 3 (see section 3.4.5), there are several approaches to computationally model the cardiac EP at the cellular level that try to reproduce the action potential (AP), the ionic currents and the dynamic changes in ion concentrations of a particular cell type, which can present different degrees of mathematical complexity and physiological realism. In our case, we aimed to study the mechanisms associated with infarct-related reentrant VTs using computational simulations, which seem to correlate with a number of underlying mechanisms at the cellular level, such as (1) AP duration (APD) adaptation due to rapid pacing rates, (2) electrotonic interactions between cells with different EP features, and (3) generation of repolarization dispersion due to APD heterogeneities potentially leading to functional propagation block, among others. Consequently, at the cellular level we required the use of complex ionic AP models, i.e., models including a specific mathematical description for the ionic current flowing through each type of transmembrane channel. These models are the most suitable ones for faithfully replicating the mechanisms involved in the onset of infarct-related reentrant VTs.

6.1.1. Healthy myocardium. Transmural heterogeneity

To reproduce the EP behaviour of the cardiomyocytes (cardiac muscle cells) which form the healthy myocardium, we used the well-known ten Tusscher model of human ventricular AP (ten Tusscher and Panfilov, 2006b), considering the EP transmural heterogeneity of the ventricular myocardium (Antzelevitch et al., 1999; Drouin et al., 1995). As shown in Figure 6.1, we defined three different transmural layers for endo-, mid- (M cells) and epicardial myocytes within the volume mesh of the 3D ventricular model, spanning 17%, 41% and 42% of the ventricular wall thickness, respectively. These values were estimated from the data reported by several experimental studies (Sicouri et al., 1994; Sicouri and Antzelevitch, 1991; Yan et al., 1998), which in addition had been used in previous simulation studies (Dux-Santoy et al., 2011, 2013). As an exception, the septum comprised a mid-myocardial layer in its interior and

endocardial layers at both LV and RV sides, excluding epicardial myocytes (see Figure 6.1). Moreover, for papillary muscles and endocardial trabeculations we considered endocardial myocytes exclusively.
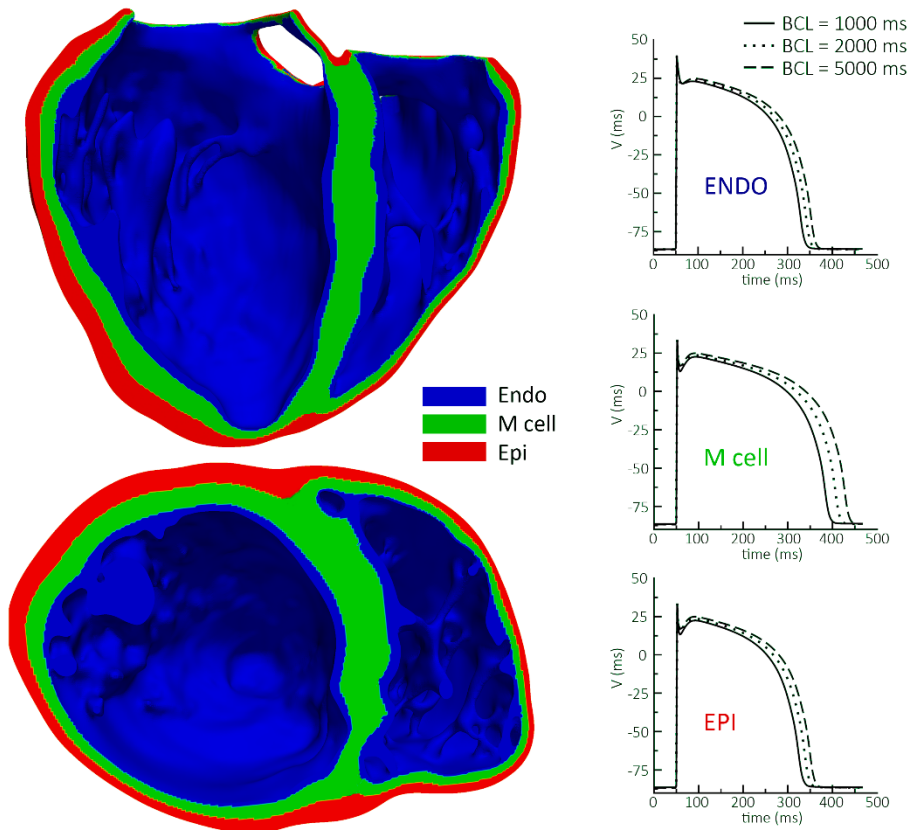
Figure 6.1. EP transmural heterogeneity of ventricular myocardium. Views of the 3D ventricular model corresponding to cross-sections in four-chamber (*upper left*) and short-axis (*lower left*) planes, showing the distribution of the three different kind of ventricular myocytes: endo-, mid- (M cells) and epicardial cells. Graphics on the right side represent the AP reproduced by ten Tusscher model (ten Tusscher et al., 2004) for the three distinct cell types stimulated at different BCLs (*basic cycle length*).

6.1.2. Infarct scar

Among other causes, the infarct scar results mainly from the deposition of collagen fibres along the healing process of the myocardial infarction (MI),

aiming to replace the myocardial necrosis (replacement or scarring fibrosis) caused by severe ischaemic injury leading to irreversible cell damage. Such MI healing process gives rise to the formation of a dense and compact core of fibrotic tissue (Sutton and Sharpe, 2000). Therefore, in the chronic stage of the MI, when its healing is already completed, the infarct scar is mostly formed by an extracellular matrix composed of collagen fibres (Cleutjens et al., 1999; Daskalopoulos et al., 2012; van den Borne et al., 2010), so macroscopically it may be considered as an inactive tissue, both electrically and mechanically.

Hence, we considered the infarct scar as a non-excitable tissue and, consequently, we modelled it as an electrical insulator at both cellular and tissue level. Then, we modelled the infarct scar in such a way that, in simulations at tissue/organ level, that region of the ventricular model acts as a fixed obstacle within the myocardium that blocks the propagation of the activation wavefront, since it cannot propagate across an electrically inactive tissue. To do so, we just defined an internal boundary in the 3D ventricular model and imposed no-flux boundary conditions at the interface between the dense fibrotic core (infarct scar) and the surrounding tissue, which mainly corresponded to the BZ.

6.1.3. Infarct border zone

As described in Chapter 5 (see section 5.1.3.2), the BZ surrounding the infarct scar is a heterogeneous region comprised of viable but remodelled myocardium, intermingled with fibrotic tissue. Therefore, the BZ is an electrophysiologically altered tissue that combines the presence of structural remodelling in the form of patchy fibrosis (Rutherford et al., 2012; Tschabrunn et al., 2016), with electrical remodelling at ionic/cellular level, since the surviving myocytes appear to exhibit EP characteristics different from those of healthy cells (Dun et al., 2004; Jiang et al., 2000; Pu and Boyden, 1997). Hence, as part of the EP modelling process at the cellular level, in the region of BZ we had to deal with two different tissues composed of distinct kind of cells: remodelled myocytes and fibrotic tissue.

6.1.3.1. Electrical remodelling in the border zone

Several experimental studies have reported electrical remodelling in the BZ, describing significant differences in the EP features of myocytes taken from the viable but still working myocardium of the BZ, compared to cells from the intact myocardium, that is, not infarcted tissue. To include such electrical remodelling of the BZ in the 3D computational model of infarcted ventricles, we generated a modified version of the ten Tusscher model (ten Tusscher and Panfilov, 2006b) aiming to reproduce the altered EP behaviour of the surviving myocytes in the BZ. In this respect, we considered the reduction in the conductance (g) of certain transmembrane ionic channels reported by several patch-clamp experiments available in the literature, all of them using cells harvested from the epicardial BZ of canine infarcted hearts. According to those data, which are gathered in Table 6.1, the conductance of peak sodium current (I_{Na}) was reduced to 38% of its normal value ($0.38 \times g_{Na}$) (Pu and Boyden, 1997) and L-type calcium current (I_{CaL}) to 31% ($0.31 \times g_{CaL}$) (Dun et al., 2004). Moreover, rapid and slow delayed rectifying potassium currents (I_{Kr} and I_{Ks}) were reduced to 30% and 20% of their normal values ($0.3 \times g_{Kr}$ and $0.2 \times g_{Ks}$), respectively (Jiang et al., 2000).

Current	Modification		Data source
I_{Na}	↓62%	→ $0.38 \times g_{Na}$	(Pu and Boyden, 1997)
I_{CaL}	↓69%	→ $0.31 \times g_{CaL}$	(Dun et al., 2004)
I_{Kr}	↓70%	→ $0.3 \times g_{Kr}$	(Jiang et al., 2000)
I_{Ks}	↓80%	→ $0.2 \times g_{Ks}$	

Table 6.1. Reductions in the conductance of several ionic channels incorporated to the ten Tusscher model of human ventricular AP in order to reproduce the electrical remodelling in the BZ.

Those changes give rise to a decrease in the upstroke velocity and maximum amplitude of the AP, mainly caused by the downregulation of I_{Na}, as well as to an increase in the APD relative to the normal values because of the reduction in repolarizing potassium currents I_{Kr} and I_{Ks}. As appreciated in Figure 6.2, the main effect of the applied changes was the prolongation of the APD, which affects in a similar degree both a single isolated cell and a cell
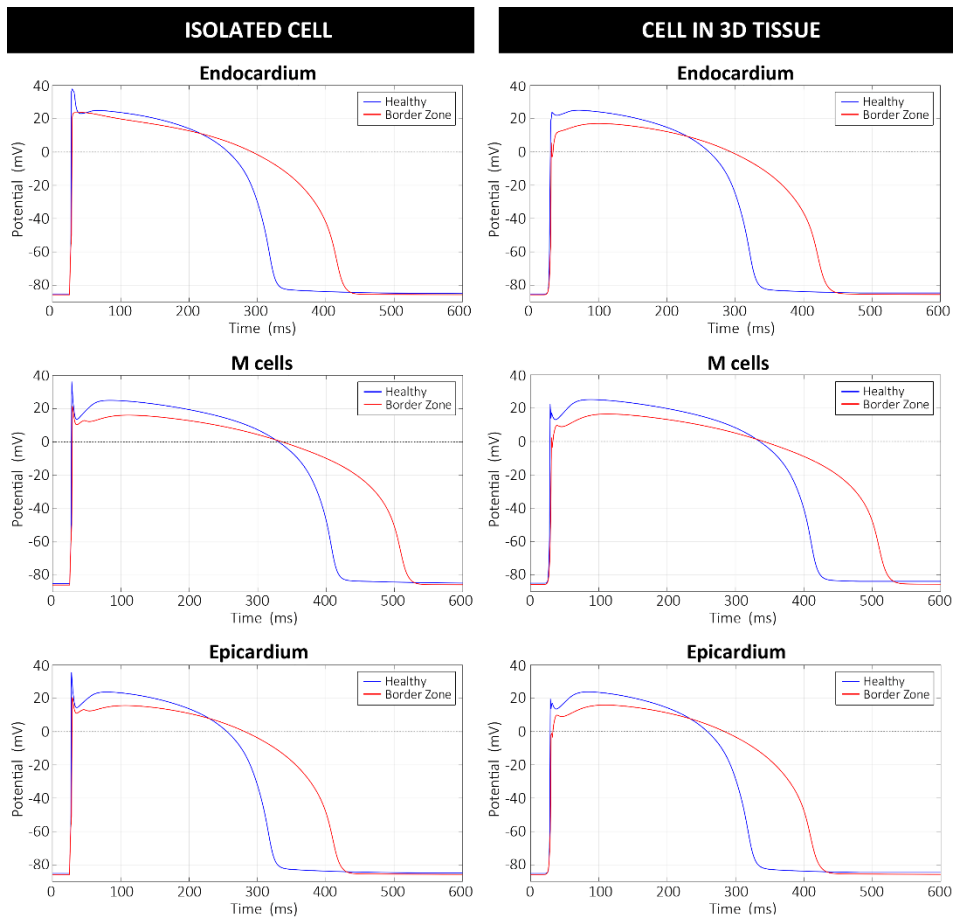
Figure 6.2. Comparison between APs generated by the original version of ten Tusscher model (ten Tusscher and Panfilov, 2006b), used in our simulations for healthy myocardium, and APs resulting from our modified version of such model for the remodelled BZ. Left column shows APs from a simulation with a single isolated cell, after stabilizing the model at a BCL of 800 ms, while right column displays APs registered from a cell embedded in a 3D tissue (i.e., surrounded by other cells) composed exclusively of remodelled myocytes.

embedded in a 3D tissue, i.e., completely surrounded by other cells. Specifically, that 3D tissue was composed of voxels (regular hexahedra) with an element edge length of 0.4 mm. Table 6.2 shows a quantitative analysis of the changes experienced by several important AP features, resulting from the modifications incorporated to the ten Tusscher model in order to reproduce the electrical remodelling in the BZ. It displays the changes both for a single isolated cell and

for a cell embedded in the 3D tissue mentioned above, which was formed by remodelled myocytes exclusively.

	Feature	Single isolated cell			Cell embedded in a 3D tissue		
		Healthy	Border Zone	Change	Healthy	Border Zone	Change
Endocardium	Maximum amplitude	37.78 mV	23.75 mV	− 37.1%	25.03 mV	17.08 mV	− 31.7%
	Maximum upstroke vel.	92.66 mV/ms	70.17 mV/ms	− 24.3%	61.26 mV/ms	47.30 mV/ms	− 29.5%
	Average upstroke vel.	40.51 mV/ms	26.58 mV/ms	− 34.4%	20.62 mV/ms	17.90 mV/ms	− 13.2%
	APD at 90%	299 ms	398 ms	+ 33.1%	304 ms	404 ms	+ 32.9%
	Resting potential	− 85.23 mV	− 85.77 mV	− 0.64%	− 85.26 mV	− 85.78 mV	− 0.61%
M cells	Maximum amplitude	36.22 mV	21.50 mV	− 40.6%	25.20 mV	16.53 mV	− 34.4%
	Maximum upstroke vel.	92.27 mV/ms	71.15 mV/ms	− 22.9%	80.05 mV/ms	36.74 mV/ms	− 54.1%
	Average upstroke vel.	40.44 mV/ms	26.84 mV/ms	− 33.6%	26.66 mV/ms	14.48 mV/ms	− 45.7%
	APD at 90%	389 ms	491 ms	+ 26.2%	394 ms	494 ms	+ 25.4%
	Resting potential	− 85.10 mV	− 85.89 mV	− 0.94%	− 85.13 mV	− 85.91 mV	− 0.91%
Epicardium	Maximum amplitude	35.47 mV	20.47 mV	− 42.3%	23.86 mV	15.96 mV	− 33.1%
	Maximum upstroke vel.	91.80 mV/ms	71.01 mV/ms	− 22.6%	83.68 mV/ms	57.09 mV/ms	− 31.7%
	Average upstroke vel.	40.22 mV/ms	26.59 mV/ms	− 33.9%	26.08 mV/ms	16.47 mV/ms	− 36.8%
	APD at 90%	298 ms	393 ms	+ 31.9%	302 ms	394 ms	+ 30.5%
	Resting potential	− 85.18 mV	− 85.90 mV	− 0.84%	− 85.21 mV	− 85.91 mV	− 0.82%

Table 6.2. Changes in AP properties produced as a consequence of the modifications applied to the ten Tusscher model in order to include the electrical remodelling in the BZ, compared to the control version (not modified) used for healthy myocardium. This table shows measures resulting from a simulation with a single isolated cell (after stabilizing ionic models at a BCL of 800 ms) and from a cell embedded in a 3D tissue (i.e., surrounded by other cells) composed exclusively of remodelled myocytes.

6.1.3.2. Structural remodelling in the border zone

Several experimental studies have observed the presence of electrical coupling between surviving myocytes and fibroblasts within the BZ in infracted

ventricles from distinct mammalian species (Camelliti et al., 2004; Mahoney et al., 2016b; Schwab et al., 2013). Thus, we decided to assess the potential arrhythmogenic effect of such heterocellular interaction in our simulations, in which fibroblasts are expected to act as electrical sources or sinks, depending on the AP phase of the coupled myocytes, thereby affecting propagation (Rohr, 2012). To do so, we modelled the patchy fibrosis in the BZ as a passive tissue able to interact electrotonically with the adjacent myocytes, instead of conside-ring it as an electrically inactive tissue, as in the case of the infarct scar. Thus, to model at the cellular level the EP consequences of the presence of electrically passive fibrotic tissue within the BZ, we used the MacCannell model for human ventricular fibroblast (MacCannell et al., 2007) in order to consider the electrotonic interaction between myocytes and fibroblasts in human ventricles.

6.2. Tissue and organ level

To perform computational simulations of cardiac EP at both tissue and organ level, it is necessary to choose a mathematical model to recreate the electrical interaction between neighbouring cardiac cells, since such interaction is what ultimately leads to the electrical propagation across the myocardial tissue. In addition, to obtain physiologically realistic propagation patterns by computational simulation with our 3D ventricular model, we had to set a number of parameters aiming to consider some features inherent to the cardiac muscle, which strongly determine the electrical propagation.

6.2.1. Electrical propagation across the myocardium

From a biophysical point of view and focusing on its EP behaviour, the cardiac muscle can be modelled as a reaction-diffusion system composed of a large set of single cells that are electrically coupled between them through the *gap junctions*, which are specialized proteins communicating the intracellular spaces of neighbouring myocytes. When a cardiomyocyte is electrically stimulated with intensity enough (i.e., above a critical threshold), such cell

depolarizes triggering an AP. This is the reaction phenomenon, since the myocyte reacts to the change in its transmembrane potential caused by the applied stimulus. Then, the difference in transmembrane potential between the excited cell and its neighbours, which are electrically coupled to the first one, generates ionic currents flowing between such cells, giving rise to the diffusion phenomenon. Such diffusive ionic currents continue flowing until making the neighbouring myocytes depolarize and develop APs as well, thereby leading to the reaction phenomenon, again. Thus, under physiological conditions, this reaction-diffusion process continues until the initial stimulus propagates through the entire myocardium.

The reaction phenomenon of that process is mathematically represented by means of ionic models that simulate the EP behaviour of myocytes, mimicking their AP as a reaction to a proper stimulus (see section 6.1). Therefore, it is necessary to include another mathematical model to cover the diffusive part of this biophysical process, which must be able to simulate the electrical propagation in the myocardium, that is, the ionic diffusion from each myocyte to the neighbouring ones.

The most widely used approach for the biophysical representation of the reaction-diffusion process of electrical propagation in cardiac muscle is the so-called *bidomain model* (Geselowitz and Miller, 1983). As introduced in Chapter 3 (see section 3.4.5), this model considers the cardiac tissue as an excitable continuum medium composed of two domains (intra- and extracellular) represented as volumetric conductors that coexist in space, although separated by cell membranes. The mathematical formulation of the bidomain model relates intra- (V_i) and extracellular (V_e) potentials by means of the two partial differential equations (PDE) written below.

$$\nabla \cdot (\boldsymbol{D_i} \cdot \nabla V_m) \ + \ \nabla \cdot (\boldsymbol{D_i} \cdot \nabla V_e) \ = \ C_m \ \frac{\partial V_m}{\partial t} \ + \ I_{ion}(V_m, v) \qquad \textbf{Eq. 6.1}$$

$$\nabla \cdot (\boldsymbol{D_i} \cdot \nabla V_m) \ + \ \nabla \cdot \big((\boldsymbol{D_i} \ + \ \boldsymbol{D_e}) \cdot \nabla V_e\big) \ = \ 0 \qquad \textbf{Eq. 6.2}$$

In these two equations (Eq. 6.1 and Eq. 6.2) the transmembrane voltage, V_m, is defined as follows:

$$V_m \ = \ V_i \ - \ V_e \qquad\qquad \textbf{Eq. 6.3}$$

The right side of Eq. 6.1 corresponds to the reaction term, where C_m is the electrical capacitance of cell membranes, which are considered as dielectric barriers separating two conductive mediums (intra- and extracellular spaces), what matches the definition of an electrical capacitor. I_{ion} represents the ionic current flux through the cell membrane, which is described by the ionic model used at the cellular level. The ionic flux depends on the transmembrane voltage, V_m, and a set of state variables (v) included in the model itself. In both PDEs (Eq. 6.1 and Eq. 6.2), $\boldsymbol{D_i}$ and $\boldsymbol{D_e}$ represent the volume-averaged conductivity tensors of intra- and extracellular spaces, respectively. Note that the bidomain model assumes different conductivities and anisotropy ratios for those two spaces, that is, for the intra- and extracellular domains (Johnston, 2016; Roth, 1992).

The main drawback of the bidomain model is the high computational burden associated with the challenging task of solving numerically an equation system consisting of a non-linear parabolic PDE (Eq. 6.1) coupled to an elliptic PDE (Eq. 6.2). The most widespread alternative to overcome this problem is the use of the *monodomain model* (Potse et al., 2006; Roth, 1988), which is a simplification derived from the bidomain approach. Such simplification comes from the assumption that variations of extracellular potential, V_e, are negligible, such that variations of transmembrane voltage, V_m, are mainly determined by the changes in the intracellular potential, V_i. Hence, the negligible impact of V_e on V_m allows uncoupling the two PDEs of the bidomain model. Mathematically, those assumptions translate into considering that conductivity tensors of the two domains included in the bidomain model ($\boldsymbol{D_i}$ and $\boldsymbol{D_e}$) are parallel and with equal anisotropy ratios, so that they are proportional, that is, related by a constant λ as shown in Eq. 6.4.

$$\boldsymbol{D_e} \ = \ \lambda \cdot \boldsymbol{D_i} \qquad\qquad \textbf{Eq. 6.4}$$

Using this expression (Eq. 6.4) to substitute $\boldsymbol{D_e}$ in Eq. 6.2 and combining the result with Eq. 6.1 in order to remove V_e, we obtain the following equation that represents the monodomain model:

$$\nabla \cdot (\boldsymbol{D} \cdot \nabla V_m) \;=\; C_m \, \frac{\partial V_m}{\partial t} \;+\; I_{ion}(V_m, v)$$

<div align="right">**Eq. 6.5**</div>

In this expression (Eq. 6.5) $\boldsymbol{D}$ is the equivalent conductivity tensor of the monodomain approach, which is defined as follows:

$$\boldsymbol{D} \;=\; \frac{\lambda}{1 + \lambda} \cdot \boldsymbol{D_i}$$

<div align="right">**Eq. 6.6**</div>

Hence, the monodomain formulation describes the reaction-diffusion process of electrical propagation in cardiac muscle by means of a single parabolic PDE (see Eq. 6.5), whose right term represents the reactive part of the problem, while the left term corresponds to the diffusion phenomenon.

Despite not being as biophysically precise as the bidomain approach, the monodomain model is very frequently used in simulation studies of cardiac EP, since it is much less computationally demanding. Moreover, it is widely assumed that, in the absence of externally applied currents, the monodomain model is a valid and accurate approximation for computational studies focused on the electrical propagation in cardiac tissue, showing no significant differences compared to the results derived from bidomain approach (Potse et al., 2006). In fact, the bidomain model is considered to be strictly necessary only in scenarios in which the assumption of negligible variations of the extracellular potential, V_e, is not applicable, usually due to the presence of externally applied currents affecting the extracellular medium (Smaill and Hunter, 2010), such as simulations related to cardiac defibrillation (Rantner et al., 2012; Trayanova et al., 2002).

Therefore, given its proven validity and its significantly lower computational cost compared to the bidomain approach, we chose the monodomain model for the electrical propagation in cardiac tissue for our simulations at the organ level, as is usually the case in most of the simulation studies related to infarct-derived VTs (see (Arevalo et al., 2016; Deng et al., 2016; Prakosa et al., 2018; Ringenberg et al., 2014), for instance).

6.2.2. Factors affecting electrical propagation

Under physiological conditions, electrical propagation through the myocardium is inherently anisotropic due to several reasons: (1) the elongated shape of cardiomyocytes, (2) their arrangement to compose the myocardial tissue, mainly defined by cardiac fibre orientation, and (3) the spatial distribution of *gap junctions* along cell membranes, which are significantly more concentrated in the terminal ends of myocytes, the so-called intercalated discs, than in their lateral sides. The combination of these factors results in an axisymmetrically anisotropic propagation in the myocardium, as the electrical current flows between neighbouring myocytes around three times faster through the intercalated discs (i.e., along longitudinal axes of myocytes) than across the myocytes lateral sides (Clerc, 1976).

Taking into consideration all the factors mentioned above, we modelled the electrical behaviour of the ventricular myocardium as an axisymmetrically anisotropic medium, where electrical wavefront propagates faster along the longitudinal axis of myocytes than in any transverse direction, that is, all directions perpendicular to the longitudinal axis of cardiac fibres. Consequently, in order to replicate such an anisotropic behaviour, we had to define two key properties in our 3D computational ventricular model: the cardiac fibre orientation, defined as the direction of the longitudinal axis of each myocyte, and two different conduction velocities (CV), referred to as longitudinal and transverse CV, respectively.

In the context of EP modelling at tissue level, CVs refer to the different velocities at which the electrical wavefront propagates through the myocardium in each direction. Longitudinal CV controls the propagation along the direction of cardiac fibres, while transverse CV affects the propagation in every direction perpendicular to the cardiac fibres. However, we cannot (and should not) directly assign the desired values for CVs. Such velocities depend heavily on conductivity values, which are parameters that must be set for the mathematical approach used at tissue level, that is, the monodomain model in our case. Nevertheless, they also depend on (1) the spatial discretization, corresponding to the volume mesh resolution determining the average distance between neighbouring nodes, and on (2) the anisotropy of myocardial tissue,

represented by the cardiac fibre orientation defining the preferential propagation direction. The volume mesh resolution, resulting from the meshing process, is known and fixed (element size cannot be modified), with an average edge length around 0.4 mm in the 3D ventricular model. Hence, it is necessary to assign the appropriate values for longitudinal and transverse conductivities in order to obtain the desired CVs along cardiac fibres and in directions perpendicular to them, respectively.

Importantly, cardiac fibre orientation and conductivities are both parameters that we defined for every hexahedral element of the 3D ventricular model individually. Therefore, this approach allowed us to define and control CVs at local level (element by element), enabling the incorporation of heterogeneities of CVs in different regions, such as healthy myocardium and BZ. In the case of conductivity values, we assigned a certain set of values to each region, that is, the same values to all those mesh elements belonging to a given kind of tissue (healthy, remodelled BZ and fibrosis).

With respect to the mathematical model that simulates the electrical propagation at tissue level, the equivalent conductivity tensor, D, is the element of the monodomain approach (see Eq. 6.5 and Eq. 6.6) that mathematically considers the cardiac fibre orientation and conductivities, both of which are parameters that were incorporated to the 3D computational model of infarcted ventricles. Conceptually, D is a tensor computed for each element of the volume mesh from the conductivity values and the cardiac fibre orientation associated with the corresponding element, such that it describes how the electrical activity in a certain node of a volume element affects (or propagates to) the adjacent nodes. From the standpoint of the electrical activity, the degree of influence of the activity in a mesh node on another node depends mainly on the relative position/distance between those two nodes. Under the assumption of axisymmetric anisotropy, the more aligned the line linking both nodes with respect to the longitudinal cardiac fibre direction, the higher the influence of each node on the other or, in other words, the faster the electrical propagation between them. Moreover, for a given conductivity, the distance separating adjacent nodes (i.e., the mesh resolution) also determines the CV at local level, since it affects the accuracy of the numerical methods used to solve the problem

of electrical propagation at tissue level. That is the reason why the volume mesh of the 3D cardiac model must have a restricted variability in edges length, aiming to avoid unexpected CV heterogeneities due to the elements size dispersion.

6.2.3. Myocardial tissue architecture. Cardiac fibre orientation

The process of including cardiac fibre orientation in the 3D ventricular model consisted of assigning to every hexahedral element of the volume mesh a unit vector defining the direction of the longitudinal axes of ventricular myocytes in the corresponding anatomical region (see Figure 6.3), which matches the preferential direction of conduction and electrical propagation. Thus, to include the anisotropy of the ventricular cardiac muscle, we wrote a custom MATLAB® code implementing the rule-based method proposed by Sebastian *et al.* (Sebastian et al., 2009) to generate the cardiac fibre orientation, which relies on the widely accepted histological studies reported by Streeter *et al.* (Streeter et al., 1969). To replicate the patterns described by Streeter *et al.* for the orientation of ventricular fibres, Sebastian *et al.* defined helix (α_h) and transmural (α_t) angles in local coordinates as follows:

$$\alpha_h \;=\; 1.9\,w \,+\, 0.86 \qquad \textbf{Eq. 6.7}$$

$$\alpha_t \;=\; 0.215\;\phi^2 \,+\, 0.0089\,\phi \,-\, 0.0093 \qquad \textbf{Eq. 6.8}$$

These angles (α_h and α_t) were defined such that the vector $\vec{v}$ defining the cardiac fibre orientation for each element of the volume mesh is given by the following expression:

$$\vec{v} \;=\; [\,\tan \alpha_t \,, 1,\, \tan \alpha_h\,] \qquad \textbf{Eq. 6.9}$$

In Eq. 6.7, w is the normalized distance between endocardium and epicardium ($w = 0$ at endocardial surface and $w = 1$ at epicardium), while in Eq. 6.8, ϕ corresponds to a polar angle that measures the distance with respect to the base of the ventricles. More precisely, ϕ represents the angle formed by the plane perpendicular to the LV long axis and the line linking the centroid of each hexahedral element and the centre point of the mitral valve.

Therefore, the direction of the vector assigned to each hexahedron of the volume mesh, in order to define the cardiac fibre orientation, depends on two parameters related to the position of the element centroid relative to the transmural depth and to the apex-to-base axis (i.e., cardiac long axis), respectively. However, both angles (helix and transmural) were defined into a local coordinates system referred to the plane of endocardial surface at local level. Hence, once the vector defining the fibre orientation for a given hexahedral element was computed (Eq. 6.9), we had to apply a linear transformation to translate it into the global coordinates system, in addition to normalizing the vector $\vec{v}$ to get the unit vector.
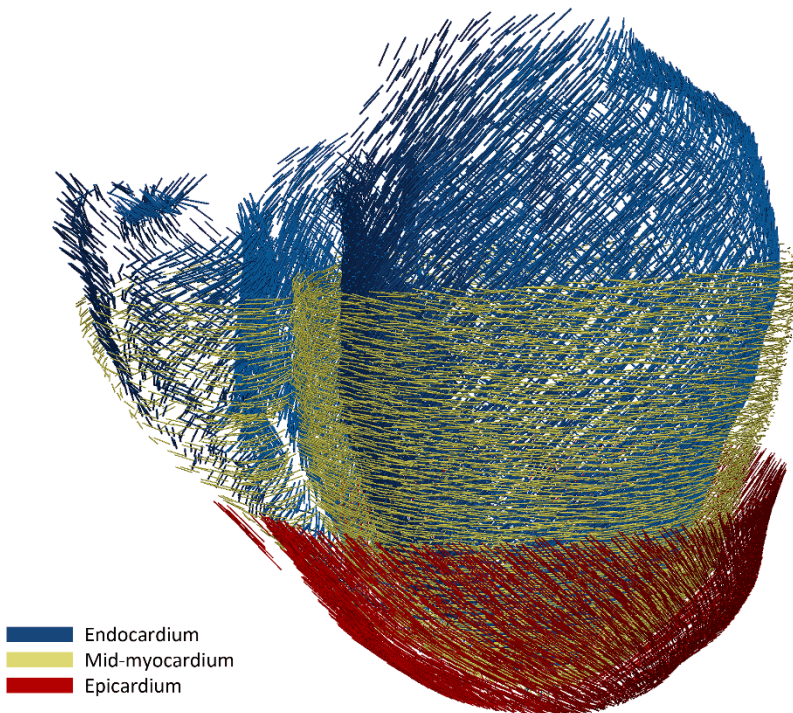
Figure 6.3. Representation of the cardiac fibre orientation included in the 3D computational model of ventricles. Left anterolateral view of the 3D ventricular model, displaying lines that represent the vectors defining the orientation of cardiac fibres on three layers at different transmural depths. One can observe the rotational variation of cardiac fibres (rotational anisotropy) along the transmural direction from endocardium to epicardium.

The strategy to assign the cardiac fibre orientation to the whole ventricular myocardium, including both ventricles, consisted on applying the described methodology in two steps: first we generated the fibre orientation for the LV, including the septum, and then for the RV free wall. As a result, we obtained a 3D distribution of cardiac fibres (unit vectors) representing the structure of the ventricular myocardium, which showed the rotational variation along the transmural direction, reproducing the rotational anisotropy described by Streeter *et al.*, as observed in Figure 6.3.
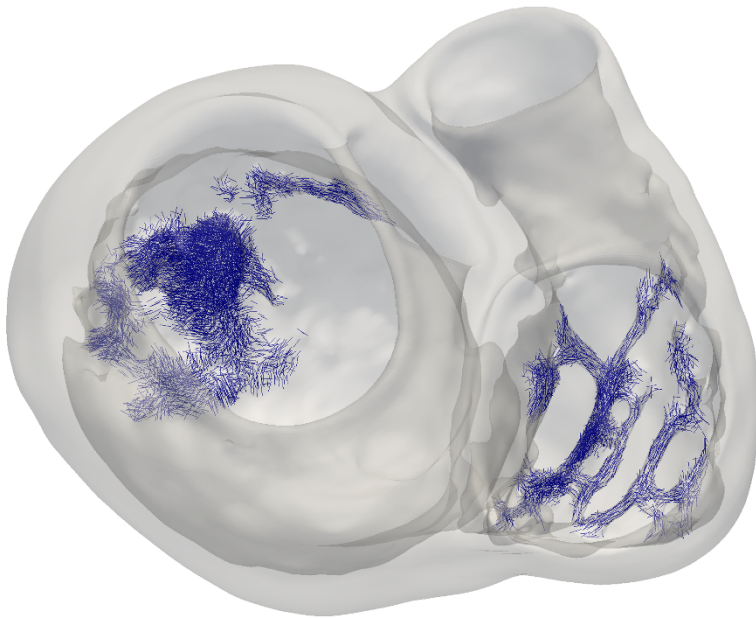
Figure 6.4. Cardiac fibre orientation assigned to papillary muscles and endocardial trabeculations. Basal view of the 3D surface model of ventricles (rendered with transparency) showing *blue* lines that represent the vectors incorporated to the computational model in order to define the cardiac fibres within the endocardial structures. As observed, more clearly in the RV, the direction of such vectors tend to be parallel to the longitudinal axis of the corresponding papillary muscle or trabeculation.

In papillary muscles and endocardial trabeculations, cardiac fibres are known to be mostly aligned parallel to the longitudinal axis of those anatomical structures (Greenbaum et al., 1981). Aiming to replicate such configuration, we performed the topological skeletonization of the volume mesh to extract the medial axes (skeleton) of each of those endocardial structures. As observed in

Figure 6.4, this enabled a proper assignment of fibre orientation within endocardial structures by aligning cardiac fibres with the axes resulting from the skeletonization process. Finally, we performed a Gaussian smoothing with a 3D kernel to soften abrupt transitions in fibres direction between the myocardial wall and papillary muscles and trabeculations, as well as at the junctions between the septum and the RV free wall.

6.2.4. Conduction velocities

As explained above (see section 6.2.2), longitudinal and transverse CVs mainly depend on the values set for longitudinal and transverse conductivities, respectively, as well as on the spatial resolution of the volume mesh. However, even using a same volume mesh with fixed cardiac fibre orientation, the relationship between a given set of conductivities for the monodomain model and the resulting CVs is not linear, which in fact is supposed to be quadratic.
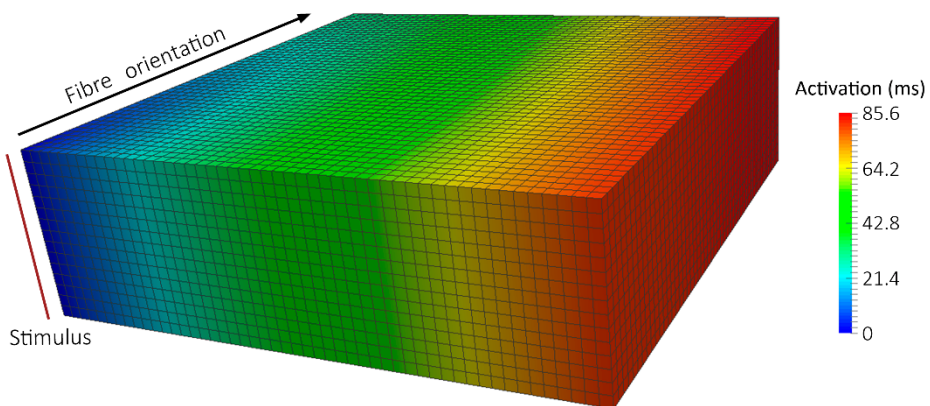
Figure 6.5. 3D slab model (20×20×6 mm) used to adjust conductivity parameters, showing the edges of voxels that form the volume mesh. Colour code represents the activation map (i.e., the activation time at which the propagation wavefront reached each node of the mesh) resulting from the application of a single stimulus on the lower left edge of the slab model (see *red line*). As observed, propagation is notably faster along the fibre orientation (see *black arrow*) than in the directions transverse to them.

Hence, due to the complex relationship between the different factors affecting the CVs (see section 6.2.2), we decided to perform a series of test simulations on a 3D slab model (20×20×6 mm) in order to set the desired CVs empirically and precisely. Such model was composed of regular hexahedral elements, that is, perfect cubes (voxels), with a fixed edge length of 0.4 mm (see Figure 6.5), thus matching the average edge length of hexahedra in the volume mesh of 3D ventricular model. The use of regular elements, with all of them showing the same shape and size, allowed us to make very accurate measures of CVs. In addition, we assigned fixed fibre orientation along the X-axis for all voxels (see Figure 6.5) to control the propagation within the 3D model and, thereby, measure accurately the CVs resulting from each tested set of conductivities.

As a procedure to adjust the CVs to the desired values, we applied a single stimulus on an edge of the 3D slab model and let it propagate through the whole model for each tested set of conductivity values. Once computed the activation map resulting from propagation of the applied stimulus (see Figure 6.5) and knowing the fibre orientation, calculating the CVs (both longitudinal and transverse) for a given set of conductivities was a trivial task.

6.2.4.1. Conduction velocities in healthy myocardium

For healthy myocardium, we performed the adjustment process of CVs explained above using the ten Tusscher model for human ventricular myocyte (ten Tusscher and Panfilov, 2006b) and the monodomain approach at tissue level (Roth, 1988). As a result, we set conductivity parameters to 0.24 S/m and 0.0455 S/m for longitudinal (σ_{Long}) and transverse (σ_{Trans}) conductivities, respectively. They resulted in a CV of 0.68 m/s along the cardiac fibre direction (longitudinal CV) and of 0.26 m/s in all transverse directions (transverse CV), values consistent with experimental measurements in human ventricles (Taggart et al., 2000), as well as in other large mammals (Caldwell et al., 2009). Importantly, we tested such set of conductivities with the three distinct versions of ten Tusscher model (endo-, mid-, epicardial myocytes) and the differences in resulting CVs were negligible.

6.2.4.2. Conduction velocities in the border zone

Within the heterogeneous infarct BZ, we had to deal with two different tissues: the electrically remodelled myocardium and the electrically passive fibrotic tissue, which represents to the structural remodelling in the BZ. For the remodelled myocardium, by means of the adjustment process of CVs described above, we set conductivity parameters to 0.05 S/m and 0.015 S/m for longitudinal (σ_{Long}) and transverse (σ_{Trans}) conductivities, respectively. Testing those values on the 3D slab model (see Figure 6.5), in combination with our modified version of ten Tusscher model for remodelled BZ (see section 6.1.3.1), we obtained CVs of 0.17 m/s in the longitudinal direction and of 0.065 m/s in the transverse directions. This means a reduction of approximately 75% with respect to the values of both CVs in healthy tissue. Thus, the CVs in the remodelled BZ were isotropically reduced to 25% of those of healthy myocardium. As in the case of healthy myocardium, we found no significant differences in CVs when compared the three cell types of the modified version of ten Tusscher model (endo-, mid- and epicardial myocytes) with the same set of values for conductivities.

We also tested the conductivity values adjusted for the BZ with the original ten Tusscher model (not modified), resulting in velocities of 0.225 m/s and 0.09 m/s for longitudinal and transverse CVs, respectively. This entails a reduction of 67% for longitudinal CV and of 65% for transverse CV, instead of 75% as in the case of our modified version of ten Tusscher model. Furthermore, testing the conductivity values used for healthy tissue (see section 6.2.4.1) with the remodelled version of ten Tusscher model, we obtained values of 0.54 m/s and 0.186 m/s for longitudinal and transverse CVs, respectively. Such values mean a reduction of 21% in longitudinal CV and of 28.5% in transverse CV, thus confirming the fact that electrical remodelling at the cellular level affects the propagation at tissue level. Such effect is a direct consequence of the reduction in peak sodium current, I_{Na}, incorporated in order to reproduce the electrical remodelling in the BZ (see section 6.1.3.1). This modification results in a lower excitability of cardiomyocytes and, consequently, in a slower propagation between neighbouring cells within the BZ due to the altered EP behaviour at the cellular level.

Tissue	Conductivities		Ionic model (*ten Tusscher*)			
			Control version		Remodelled version	
Healthy tissue	σ_{Long}	0.24 S/m	CV_{Long}	0.68 m/s	CV_{Long}	0.54 m/s ($\downarrow$21%)
	σ_{Trans}	0.0455 S/m	CV_{Trans}	0.26 m/s	CV_{Trans}	0.186 m/s ($\downarrow$28.5%)
BZ with CVs reduced to 25% ($CVs = 0.25 \times CV_{Healthy}$)	σ_{Long}	0.05 S/m	CV_{Long}	0.225 m/s ($\downarrow$67%)	CV_{Long}	0.17 m/s ($\downarrow$75%)
	σ_{Trans}	0.015 S/m	CV_{Trans}	0.09 m/s ($\downarrow$65%)	CV_{Trans}	0.065 m/s ($\downarrow$75%)
BZ with CVs reduced to 50% ($CVs = 0.50 \times CV_{Healthy}$)	σ_{Long}	0.12 S/m	Not tested		CV_{Long}	0.345 m/s ($\downarrow$50%)
	σ_{Trans}	0.03 S/m			CV_{Trans}	0.13 m/s ($\downarrow$50%)
BZ with CVs reduced to 75% ($CVs = 0.75 \times CV_{Healthy}$)	σ_{Long}	0.22 S/m	Not tested		CV_{Long}	0.515 m/s ($\downarrow$25%)
	σ_{Trans}	0.0485 S/m			CV_{Trans}	0.195 m/s ($\downarrow$25%)

Table 6.3. Values of conductivities used in computational simulations at the organ level both for healthy myocardium and for different degrees of remodelling in the BZ at tissue level. This table also shows the CVs resulting from the combination of such conductivities with the control (not modified) and the remodelled version of ten Tusscher model along with the reduction relative to the CVs in healthy tissue.

As we will explain in detail in the next chapter (Chapter 7), we also performed a few additional simulations in order to test different values for conductivities in the BZ, all of them using our remodelled version of ten Tusscher model. Besides the reduction to 25%, we also tested CVs in the BZ reduced to 50% and to 75% with respect to CVs of healthy myocardium. For a reduction of 50% in CVs ($CV_{Long} = 0.345$ m/s and $CV_{Trans} = 0.13$ m/s) we set conductivity parameters to 0.12 S/m and 0.03 S/m for longitudinal and transverse conductivities, respectively. To reduce CVs only to 75% ($CV_{Long} = 0.515$ m/s and $CV_{Trans} = 0.195$ m/s) we set conductivities to 0.22 S/m and 0.0485 S/m for longitudinal (σ_{Long}) and transverse (σ_{Trans}) directions, respectively. Table 6.3 shows all values of conductivity parameters used in our computational simulations at the organ level, together with the resulting CVs depending on the version of the ionic model at the cellular level: control (not modified) or remodelled version of ten Tusscher model.

Regarding fibrotic regions within the BZ, represented by the MacCannell model of ventricular fibroblast, they behave as a passive tissue that only enables passive propagation due to electrotonic conduction (i.e., only diffusion without reaction), rapidly leading to conduction blocks within the fibrotic tissue due to the attenuation of propagated potentials. Therefore, a specific CV defined for the fibrotic tissue might appear an irrelevant parameter. Nevertheless, the conductivity value assigned to fibrotic elements determines the coupling degree between myocytes and fibroblasts, thus defining the magnitude of the electrotonic interaction between fibroblasts and adjacent myocytes (MacCannell et al., 2007), with fibroblasts acting as electrical sources or sinks depending on the AP phase (Rohr, 2012). Then, we considered fibrosis in the BZ as an isotropic tissue, that is, with the same conductivity for longitudinal and transverse directions. We assigned a conductivity of 0.1 S/m for fibrotic elements within the BZ, what means a reduction of about 60% with respect to the longitudinal conductivity (not CV) in healthy myocardium.

6.3. Whole body level: 3D torso model

In relation to the EP properties of the torso, we considered a specific conductivity for each one of the organs and tissues included in the 3D torso model, aiming to compute the ECG signals to be registered on the body surface. As described in Chapter 5, we used the software TetGen to perform the volume meshing of the 3D torso model, using as a template the set of surfaces representing the different organs and tissues included in the model (see Figure 5.16[b]). Besides generating the tetrahedral volume mesh, TetGen also labelled every tetrahedral element in order to assign it to a specific region, using the mentioned surfaces as a reference. Therefore, each tetrahedral element of the volume mesh resulting from the meshing process, was assigned to a certain organ or anatomical structure. Importantly, all those elements not included in any specific anatomical structure after this first step of the labelling process, were finally tagged as *general torso*. Figure 6.6 shows the result of the labelling process of the tetrahedral volume mesh of the 3D torso model. The smoothness of the external surface of the region of ventricles, compared to the rest of structures, is a consequence of the refinement of tetrahedral elements in that

region for the sake of numerical accuracy, as commented in Chapter 5 (see section 5.2.2).

Conductivity values assigned to different organs and tissues were taken from the literature (Bradley et al., 2000; Bressler and Ding, 2006; Gabriel et al., 1996; Klepfer et al., 1997; MacLeod et al., 1991), with bones and blood having the lowest and the highest conductivity, respectively (see Table 6.4). As in (Klepfer et al., 1997), for the region labelled as general torso, that is, the space not included in any particular organ or anatomical structure, we set a conductivity of 0.239 S/m. Such value was calculated as an average of the conductivities of several other tissues, including the skeletal muscle that was not considered as a specific region in the 3D torso model.
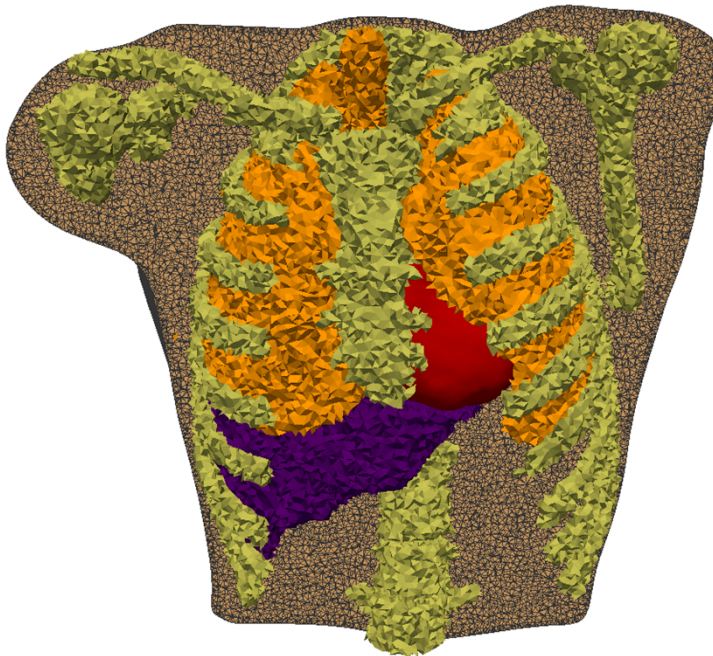
Figure 6.6. Anterior view of the tetrahedral volume mesh of the 3D torso model, showing all organs and anatomical structures included in the model, which are displayed over a coronal cross-section of the portion of volume mesh labelled as general torso that shows the edges forming the tetrahedral elements. Different colours indicate which organ or anatomical structure each tetrahedral element was assigned to, as a result of the labelling process of volume mesh: lungs (*orange*), bones (*yellow*), liver (*purple*) and ventricles (*red*). Although not visible in this view, atria and blood pools of the four cardiac chambers are also included in the 3D torso model.

Furthermore, we considered isotropic propagation for all of the organs and tissues included in the 3D torso model, except for the ventricular myocardium. Indeed, we did not assign predetermined conductivity values to those tetrahedra corresponding to the ventricular myocardium. Instead of that, we used a custom MATLAB® code to map the conductivities assigned to the hexahedral elements of the 3D computational ventricular model into the tetrahedral elements of torso model corresponding to ventricular myocardium. Thus, we kept the heterogeneities at tissue level represented by different conductivity parameters for healthy tissue, remodelled BZ and patchy fibrosis, as well as the myocardial anisotropy defined by the cardiac fibre orientation in order to account for the anisotropic propagation within the ventricular tissue.

Organ / Tissue	Conductivity (S/m)
Bones	2.0×10^{-2}
Liver	2.77×10^{-2}
Lungs	3.89×10^{-2}
Blood	70.0×10^{-2}
Atrial myocardium	45.9×10^{-2}
General torso	23.9×10^{-2}

Table 6.4. Conductivity values assigned to the different organs and tissues included in the computational 3D torso model**.**

Chapter 7

Personalized Electrophysiological Study using Computational Simulation

This chapter is devoted to present our pipeline of computational simulation of cardiac electrophysiology (EP), which aims to perform reliable personalized *in-silico* EP studies of infarct-related ventricular tachycardias (VT). First, we give information about the software and hardware we used to perform our computational simulations of cardiac EP. Then, we describe our simulation pipeline at the organ level, detailing which kind of simulations we conducted and how we carried them out aiming to replicate the clinical VT suffered by the specific patient, whose data were used to build the 3D ventricular model. Moreover, we explain the approach used to conduct the simulations at the torso level in order to compute the simulated ECGs registered on the body surface. Finally, we present a detailed report of the main results derived from our simulations of cardiac EP, at both organ (ventricles) and body level (torso), as well as a comprehensive discussion on those results.

Although presented here in a considerably further extended fashion, it must be noted that part of the content of this chapter was already included in a research article entitled "*Personalized cardiac computational models: from clinical data to simulation of infarct-related ventricular tachycardia*", which was recently published in the indexed international journal *Frontiers in Physiology* in May 2019 (Lopez-Perez et al., 2019).

7.1. Simulation software

To perform simulations at the organ level, as well as the test simulations with the 3D slab model described in Chapter 6 (see section 6.2.4), we used a software called ELVIRA (Heidenreich et al., 2010a), which was created by researchers from the Group of Structural Mechanics and Materials Modelling of the University of Zaragoza (Zaragoza, Spain) in collaboration with the Centre for Research and Innovation in Bioengineering (Ci^{2}B) from the Polytechnic University of Valencia (Valencia, Spain). It is a FEM solver written in FORTRAN 90 (IBM, Armonk, NY, USA) and specifically developed for solving the anisotropic reaction-diffusion equation of the monodomain model for cardiac EP (see Eq. 6.5 in Chapter 6) by means of parallel computing, making use of the operator splitting technique (Keener and Bogar, 1998). Therefore, every simulation performed with ELVIRA is solved using the monodomain approach at the tissue level (Roth, 1988).

Regarding our particular simulations, we applied the conjugate gradient method with an integration time step (*dt*) of 0.02 ms to compute the numerical solution of our EP problems. On the other hand, spatial discretization is determined by the spatial resolution of the FEM volume mesh that defines the geometry of the problem. Thus, in all of our simulations, spatial discretization was of 0.4 mm, both for organ simulations with the 3D ventricular model (average edge length of about 0.4 mm) and for test simulations with the 3D slab model (fixed edge length of 0.4mm). Furthermore, we used implicit integration for the parabolic partial differential equation (PDE) of the monodomain model (tissue level) and explicit integration with adaptive time stepping for systems of ordinary differential equations (ODE) associated with ionic models used at

cellular level: ten Tusscher model for human ventricular cardiomyocyte (ten Tusscher and Panfilov, 2006b) and MacCannell model for human ventricular fibroblast (MacCannell et al., 2007).

With respect to the ionic models employed at cellular level, both the ten Tusscher model of human ventricular cardiomyocyte (ten Tusscher and Panfilov, 2006b), used for healthy ventricular myocardium, and the MacCannell model of human ventricular fibroblast (MacCannell et al., 2007), used for fibrotic tissue in the BZ, were already implemented in ELVIRA. On the contrary, our modified version of ten Tusscher model for electrically remodelled BZ, described in Chapter 6 (see section 6.1.3.1), was not included in the original version of the solver. Hence, we had to modify the source code of ELVIRA in order to add an extra ionic model, what affected several modules of this software since its structure was not originally conceived to ease the addition of new models. That procedure involved recompiling the entire code of ELVIRA and testing the performance of the new extended version of such software before conducting our computational simulations at the organ level.

7.2. Simulation hardware

To carry out our computational simulations of cardiac EP, performed with the software ELVIRA, we used three multi-CPU computers specifically designed for parallel computing, all of them running Scientific Linux (release 6.9, Carbon)[16]. All those machines had an identical architecture comprising 128 GB of RAM and 64-bit AMD processors with a total of 64 cores at 2.3 GHz (4 × AMD Opteron 6376 processor)[17]. Importantly, they did not work jointly as a HPC (high-performance computing) cluster, so each simulation was computed on a single computer, what means that we were only able to perform one simulation at a time per machine.

---

[16] Scientific Linux.   https://www.scientificlinux.org/
[17] AMD Opteron 6376 processor.   https://www.amd.com/en/products/cpu/6376

Regarding the computational performance, simulating one second of EP activity on our 3D ventricular model (4 million nodes and 3.71 million hexahedral elements) with ELVIRA, usually took around seven hours of computing on one of the machines described above.

7.3. Computational simulation at the organ level

All simulations at the organ level (ventricles) were performed on eight different versions of our patient-specific 3D ventricular model. The computational representation of both healthy myocardium and infarct scar remained unchanged across all model versions. Hence, the only difference between those eight model versions was the way of modelling the BZ. As shown in Table 7.1, we generated eight different representations of the BZ by combining the presence or absence of electrical remodelling in such region (modified or control version of ten Tusscher model, respectively) with four different levels of image-based patchy fibrosis: 0% (no fibrosis), 10%, 20% and 30%. Such approach allowed us to independently assess the arrhythmogenic effect of structural (patchy fibrosis) and electrical remodelling within the BZ, as well as the combination of both factors.

Model version		Fibrosis level in BZ	EP remodelling in BZ
model *#1*	(noER+00fib)	0%	
model *#2*	(noER+10fib)	10%	
model *#3*	(noER+20fib)	20%	NO
model *#4*	(noER+30fib)	30%	
model *#5*	(ER+00fib)	0%	
model *#6*	(ER+10fib)	10%	
model *#7*	(ER+20fib)	20%	YES
model *#8*	(ER+30fib)	30%	

Table 7.1. Eight different versions of the computational model of ventricles used for simulations at the organ level, classified according to the kind of remodelling included in the BZ: electrical (EP) and/or structural (patchy fibrosis). Abbreviations: noER – no electrical remodelling in BZ; ER – electrical remodelling in BZ; 00fib – 0% patchy fibrosis in BZ; 10fib – 10% patchy fibrosis in BZ; 20fib – 20% patchy fibrosis in BZ; 30fib – 30% patchy fibrosis in BZ.

Moreover, we used the same conductivity values for the BZ in all versions of the computational model, both for those versions including a combination of structural and electrical remodelling (models *#6-8*) and for those ones including only structural (models *#2-4*), only electrical (model *#5*) or no remodelling (model *#1*) in the BZ. Note that we reduced conductivities in the BZ with respect to the values used in healthy tissue, leading to a reduction in CVs within the BZ. Those CVs were consequently reduced to 25% or 35% with respect to healthy myocardium, that is, the conduction was 75% or 65% slower than in healthy tissue, depending on whether the model version included or not electrical remodelling in the BZ, respectively (for more details see section 6.2.4.2 in Chapter 6). However, for the sake of clarity, hereinafter we will refer to that feature as CVs reduced to 25%, using the abbreviation CVsBZ-25%, regardless of the mentioned model version includes electrical remodelling in the BZ or not. We will explicitly mention such difference along the text only when it is necessary to avoid any important misunderstanding. Therefore, we used the same set of reduced conductivities at the tissue level for the BZ in all versions of ventricular model, regardless of what kind of remodelling they included in the peri-infarct region corresponding to the BZ: electrical, structural (fibrosis), both or neither.

After accomplishing our simulation pipeline (explained in sections below) with the eight model versions listed in Table 7.1, model *#6* (ER+10fib) was revealed as one of the most pro-arrhythmogenic configurations among the eight tested settings, since it was one of the model versions most prone to inducing VTs in the *in-silico* tests. Thus, we decided to perform some additional simulations with the model *#6* (ER+10fib) in order to study the effect of changing the conductivities within the BZ. More specifically, we tested two new sets of values for conductivity parameters, which in combination with our remodelled version of ten Tusscher model resulted in CVs in the BZ reduced to 50% and 75% with respect to CVs of healthy tissue, that is, with an electrical conduction 50% and 25% slower than in healthy myocardium, respectively (see Chapter 6, section 6.2.4.2). Hence, we performed simulations using the model *#6* (ER+10fib) with three different sets of CVs in the BZ, reduced to 25%, 50% and 75% with respect to healthy tissue, which will be referred to throughout the text by the abbreviations CVsBZ-25%, CVsBZ-50% and CVsBZ-75%, respectively.

As we will describe in detail in the following sections, our pipeline of simulation of cardiac EP at the organ level included three main steps. First, we performed a stabilization of myocyte-fibroblast coupling, only for those model versions including fibrosis within the BZ (models *#2-4* and *#6-8*). After that, we carried out a stabilization of the 3D ventricular model in sinus rhythm, also serving as a validation step. Finally, we applied protocols of programmed electrical stimulation (PES) on the stabilized ventricular model aiming to test VT inducibility *in-silico*, that is, by computational simulation.

7.3.1. Stabilization of myocyte-fibroblast coupling

Adjacent myocytes and fibroblasts are known to interact by coupling and signalling between them in both healthy and diseased myocardium (Kohl and Gourdie, 2014; Mahoney et al., 2016b; Ongstad and Kohl, 2016). Electrotonic interaction induces changes in myocytes coupled to fibroblasts, such as elevation of resting potential (less negative) and APD reduction. These are the main consequences of the effect of fibroblasts, which act as electrical sources when coupled myocytes are in resting state, giving rise to resting potential elevation, and as electrical sinks along the activation and repolarization phases of surrounding myocytes, leading to APD reduction due to accelerated repolarization (MacCannell et al., 2007; Zeigler et al., 2016). Thus, we needed to stabilize these myocyte-fibroblast electrotonic couplings as a first step of our simulation pipeline to ensure that those interactions reach the steady state. Then, for all models including any level of patchy fibrosis in the BZ (10% [*#2*, *#6*], 20% [*#3*, *#7*] or 30% [*#4*, *#8*]), we performed a first simulation of 1 second without applying any stimulus on the 3D ventricular model, aiming to reach the steady state in all myocyte-fibroblast couplings.

7.3.2. Sinus activation

Once we had the patient-specific 3D ventricular model and the 3D torso model completely constructed and ready for simulations, as well as both models coupled as a whole, we tried to reproduce patient's ECG in sinus rhythm by

computational simulation, as a strategy to test and validate the performance of our computational models. Nevertheless, replicating by computational simulation an activation sequence matching the sinus activation of a particular subject is far from being a trivial task.

In the human ventricles, electrical activation is known to be initially triggered from a number of sites located in subendocardial layers (next to the endocardial surfaces) due to the presence of Purkinje-myocardium junctions (Durrer et al., 1970; Opthof et al., 2017). We did not include cardiac conduction system (CCS) in our 3D ventricular model, but we did have endocardial EAMs with checked LAT annotations for both ventricles. Thus, we decided to use those CARTO® data to generate a stimulation sequence aiming to reproduce the patient's activation pattern as accurately as possible.
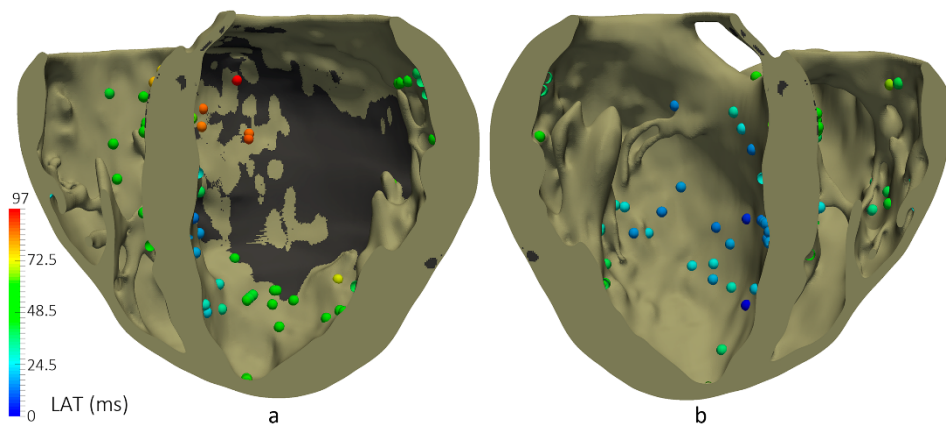
Figure 7.1. Patient-specific stimulation sequence derived from endocardial CARTO® maps recorded in sinus rhythm during the real EP study. Anterior (*a*) and posterior (*b*) views of a coronal cross-section (four-chamber plane) of the 3D ventricular model, with infarct scar represented in *dark grey*. Spheres correspond to CARTO® points projected onto LV (84 points) and RV (49 points) endocardial surfaces, with colour code representing LAT values for each point, which was measured from EGMs recorded via CARTO® system.

After the checking process described in Chapter 4 (see section 4.5.1), we preserved 133 endocardial CARTO® points (84 from LV and 49 from RV) mapped onto the endocardial surfaces of our 3D ventricular model, as shown in Figure 7.1. In an attempt to reproduce patient's activation sequence, we used those points as stimulation sites, applying a stimulus at each one of them at the time

instant given by the checked LAT value associated with the corresponding endo-cardial CARTO® point. Hence, the endocardial CARTO® point with the earliest LAT was the first stimulated site (i.e., activated at t = 0 ms) and the rest of points were sequentially stimulated until reaching the latest activated point (highest LAT value) according to recorded EAMs. The earliest activated points (lowest LAT values) were located at mid-apical level on septal wall of LV endocardium (see dark blue spheres in Figure 7.1[b]), while the latest activated points were on the posterior wall (see red and orange spheres in Figure 7.1[a]) within the region that surrounds the scarred tissue, which corresponds to the BZ.

To perform simulations of sinus activation, we took the final state of the stabilization of myocyte-fibroblast coupling as the starting point (i.e., initial state for t = 0 ms), in the case of models including fibrosis within the BZ. Then, we applied the CARTO®-derived endocardial stimulation sequence to simulate six heartbeats at a basic cycle length (BCL) of 800 ms, thus matching patient's heart rate in sinus rhythm (75 bpm) during the real EP study conducted prior to RFA procedure. This heart rate was measured from the ECG recordings included in the CARTO® data. Note that we simulated six beats, rather than only one, to stabilize the computational ventricular model in sinus rhythm before the application of pacing protocols for testing VT inducibility. Finally, we computed on the 3D torso model the extracellular potentials resulting from the simulated ventricular activity (this approach is addressed in section 7.4). Importantly, we only computed the extracellular potentials derived from the sixth sinus activation, thus obtaining simulated ECG for a single heartbeat with the aim to compare those simulated signals to patient's recordings.

Therefore, the aim of this sinus activation simulation was twofold: (1) stabilize the model prior to *in-silico* VT inducibility tests and (2) test and validate the performance of the developed computational models (ventricles and torso), including the EP modelling associated with them. Regarding this latter goal, the idea was to test the ability of our computational models (torso-ventricles set) to replicate the patient's ECG in sinus rhythm. To do so, we stimulated the ventricular model by the patient-specific sinus activation sequence provided by CARTO® data, with the aim to compare the features of simulated and real ECGs and measure the correlation between them. However, it is important to remark

that this is a validation step that is not strictly necessary to explore the VT inducibility by *in-silico* tests. Thus, our simulation pipeline could seamlessly work without invasively recorded CARTO® data.

7.3.3. *In-silico* VT inducibility tests

At the EP laboratory, electrophysiologists usually apply pacing protocols (PES protocols) specifically aimed at testing VT inducibility as part of the EP study conducted just before the RFA procedure. Hence, the final goal of our simulation pipeline was to reproduce *in-silico* those pacing protocols in order to test VT inducibility by means of computational simulation. Despite having the possibility of virtually testing any site in our 3D ventricular model, we selected two points from CARTO® EAMs that the electrophysiologists had chosen (and labelled) as pacing sites during the *in-vivo* EP study. The application of PES protocols at those two sites, both located on posterior LV wall, in the vicinity of infarct scar (see Figure 7.2), managed to successfully induce the patient's clinical VT at the EP laboratory. One of those pacing sites, which we called *endo#1*, was located on LV endocardium at mid-basal level, within the BZ and almost completely surrounded by scar tissue (see green sphere in Figure 7.2[a]). The other site, called *epi#1*, was on the epicardial surface of LV posterior wall at mid-apical level, beneath the apical border of infarct scar (see red sphere in Figure 7.2[b]). After testing VT inducibility from those two pacing sites, we decided to add another point in order to assess the influence of the location of a given pacing site on VT inducibility. We also placed this third point on the epicardial LV posterior wall (*epi#2*), more precisely at basal level, above the basal side of infarct scar (see blue sphere in Figure 7.2[b]).

To perform our *in-silico* tests of VT inducibility, we applied (simulated) PES protocols delivered from each one of the three chosen pacing sites (*endo#1*, *epi#1* and *epi#2*) and, furthermore, on each one of the eight versions of the computational model of ventricles (versions *#1-8*, see Table 7.1). Therefore, we tested VT inducibility in 24 different settings. Importantly, we applied the same PES protocol used by electrophysiologists in the EP study undergone by the real patient prior to RFA procedure. First, starting from the final state of previous

stabilization in sinus rhythm (six heartbeats), we paced the ventricles with a train of six stimuli delivered from the tested pacing site at a BCL of 600 ms (S1 phase), followed by a single premature stimulus coupled at a shorter interval (S2 phase). We began applying the S2 stimulus coupled at 400 ms after the last S1 stimulus. Then, if VT was not induced, we repeated that stimulation protocol (S1 followed by S2) reducing the coupling interval (CI) between last S1 and S2 stimulus in steps of 10 ms each time. We continued reducing the S1-S2 interval until reaching positive VT induction or propagation block at pacing site, i.e., S2 stimulus failed to propagate because the myocardial tissue at pacing site still remained in refractory period. In the latter case, when VT was non-inducible by means of a single S2 stimulus, we repeated the PES protocol adding another premature stimulus (S3 phase) after the S2 phase, with both S2 and S3 stimuli coupled at the same CI. That is, the coupling time between S2 and S3 stimuli was the same as the time elapsed from the last S1 stimulus to S2. When a PES protocol including S3 phase was unable to induce VT, then we assumed negative result for VT inducibility test for the assessed setting: PES protocol applied at a given pacing site (three distinct locations) on a certain version of ventricular model (eight different versions depending on BZ modelling).
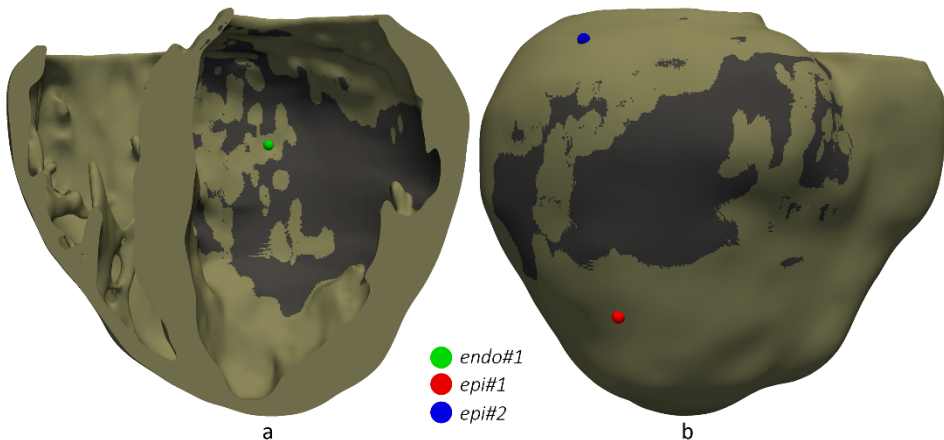
Figure 7.2. Pacing sites for the application of PES protocols aiming to test VT inducibility by computational simulation. (*a*) Anterior view of a sagittal cross section (4-chamber plane) of the 3D ventricular model, showing the location of one of the pacing sites at endocardial level (*endo#1*) chosen by electrophysiologists during the real EP study. (*b*) Posterior view of the 3D ventricular model, showing two pacing sites at epicardial level, one of them selected by electrophysiologists (*epi#1*) and another added by us (*epi#2*). In both views of 3D model (*a* and *b*), dark grey region represents the infarct scar.

7.4. Computational simulation at the torso level. Simulation of the ECG

To obtain the simulated ECG signals registered on the body surface, first we had to compute extracellular potentials, V_e, in ventricular myocardium and then compute the extracellular potentials generated by that electrical activity in the ventricles across the entire 3D torso model (from the heart up to body surface). Nevertheless, extracellular space is missing in monodomain model, which we used at the tissue level for our organ simulations (see Chapter 6, section 6.2.1). Therefore, for that task we used an approximation of the bidomain model, which was proposed by Keller *et al.* (Keller et al., 2010) and already used in previous works by our group (Ferrer-Albero et al., 2017; Martinez-Mateu et al., 2018). Such approximation of the bidomain model comprises several steps that we explain below.

First, we interpolated transmembrane potentials, V_m, computed for the ventricle domain (simulation at the organ level), from the nodes of the hexahedral mesh of the 3D ventricular model to those nodes of the tetrahedral mesh of 3D torso model labelled as ventricular myocardium. Note that transmembrane potentials in the ventricles, V_m, were previously computed by simulation at the organ level, using monodomain model by means of ELVIRA solver. Then, combining the elliptic partial differential equation (PDE) of bidomain model (see Eq. 6.2) and the assumptions on conductivity tensors ($\boldsymbol{D_i}$ and $\boldsymbol{D_e}$) from monodomain approach (Eq. 6.4 and Eq. 6.6) (see equations in Chapter 6, section 6.2.1), we obtain the following expression that relates transmembrane voltage, V_m, and extracellular potentials, V_e, within the ventricles domain (Ω_H).

$$\nabla \cdot (\boldsymbol{D} \cdot \nabla V_e) \; = \; \frac{-1}{1 + \lambda} \; \nabla \cdot (\boldsymbol{D} \cdot \nabla V_m) \quad in \quad \Omega_H \qquad \textbf{Eq. 7.1}$$

$\boldsymbol{D}$ is the equivalent conductivity tensor of monodomain model and λ is the constant of proportionality that relates the conductivity tensors $\boldsymbol{D_i}$ and $\boldsymbol{D_e}$.

Then, to solve Eq. 7.1 in order to compute extracellular potentials, V_e, from the interpolated transmembrane voltage, V_m, we considered that the

ventricles were isolated from the rest of torso model and immersed in a non-conducting bath, what results in Neumann boundary conditions on the interface between ventricles and surrounding medium ($\partial\Omega_H$) defined as follows:

$$\boldsymbol{n_H} \cdot (\boldsymbol{D} \cdot \nabla V_e) \;=\; 0 \quad on \quad \partial\Omega_H \qquad\qquad \textbf{Eq. 7.2}$$

In that equation (Eq. 7.2), $\boldsymbol{n_H}$ is the unit vector normal to the external surface of ventricles, $\partial\Omega_H$, pointing outwards.

Once extracellular potentials in the ventricles, V_e, were computed, then we did consider the whole 3D torso domain (Ω_T) to compute such potentials from the ventricles up to the torso surface. Considering the torso as a solid conductor, we computed extracellular potentials in the torso domain by means of the following Laplace equation:

$$\nabla \cdot (\boldsymbol{D_T} \cdot \nabla V_T) \;=\; 0 \quad in \quad \Omega_T \qquad\qquad \textbf{Eq. 7.3}$$

In such equation (Eq. 7.3) V_T represents extracellular potentials within the domain of torso model (except for the ventricles) and $\boldsymbol{D_T}$ is the heterogeneous conductivity tensor of the 3D torso model defining the conduction properties specific to each organ/tissue. $\boldsymbol{D_T}$ was computed for every tetrahedral element of the volume mesh of the 3D torso model using the different conductivities chosen for each kind of tissue, considering isotropic conduction all over the torso except for the region of ventricular tissue, where we preserved the axisymmetric anisotropy inherent to cardiac muscle (see Chapter 6, section 6.3).

To obtain extracellular potentials, V_T, all over the torso, we solved Eq. 7.3 by applying Dirichlet boundary conditions to force the continuity of extracellular potentials at ventricles-torso interface ($\partial\Omega_{HT}$), as shown in Eq. 7.4. In addition, we considered that the torso was surrounded by a non-conducting medium, thus imposing Neumann boundary conditions on the external surface of torso model ($\partial\Omega_T$), as defined in Eq. 7.5, where $\boldsymbol{n_T}$ is the unit vector normal to the torso surface pointing outwards.

$$V_e \;=\; V_T \qquad on \quad \partial\Omega_{HT} \qquad\qquad \textbf{Eq. 7.4}$$

$$\boldsymbol{n_T} \cdot (\boldsymbol{D} \cdot \nabla V_T) \;=\; 0 \quad on \quad \partial\Omega_T \qquad\qquad \textbf{Eq. 7.5}$$

Finally, we addressed this problem by means of the FEM method, using the conjugate gradient method and incomplete Cholesky decomposition as a preconditioner for computing a numerical solution. In addition, we used a temporal resolution of 1 ms and the heterogeneous spatial resolution defined by the edges length of the tetrahedral volume mesh of torso model, as described in Chapter 5 (see section 5.2.2).
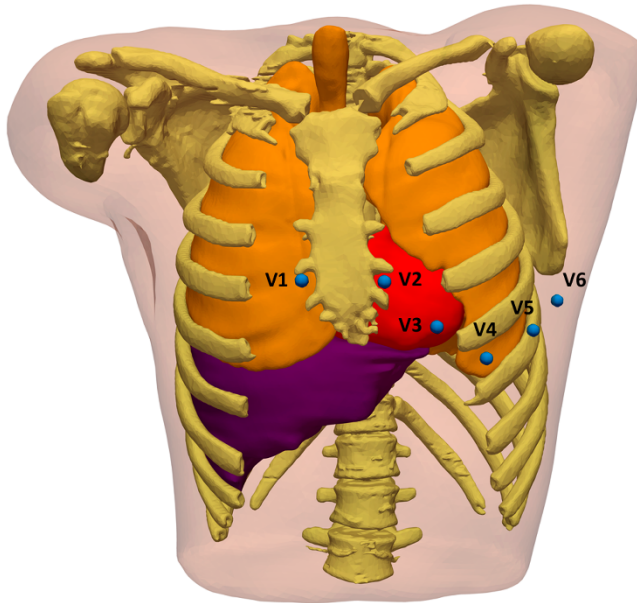
Figure 7.3. Anterior view of 3D torso model, showing the 3D surfaces that represents all organs and tissues included in that model: torso contour (rendered with transparency), bones, lungs, liver and ventricles. Although not visible in this view, atria and blood pools of four cardiac chambers are also included in 3D torso model. *Blue spheres* on torso surface represent the location of the six virtual electrodes defined for the registration of simulated ECG signals, matching the standard positions of precordial leads.

As in the case of the software ELVIRA, the MATLAB® code that we used to compute extracellular potentials across the torso model by means of this approximation of bidomain model, was originally implemented by researchers from the University of Zaragoza (Zaragoza, Spain). However, we had to

thoroughly modify the original version of that MATLAB® code in order to adapt it to our 3D models (ventricles and torso) and our simulation settings, as well as to parallelize the code aiming to speed up the computation of extracellular potentials within the 3D torso model.

ECG signals represent the manifestation of the electrical activity of the heart registered on the body surface. Then, after computing the extracellular potentials in the entire torso model resulting from the electrical activity in the ventricles, to obtain the simulated ECG signals we defined six virtual electrodes on the torso surface, that is, we selected six nodes of the volume mesh located on the 3D model surface. The location of those virtual electrodes corresponds to the standard positions of the six precordial ECG leads, as shown in Figure 7.3. Therefore, simulated ECG signals correspond to the extracellular potentials, V_T, generated by the previously simulated electrical activity in the ventricles, registered onto torso surface with a temporal resolution of 1 ms.

7.5. Computational simulation results

This section gathers a detailed description of all the results derived from the different steps of the simulation pipeline described above, both at the organ (ventricles) and at the torso level (simulated ECGs).

7.5.1. Stabilization of myocyte-fibroblast coupling

As observed in Figure 7.4, even in the absence of external stimulation, the significant difference in resting potential between coupled myocytes (around –85 mV) and fibroblasts (around –49 mV) initially generated a current flowing from fibroblasts to myocytes with enough intensity to trigger an AP in a number of myocytes, thereby generating several activation wavefronts spreading through the entire ventricular myocardium (see Video S1[18]). Thus, in

---

[18] **Video S1:** Stabilization of myocyte-fibroblast couplings on model *#3* (noER+20fib).
https://youtu.be/f8_QJSOsqQ4

this case fibroblasts act as electrical sources, since current flows from fibroblasts to surrounding myocytes.
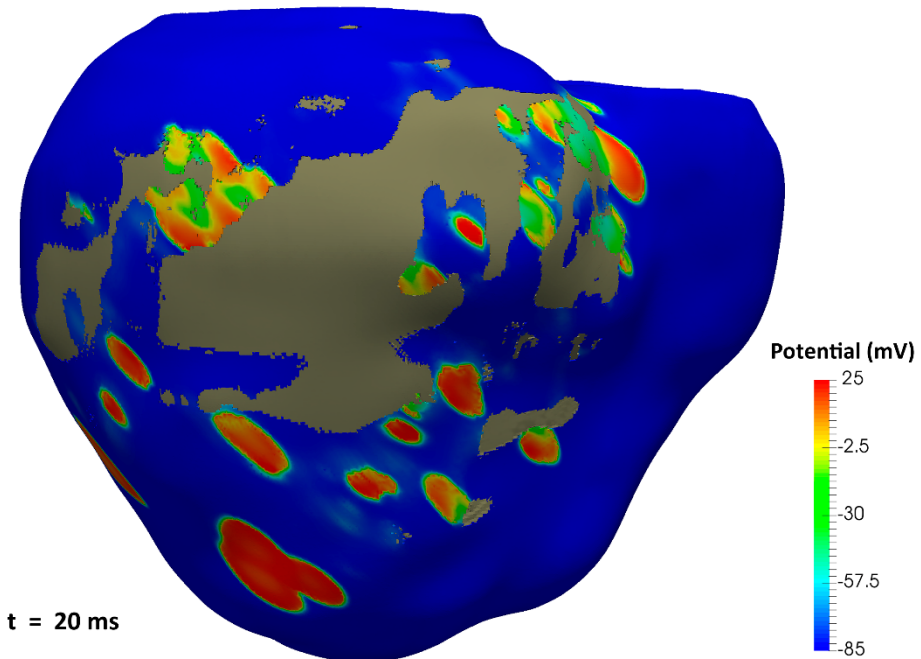
Figure 7.4. Multiple spontaneous activations during the stabilization process of myocyte-fibroblast electrotonic couplings. Posterior view of the 3D ventricular model corresponding to a computational simulation on model *#3* (noER+20fib), without any stimulus applied on the model. It corresponds to the potential map at 20 ms of simulation, showing multiple foci of ectopic-like activations generated due to electrotonic interaction between myocytes and fibroblasts in the region corresponding to the BZ. The large grey region in the 3D ventricular model represents the infarct scar, which constitutes an obstacle for electrical propagation since it was modelled as a non-excitable tissue (electrical insulator).

After such initial multi-foci ectopic-like activation (Figure 7.4), all myocyte-fibroblast couplings remained stable in absence of stimulation. In Figure 7.5, it is observed how the abrupt transitions in resting potentials around the fibrotic patches within the BZ at the beginning of the simulation on model *#3* (noER+20fib), turns into much smoother potential gradients in the steady state reached as a result of that stabilization process. Therefore, the final state of these stabilization simulations later served as a starting point (i.e., initial state for t = 0 ms) for the following ones in our simulation pipeline.
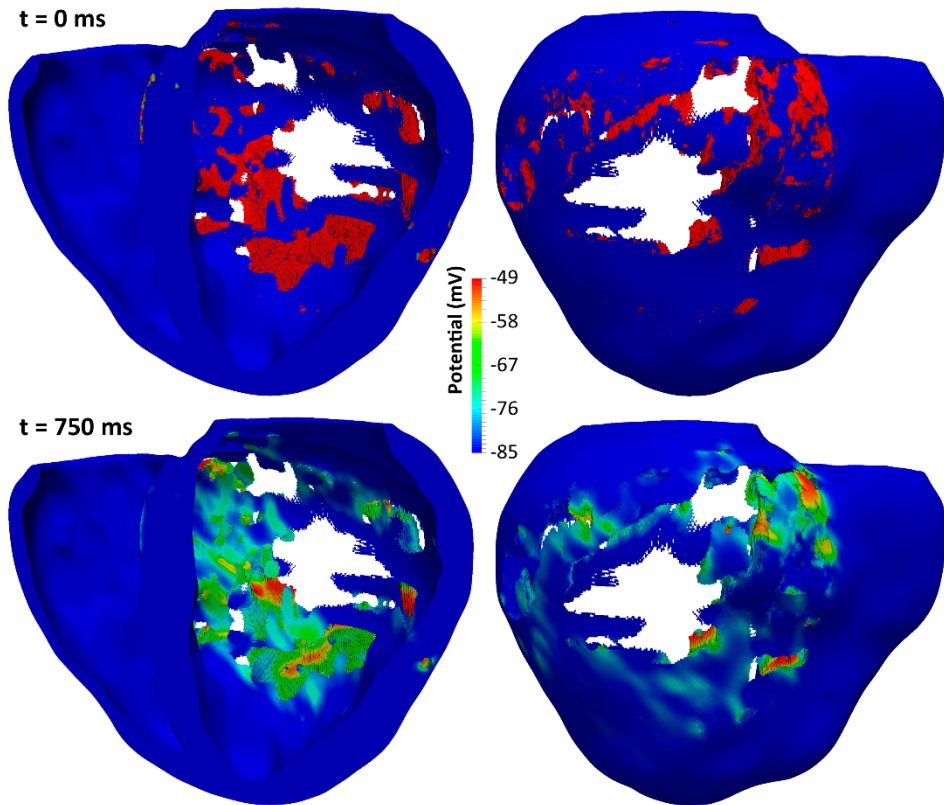
Figure 7.5. Steady state after the stabilization of myocyte-fibroblast couplings on model *#3* (noER+20fib). Top row shows potential maps at the beginning of the simulation (t = 0 ms), while bottom row displays the same maps after the stabilization (t = 750 ms), when steady state has already been reached. Both rows show an anterior view of a coronal cross-section (4-chamber plane) of ventricular model (*left panel*) that exposes the endocardium of LV posterior wall and a posterior view of the model (*right panel*) showing the epicardial surface. Note that the tissue corresponding to the infarct scar was removed to allow a better visualization of the stabilization process of myocyte-fibroblast coupling within the intramural layers. Comparing the potential maps on both rows, one can appreciate a notable difference in resting potentials in those regions infiltrated with patchy fibrosis (regions with elevated resting potentials). At the beginning of the simulation (*top row*), there are abrupt transitions around the fibrotic patches, showing two strongly differentiated resting potential levels, turning into much smoother potential gradients in steady state after the stabilization (*bottom row*).

7.5.2. Simulations of sinus activation

7.5.2.1. Simulations at the organ level

In this section, we present and compare the results of simulations of CARTO®-derived sinus activation, performed with all versions of the 3D ventricular model. The videos corresponding to each of those simulations are available [online](#)[19], all of which show the propagation of the last of the six heartbeats simulated in sinus rhythm at a BCL of 800 ms (i.e., 75 bpm).

Features of sinus activation simulated at the organ level

Figure 7.6 and Figure 7.7 display activation maps (LATs) corresponding to the propagation of the sixth heartbeat simulated on model *#1* (noER+00fib) and model *#8* (ER+30fib), respectively. Note that they are the two model versions that represent the two opposite poles in relation to the remodelling level included in the BZ. That is, models *#1* (noER+00fib) and *#8* (ER+30fib) were respectively modelled with the lowest and the highest level of BZ remodelling, both electrical and structural (fibrosis). As shown, activation and propagation patterns are very similar for these two versions of the ventricular model, and also for the rest of them (see the [videos](#)). In both cases, as well as for the rest of model versions, activation begins at the endocardial surface of the LV side of the septum and the latest activated regions mainly concentrate around the infarct scar, matching the tissue corresponding to the BZ. In all simulations (with all model versions), 90% of excitable ventricular tissue (excluding the non-conducting infarct scar) was activated in less than 100 ms, raising up to 95% of tissue in less than 120 ms. However, certain regions of the BZ show very late activation times, with the latest activated tissue corresponding to the epicardial isthmus in all cases (see Figure 7.6[d] and Figure 7.7[d]). In the worst case (model *#8* – ER+30fib), the activation in such isthmus lasted up to 296 ms (see Figure 7.7 and Table 7.2). Therefore, activation maps from simulations of CARTO®-derived sinus activation were very similar for all versions of the ventricular model. The only remarkable difference between models was the

---

[19] **Sinus activation.** Videos corresponding to the simulations of CARTO®-derived sinus activation.   https://www.youtube.com/playlist?list=PL98EKQIbetNobrKiaro9H3KI2FjcGpT7j

total time that tissue corresponding to the BZ took to be fully activated. The highest LAT value, located within the epicardial isthmus in all cases, ranged from 243 ms for model *#1* (noER+00fib) to 296 ms for model *#8* (ER+30fib) (see Table 7.2).
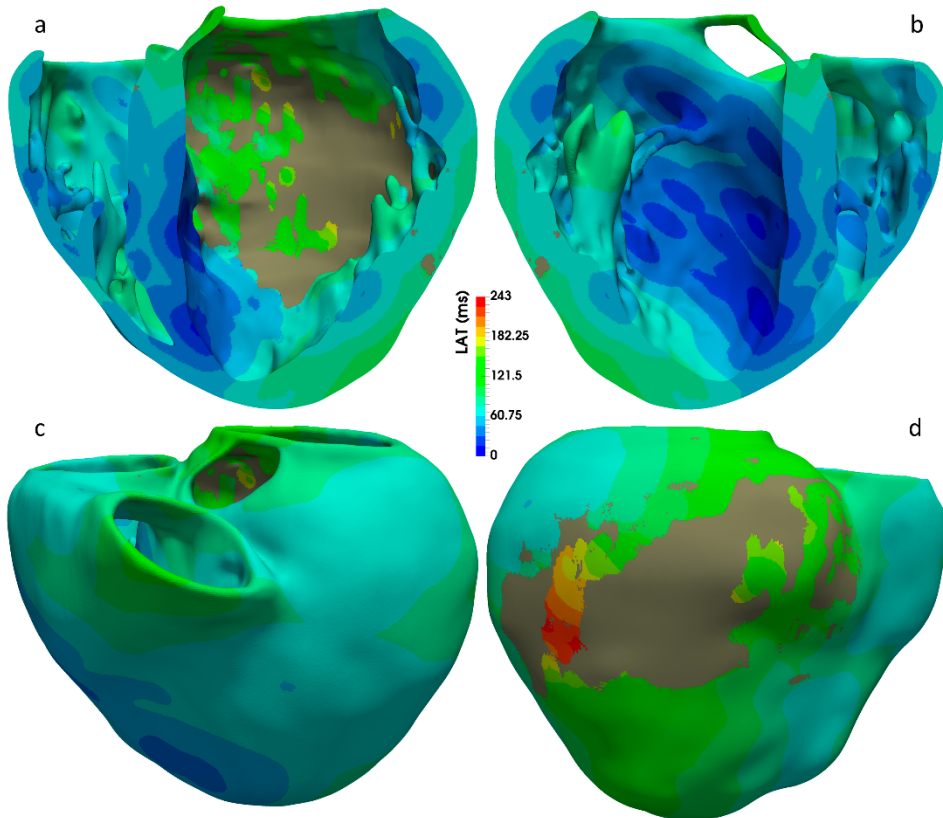
Figure 7.6. Activation maps resulting from the sixth heartbeat in simulation of CARTO®-derived sinus activation on model *#1* (noER+00fib), which is the model version with the lowest degree of BZ remodelling. Different views of the 3D ventricular model, showing anterior (*a*) and posterior (*b*) views of a coronal cross-section (4-chamber plane) that exhibit endocardial and transmural activation, as well as anterior (*c*) and posterior (*d*) views of the whole model displaying epicardial activation. The earliest activated regions are on the LV side of septum, while the latest one is the epicardial isthmus crossing the infarct scar. The grey region in the model corresponds to the infarct scar modelled as a non-conducting tissue (electrical insulator).

Factors affecting the propagation in the BZ during sinus activation

Those significant differences in the delayed activation of the BZ can be appreciated in the plots of Figure 7.8, which represent the evolution of the activation of BZ tissue for all model versions during the last beat in sinus activation simulations. In all cases, those plots show a quite similar linear evolution of BZ activation at the beginning, followed by a final segment in which activation times increase exponentially, with notable differences between distinct model versions. Such differences in the final phase of the activation were caused by both electrical remodelling and the presence of patchy fibrosis in the BZ. Note that electrical remodelling promoted longer activation delays than fibrosis, as quantitatively summarized in Table 7.2. Anyhow, those longer delays in model versions including electrical remodelling (models *#5-8*) were expected. Remember that the set of reduced conductivities used in the BZ made CVs in that region decrease to 25% with respect to healthy tissue (i.e., 75% slower conduction) because of partial inactivation of peak sodium current (I_{Na}) associated with the electrical remodelling included in models *#5-8*. By contrast, the absence of electrical remodelling (i.e., no inactivation of I_{Na}) enabled a slightly better conservation of CVs for the same set of conductivity values, so that in models *#1-4* CVs in the BZ were only reduced to 35% with respect to healthy tissue (i.e., 65% slower conduction).

Nevertheless, neither electrical remodelling nor fibrosis had an impact on activation as large as the one caused by the different CVs used in the BZ (different conductivities, actually). As expected, the data collected in Table 7.3 confirm the great influence on the activation delays in the BZ resulting from the reduction in CVs in that region. Thus, compared with electrical remodelling and presence of patchy fibrosis, the specific set of values chosen for CVs in the BZ was the factor that most deeply affected propagation in the BZ. This can be appreciated in Figure 7.8, where the three distinct plots for model *#6* (ER+10fib), with different values for CVs in the BZ, notably differ from each other.

Another important effect, specifically caused by the presence of patchy fibrosis in the BZ, was the generation of patches of non-activated tissue (see black patches in Figure 7.7). Such regions were never activated (transmembrane
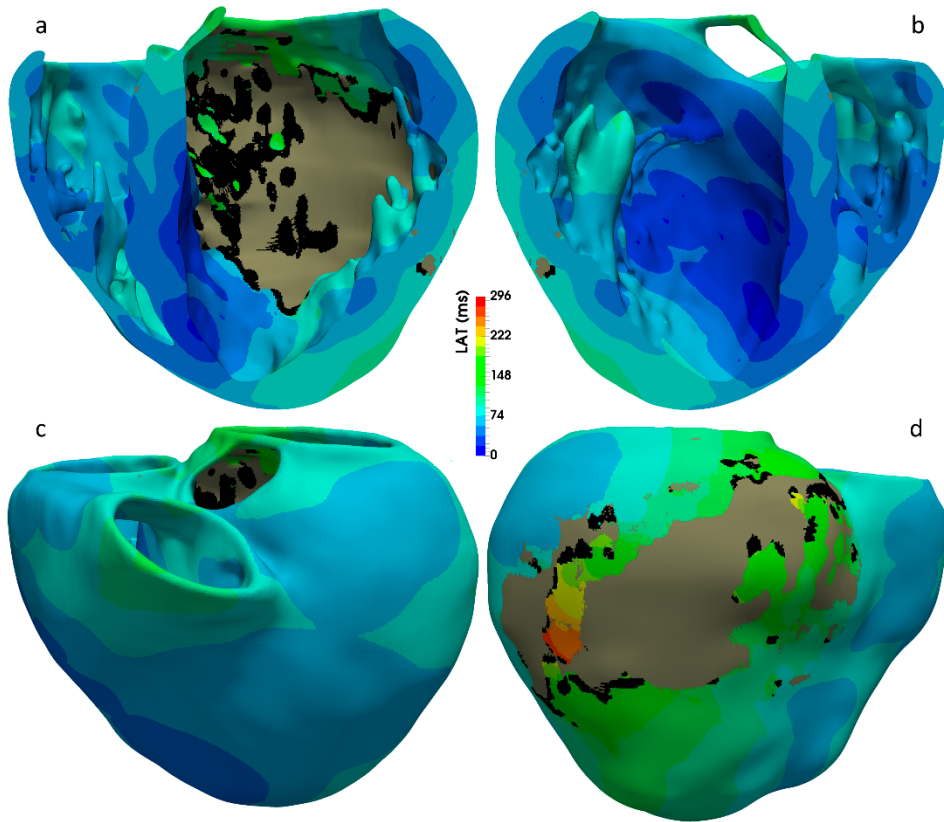
Figure 7.7. Activation maps resulting from the sixth heartbeat in simulation of CARTO®-derived sinus activation on model *#8* (ER+30fib), which is the model version with the highest degree of BZ remodelling. Different views of the 3D ventricular model, showing anterior (*a*) and posterior (*b*) views of a coronal cross-section (4-chamber plane) that exhibit endocardial and transmural activation, as well as anterior (*c*) and posterior (*d*) views of the whole model displaying epicardial activation. The earliest activated regions are on the LV side of septum, while the latest one is the epicardial isthmus crossing the infarct scar. The grey region in the model represents the infarct scar modelled as a non-conducting tissue (electrical insulator). Black patches correspond to not activated pieces of tissue due clustered accumulations of fibrotic elements (mesh elements modelled as fibroblasts) within the BZ.

potential did not reach the level of 0 mV) because of clustered accumulations of fibrotic elements modelled as fibroblasts, which caused blocks of the electrotonic propagation within those fibrotic patches due to the rapid decrease of propagated potentials. Although there are subtle differences depending on the presence of electrical remodelling and the degree of reduction in CVs, in all cases

the percentage of non-activated tissue is slightly lower than fibrosis level within the BZ (see Table 7.2 and Table 7.3). This indicates that only a little number of fibroblasts were depolarized (i.e., their transmembrane potentials exceed the level of 0 mV) when they were reached by the propagation wavefront.
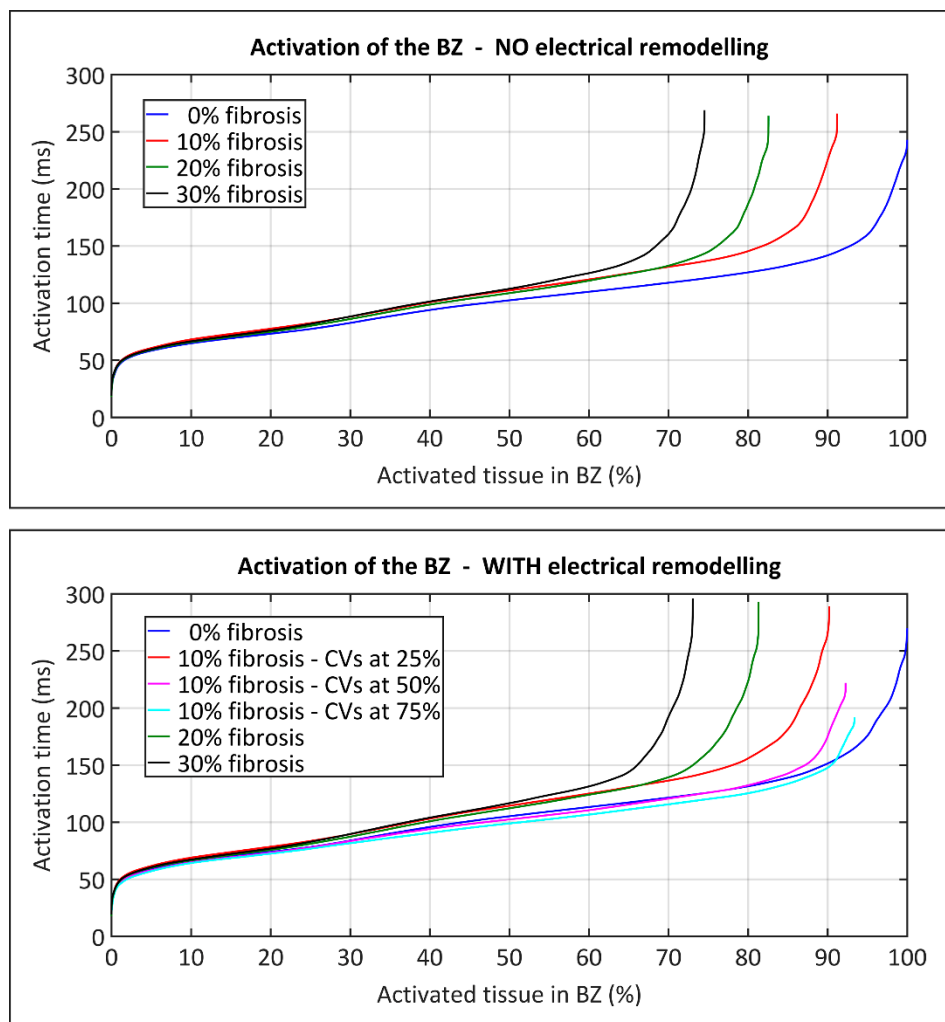
Figure 7.8. Evolution of the activation of tissue corresponding to the BZ, resulting from the sixth heartbeat in simulations of sinus activation, performed with all versions of our 3D ventricular model. Note that in those model versions including any level of patchy fibrosis in the BZ, the portion of successfully activated tissue could not reach 100% due to accumulations of fibrotic elements (mesh elements modelled as fibroblasts) within the BZ.

Repolarization dispersion around the infarct scar during sinus activation

Besides the activation maps, we also represented APD maps of all simulations of sinus activation to study the repolarization patterns. Figure 7.9 and Figure 7.10 show the APD maps resulting from the sixth heartbeat in simulations of CARTO®-derived sinus activation on all model versions with CVsBZ-25%. As observed, those APD maps reveal a remarkable repolarization dispersion (or APD heterogeneity) around the infarct scar, caused by both electrical remodelling and the presence of fibrosis in the BZ.

		Fibrosis level in the BZ			
		0%	10%	20%	30%
No EP remod. in the BZ	*Max. LAT*	243 ms	264 ms	266 ms	269 ms
	% of BZ activated	100%	91.2%	82.5%	74.5%
With EP remod. in the BZ	*Max. LAT*	270 ms	289 ms	293 ms	296 ms
	% of BZ activated	100%	90.2%	81.3%	73%

Table 7.2. Activation of the BZ in CARTO®-derived sinus activation simulations, performed with all model versions with CVsBZ-25%. This table gathers information about the total time (*max. LAT*) that electrical propagation took to fully activate the BZ tissue, as well as the percentage of such tissue (*% of BZ activated*) that was successfully activated (i.e., depolarized) depending on fibrosis level in the BZ.

	CVs in the BZ with respect to CVs in healthy tissue		
	CVsBZ-25%	CVsBZ-50%	CVsBZ-75%
Max. LAT	289 ms	222 ms	192 ms
% of BZ activated	90.2%	92.2%	93.4%

Table 7.3. Activation of the BZ in CARTO®-derived sinus activation simulations, performed with model *#6* (ER+10fib) and different values for CVs in the BZ: CVsBZ-25%, CVsBZ-50% and CVsBZ-75%. This table collects information about the total time (*max. LAT*) that electrical propagation took to fully activate the BZ tissue, as well as the percentage of such tissue (*% of BZ activated*) that was successfully activated (i.e., depolarized) depending on the degree of reduction in CVs of the BZ.

The incorporation of electrical remodelling, described in Chapter 6 (see section 6.1.3.1), transformed the BZ into a region where APDs were longer than

in healthy tissue. As expected, this affected the repolarization patterns, since it created regions with longer APDs around the infarct scar, thus increasing repolarization dispersion in that region of the ventricular model. This effect can be well appreciated in Figure 7.9 by comparing the APD maps from model *#1* (noER+00fib) and model *#5* (ER+00fib), or from model *#2* (noER+10fib) and model *#6* (ER+10fib).
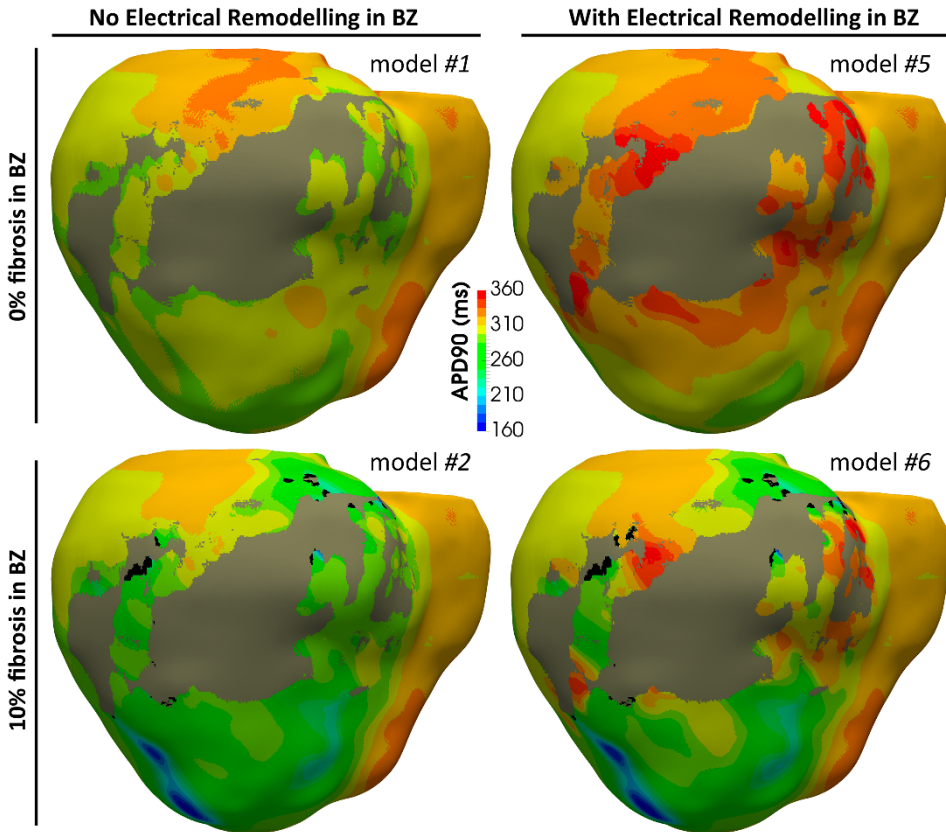
Figure 7.9. APD maps showing the epicardial surface of the posterior wall of ventricular model, exhibiting notable differences in repolarization patterns resulting from sinus activation simulations between four versions of the model, combining two different levels of image-based patchy fibrosis (0% and 10%) with and without electrical remodelling in the BZ. These maps correspond to the sixth heartbeat in simulations of CARTO®-derived activation sequence at BCL of 800 ms (75 bpm). Both electrical remodelling and the presence of patchy fibrosis in the BZ affected APDs in that region, creating repolarization dispersion around the infarct scar. The little black regions in the two model versions including 10% fibrosis in BZ (*bottom row*) correspond to patches of not activated tissue due to accumulations of fibrotic elements (fibroblasts).
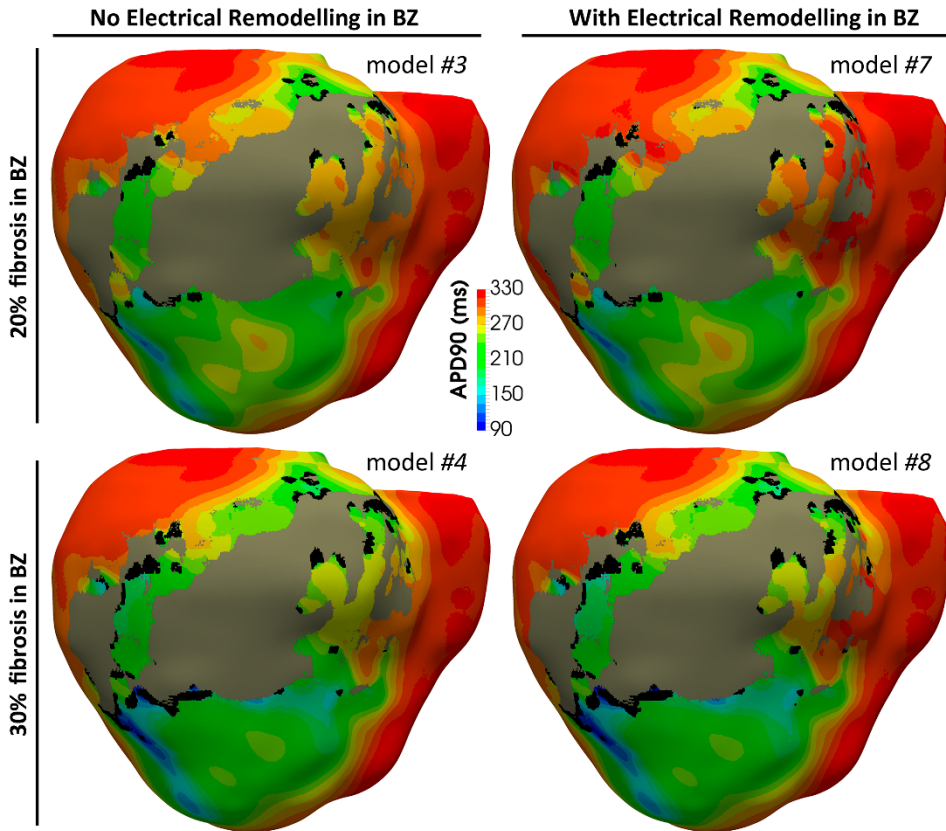
Figure 7.10. APD maps showing the epicardial surface of the posterior wall of ventricular model, exhibiting notable differences in repolarization patterns resulting from sinus activation simulations between four versions of the model, combining two different levels of image-based patchy fibrosis (20% and 30%) with and without electrical remodelling in the BZ. These maps correspond to the sixth heartbeat in simulations of CARTO®-derived activation sequence at BCL of 800 ms (75 bpm). Both electrical remodelling and the presence of patchy fibrosis in the BZ affected APDs in that region, creating repolarization dispersion around the infarct scar. The increase of fibrosis level progressively shortens APDs in certain regions of the BZ, also expanding the patches of non-activated tissue (*black regions*) due to accumulations of fibrotic elements (fibroblasts).

In contrast, the existence of patchy fibrosis within the BZ caused the opposite effect, as it induced APD reduction around the fibrotic patches, what also increased the dispersion in repolarization patterns. This was caused by the electrotonic load exerted on myocytes by the adjacent fibroblasts, which acted as electrical sinks leading to a faster repolarization of such myocytes and,

consequently, to shorter APDs. See, for instance, the effect of introducing 10% patchy fibrosis in the BZ on APD maps in Figure 7.9. The higher the fibrosis level within the BZ, the greater the APD reduction in such region and, consequently, the greater the repolarization dispersion generated around the infarct scar. One can clearly note this effect by observing the evolution of APD maps as a function of fibrosis level within the BZ in Figure 7.9 and Figure 7.10. The amount and size of patches of non-activated tissue due to clustered accumulations of fibrotic elements also increased depending on the fibrosis level in the BZ (see black patches on APDs maps in Figure 7.9 and Figure 7.10).

Therefore, the combination of those two opposite effects (APD increase caused by electrical remodelling and APD decrease induced by patchy fibrosis) led to strong dispersion in repolarization patterns in the region of BZ, which might result in a considerable increase in the arrhythmogenic potential of the viable but remodelled tissue that surrounds the infarct scar (Hegyi et al., 2018; Kléber and Rudy, 2004; Laurita and Rosenbaum, 2000). Furthermore, probably due to the morphological (geometrical) features of the epicardial isthmus, such APD heterogeneity appeared to be especially important around the two terminal ends of that structure, as appreciated in APD maps from models *#5* (ER+00fib) and *#6* (ER+10fib) (see Figure 7.9) or from models *#3* (noER+20fib) and *#7* (ER+20fib) (see Figure 7.10).

7.5.2.2. Simulations at the torso level. Simulated ECGs

Regarding the simulations of cardiac EP at the torso level, Figures 7.11, 7.12 and 7.13 show simulated ECGs computed from precordial leads, obtained with all versions of the ventricular model, also showing patient's ECG to compare it with simulated ones. We obtained those ECG signals by computing across the 3D torso model the extracellular potentials (see section 7.4) resulting from the sixth heartbeat in simulations of CARTO®-derived sinus activation. As observed in those three figures, our body level approach (with ventricular model stimulated by CARTO®-derived activation sequence) allowed obtaining ECGs in sinus rhythm with precordial leads showing good signal correlation with real ECGs (see legends in figures), as well as very similar R-wave progression. Signal

correlation between simulated and real ECGs ranged from 80% to 96% for V1 (Figure 7.11), V4 (Figure 7.12), V5 and V6 (Figure 7.13). However, these values fell to around 70% for V2 (Figure 7.11) and V3 (Figure 7.12), in which the QRS complex presented a biphasic polarity in the real ECG that simulated signals could not properly reproduce. V2 and V3 showed a little negative S wave in simulated signals that is much less pronounced than in real ones. Nevertheless, the width of QRS complex in simulated signals was highly similar to that of real ECG in all precordial leads.

Influence of BZ remodelling on simulated ECG in sinus rhythm

Comparing simulated ECGs resulting from model versions with and without electrical remodelling in the BZ (see Figures 7.11, 7.12 and 7.13), inclusion or absence of such kind of remodelling did not appear to have an important impact on simulated ECGs in sinus rhythm. Conversely, the presence of fibrosis in the BZ did cause a significant ST segment deviation in the simulated signals, whose polarity matched that observed in real ECGs in all precordial leads. See ST elevation in V1 (Figure 7.11) or depression in V5 and V6 (Figure 7.13), for instance. This is the manifestation at the torso level (i.e., on simulated ECGs) of the early repolarization of the tissue around the infarct scar induced by the fibroblasts infiltrated within the BZ. As observed in Figure 7.14, in model *1* (noER+00fib) repolarization has not begun yet at instant t = 250 ms. By contrast, at the same time instant, model versions including any fibrosis level in the BZ (models *2,3,4*) do show pieces of tissue around the infarct scar in which repolarization process has already begun, thus giving rise to a ST segment deviation in simulated ECGs. Furthermore, Figure 7.14 shows that the higher the fibrosis level included in the BZ, the earlier the start of repolarization process around the infarct scar because of a stronger electrotonic load caused by a larger amount of infiltrated fibroblasts that act as electrical sinks.
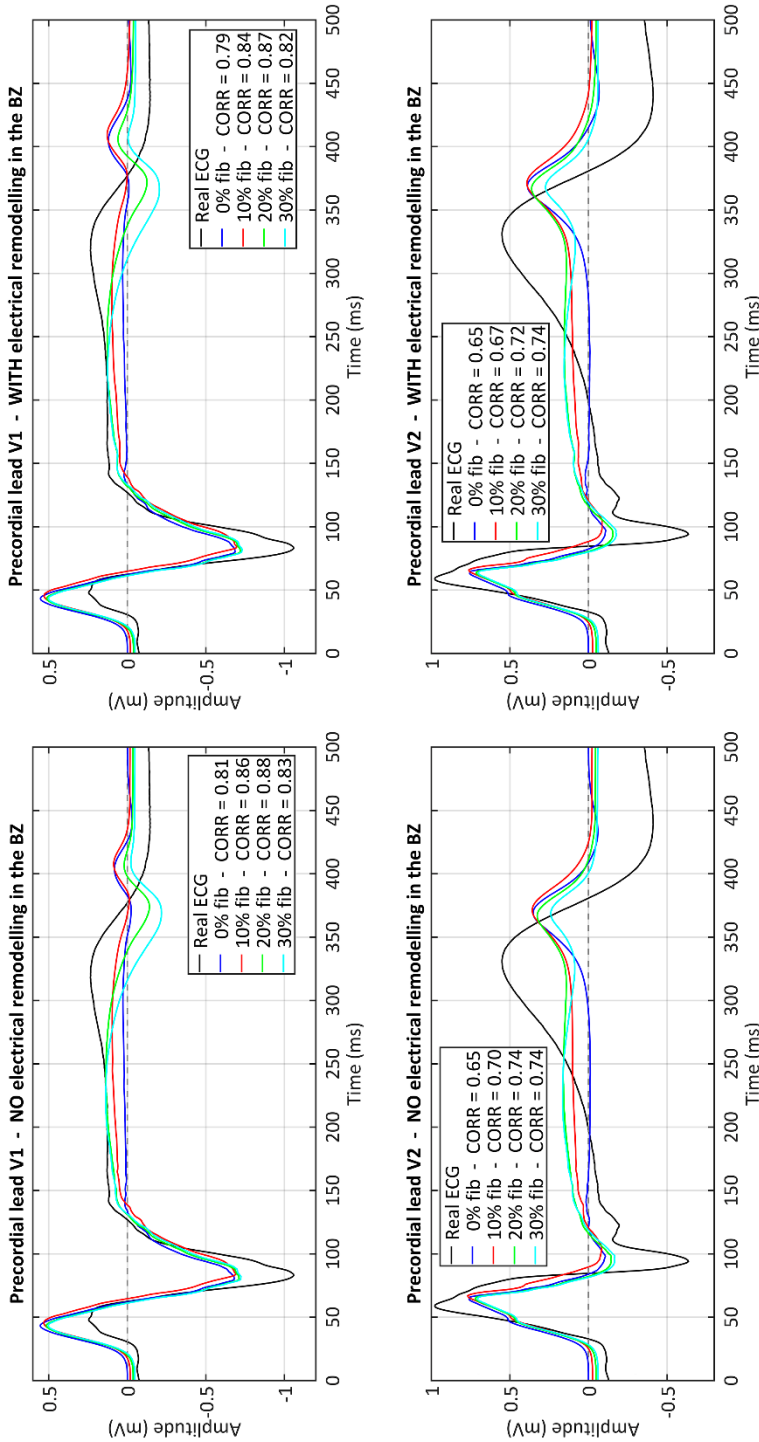
Figure 7.11. Simulated ECGs resulting from the sixth heartbeat in simulations of CARTO®-derived sinus activation. Signals corresponding to V1 and V2 precordial leads, comparing real ECG (*black*) with ECGs simulated by means of all model versions with (*right panels*) and without (*left panels*) electrical remodelling and CVsBZ-25%. Cross-correlation coefficients (*CORR*) between real and simulated signals are included in the legend of every plot.
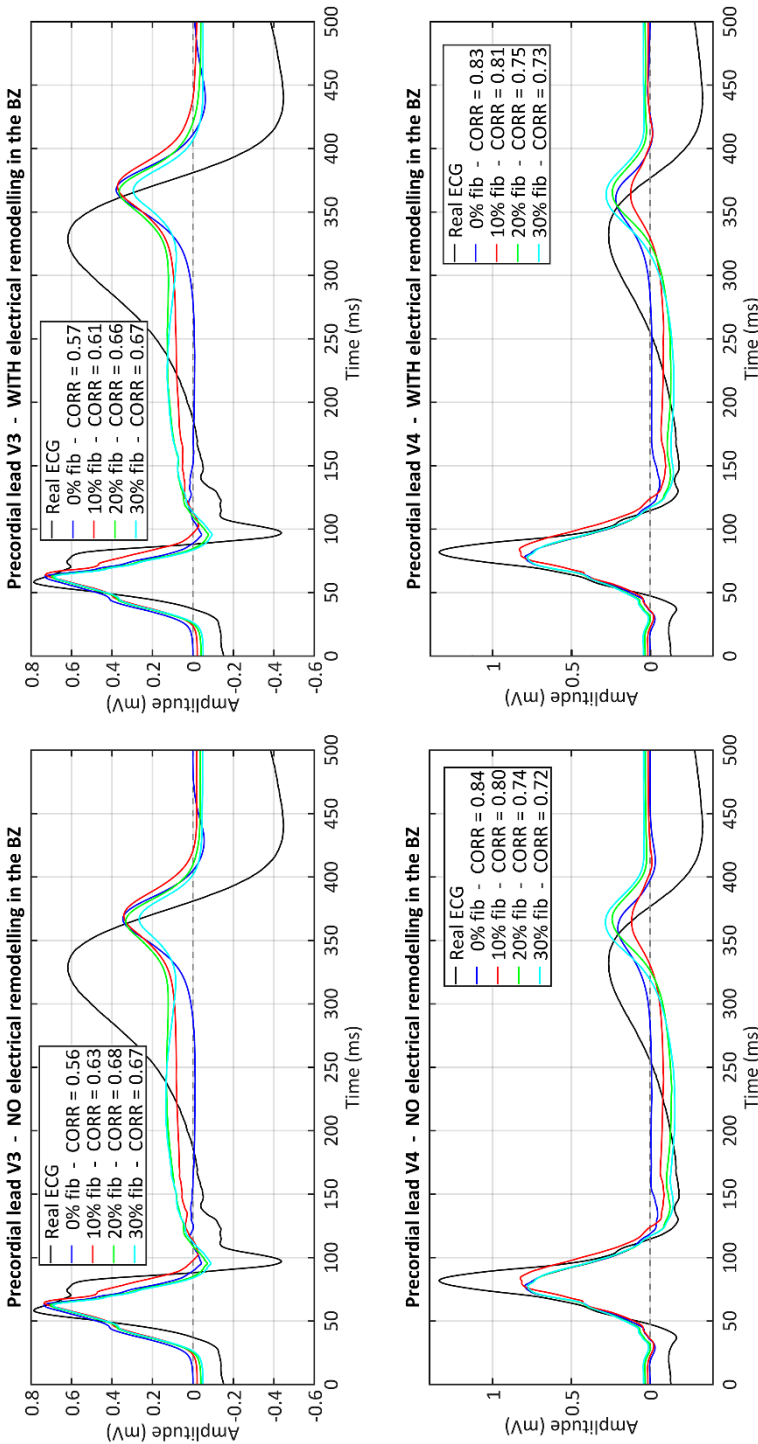
Figure 7.12. Simulated ECGs resulting from the sixth heartbeat in simulations of CARTO®-derived sinus activation. Signals corresponding to V3 and V4 precordial leads, comparing real ECG (*black*) with ECGs simulated by means of all model versions with (*right panels*) and without (*left panels*) electrical remodelling and CVsBZ-25%. Cross-correlation coefficients (*CORR*) between real and simulated signals are included in the legend of every plot.
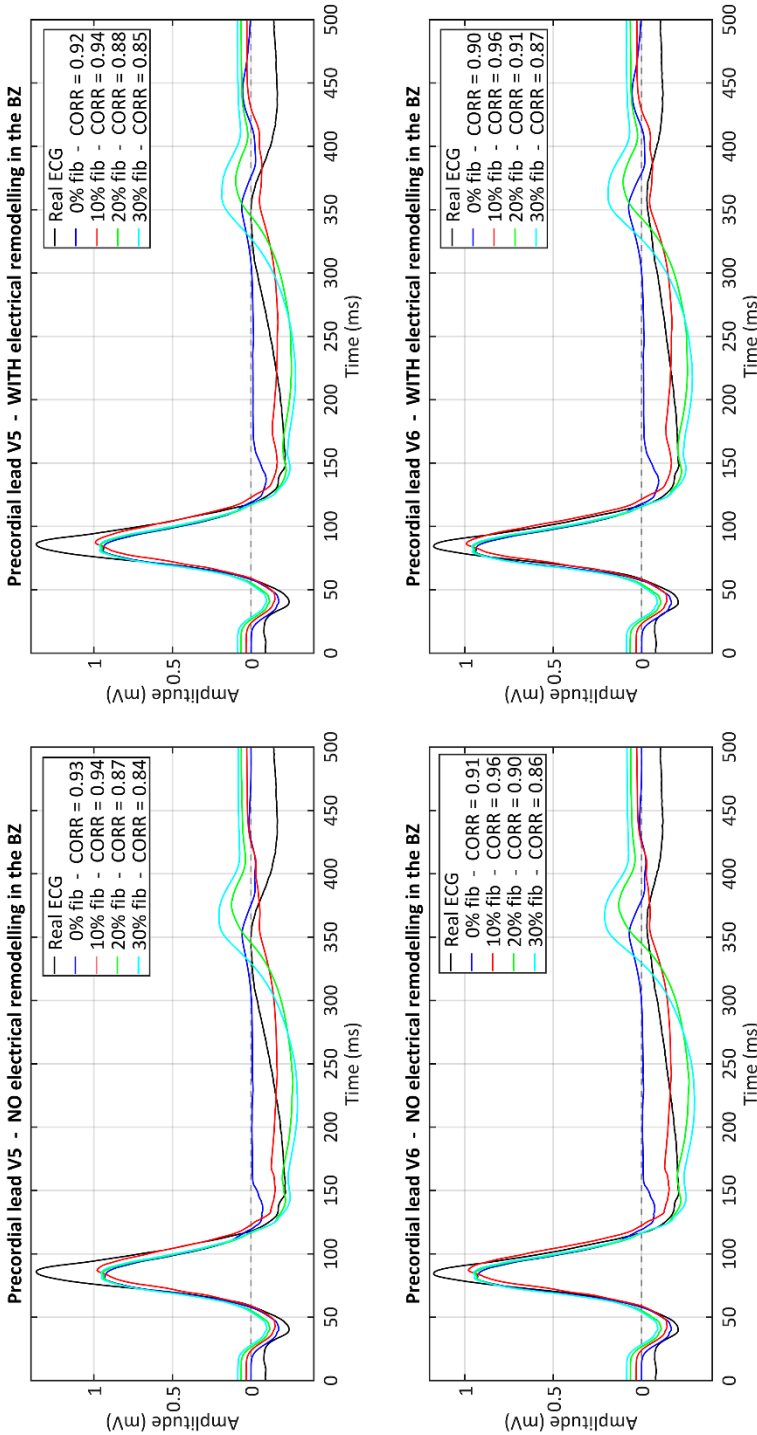
Figure 7.13. Simulated ECGs resulting from the sixth heartbeat in simulations of CARTO®-derived sinus activation. Signals corresponding to V5 and V6 precordial leads, comparing real ECG (*black*) with ECGs simulated by means of all model versions with (*right panels*) and without (*left panels*) electrical remodelling and CVsBZ-25%. Cross-correlation coefficients (*CORR*) between real and simulated signals are included in the legend of every plot.

The most important difference between real and simulated ECGs, which affected all precordial leads, was related to the repolarization phase. There was a good coincidence in T wave polarity between real and simulated ECGs in all precordial leads, except for V1 in which simulated signals showed a biphasic T wave that differed from the real one (see Figure 7.11). However, in all precordial leads from all model versions, simulated ECGs showed a delayed T wave with respect to real signals. This is most probably due to the fact that the waveform of the T wave strongly depends in the regional differences in APD, and we must remember that the simulated AP waveforms were not patient-specific. As in the case of ST segment, electrical remodelling in the BZ seemed to cause no significant impact on the repolarization phase of simulated ECGs, that is, on the T wave of simulated signals. Nonetheless, again the presence of fibrosis in the BZ did have certain effect on the T wave magnitude, which was particularly notable on V1 (Figure 7.11), V4 (Figure 7.12), V5 and V6 (Figure 7.13).

Impact of CVs in the BZ on simulated ECGs in sinus rhythm

Additionally, aiming to assess the impact of changes in CVs in the BZ on simulated ECGs, we computed the ECGs resulting from our sinus rhythm simulation on model *6* (ER+10fib) with different sets of values for CVs in the BZ. Figure 7.15 and Figure 7.16 show the real ECG at precordial leads compared with simulated signals obtained from the sixth heartbeat in simulations of CARTO®-derived sinus activation on model *6* (ER+10fib) with CVsBZ-25%, CVsBZ-50% and CVsBZ-75%. As observed in such figures, those changes in CVs had a slight effect on the simulated signals, as manifested by insignificant changes in coefficients of signal correlation for all precordial leads (see plots legends). When we increased CVs in the BZ from 25% to 50% or 75% with respect to healthy tissue, it resulted in a subtle reduction in QRS complex width in the simulated signals for all precordial leads, with no notable differences between models with CVsBZ-50% and CVsBZ-75%. Moreover, only on V2 and V3 (Figure 7.15) distinct values for CVs in the BZ appeared to have a slight impact on ST segment deviation. With respect to repolarization phase, the increase of CVs in the BZ slightly affected T wave magnitude, again with no significant differences between models with CVsBZ-50% and CVsBZ-75%.

model *#1*
[no ER + 0% fibrosis in BZ]

model *#2*
[no ER + 10% fibrosis in BZ]

model *#3*
[no ER + 20% fibrosis in BZ]

model *#4*
[no ER + 30% fibrosis in BZ]

Potential (mV)
25
-2.5
-30
-57.5
-85
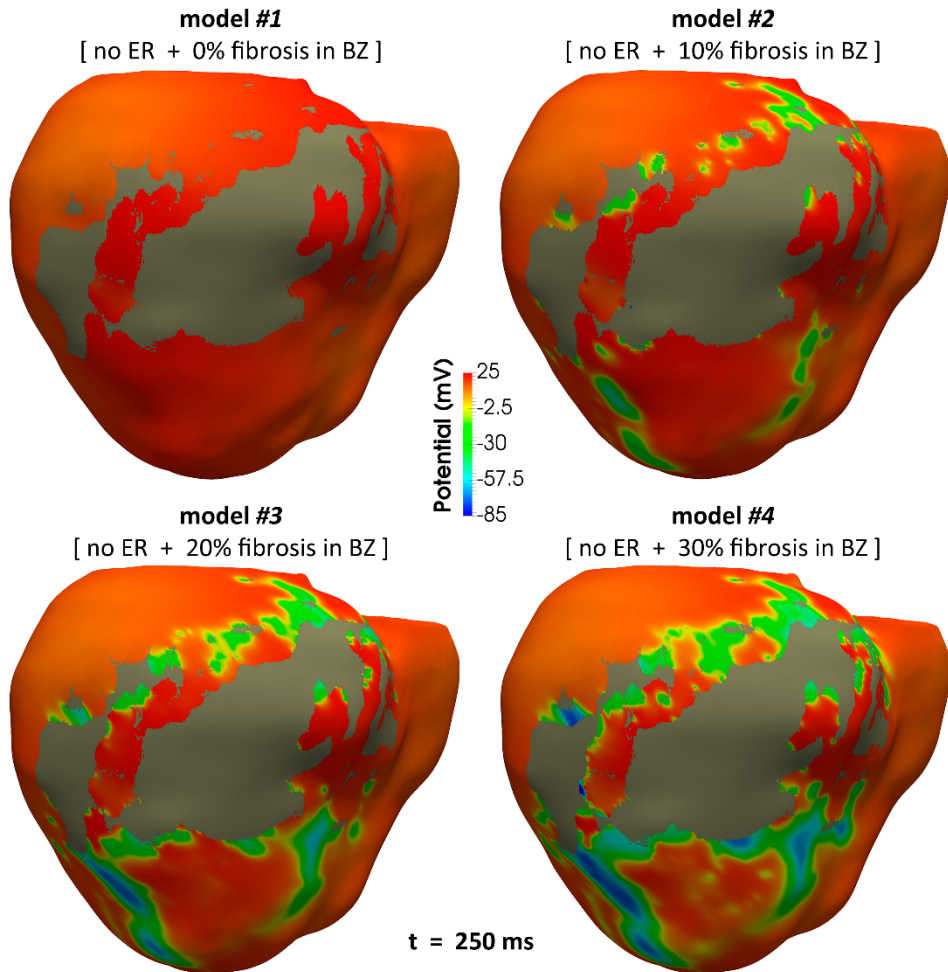
t = 250 ms

Figure 7.14. Potential maps corresponding to time instant t = 250 ms in simulations of CARTO®-derived sinus activation, performed on the four versions of ventricular model that did not include electrical remodelling (ER) in the BZ (models *#1,2,3,4*). As observed in these posterior views of the ventricular model, the higher the level of image-based patchy fibrosis included in the BZ, the earlier the repolarization of the BZ tissue that surrounds infarct scar. The grey region in the model represents the infarct scar modelled as a non-conducting tissue (electrical insulator).
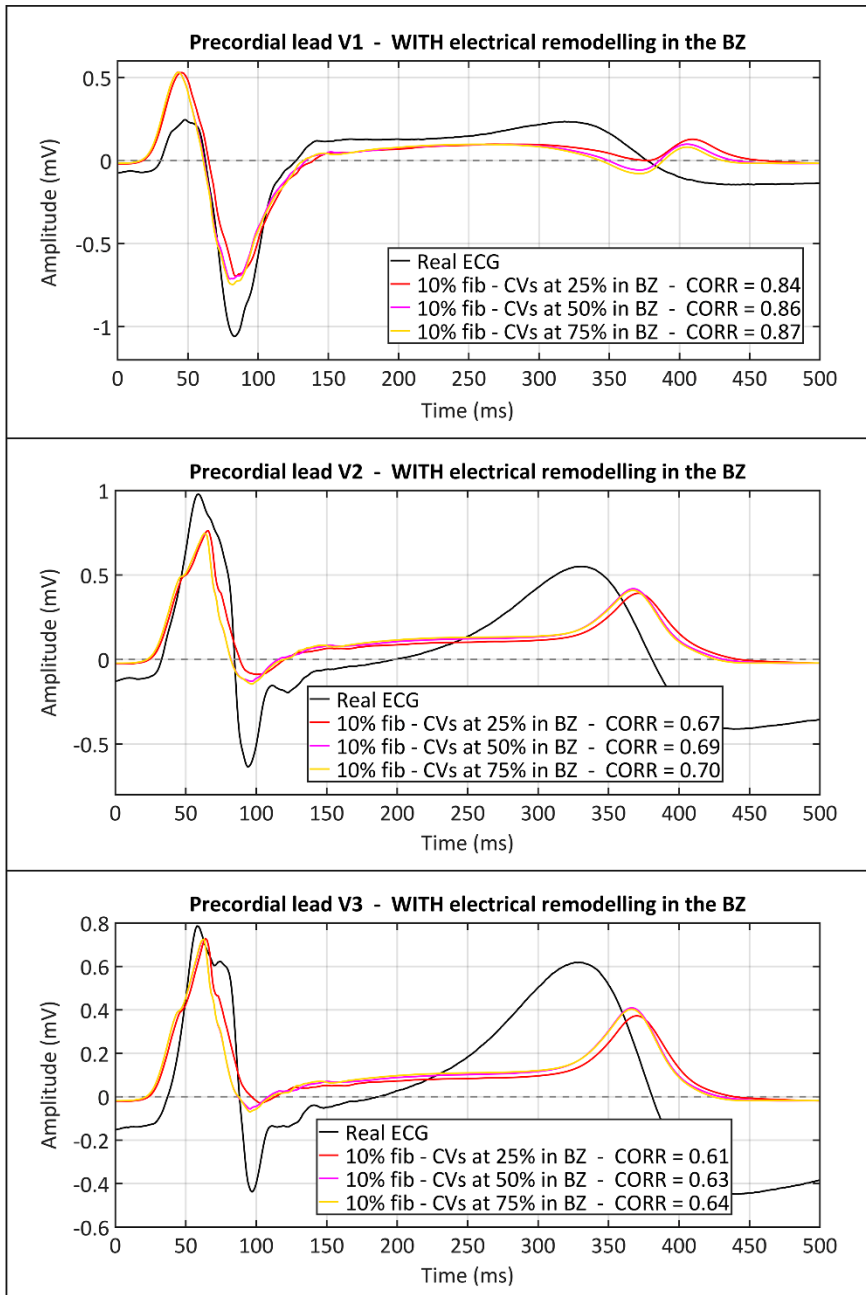
Figure 7.15. Simulated ECGs resulting from the sixth heartbeat in simulations of CARTO®-derived sinus activation. Signals corresponding to V1, V2 and V3 precordial leads, comparing real ECG (*black*) with ECGs simulated by means of model *#6* (ER+10fib) with CVsBZ-25%, CVsBZ-50% and CVsBZ-75%. Cross-correlation coefficients (*CORR*) are included in the legend of every plot.
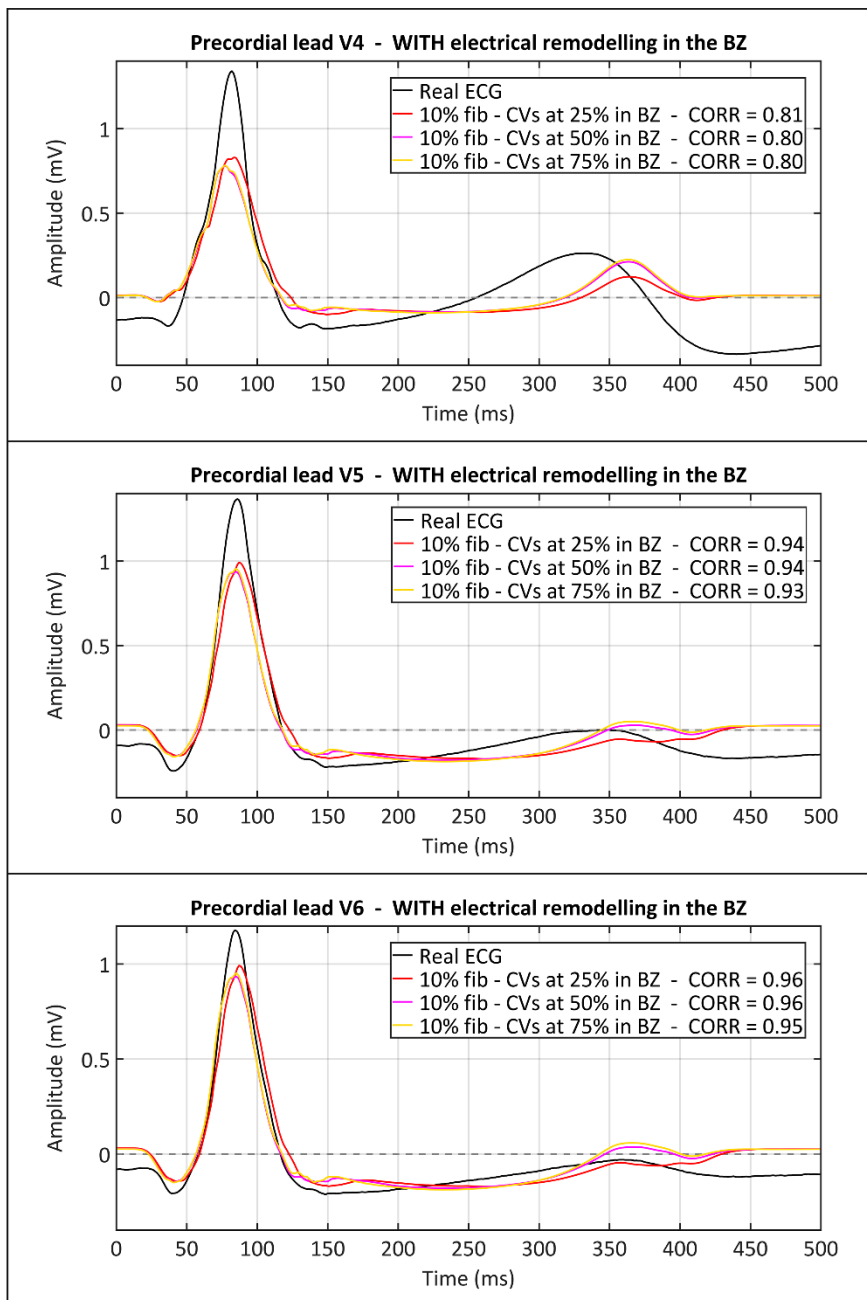
Figure 7.16. Simulated ECGs resulting from the sixth heartbeat in simulations of CARTO®-derived sinus activation. Signals corresponding to V4, V5 and V6 precordial leads, comparing real ECG (*black*) with ECGs simulated by means of model *#6* (ER+10fib) with CVsBZ-25%, CVsBZ-50% and CVsBZ-75%. Cross-correlation coefficients (*CORR*) are included in the legend of every plot.

7.5.3. *In-silico* VT inducibility tests

7.5.3.1. Simulations at the organ level

Aiming to test VT inducibility by computational simulation (*in-silico* tests), we simulated the application of PES protocols (the same protocol used at EP laboratory) on the eight different versions of our patient-specific ventricular model, from three distinct pacing sites for each model version. Table 7.4 summarizes the results of those *in-silico* tests, all of them with CVsBZ-25% (i.e., CVs 75% slower than healthy tissue). From those 24 different simulation settings (eight model versions and three pacing sites) we obtained positive VT induction in six of those scenarios and negative results in the rest of them. As shown in Table 7.4, we achieved positive VT induction with four out of the eight versions of ventricular model (models *4-7*) and only from two out of the three tested pacing sites (*endo#1* and *epi#1*). Importantly, those two pacing sites were the same points from where VT was successfully induced in the real study performed in the EP laboratory. On the contrary, the application of PES protocol from pacing site *epi#2*, which was not tested in the clinic, was unable to trigger VT on any ventricular model version. The videos corresponding to all simulations that succeeded in VT induction are available here[20], and also several videos showing simulations of VT tests with negative result are available online[21].

In-silico tests leading to positive VT induction

Regardless of the pacing site and the ventricular model version, all induced VTs showed a common mechanism that always resulted in the same infarct-related monomorphic VT. Figure 7.17 displays several potential maps corresponding to different time instants of the simulation resulting from applying PES protocol at pacing site *epi#1* on model *#6* (ER+10fib), leading to positive VT induction (see Video S2[22]). On the other hand, Figure 7.18 shows the

---

[20] **Positive VT induction.** Videos of all those simulations that resulted in a positive VT induction. www.youtube.com/playlist?list=PL98EKQIbetNq4MdEMpVkOd6bx0TQNYDXZ
[21] **Negative VT induction.** Videos of eight different simulations that resulted in a negative VT induction.
　　　www.youtube.com/playlist?list=PL98EKQIbetNpgBP8NT9CpQ2WmhqOPhSeR
[22] **Video S2.** Positive VT induction on model *#6* (ER+10fib) from pacing site *epi#1*.
　　　https://youtu.be/1LepgvOTBJI

VT induced from pacing site *endo#1* on model *#7* (ER+20fib) (see <u>Video S3</u>[23]).

Model version	Pacing Site		
	endo#1	*epi#1*	*epi#2*
model *#1* (noER+00fib)	no VT fail at 370 ms	no VT fail at 340 ms	no VT fail at 350 ms
model *#2* (noER+10fib)	no VT fail at 330 ms	no VT fail at 320 ms	no VT fail at 350 ms
model *#3* (noER+20fib)	no VT fail at 320 ms	no VT fail at 280 ms	no VT fail at 350 ms
model *#4* (noER+30fib)	no VT fail at 310 ms	Stim : S3 CI : 290 ms CL : 510 ms HR : 117 bpm	no VT fail at 350 ms
model *#5* (ER+00fib)	no VT fail at 380 ms	Stim : S2 CI : 360 ms CL : 506 ms HR : 118 bpm	no VT fail at 350 ms
model *#6* (ER+10fib)	Stim : S3 CI : 370 ms CL : 526 ms HR : 114 bpm	Stim : S2 CI : 360 ms CL : 526 ms HR : 114 bpm	no VT fail at 350 ms
model *#7* (ER+20fib)	Stim : S3 CI : 370 ms CL : 520 ms HR : 115 bpm	Stim : S2 CI : 360 ms CL : 520 ms HR : 115 bpm	no VT fail at 350 ms
model *#8* (ER+30fib)	no VT *not tested until failure*	no VT *not tested until failure*	no VT fail at 350 ms

Table 7.4. Results of *in-silico* tests of VT inducibility performed on the eight versions of ventricular model and from three distinct pacing sites, with CVsBZ-25%. In cases of positive VT induction, this table details premature stimulus (S2 or S3) responsible for the unidirectional block triggering reentrant VT, CI at which such stimulus was delivered, and CL and heart rate (HR) associated with induced VT. For cases of negative VT induction, we also include the CI at which premature stimuli failed to propagate.

---

[23] **Video S3.** Positive VT induction on model *#7* (ER+20fib) from pacing site *endo#1*.
https://youtu.be/qshQTkZPE0k
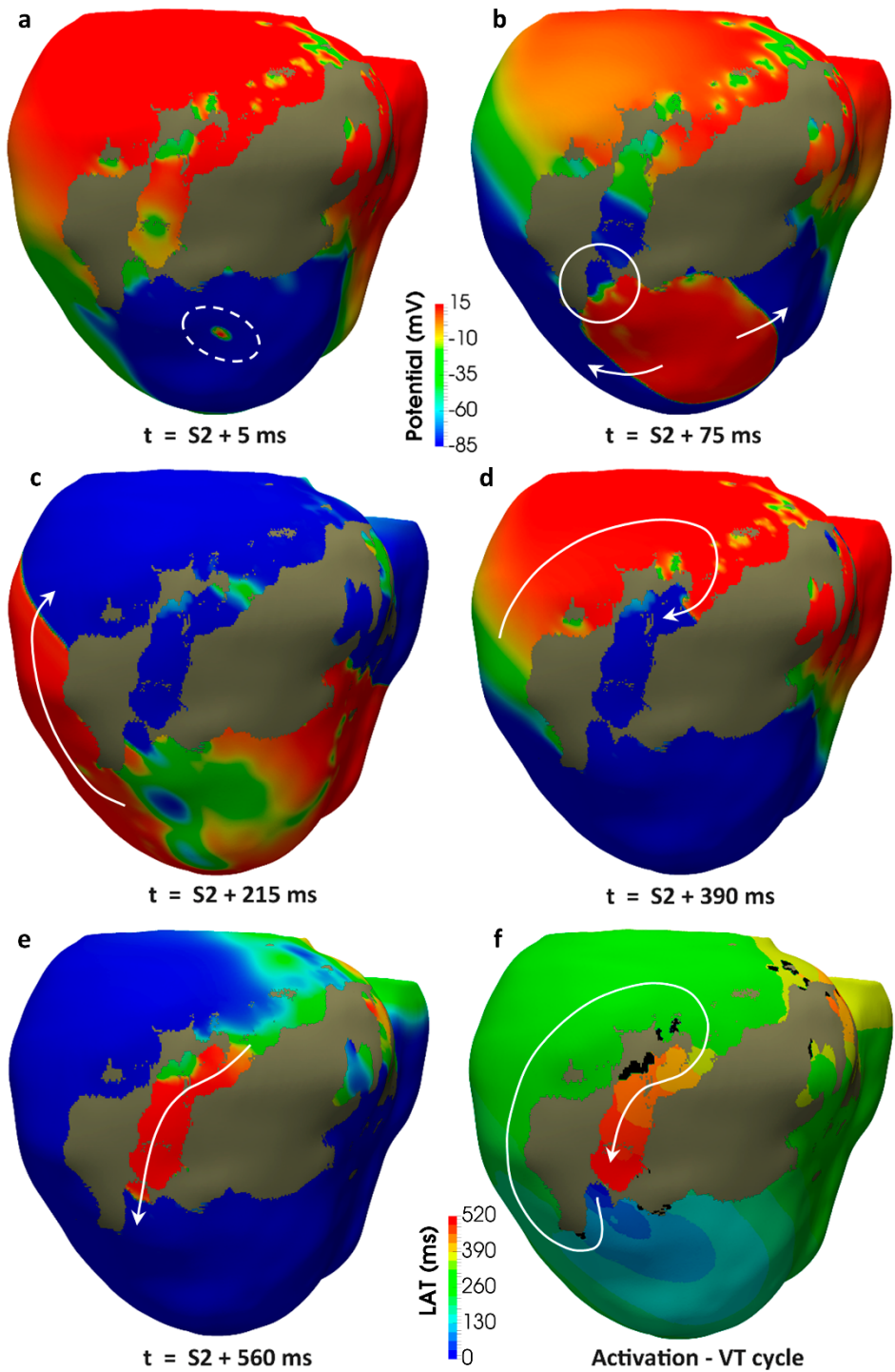
Figure 7.17. (*see description on the next page*)

Figure 7.17. (*see figure on the previous page*) Reentrant monomorphic VT induced *in-silico* on model *#6* (ER+10fib) by PES protocol delivered from pacing site *epi#1*. Posterior views of 3D ventricular model displaying potential maps at different time instants of the PES protocol leading to positive VT induction. White arrows indicate propagation direction. (*a*) After S1 phase, only one premature stimulus S2 was applied at CI of 360 ms (see dashed white ellipse). (*b*) Wavefront generated by S2 stimulus causes functional propagation block at the lower side of epicardial isthmus (see white circle), while it continues propagating all around infarct scar (grey region). (*c*) Wavefront propagates across lateral wall of LV, surrounding the scar. It travels from the lower (apical) towards the upper (basal) side of MI. Observe that propagation wavefront could not enter epicardial isthmus through its lower end because of functional propagation block, caused by S2 stimulus. (*d*) Wavefront reaches the upper side of epicardial isthmus after surrounding the infarct scar along the LV lateral wall. (*e*) Wavefront enters through the upper side of epicardial isthmus, propagating across the channel until leaving it through its lower side (unidirectional functional block). Then, it propagates again around the scar, thus triggering reentrant activity that will lead to a self-sustained monomorphic VT. (*f*) Activation map (LATs) of a cycle of induced VT, confirming that epicardial isthmus constitutes a CC that acts as structural substrate for this infarct-related monomorphic VT. For a more comprehensive analysis of this simulation, see Video S2.

Figure 7.18. (*see figure on the next page*) Reentrant monomorphic VT induced *in-silico* on model *#7* (ER+20fib) by PES protocol delivered from pacing site *endo#1*. Posterior views of 3D ventricular model displaying potential maps at different time instants of the PES protocol leading to positive VT induction. White arrows indicate propagation direction. (*a*) The propagation wavefront generated by second premature stimulus S3, applied on the endocardium, reaches epicardial surface (see dashed white circle). Simultaneously, the wavefront resulting from the first premature stimulus S2 still continues propagating across the ventricles, such that it is entering through the two ends of epicardial isthmus, what will lead to a collision inside the channel. (*b*) The wavefront generated by S3 stimulus causes propagation block at the lower side of epicardial isthmus (see white circle). At the same time, the wavefront is trying to enter the channel through its upper end, while it also propagates around the infarct scar, such that a collision will happen at LV lateral wall. (*c*) Wavefront was able to enter through the upper end of epicardial isthmus, so it propagates across the channel in downward direction. Furthermore, tissue surrounding the lower end of isthmus is almost completely repolarized. (*d*) Wavefront coming from inside the channel was also able to cross the lower end of isthmus (unidirectional functional block), thus propagating again all around the infarct scar. (*e*) Propagation wavefront surrounds the scar and enters again through the upper side of epicardial isthmus, thus triggering reentrant activity that will lead to a self-sustained monomorphic VT. (*f*) Activation map (LATs) of a cycle of induced VT, confirming that epicardial isthmus constitutes a CC that acts as structural substrate for this infarct-related monomorphic VT. For a more comprehensive analysis of this simulation, see Video S3.
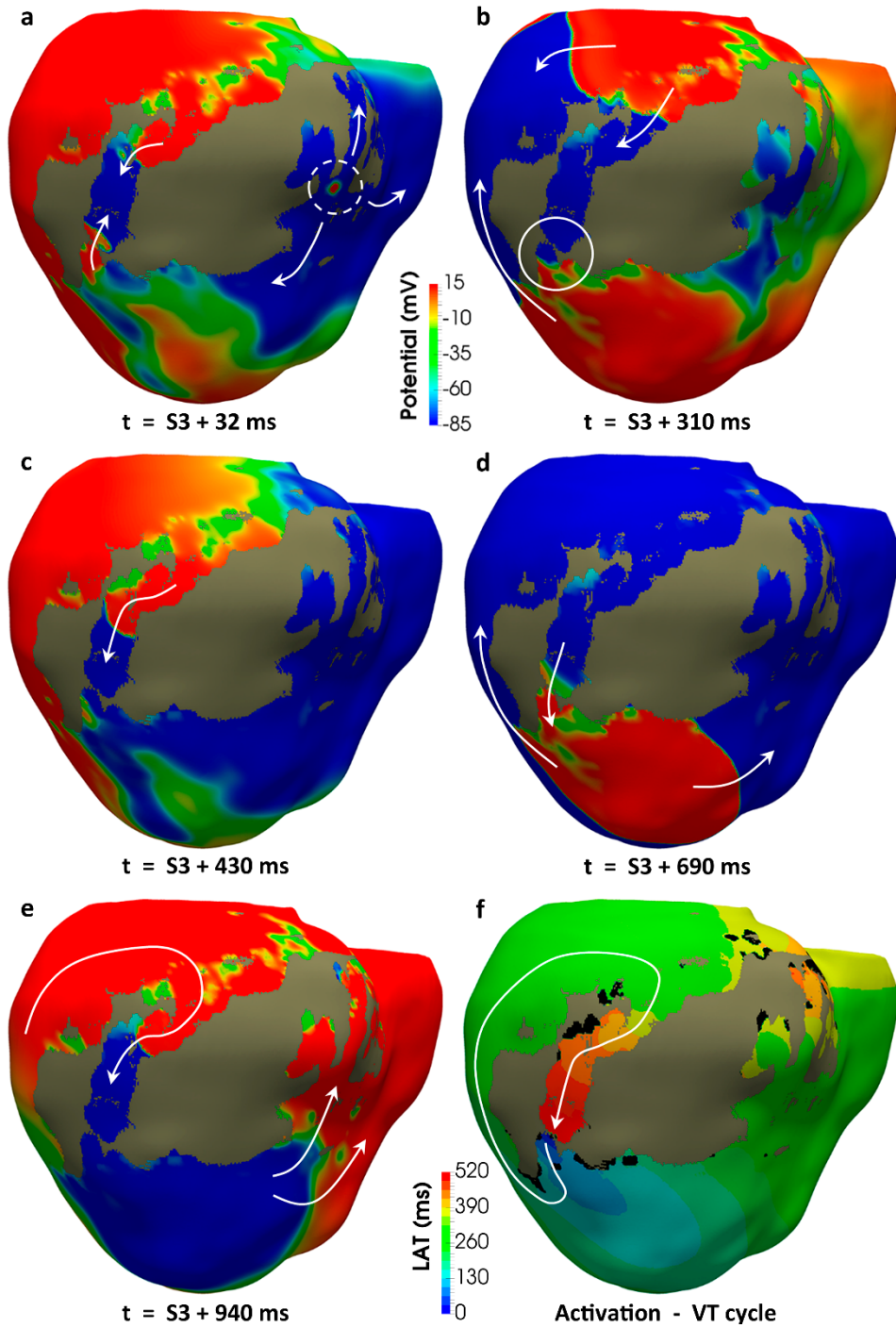
Figure 7.18. (*see description on the previous page*)

The propagation pattern depicted in Figure 7.17, resulting from S2 stimulus delivered from point *epi#1* (Figure 7.17[a]), shows how the functional propagation block appeared at the lower (apical) side of the epicardial isthmus (Figure 7.17[b]), thus impeding the entry of the wavefront through its lower end. Meanwhile, propagation wavefront continued propagating around infarct scar (Figure 7.17[c]), such that it reached the upper (basal) side of MI and entered epicardial isthmus through its upper end (Figure 7.17[d]), triggering the onset of reentrant activity. Then, the wavefront propagated across the isthmus in downward direction to later leave it through its lower end (Figure 7.17[d]), confirming that previous propagation block was a functional unidirectional block. After that, the activation wavefront travelled around the infarct scar and entered again through the upper side of epicardial isthmus, thus leading to self-sustained reentry. This corroborated that the epicardial isthmus actually was a slow conducting channel (CC), which acted as a structural substrate that supported the reentrant activity related to this particular VT, as we previously hypothesized in Chapter 5 (see section 5.1.6). Therefore, such epicardial CC enabled the perpetuation of self-sustained reentry on model *#6* (ER+10fib), responsible for an infarct-related monomorphic VT with a cycle length (CL) of 526 ms (see Table 7.4). Figure 7.17[f] displays the activation map (LAT) of a VT cycle, which is characterized by a clockwise macroreentrant propagation pattern supported by the epicardial CC, with the wavefront entering CC through its upper end and leaving it through the lower one.

On the other hand, Figure 7.18 depicts the propagation pattern resulting from S3 stimulus applied at pacing site *endo#1* (Figure 7.18[a]) on model *#7* (ER+20fib). In this case, although the propagation pattern leading to the onset of reentrant activity supported by the epicardial CC is different compared to the previous one, the specific event that triggered such reentry was exactly the same. In this simulation, S3 stimulus caused functional unidirectional propagation block at the lower end of epicardial CC (Figure 7.18[b]), as S2 stimulus did in the case of model *#6* (ER+10fib) paced from *epi#1* (Figure 7.17[b]). This allowed the wavefront to cross the CC from upper to lower side (Figure 7.18[c]), such that it was able to leave CC through its lower end and propagate around the infarct scar (Figure 7.18[d]). Finally, the S3 stimulus delivered from *endo#1* on model *#7* (ER+20fib) triggered the same reentrant

pattern (Figure 7.18[e]) previously observed on model *6* (ER+10fib) (Figure 7.17[d]). Indeed, comparing activation maps representing a VT cycle displayed in Figure 7.17[f] and Figure 7.18[f], no appreciable variation is observed. Both maps are characterized by an identical clockwise macroreentrant propagation pattern supported by the epicardial CC, with similar LAT values. The only notable difference is the amount of non-activated tissue (black patches) depending on patchy fibrosis level included in the BZ of each model version: 10% and 20% fibrosis for model *6* (ER+10fib) and model *7* (ER+20fib), respectively.

Impact of CVs in the BZ on VT inducibility

After performing all simulations for testing VT inducibility under the 24 different settings detailed in Table 7.4, we chose model *6* (ER+10fib) and pacing site *epi#1* to perform some additional tests. These extra simulations aimed to study the influence of different CVs in the BZ on VT inducibility, as well as on the features and mechanisms related to induced VTs. As shown in Table 7.5, *in-silico* test on model *6* (ER+10fib) with CVsBZ-50%, also resulted in positive VT induction (see Video S4[24]). In this case, the reentry leading to infarct-related VT was triggered again by unidirectional functional propagation block at the lower end of epicardial CC, caused by the second premature stimulus (S3 phase) applied at a CI of 320 ms. Note that such interval was notably shorter than the successful one in the case of model *6* (ER+10fib) with CVsBZ-25% (CI of 360 ms, see in Table 7.5), in which furthermore VT was induced by a single premature stimulus (S2 phase) with no need for a second one. Moreover, as a result of faster conduction across the BZ and, consequently, through the epicardial CC, induced VT was also faster, with a CL of 425 ms. It is significantly shorter (around 20% shorter) compared to the cycle of VT induced with CVsBZ-25%, which provided VT with CL of 526 ms (see Table 7.5). However, in the test on model *6* (ER+10fib) with values for CVsBZ-75% (i.e., CVs 25% slower than in healthy tissue), the result of VT inducibility was negative. As shown in Video S5[25], in

---

[24] **Video S4.** Positive VT induction on model *6* (ER+10fib) from pacing site *epi#1*, with CVsBZ-50%.   https://youtu.be/13Td_t8MWOE

[25] **Video S5.** Negative VT induction on model *6* (ER+10fib) from pacing site *epi#1*, with CVsBZ-75%.   https://youtu.be/HMMrHHb3YqM

which even a third premature stimulus (S4 phase) was applied at a CI of 310 ms, with this model configuration propagation block never happened at any of the epicardial CC ends. Finally, premature stimuli failed to propagate at pacing site at a CI of 290 ms, without having been able to trigger any kind of reentrant activity at any longer CI.

CVs in the BZ	Results		
Reduced to 25% **(CVsBZ-25%)**	Stim :	S2	
	CI :	360 ms	
	CL :	526 ms	
	HR :	114 bpm	
Reduced to 50% **(CVsBZ-50%)**	Stim :	S3	
	CI :	320 ms	
	CL :	425 ms	
	HR :	141 bpm	
Reduced to 75% **(CVsBZ-75%)**	no VT − fail at 290 ms		

Table 7.5. Results of *in-silico* tests of VT inducibility performed on model *#6* (ER+10fib), with three different sets of values for CVs in the BZ: CVsBZ-25%, CVsBZ-50% and CVsBZ-75%. In those three simulations, PES protocols were applied at pacing site *epi#1*. In cases of positive VT induction, this table details the premature stimulus (S2 or S3) responsible for the unidirectional block triggering reentrant VT, CI at which such stimulus was delivered, and CL and heart rate (HR) associated with induced VT. For cases of negative VT induction, CI at which premature stimuli failed to propagate is specified.

Repolarization dispersion as a mechanism related to VT

Figure 7.19 displays APD maps resulting from the propagation of the last S1 stimulus applied at pacing site *epi#1*, corresponding to the four ventricular model versions that enabled positive VT induction in *in-silico* tests with CVsBZ-25%. As observed, all those models present significant repolarization dispersion around the infarct scar, either caused by (1) high levels of patchy fibrosis (30%) in the absence of electrical remodelling (model *#4* – noER+30fib), (2) electrical remodelling with no fibrosis in the BZ (model *#5* – ER+00fib) or (3) the combination of both factors (models *#6* [ER+10fib] and *#7* [ER+20fib]). In spite of exhibiting considerable differences between them, APD maps from models

model *#4*
[no ER + 30% fibrosis in BZ]

model *#5*
[with ER + 0% fibrosis in BZ]

model *#6*
[with ER + 10% fibrosis in BZ]

model *#7*
[with ER + 20% fibrosis in BZ]

APD90 (ms)

350
287.5
225
162.5
100
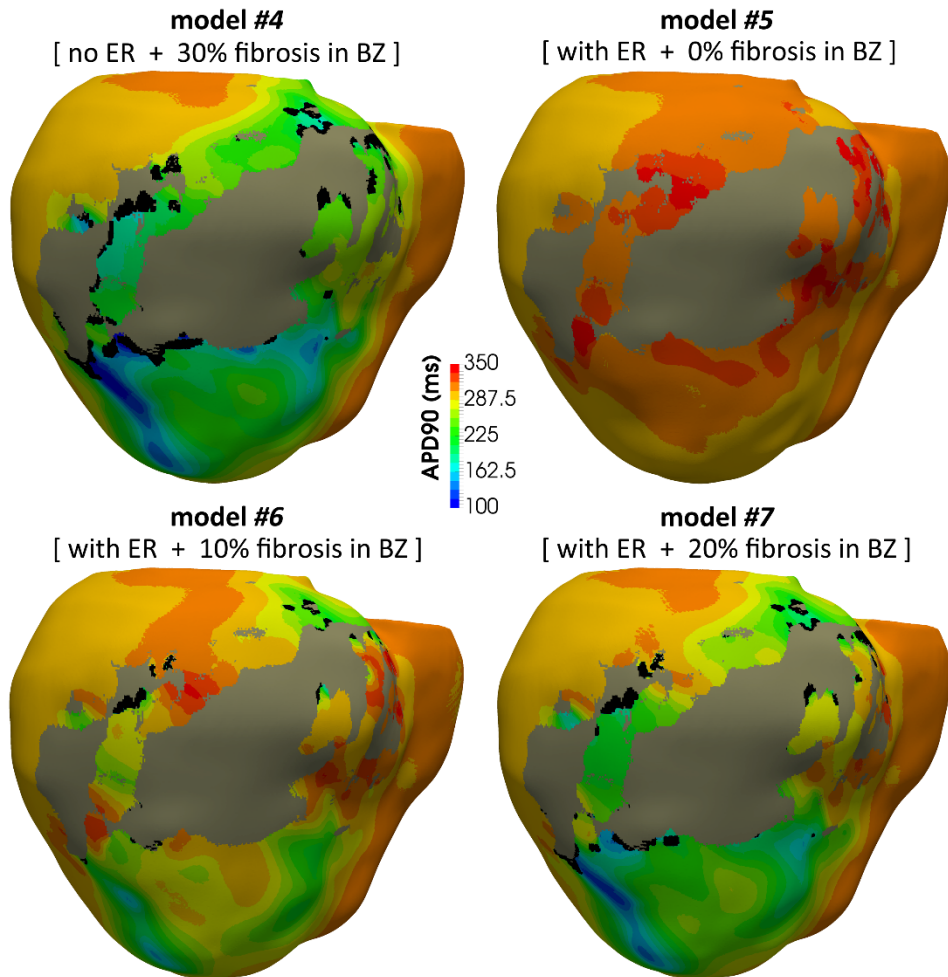
Figure 7.19. APD maps resulting from the propagation of the last stimulus of S1 phase delivered from pacing site *epi#1*. These maps correspond to posterior views of the four ventricular model versions that enabled positive VT induction in *in-silico* tests. All of them reveal significant repolarization dispersion around the infarct scar, either caused by high fibrosis level (model *#4* – noER+30fib), by electrical remodelling (ER) (model *#5* – ER+00fib) or by combination of both factors in the BZ (models *#5* [ER+00fib] and *#6* [ER+10fib]). Furthermore, at both sides of epicardial isthmus, there are regions with longer APDs compared to surrounding tissue, thus giving rise to strong repolarization gradients at the two terminal ends of CC. Black regions correspond to not activated tissue due to fibrosis accumulation.

#5 (ER+00fib), *#6* (ER+10fib) and *#7* (ER+20fib) share a common feature. At both terminal ends of the epicardial CC, such maps revealed the presence of regions with longer APDs compared to surrounding tissue. This caused large repolarization gradients at both sides of the CC. By contrast, in model *#4* (noER+30fib) such repolarization gradients at terminal ends of epicardial isthmus are not so evident. It is noteworthy that, among the four model versions that provided positive VT induction from point *epi#1* in the *in-silico* tests, model *#4* (noER+30fib) was the only version in which VT could not be induced by a single premature stimulus S2. Model *#4* (noER+30fib) required a second premature stimulus (S3 phase), along with a notably shorter CI (see Table 7.4), to give rise to a unidirectional propagation block at the lower end of the CC leading to the macroreentry responsible for infarct-related VT, as can be appreciated in Video S6[26]. Thus, it seems very likely that the lack of remarkable repolarization gradients at any side of the CC resulting from the propagation of the last S1 stimulus, was the main reason why model *#4* (noER+30fib) needed a S3 stimulus with a shorter CI to succeed in inducing VT in the *in-silico* tests.
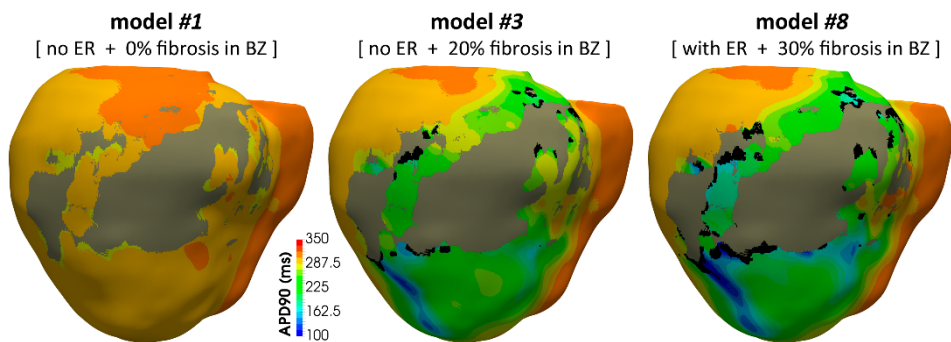
Figure 7.20. APD maps resulting from the propagation of the last stimulus of S1 phase delivered from pacing site *epi#1*. These maps correspond to posterior views of three out of the four ventricular model versions that resulted in negative VT induction in *in-silico* tests. Model *#1* (noER+00fib) presents quite regular repolarization pattern due to the absence of remodelling in the BZ. By contrast, the maps for models *#3* (noER+20fib) and *#8* (ER+30fib) do reveal notable repolarization dispersion, mainly caused by the presence of fibrosis in the BZ. However, they do not show large repolarization gradients at any of the two epicardial CC ends. Black patches correspond to not activated tissue due to fibrosis accumulation.

---

[26] **Video S6.** Positive VT induction on model *#4* (noER+30fib) from pacing site *epi#1*.
https://youtu.be/nJAsVjX_67A

The APD maps shown in Figure 7.20, also resulting from the propagation of the last S1 stimulus from point *epi#1*, correspond to three of those ventricular model versions that failed to induce VT in *in-silico* tests, from any of the three tested pacing sites. As a consequence of the absence of any type of remodelling in the BZ (only reduction in CVs), model *#1* (noER+00fib) exhibited a quite regular repolarization pattern around the infarct scar. It only showed a subtle APD gradient at the interface between the infarct scar and the excitable tissue that surrounded it. Conversely, models *#3* (noER+20fib) and *#8* (ER+30fib) did reveal considerable APD heterogeneity around the scar, mainly caused by presence of patchy fibrosis within the BZ, in both cases. Nonetheless, in contrast to that observed in Figure 7.19, neither of those APD maps (models *#3,8*) presented regions with APDs significantly longer than their surrounding tissue at any of the epicardial CC ends. Therefore, regardless of the degree of APD heterogeneity shown in APD maps, the propagation of the last S1 stimulus across those three model versions (models *#1,3,8*) was unable to cause considerable repolarization gradients at any of the two terminal ends of the CC. It seems highly probable that such feature is strongly correlated with the inability of those model versions to succeed in any of the *in-silico* tests of VT inducibility. They never gave rise to unidirectional blocks leading to the onset of reentrant activity, regardless of the pacing site from which PES protocols were delivered.

Factors affecting the propagation in the BZ during PES protocol

Regarding the activation of tissue corresponding to the BZ, which includes the epicardial CC that supported the macroreentrant activity responsible for the monomorphic VT, Figure 7.21 displays the evolution of the activation during the propagation of the last S1 stimulus applied at pacing site *epi#1*, on each one of the eight ventricular model versions with CVsBZ-25%. In all cases, activation of the BZ looks quite linear, except for a very small final segment in which activation times increased exponentially. As in the case of sinus activation, inclusion of electrical remodelling did not appear to cause a great impact on the activation of BZ during the S1 phase of PES protocols. It simply introduced slight activation delays with respect to models without that
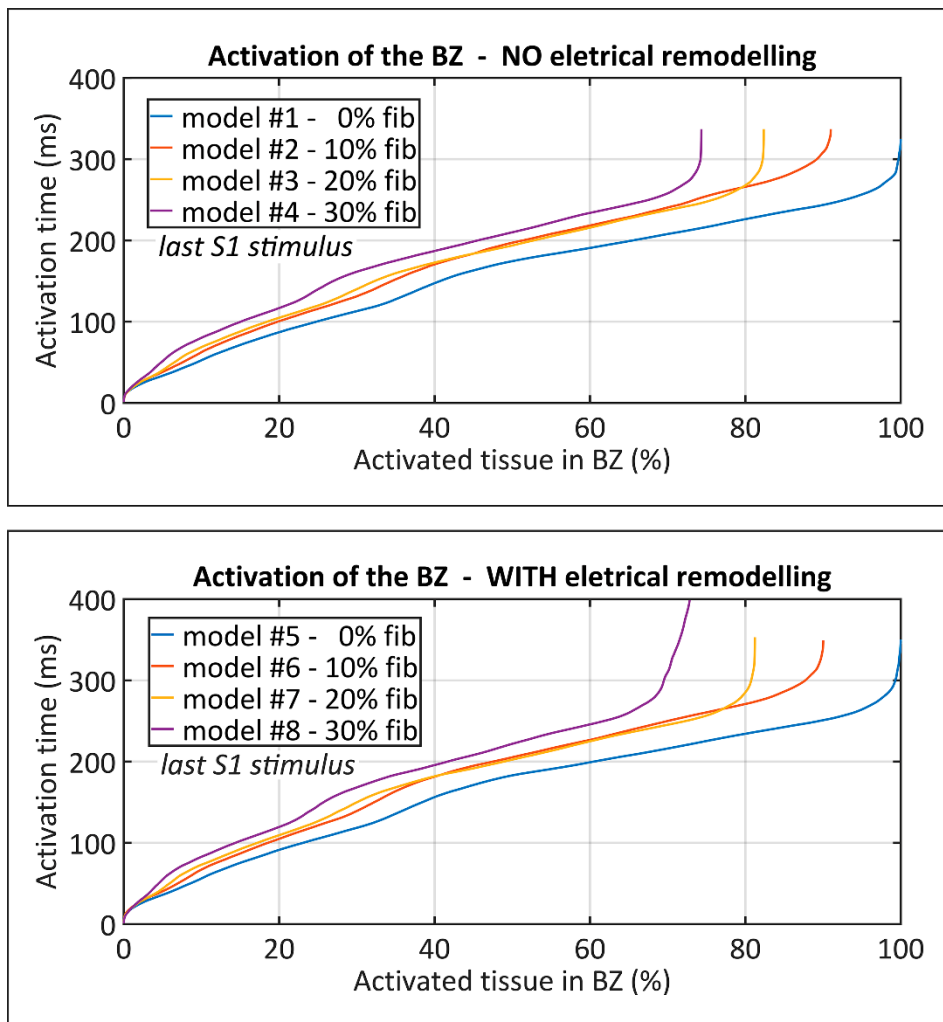
Figure 7.21. Evolution of the activation of tissue corresponding to the BZ, resulting from the last stimulus of S1 phase (six stimuli at BCL of 600 ms) applied at pacing site *epi#1*. Plots correspond to simulations of VT inducibility tests performed on all versions of the 3D ventricular model with CVsBZ-25%. Note that in those model versions including any level of patchy fibrosis in the BZ, the portion of successfully activated tissue could not reach 100% due to accumulations of fibrotic elements (mesh elements modelled as fibroblasts) within the BZ.

sort of remodelling, as well as little reductions in the amount successfully activated tissue (i.e., depolarized) for a given fibrosis level in the BZ. Again, this was the main consequence of combining electrical remodelling in the BZ with a

set of reduced conductivities. In model versions without electrical remodelling (models *1-4*), such lower conductivities resulted in CVs in the BZ reduced to 35% with respect to healthy myocardium (that is, 65% slower conduction). Instead, the same conductivity values made CVs in the BZ decrease to 25% with respect to healthy tissue (i.e., 75% slower conduction) in models *5-8*, due to the partial inactivation of sodium peak current (I_{Na}) associated with the electrical remodelling introduced in that region.

On the other hand, introduction of fibrosis did clearly affect propagation across the BZ, depending on the fibrosis level. It seems that the electrotonic load exerted on myocytes by those fibroblasts infiltrated in the BZ slowed down propagation in that region, as reflected by the evolution of slopes in Figure 7.21. Another important influence of the presence of fibrosis was the proportional increase of the amount of not activated tissue as a function of fibrosis level, due to clustered accumulations of fibrotic elements within the BZ. However, the combination of such circumstance with the slowing-down of propagation across BZ, curiously prevented the introduction of any fibrosis level from causing significant variations in the total time needed to fully activate the conducting portion of BZ tissue, as appreciated in Figure 7.21. An additional unexpected effect observed in Figure 7.21, was the fact that activation plots for models with 10% and 20% fibrosis in the BZ, did not differ significantly between them, except for the final segment related to the specific amount of not activated tissue. Hence, both levels of image-based patchy fibrosis (10% and 20%) caused very similar degree of slowing-down of propagation in the BZ, regardless of the presence or absence of electrical remodelling.

In summary, electrical remodelling introduced slight activation delays affecting the total time needed to fully activate the BZ tissue, while the presence of fibrosis slowed down the propagation across the BZ, but without causing significant increases in the total activation time due to reductions in the fraction of excitable tissue in the BZ. With respect to model *8* (ER+30fib), it was a special case that we will discuss below, since that configuration gave rise to permanent propagation blocks that strongly altered propagation patterns within the BZ.

Figure 7.22 shows the evolution of BZ activation, also during the propagation of the last S1 stimulus delivered from point *epi#1*, corresponding in this case to model *#6* (ER+10fib) with the three different set of values for CVs in the BZ that we tested. As expected, the increase in CVs of BZ, from 25% to 50% and 75% with respect to healthy tissue, speeded up propagation across the BZ, and also produced slight increments in the amount of activated tissue in such region. This latter effect was a consequence of the increase in the conductivities that affect myocyte-fibroblast couplings. This allowed the depolarization (activation) of a slightly larger number of coupled fibroblasts, due to their stronger electrotonic interaction as electrical sinks, which in turn was induced by those higher conductivity values. Moreover, it should be highlighted that the increment in CVs in the BZ from 25% to 50% with respect to healthy tissue caused an impact on propagation greater than the increase from 50% to 75%. This suggests that the relationship between CVs at the tissue level and the global acceleration or deceleration of propagation across the entire BZ is non-linear in our ventricular model, that is, it is not proportional.
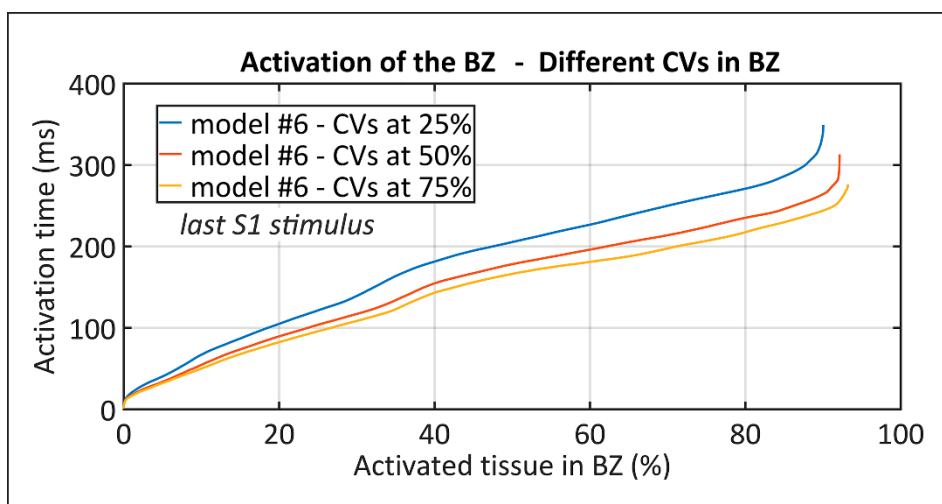
Figure 7.22. Evolution of the activation of tissue corresponding to the BZ, resulting from the last stimulus of S1 phase (six stimuli at BCL of 600 ms) delivered from pacing site *epi#1*. Plots correspond to simulations of VT inducibility tests performed on model *#6* (ER+10fib) with CVsBZ-25%, CVsBZ-50% and CVsBZ-75%.

Propagation in the BZ during VT

The evolution of the activation during a cycle of the infarct-related monomorphic VT of the tissue composing the BZ, is shown in Figure 7.23, for all those ventricular model versions that provided positive VT induction in *in-silico* tests, including model *#6* (ER+10fib) with CVsBZ-50%. To define that VT cycle, we took as a starting point the moment in which the propagation wavefront leaves the epicardial CC through its lower end, after crossing it in downward direction (from base to apex), as it is represented in Figure 7.17[f] and Figure 7.18[f]. Thus, the end of the VT cycle corresponds to the time instant when the wavefront coming from the interior of the CC reaches again its lower end, after completing the pathway of the macroreentry responsible for the VT. As one can observe, model *#6* (ER+10fib) with CVsBZ-50% is the model version with the fastest propagation across the BZ due to increased CVs and, consequently, with the shortest VT cycle length (see Table 7.5). The other four model versions (models *#4-7*), all of them with CVsBZ-25%, just present subtle differences in the length of VT cycle, from 506 to 526 ms (see Table 7.4). According to our definition of the VT cycle, the final segment of the activation plots corresponds to the activation of the tissue that forms the epicardial CC. As shown in Figure 7.17[f] and Figure 7.18[f], at around 400 ms, the CC that crosses the infarct scar is nearly the only fraction of myocardial tissue that has not been activated yet. In this final segment one can appreciate the main differences between the four activation plots displayed in Figure 7.23. In that final part, the almost linear trend turns into an exponential increase of activation times, coinciding with the activation of the epicardial CC. Thus, it indicates that the remodelling included in the BZ, based on the DE-MRI in the case of fibrosis, strongly affects propagation across the epicardial CC that supports infarct-related VT. Furthermore, these plots reflect again the fact that the higher the fibrosis level, the smaller the portion of successfully activated tissue due to accumulations of fibrotic elements within the BZ. With respect to the quasi-linear segment, there seems to be no significant differences in the initial activation of BZ between models *#5* (ER+00fib) and *#6* (ER+10fib) (RM20). However, there is a surprisingly high coincidence in the evolution of the initial activation of BZ between model *#4* (noER+30fib) and model *#7* (ER+20fib).
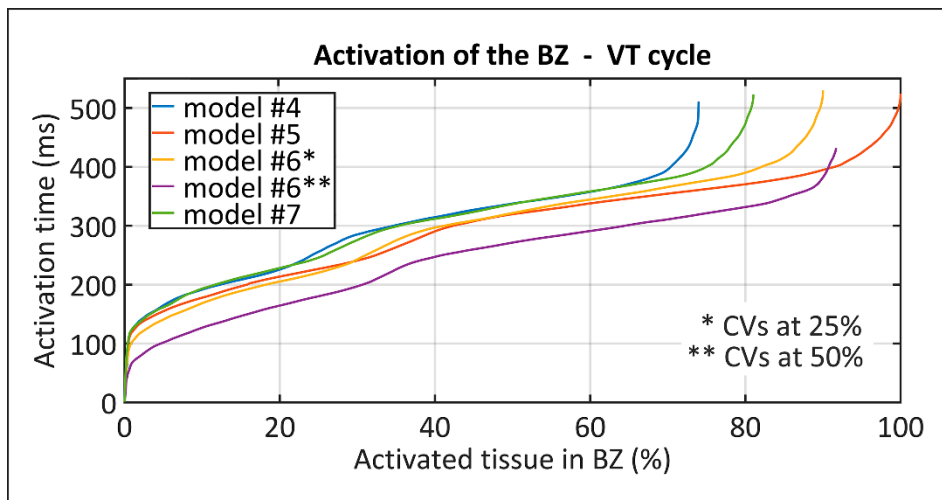
Figure 7.23. Evolution of the activation of tissue corresponding to the BZ during a cycle of infarct-related monomorphic VT, corresponding to all those versions of 3D ventricular model that enabled positive VT induction in *in-silico* tests.

Factors leading to negative VT induction in *in-silico* tests

Focusing now on unsuccessful VT tests, there were four versions of ventricular model (models *#1,2,3* and *#8*) that failed to induce VT in all *in-silico* tests, from every pacing site. Actually five, if we include tests from point *epi#*1 performed on model *#6* (ER+10fib) with CVsBZ-75%. As previously mentioned, model *#8* (ER+30fib) was a special case, since that configuration produced permanent bidirectional blocks at the lower side of epicardial CC, even blocking the propagation of stimuli of S1 phase, regardless of pacing site (see Video S7[27] and Video S8[28]).

The application of PES protocols from pacing site *epi#2* never managed to induce VT in any case. Regardless of model version, premature stimuli (S2-S3) delivered from *epi#2* were unable to cause a functional propagation block at any

---

[27] **Video S7.** Negative VT induction on model *#8* (ER+30fib) from pacing site *epi#1*.
　　　https://youtu.be/DDr1Ag_XSSE
[28] **Video S8.** Negative VT induction on model *#8* (ER+30fib) from pacing site *endo#1*.
　　　https://youtu.be/mxE9i4ANqXg

of the epicardial CC ends (see Video S9[29], for instance). Only applying a third premature stimulus (S4 phase) we were able to induce propagation block at the upper (basal) end of CC on model *5* (ER+00fib). However, that functional block did not trigger reentrant activity, since the propagation wavefront derived from S4 stimulus could not enter the CC through its lower side, because it collided with the wavefront generated by S3 stimulus that still was propagating across the CC in downward direction (see Video S10[30]). Furthermore, premature stimuli (*S2-S3*) applied at point *epi#2* failed to propagate at the same CI (350 ms) for every model version. This feature indicates that such pacing site was placed out of the BZ or, in other words, it was located in a region of healthy tissue. That is the reason why the different versions of remodelling included in the BZ, both electrical and structural (in the form of patchy fibrosis), did not alter APDs in that piece of tissue across model versions. Consequently, refractory periods in such region remained unaltered, thus avoiding the variation of the minimum tolerated CI for premature stimuli as a function of the model version, as it did occur in tests performed from points *endo#1* and *epi#1* (see Table 7.4).

In the case of VT *in-silico* tests with PES protocols applied from *epi#1*, the final result was negative for models *#1* (noER+00fib), *#2* (noER+10fib) and *#3* (noER+20fib) (see Table 7.4), because premature stimuli never managed to cause functional propagation blocks at any of the epicardial CC ends, thus preventing the onset of the reentry leading to infarct-related VT. As shown in Video S11[31], the propagation wavefront derived from the two premature stimuli (S2-S3) delivered from *epi#1* entered the CC through its lower end, so that a collision against the wavefront that surrounded the infarct scar always happened at the upper side of channel. This behaviour suggests that the inability of PES protocols to cause functional propagation blocks at any of the epicardial CC ends, especially at the lower one in this particular case, was strongly related to the absence of large APD gradients at those regions, as observed in Figure 7.20.

---

[29] **Video S9.** Negative VT induction on model *#6* (ER+10fib) from pacing site *epi#2*.
    https://youtu.be/m11Z1QdmHNU
[30] **Video S10.** Negative VT induction on model *#5* (ER+00fib) from pacing site *epi#2*.
    https://youtu.be/XWC9MMWigh0
[31] **Video S11.** Negative VT induction on model *#3* (noER+20fib) from pacing site *epi#1*.
    https://youtu.be/iMUctH2WiRM

As for pacing site *endo#1*, negative results were similar to those of point *epi#1*, although including model *#4* (noER+30fib) in this case (see Table 7.4). The main difference with respect to pacing from *epi#1* is the fact that the wavefront generated by stimuli applied at *endo#1* entered the CC through its two terminal ends, so that collision always took place inside the channel, near to its central part, as displayed in <u>Video S12</u>[32]. By contrast, on model *#5* (ER+00fib) the second premature stimulus (S3 phase) delivered from *endo#1* did produce functional propagation block at the lower end of the epicardial CC, while the propagation wavefront entered through the upper side. However, that situation finally resulted in non-sustained reentry, since propagation was blocked again when the wavefront coming from inside the CC attempted to pass through its lower end (see <u>Video S13</u>[33]). Therefore, in that case, the generation of bidirectional block at the lower side of the CC aborted the onset of self-sustained reentrant activity able to trigger an infarct-related VT. Importantly, in spite of being bidirectional, it was a functional (not structural) propagation block that only appeared as a result of the configuration of that particular VT test (model *#5* [ER+00fib] paced from point *endo#1*), in contrast to the permanent bidirectional block observed in all *in-silico* test on model *#8* (ER+30fib).

7.5.3.2. Simulations at the torso level. Simulated ECGs

After completing all *in-silico* tests of VT inducibility at the organ level, we used the 3D torso model to compute extracellular potentials all over the torso to obtain the simulated ECGs. We computed the six precordial leads of simulated ECGs for all induced VTs, aiming to compare those simulated signals to patient's recordings and, thereby, assess the degree of similarity between real and simulated signals. Indeed, this is exactly how electrophysiologists determine at EP laboratory whether a particular VT induced by means of PES protocols matches the clinical VT previously suffered by the patient or, on the contrary, if it is a different VT. They just compare the ECG registered during the

---

[32] **Video S12.** Negative VT induction on model *#6* (ER+10fib) from pacing site *endo#1*.
      <u>https://youtu.be/lV_hen97G8M</u>
[33] **Video S13.** Negative VT induction on model *#5* (ER+00fib) from pacing site *endo#1*, due to bidirectional functional propagation block.   <u>https://youtu.be/xtdoWtn-DGs</u>

induced VT with the recordings of clinical VT in order to visually inspect the correlation between them. Hence, as a final step of our pipeline based on computational simulation, making use of our 3D torso model we computed simulated ECGs to reproduce that diagnostic test. Moreover, in such a way we fulfilled our initial premise of only including non-invasive clinical data in our pipeline, since simulation results can be evaluated and validated against non-invasive recordings, such as ECG, rather than against invasively recorded datasets, as it is the case of EAMs.

Simulated ECGs resulting from *in-silico* induced VTs

Figures 7.24, 7.25 and 7.26 show signals corresponding to the six precordial leads of ECGs, computed from VTs induced on models *4-7* and, in addition, on model *6* (ER+10fib) with CVsBZ-50% (instead of CVsBZ-25%). Together with those signals, such plots also represent a fragment of the real ECG registered in the EP laboratory during one of the episodes of positive VT induction along the EP study. Importantly, such real VT was considered the same as the clinical one by the experienced electrophysiologists who performed EP study and posterior RFA procedure. On the other hand, note that two distinct versions of the ventricular model (models *6* [ER+10fib] and *7* [ER+20fib]) enabled positive VT induction from more than one pacing site, from *endo#1* and *epi#1*. Nevertheless, since the induced VT was always the same, characterized by the clockwise macroreentrant pattern through the epicardial CC, all VTs induced on a certain model version showed exactly the same features regardless of the pacing site at where PES protocol was applied, as detailed in Table 7.4. That is the reason why we do not show simulated ECGs computed from models *6* (ER+10fib) and *7* (ER+20fib) twice, because there is no difference between simulated signals for VTs induced from *endo#1* and *epi#1* on the same model version.
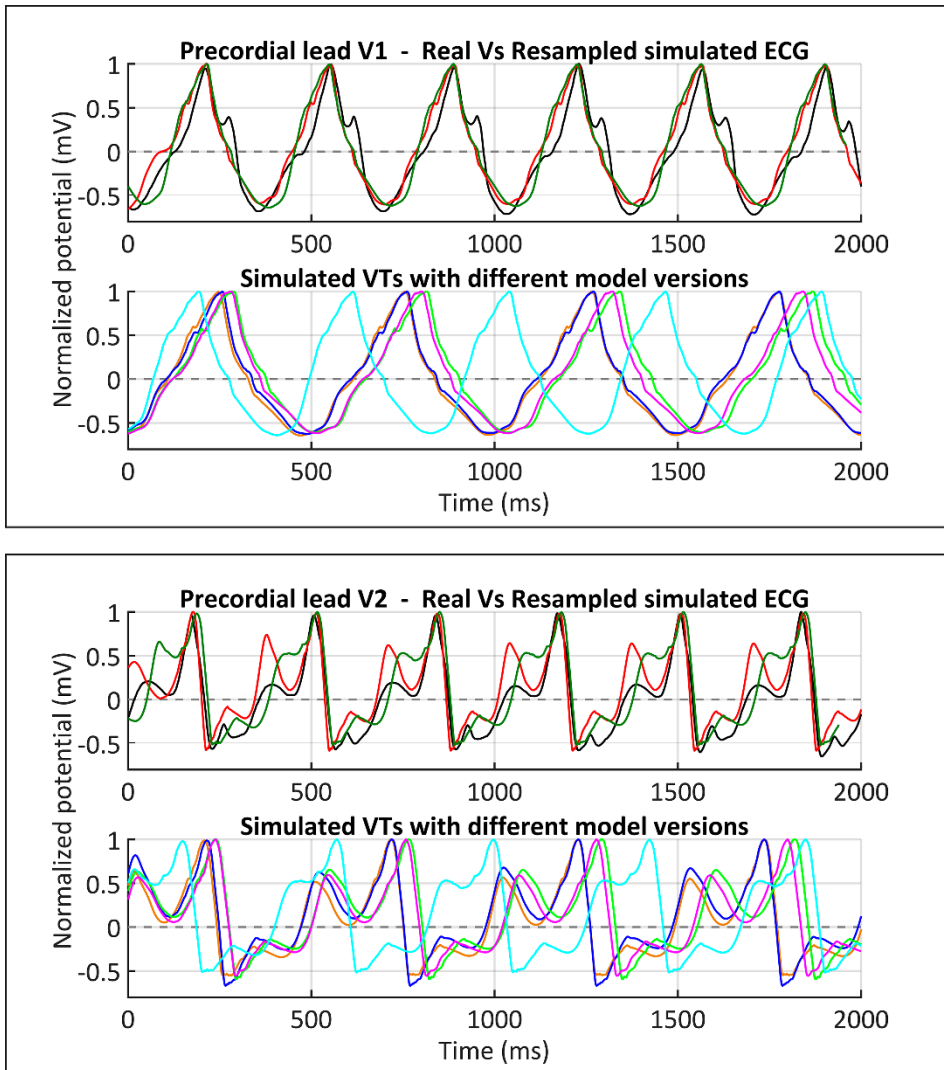
Figure 7.24. ECGs during clinical and *in-silico* induced VTs. Signals corresponding to V1 and V2 precordial leads, displaying real ECG (*black*) and ECGs simulated with different versions of ventricular model. Simulated ECGs correspond to all model versions that enabled positive VT induction by *in-silico* tests: models *#4* (noER+30fib) (*orange*), *#5* (ER+00fib) (*blue*), *#6* (ER+10fib) (*light green*) and *#7* (ER+20fib) (*magenta*). ECG computed from model *#6* (ER+10fib) with CVsBZ-50% (instead of CVsBZ-25%) is also represented (*cyan*). Resampled versions of simulated ECGs obtained from model *#6* (ER+10fib), with CVsBZ-25% (*red*) and CVsBZ-50% (*dark green*), are displayed together with patient's ECG (*black*) to ease the visual comparison of waveforms between real signal and simulated ones.

Figure 7.25. ECGs during clinical and *in-silico* induced VTs. Signals corresponding to V3 and V4 precordial leads, displaying real ECG (*black*) and ECGs simulated with different versions of ventricular model. Simulated ECGs correspond to all model versions that enabled positive VT induction by *in-silico* tests: models *#4* (noER+30fib) (*orange*), *#5* (ER+00fib) (*blue*), *#6* (ER+10fib) (*light green*) and *#7* (ER+20fib) (*magenta*). ECG computed from model *#6* (ER+10fib) with CVsBZ-50% (instead of CVsBZ-25%) is also represented (*cyan*). Resampled versions of simulated ECGs obtained from model *#6* (ER+10fib)*,* with CVsBZ-25% (*red*) and CVsBZ-50% (*dark green*), are displayed together with patient's ECG (*black*) to ease the visual comparison of waveforms between real signal and simulated ones.

Figure 7.26. ECGs during clinical and *in-silico* induced VTs. Signals corresponding to V5 and V6 precordial leads, displaying real ECG (*black*) and ECGs simulated with different versions of ventricular model. Simulated ECGs correspond to all model versions that enabled positive VT induction by *in-silico* tests: models *#4* (noER+30fib) (*orange*), *#5* (ER+00fib) (*blue*), *#6* (ER+10fib) (*light green*) and *#7* (ER+20fib) (*magenta*). ECG computed from model *#6* (ER+10fib) with CVsBZ-50% (instead of CVsBZ-25%) is also represented (*cyan*). Resampled versions of simulated ECGs obtained from model *#6* (ER+10fib)*,* with CVsBZ-25% (*red*) and CVsBZ-50% (*dark green*), are displayed together with patient's ECG (*black*) to ease the visual comparison of waveforms between real signal and simulated ones.

A first conclusion that one can draw by observing the regular pattern of all simulated ECGs is the fact that induced VT undoubtedly corresponds to a monomorphic VT, as the ones typically derived from infarct-related reentrant activities supported by CCs associated with healed or chronic MIs (Aliot et al., 2009; de Bakker et al., 1988). For model versions with CVsBZ-25%, one can observe subtle differences between models in the frequency of the simulated signals, with very little variations in heart rates just ranging from 114 bpm (model *#6* – ER+10fib) to 118 bpm (model *#5* – ER+00fib), as specified in Table 7.4. Thus, model *#6* (ER+10fib) with CVsBZ-50% provided a considerably faster VT, showing a heart rate of 141 bpm (see Table 7.5), which is about 23% faster than the case with CVsBZ-25%.

Impact of BZ remodelling on simulated ECGs from *in-silico* induced VTs

Regarding ECG morphology, signals resulting from model versions with CVsBZ-25% are very similar between them. Only simulated ECG from model *#5* (ER+00fib) showed some worth-mentioning differences in the main upstroke on V3 and V4 leads (see Figure 7.25) and, although less pronouncedly, also on V5 and V6 (see Figure 7.26). Such differences correlate with the fact that model *#5* (ER+00fib) was the only model version with no fibrosis in the BZ that provided positive VT induction in *in-silico* tests. Consequently, it was the model version leading to the fastest VT, with CL of 506 ms and heart rate of 118 bpm (see Table 7.4), and also the only one in which the whole BZ tissue was successfully activated (see Figure 7.23). Furthermore, such main upstroke in signals of V3, V4, V5 and V6 leads corresponds exactly to the time window during which the propagation wavefront (1) approached the basal side of the MI, after surrounding the infarct scar in apex-to-base direction, then (2) entered through the upper end of the epicardial CC and, finally, (3) crossed the CC downwards until reaching its lower side (see Video S14[34], from t = 2110 ms to t = 2340 ms, for example). This observation further confirmed the strong influence of remodelling in the BZ, specially the presence of fibrosis, on the propagation across the epicardial CC in our ventricular model. Moreover, model *#5*

---

[34] **Video S14.** Positive VT induction on model *#5* (ER+00fib) from pacing site *epi#1*.
https://youtu.be/u8NAd3TvQ0g

(ER+00fib) was also the only model version leading to positive VT induction that did not experience early repolarization in the tissue surrounding the infarct scar, because of the absence of patchy fibrosis within the BZ, as observed in APD maps displayed in Figure 7.19. Therefore, such lack of early repolarized regions in model *5* (ER+00fib) also influenced the morphology of simulated ECGs, thereby intensifying differences in the waveform of computed signals with respect to those models including fibrosis in the BZ (models *4,6,7*). Such an important impact of the presence of fibrosis in the BZ on simulated ECGs was already observed in the signals computed from simulations of sinus activation, in which fibrosis led to significant deviations of ST segment (see section 7.5.2.2).

Influence of CVs in the BZ on simulated ECGs from *in-silico* induced VTs

Besides showing a higher frequency, ECGs computed from the VT induced on model *6* (ER+10fib) with CVsBZ-50% exhibited some notable morphological differences with regard to signals computed from model versions with CVsBZ-25%. Those discrepancies are mainly notable on V2 (see Figure 7.24) and V3 leads (see Figure 7.25), and also on V4 in a lesser extent. Such deviations in simulated ECGs between model *6* (ER+10fib) with CVsBZ-50% and the rest of model versions were caused by a shift during the VT cycle in the synchronization of activation-repolarization pattern of BZ with respect to the pattern of healthy tissue. This was a consequence of modifying CVs in the BZ, what strongly altered propagation in that region, while keeping CVs in the healthy tissue, where activation-repolarization pattern remained nearly unchanged. Let us take the signal corresponding to V3 lead to illustrate such discrepancies, in which the major difference is in the trough located between the two positive peaks that appears in each VT cycle (see Figure 7.25). In the signal obtained from every model version with CVsBZ-25%, such trough is considerably deeper than in the signal resulting from model *6* (ER+10fib) with CVsBZ-50%. In all model versions, that point on V3 corresponds to the moment in which ventricular tissue is almost completely repolarized after the activation derived from previous VT cycle, as shown in Figure 7.27. If we observe the potential map corresponding to that instant on model *6* (ER+10fib) with CVsBZ-25% (see upper panel in Figure 7.27,
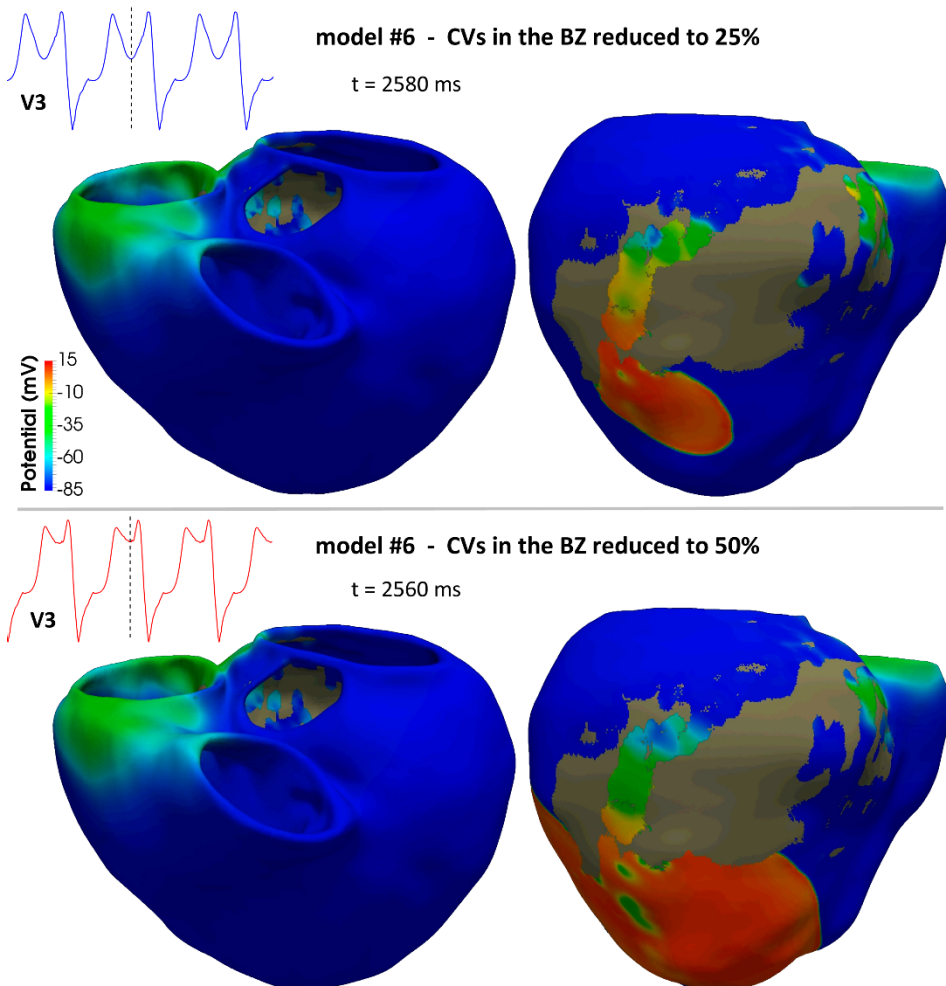
Figure 7.27. Potential maps during VT cycle, corresponding to model *#6* (ER+10fib) with CVsBZ-25% (*upper panel*) and CVsBZ-50% (*lower panel*). Each panel shows an anterior (*left*) and a posterior (*right*) of ventricular model, displaying potential map corresponding to the instant of VT cycle associated with the point marked by a dashed line on precordial lead V3. As observed in posterior views, the propagation wavefront associated with reentrant activity is not as spread around infarct scar in the case of CVsBZ-25% (see in Video S2) as in model version with CVsBZ-50% (see in Video S4), while repolarization pattern is exactly in the same state in both cases (look at potentials around tricuspid valve).

or look for t = 2580 ms in Video S2[35]), we can moreover see that propagation wavefront has already left the CC through its lower end and it is propagating across the conducting tissue located below the infarct scar. However, if we inspect the same moment in VT cycle on model *6* (ER+10fib) with CVsBZ-50% (see lower panel in Figure 7.27, or look for t = 2560 ms in Video S4[36]), we can clearly appreciate that the propagation around the infarct scar is further spread in this case. It was a result of a faster conduction across BZ and, consequently, across the epicardial CC supporting the reentry responsible for VT. Therefore, those important variations in the activation pattern associated with the reentrant activity with respect to the repolarization pattern of the rest of myocardial tissue, arisen as a consequence of varying CVs only in the BZ, gave rise to those significant differences observed in the waveform of several precordial leads.

Comparison between real and simulated ECGs during VT episodes

The real VT induced and registered during the actual EP study undergone by the patient, which matches the clinical VT, is displayed in the upper plots in Figures 7.24, 7.25 and 7.26. It showed a frequency of 175 bpm, what means a VT cycle length of 340 ms. This is considerably faster than simulated VTs on any version of our ventricular model; around 50% faster with respect to models with CVsBZ-25% (114 - 118 bpm vs 175 bpm), and even 24% faster than VT induced on model *6* (ER+10fib) with CVsBZ-50% (141 bpm vs 175 bpm).

Lastly, aiming to compare the morphology of precordial leads resulting from simulated VTs with the real ECG corresponding to clinical VT, we resampled signals obtained from model *6* (ER+10fib) with both CVsBZ-25% and CVsBZ-50%. By doing so, we removed the frequency variability to ease the visual assessment. As appreciated in Figures 7.24, 7.25 and 7.26, such comparison revealed a high degree of similarity in the waveform of all precordial leads between ECGs of real and simulated VTs. Such good correlation was even higher

---

[35] **Video S2.** Positive VT induction on model *6* (ER+10fib) from pacing site *epi#1*, with CVsBZ-25%. https://youtu.be/1LepgvOTBJI

[36] **Video S4.** Positive VT induction on model *6* (ER+10fib) from pacing site *epi#1*, with CVsBZ-50%. https://youtu.be/13Td_t8MWOE

in the case of model *#6* (ER+10fib) with CVsBZ-25%, with all signals nearly reproducing every single deflection observed on each precordial lead of the real ECG. As already happened in the case of simulations of sinus activation, the major differences with respect to real ECG appeared in V2 lead (see Figure 7.24) and, to a lesser extent, also in V3 (see Figure 7.25). As observed, in the first of the two positive peaks appreciated in those precordial leads during each VT cycle, simulated signals showed an amplitude larger than that of real ECGs, being such deviation more marked on V2 than on V3. Therefore, in spite of considerable discrepancy in VT frequency, the morphology of ECGs resulting from simulated VTs exhibited very high correlation with patient's ECG corresponding to real VT.

7.6. Discussion

7.6.1. Simulations of sinus activation

Regarding personalization of cardiac sinus activation, some authors already exploited data from EAMs to adjust the electrical propagation using simplified EP models by adapting the so-called apparent conductivities (Chen et al., 2016; Chinchapatnam et al., 2008; Relan et al., 2011). On the contrary, from the beginning we decided to exclude every kind of invasively-recorded data from the design of our pipeline, so we refused to use the data provided by EAMs to personalize cardiac EP in our patient-specific computational model of the ventricles. The idea was to develop a pipeline to construct personalized 3D models able to perform prospective and predictive EP studies by computational simulation (*in-silico* studies) prior to RFA procedures, rather than retrospective studies after the interventions due to the need of using invasively-recorded EP data. Then, we simply benefited from CARTO® data to test and validate the performance of our body level approach (ventricles-torso coupled models) by means of simulated ECGs resulting from the sinus activation sequence provided by endocardial EAMs. However, the major limitation of EAMs is precisely the lack of automatic tools to annotate LATs accurately, especially in regions showing pathological EGMs due to the presence of fibrosis and scarred tissue, as well as to fit those data to a given 3D model.

Observations on simulations of sinus activation at the organ level

At the organ level, activation maps (LATs) resulting from simulations of CARTO®-derived sinus activation on our ventricular model (see Figure 7.6 and Figure 7.7) were very similar across all model versions. The only considerable difference between them was related to the delays in late activation of BZ, especially in the epicardial isthmus of surviving tissue that crossed through the infarct scar. However, those simulations did show remarkable variations at the organ level in repolarization patterns around the infarct scar between different ventricular model versions (see APD maps in Figure 7.9 and Figure 7.10). Importantly, repolarization dispersion (i.e., APD heterogeneity) observed in APD maps was particularly pronounced around the two ends of the epicardial isthmus. This feature presumably had a great influence on the mechanism underlying unidirectional propagation blocks that triggered infarct-related monomorphic VTs in this particular case.

Influence of BZ remodelling on simulated ECGs in sinus rhythm

Concerning the various factors considered for the different ways of modelling the BZ, simulations of CARTO®-derived sinus activation sequence with the eight distinct versions of our ventricular model revealed that the presence of fibrosis was the only element that clearly had significant influence on results at the torso level, that is, on simulated ECGs. As shown in Figures 7.11, 7.12 and 7.13, incorporation of any level of image-based patchy fibrosis (modelled as fibroblasts) had considerable impact on ST segment. The polarity of the ST segment deviation in simulated signals agreed with that observed in real ECG in all precordial leads. In the case of simulated ECGs, it was mainly caused by the early repolarization of the BZ tissue, resulting from the APD reduction around infarct scar due to the presence of fibrotic patches (see Figure 7.14). The electrotonic load exerted by fibroblasts infiltrated in the BZ, which acted as electrical sinks, accelerated the repolarization of surrounding myocytes, thus shortening their APDs. Therefore, such effect on ST segment in simulated ECGs was the manifestation at the torso level of that considerable repolarization dispersion observed around infarct scar (organ level), resulting from the presence of fibrosis within the BZ. Furthermore, fibrosis in the BZ also caused a subtle level-dependent effect on the T wave magnitude in simulated ECGs.

Impact of CVs in the BZ on simulated ECGs in sinus rhythm

On the contrary, the different set of values tested for CVs in the BZ only had slight effect on the QRS complex duration and on T wave amplitude, while the inclusion of electrical remodelling did not seem to have any notable impact on ECGs simulated from CARTO®-derived sinus activation. Note that the volume of the BZ only corresponds to 8.5% of LV myocardium, falling to 6.5% with respect to the entire ventricular tissue including both ventricles (for more details see Chapter 5, section 5.1.3). Thus, it is not too surprising that certain kind of alterations in such a small ventricular region was not evidently reflected in a physiological phenomenon at the torso level, such as ECG in sinus rhythm.

Repolarization phase in simulated ECGs in sinus rhythm

The main general difference between real ECG and simulated signals, regardless of the specific version of ventricular model, was the delay of the T wave onset in simulated signals with respect to real ones. Since T wave corresponds to the repolarization of ventricles and this issue affected equally all model versions, it indicates that such delay was related to a modelling parameter associated not only with the BZ but with the whole ventricular tissue, that is, with the entire model. Hence, this suggests that APDs of ten Tusscher model (ten Tusscher and Panfilov, 2006b), which we used to reproduce the EP behaviour of human ventricular myocyte both for healthy tissue and for BZ, are longer than patient's APDs. The implications of this difference in such an important EP feature will be discussed in more detail in the next section (see section 7.6.2).

Sources of error affecting the simulated ECGs

Simulated signals for V2 (Figure 7.11) and V3 (Figure 7.12) were the two precordial leads that exhibited the most significant differences compared to real ECG, not only in repolarization phase but also in QRS complex. In both precordial leads (V2 and V3), the real ECG showed a prominent negative S wave that our simulations at the torso level could not properly reproduce. However, considering that the real ECG was recorded during the EP study performed

immediately prior to RFA procedure, this might be caused (at least, partially) by the following circumstance. In the EP laboratory, a pad for defibrillation shocks is usually fixed on the left side of patient's chest, thus forcing the relocation of V2 and (sometimes) V3 electrodes away from their standard positions. Thus, since we placed virtual electrodes for simulated ECG at the standard positions of precordial leads (see Figure 7.3), this is likely an important error source specifically affecting V2 and V3. Moreover, such hypothesis was further supported by the fact that V2 and V3 were also the most different signals obtained from simulated VTs compared to real ECG (see Figure 7.24 and Figure 7.25). Therefore, it seems highly probable that V2 and V3 electrodes were not placed at its standard positions in the EP laboratory. This gives an idea of the importance of knowing the exact position of ECG electrodes from which signals were registered when the final goal of a simulation study on cardiac EP is to reproduce patient's ECG. Indeed, electrodes misplacement is known to be an important source of intra-individual variability in ECG recordings (Kania et al., 2014; Schijvenaars et al., 2008; Wenger and Kligfield, 1996).

Another significant, and in our case unknown, source of variability affecting simulated ECGs is the position and orientation of the heart inside the torso model and, consequently, its position with respect to the location of precordial lead electrodes (Hoekema et al., 2001; MacLeod et al., 2000; Nguyên et al., 2015). Since we had to adapt an already existing torso model rather than creating a full patient-specific one, as shown in Chapter 5 (see section 5.2.1), it is possible that the geometrical position and orientation of ventricular model into the torso model did not match exactly the heart position into patient's body. Hence, this represents an undetermined source of error that could alter simulated ECGs to a certain (and unknown) extent, affecting all precordial leads.

Similarity between real and simulated ECGs in sinus rhythm

Despite current limitations, including uncertainty in LAT annotations, possible precordial leads misplacement and possible inaccurate heart orientation into the torso model, together with the lack of any kind of personalization of cardiac EP, our body level approach provided interesting results for simulated ECGs obtained from patient-specific sinus activation

sequence. All precordial leads showed reasonably good signal correlation with real ECGs (between 80% and 96% for V1, V4, V5 and V6, and around 70% for V2 and V3), as well as similar R-wave progression (see Figures 7.11, 7.12 and 7.13). This, along with good agreement in QRS complex duration, indicates that chosen values for CVs in healthy myocardium and for conductivities of organs and structures in 3D torso model seem to be within a proper range. Moreover, the coincidence in T wave polarity between real and simulated ECGs (except for V1) suggests an appropriate definition of transmural layers (endo, mid, epi), since transmural heterogeneity is known to have great influence on repolarization phase (i.e., on T wave) in organ-level simulations (Okada et al., 2011; Perotti et al., 2015).

Usefulness of computing simulated ECGs in sinus rhythm

In conclusion, we strongly believe that these attempts to replicate the patient's ECG in sinus rhythm represent an important step in the validation of a pipeline like ours, which aims to reproduce the cardiac EP of a given patient as faithfully as possible in order to predict the mechanisms underlying a particular VT. Furthermore, it can be really helpful in adjusting some key parameters, such as CVs, APDs or transmural heterogeneity. However, this kind of validation processes are usually omitted in most of the studies that also aim for planning of RFA procedures or risk stratification, which commonly exclude 3D torso model from their approaches (see (Arevalo et al., 2016; Ashikaga et al., 2013; Cedilnik et al., 2018; Deng et al., 2016; Prakosa et al., 2018; Ringenberg et al., 2014), among others).

7.6.2. *In-silico* VT inducibility tests

The ultimate goal of our approach for computational simulation using image-based patient-specific 3D models was to reproduce clinical VTs *in-silico* aiming to study their related mechanisms and, mainly, to identify the pathways of reentry circuits responsible for those infarct-related VTs as ablation targets.

Ability to reproduce EP studies using computational simulation

Certainly, there was significant discrepancy in frequency between simulated and real VTs. Nevertheless, according to the expert electrophysiologists involved in this project, the resemblance in the morphology of simulated and real ECGs was close enough (see Figures 7.24, 7.25 and 7.26) to conclude that both VTs (clinical and simulated) were exactly the same (or at least followed the same pathways). Only the V2 and V3 lead ECGs showed worth-mentioning differences with respect to the ECG of clinical VT. Such discrepancies were very likely caused by inaccurate placement of those two electrodes in the EP laboratory, as discussed above. Therefore, if this *in-silico* EP study (that is, our approach) had been performed prior to the RFA procedure, it would have allowed to detect the epicardial CC as the optimal ablation target in this particular case, as it actually was in the real EP study. It must be highlighted that it would have been possible, since our pipeline exclusively requires non-invasive data that are commonly registered before real EP studies.

Furthermore, the *in-silico* tests of VT inducibility enabled positive VT induction from the two pacing sites (*endo#1* and *epi#1*) that had previously triggered the VT in the EP laboratory in the real heart. Instead, the tests failed to induce VT from point *epi#2*, which was an extra point not tested in the real EP study that we added with the aim of assessing the influence of pacing sites location on VT inducibility. Hence, according to all those results, we can consider that our approach was able to accurately reproduce the outcomes of the real EP study, in this particular case. Note that it was possible even in spite of the lack of cardiac EP personalization and the considerable list of factors adding uncertainty to our simulation results, such as (1) the poor knowledge of the complex EP features of the BZ in human chronically infarcted hearts, (2) the exact location of electrodes for precordial leads or (3) precise position and orientation of heart inside the torso, among others.

Similarity between real and simulated ECGs during VT episodes

On the other hand, morphological correlation between real ECG and simulated ECGs (obtained from *in-silico* induced VTs) was higher in the case of

model versions with CVsBZ-25% than for model *#6* (ER+10fib) with CVsBZ-50% (see Figures 7.24, 7.25 and 7.26). This might suggest that the ratio of CVs between BZ and healthy myocardium in patient's ventricles was closer to 25% than to 50%. Nonetheless, the delayed T wave observed in ECGs derived from simulations of sinus activation (see Figures 7.11, 7.12 and 7.13), indicates that the APDs of patient's heart were shorter than those of ten Tusscher model (ten Tusscher and Panfilov, 2006b), which we used to reproduce the AP of human ventricular myocyte. Thus, lower values for APDs would alter repolarization patterns during VT cycles in simulations at the organ level, what could evidently have considerable impact on the morphology of ECGs resulting from simulated VTs. Consequently, if APDs were changed in our ventricular model, the previous statement about CVs in patient's heart would no longer be valid. In such a case, new simulations should be conducted to assess again VT inducibility, as well as activation-repolarization patterns during VT cycle and the morphology of simulated ECGs computed from *in-silico* induced VTs.

Regarding the major discordance between simulated and real ECGs, which is the important difference in the frequency of *in-silico* induced VTs (114 - 141 bpm) compared to real VT (175 bpm), we hypothesize that it probably arose from the complex interrelation between several EP features, such as APDs and (specially) CVs, both in BZ and in healthy myocardium, and the interconnection of all those factors with the overall EP behaviour at the organ level. It must be highlighted again that we did not personalize any EP parameter in our computational models, so that values for CVs and APDs, as well as organ/tissue conductivities in the torso model, were not customized but based on population data. Therefore, it is not surprising that our models were not able to accurately reproduce the highly complex relationship between those factors and the activation-repolarization patterns at the organ level, which becomes even more complex when the interrelation between the EP behaviour of BZ and healthy tissue must be considered.

Relationship between CVs in the BZ and VT inducibility

It is well-known that the QRS complex duration in the ECG is mostly related to the CVs in ventricular myocardium, since QRS corresponds to the

electrical activation of ventricles. Thus, QRS duration is assumed to match the time that ventricular myocardium takes to be fully activated. The higher the CVs in ventricles, the faster the electrical propagation across ventricular tissue and, consequently, the narrower the QRS complex in the ECG, and vice versa. Then, the high concordance of QRS complex duration between real ECG and simulated ECGs computed from simulations of CARTO®-derived sinus activation (see Figures 7.11, 7.12 and 7.13), indicates that the values chosen for CVs of healthy myocardium in our ventricular model (based on population data) must be close to real CVs in patient's ventricles. Therefore, this suggests that the main factor hampering the induction of faster VTs in *in-silico* tests was specifically related to low values for CVs in the BZ, rather than a set of wrong values affecting the whole model including healthy myocardium.

In any case, CL of all VTs induced *in-silico* (425 - 526 ms) was significantly longer than that of real VT (340 ms), or in other words, the reentrant activity responsible for clinical VT was faster than any of the simulated reentries. As discussed above, the most feasible reason to explain such a great difference is the fact that electrical conduction across BZ and, consequently, through the epicardial CC supporting reentrant activity, was slower in our ventricular model than in patient's heart. That is the reason why an increase of CVs in the BZ in model *#6* (ER+10fib) up to CVsBZ-50%, certainly resulted in a faster reentry (i.e., with shorter CL) (compare Video S2[37] to Video S4[38]), although still 24% slower than real one. However, such modification of CVs gave rise to some changes in the waveform of several precordial leads, resulting in a poorer signal correlation between real and simulated ECGs (see Figures 7.24, 7.25 and 7.26). Moreover, *in-silico* tests were unable to induce VT on model *#6* (ER+10fib) when CVs in the BZ were further increased to CVsBZ-75%, that is, when electrical conduction across BZ was only 25% slower than in healthy myocardium. In that case, premature stimuli (S2-S3) associated with PES protocols failed to propagate at pacing site (*epi#1*) at a CI of 290 ms, which was too short to induce VT in that model version. The wavefront resulted from any stimulus applied at a longer CI

---

[37] **Video S2.** Positive VT induction on model *#6* (ER+10fib) from pacing site *epi#1*, with CVsBZ-25%.   https://youtu.be/1LepgvOTBJI

[38] **Video S4.** Positive VT induction on model *#6* (ER+10fib) from pacing site *epi#1*, with CVsBZ-50%.   https://youtu.be/13Td_t8MWOE

could not cause a functional propagation block at the lower end of the epicardial CC (see Video S5[39]), as it did happen in other model versions leading to the onset of reentry. Hence, this suggests that the faster the electrical conduction in the BZ, the shorter the CI needed to generate a wavefront able to reach the lower end of the CC within the time window in which the tissue in that region is vulnerable to functional propagation blocks. Indeed, in the case of model *#6* (ER+10fib) with CVsBZ-25%, a single premature stimulus (S2) applied at a CI of 360 ms was enough to trigger reentrant VT, while the same model version with CVsBZ-50% required a second stimulus (S3) delivered at a significantly shorter CI (320 ms) to produce functional propagation block in the epicardial CC. Therefore, the results of these computational simulations performed with different conductivity values highlighted the important influence of CVs in the BZ (which includes CCs) on those mechanisms leading to the initiation of infarct-related reentrant VTs, as well as on the features of those VTs, such as their frequency or ECG morphology.

Convenience of cardiac EP personalization

Those results, together with the late repolarization responsible for the delayed T wave observed in simulated ECGs derived from simulations of sinus activation (see Figures 7.11, 7.12 and 7.13), supported again the conjecture that APDs in the patient's ventricles were shorter than APDs of the ten Tusscher model (ten Tusscher and Panfilov, 2006b) used in our computational models. Hence, choosing an ionic model with basal APD shorter than the ten Tusscher one, both for healthy myocardium and for electrically remodelled BZ, would allow propagation of premature stimuli (S2-S3) applied at shorter CIs. Then, that modification in the EP modelling might enable the generation of functional propagation blocks, even in spite of relatively fast conduction across the BZ, thus triggering the onset of reentries that would lead to faster VTs due to higher CVs in the BZ. However, such hypothesis should be assessed by means of a new simulation study. The variation of APDs would also alter repolarization patterns,

---

[39] **Video S5.** Negative VT induction on model *#6* (ER+10fib) from pacing site *epi#1*, with CVsBZ-75%. https://youtu.be/HMMrHHb3YqM

as well as APD gradients around the epicardial CC ends, which seem to be strongly related to those functional blocks responsible for VT onset.

As a conclusion, we believe that the incorporation to our pipeline of a coarse personalization process of certain parameters of cardiac EP, could likely improve the performance of our approach in terms of a more accurate reproduction of the EP behaviour of patient's ventricles. Consequently, it might translate into higher similarity between *in-silico* induced VTs and clinical VTs and, thus, into an enhanced potential to predict optimal RFA targets. Maybe, some EP features, such as APDs or CVs of healthy myocardium, could be adjusted based on several measures from patient's ECG in sinus rhythm (QRS duration, ST segment length, etc.). Perhaps, that customization process might even benefit from the recent paradigm of "populations of models" (Britton et al., 2013; Lawson et al., 2018; Muszkiewicz et al., 2016), simply by selecting that version of a given ionic model that better fits the specific features inferred from patient's ECG. There are just a few precedents in this regard (Chen et al., 2016; Gillette et al., 2018; Relan et al., 2011), so further studies should be carried out to test those hypotheses about the convenience of coarsely personalizing cardiac EP from non-invasive datasets, as well as the expected impact of APDs and CVs in the BZ on VT features and even on VT inducibility.

Ventricular model versions leading to positive VT induction

Focusing on the simulation results at the organ level, we managed to induce infarct-related VT by means of *in-silico* tests in seven out of the 26 settings that we assessed, including the two additional tests on model *#6* (ER+10fib) with increased CVs in the BZ. Those successful results were achieved on four (models *#4-7*) out of the eight versions of the ventricular model, with both CVsBZ-25% and CVsBZ-50%, and from two (*epi#1* and *endo#1*) out of the three tested pacing sites. Among the four model versions that enabled positive VT induction, three of them (models *#5,6,7*) included electrical remodelling in the BZ. Model *#4* (noER+30fib) provided positive VT induction exclusively from pacing site *epi#1* (not from *endo#1*), being the unique successful configuration without electrical remodelling, although with the highest fibrosis level (30%) in the BZ. Furthermore, it was the only model version that required the application

of a second premature stimulus (S3 phase) from point *epi#1* at CI of 290 ms, which is significantly shorter than the CI of 360 ms that was enough to trigger infarct-related VT on models *#5,6,7* by means of a single premature stimulus (S2 phase) from the same pacing site (see Table 7.4).

Repolarization dispersion as a factor increasing susceptibility to VT

The APD maps displayed in Figure 7.19, corresponding to the propagation of the last S1 stimulus across the four successful model versions, show that the three configurations with electrical remodelling (models *#5,6,7*) gave rise to large APD gradients around both terminal ends of the epicardial CC. Conversely, such feature was not so clearly appreciated on model *#4* (noER+30fib). Those longer APDs at the CC ends and, consequently, longer refractory periods, made such regions especially prone to give rise to functional unidirectional propagation blocks, since those pieces of tissue needed more time to recover its excitability than the surrounding myocardium. Hence, the results of our simulation study indicate that, in the presence of a CC with slowed conduction that crosses the infarct scar, repolarization dispersion due to APD heterogeneity is an essential factor in promoting the onset of reentrant activity. Moreover, that repolarization dispersion around the ends of the CC, responsible for the strong APD gradients causing propagation blocks that triggered reentrant activity, correlates with the electrical remodelling in the BZ much closer than with the presence of patchy fibrosis. In other words, although based on a unique MI geometry, our simulation study suggests that the arrhythmogenic potential of a chronically infarcted human heart is more strongly correlated with the electrical remodelling in the BZ than with the existence of fibrosis in that region. This is in agreement with that observed in (Arevalo et al., 2013) and more recently discussed in (Trayanova et al., 2017). Such studies concluded that the presence of fibrosis within the BZ (randomly distributed patchy fibrosis, in those cases) is not an essential component in cardiac computational models aiming to predict infarct-related reentrant circuits, as long as electrical remodelling and reduction in CVs in the BZ are considered. In fact, model *#5* (ER+00fib) provided positive VT induction from pacing site *epi#1* by means of a single premature stimulus (S2). Concerning pacing site *endo#1*, model *#5* (ER+00fib) was not able

to induce VT, although it did lead to the onset of non-sustained reentry due to the generation of functional (not permanent) bidirectional propagation block at the lower side of the epicardial CC (see Video S13[40]), while model *#4* (noER+30fib) never gave rise to any propagation block from *endo#1*.

Influence of fibroblasts in the BZ on the mechanisms related to VT

Nevertheless, despite failing from pacing site *endo#1*, it is true that model *#4* (noER+30fib) enabled positive VT induction without electrical remodelling in the BZ from *epi#1*. In such a case, we hypothesize that the generation of the functional unidirectional propagation block that triggered reentry did not result from large APD gradients at the lower end of the CC, but otherwise from a combination of other kind of factors specifically related to the high fibrosis level (30%) within the BZ. As observed in Figure 7.21, our simulation results showed that the presence of infiltrated fibroblasts caused slowing-down of electrical propagation across the BZ depending on fibrosis level. Experimental studies with cultured cells confirm that such density-dependent deceleration of conduction derives from reduced excitability of cardiomyocytes associated with partial inactivation of their sodium channels (Miragoli et al., 2006). This is in turn caused by elevation of the resting potential of myocytes because of the electrotonic interaction with fibroblasts, whose resting potential is less negative than that of myocytes. In our pipeline, we could clearly observe such effect at the end of simulations aiming to stabilize myocyte-fibroblasts couplings within the BZ (see Figure 7.5). Moreover, a density of 30% fibrotic tissue in the BZ modelled as fibroblasts caused a significant APDs reduction around the infarct scar (see Figure 7.19), again as a result of the electrotonic interactions through heterocellular couplings (myocyte-fibroblast). Thereby, the consequent decrease in refractory periods allowed the feasibility of applying premature stimulus (S2-S3) at short CIs. In combination with slowed propagation and reduced excitability in the BZ, probably exacerbated at both sides of the epicardial CC due to source-sink mismatches, such a demanding pacing rates managed to stress the tissue at the lower end of the CC enough to finally induce

---

[40] **Video S13.** Negative VT induction on model *#5* (ER+00fib) from pacing site *endo#1*, due to bidirectional functional propagation block. https://youtu.be/xtdoWtn-DGs

a unidirectional propagation block, thus giving rise to the self-sustained macroreentry responsible for monomorphic VT.

Pro-arrhythmic effect of intermediate fibrosis levels in the BZ

Focusing exclusively on those successful model versions that included electrical remodelling in the BZ (models *#5-7*), fibrosis was not strictly necessary to enable positive VT induction, as in the case of model *#5* (ER+00fib). However, moderate fibrosis levels are thought to increase arrhythmogenicity, since it appeared to ease the onset of reentrant VTs in our simulation study. That was the case of models *#6* (ER+10fib) and *#7* (ER+20fib), with 10% and 20% image-based patchy fibrosis within the BZ, respectively. They were the two only model versions that succeeded in *in-silico* tests with PES protocols delivered both from *epi#1* and from *endo#1*. We think this synergic pro-arrhythmic effect of the combination of electrical remodelling and moderate densities of patchy fibrosis in the BZ may arise from several factors: (1) the additional slowing-down of propagation across the BZ induced by the presence of fibrosis (see Figure 7.21), (2) the formation of obstacles for electrical conduction due to clustered accumulations of fibrotic elements within the BZ (see black patches in Figure 7.19), which distort and delay propagation wavefronts that are forced to surround such barriers (de Bakker et al., 1993; Dhanjal et al., 2017), and (3) a further decrease of tissue excitability because of the electrotonic interaction between fibroblasts and electrically remodelled myocytes in the BZ (Miragoli et al., 2006), what likely promotes the generation of those functional propagation blocks responsible for reentrant VTs (Xie et al., 2009; Zlochiver et al., 2008).

Anti-arrhythmic effect of high fibrosis levels in the BZ

In contrast, our simulation study revealed that the combination of electrical remodelling with higher fibrosis levels (30% or more) may become an obstacle to induce VT, rather than a pro-arrhythmic configuration. In our case, regardless of both the pacing site and the configuration of PES protocols (number of premature stimuli, CI length, etc.), model *#8* (ER+30fib) gave rise to permanent bidirectional propagation block at the lower side of epicardial CC,

which prevented from the onset of sustained reentries. One might think that such effect was caused by massive accumulation of fibrotic elements at the lower side of the CC, thereby leading to a structural propagation block due to the formation of a physical barrier. However, model *4* (noER+30fib), which included exactly the same amount and image-based distribution of fibrotic elements as model *8* (ER+30fib), did not show any kind of persistent propagation block, even allowing positive VT induction from point *epi#1*. Therefore, that permanent block in model *8* (ER+30fib) was not a purely structural one but a functional bidirectional block specifically caused by the combination of electrical remodelling and 30% image-based patchy fibrosis in the BZ. The considerable accumulation of fibroblast around the lower end of the epicardial CC reduced the excitability of its still conducting tissue, due to partial inactivation of sodium channels caused by electrotonic myocyte-fibroblast interaction. Additionally, tissue excitability was further decreased as a consequence of the reduction in sodium channel conductivity associated with the electrical remodelling in the BZ. Hence, we finally concluded that the combination of all those effects resulted in such a strong inactivation of sodium channels that myocytes located at the lower terminal end of the epicardial CC became completely unable to trigger a depolarization, thus leading to the persistent functional propagation block in model *8* (ER+30fib). On the other hand, although model *4* (noER+30fib) did not show permanent blocks, it did exhibit the consequences of partial tissue inactivation induced by its high fibrosis level. Because of the intense electrotonic load exerted by such an important number of fibroblasts, every time that the propagation wavefront reached the lower end of the epicardial CC, it took notably longer to cross to the other side on model *4* (noER+30fib) than on any other model version, except for model *8* (ER+30fib), evidently. Moreover, this conduction delay at the lower side of the CC happened always, regardless of the propagation direction, both from inside the channel towards the apical side of MI and in opposite direction, as can be observed in Video S6[41].

---

[41] **Video S6.** Positive VT induction on model *4* (noER+30fib) from pacing site *epi#1*. https://youtu.be/nJAsVjX_67A

All those effects observed in our simulation study resulting from the combination of electrical remodelling and different fibrosis levels in the BZ match the conclusions reached in a previous work (McDowell et al., 2011). This is also a simulation study using a 3D model of infarcted rabbit ventricles built from high-resolution *ex-vivo* images, which included electrical remodelling similar to ours in the BZ. Additionally, that work assessed the influence on infarct-related arrhythmogenicity of various fibrosis levels (0%, 10% and 30%) within the BZ, introduced as randomly distributed diffuse fibrosis in that case. McDowell *et al.* concluded that intermediate densities of diffuse fibrosis (10%) in the BZ increases vulnerability to infarct-related VTs with respect to the case of no fibrosis. By contrast, they observed a protective role against VT as a result of high fibrosis levels (30%), due to the generation of persistent propagation blocks that hampered the onset of reentrant activities instead of promoting them. Therefore, our approach of image-based patchy fibrosis in the BZ of human chronically infarcted ventricles, resulted in a density-dependent impact on infarct-related arrhythmogenicity similar to that observed in that work as a consequence of random diffuse fibrosis in rabbit ventricles (McDowell et al., 2011).

Influence of pacing sites location on VT inducibility

The absolute failure of pacing site *epi#2*, along with the fact that models *#4* (noER+30fib) and *#5* (ER+00fib) enabled positive VT induction from point *epi#1* while they failed from *endo#1*, gives an idea of the key importance of the location of a given pacing site on the final result of VT inducibility tests. This is also endorsed by other unexpected results, as it was the case of model *#5* (ER+00fib) paced from point *endo#1*, which was the only configuration that gave rise to non-persistent functional bidirectional block at the lower side of the epicardial CC, thus avoiding the onset of sustained reentry (see Video S13[42]). Moreover, location of pacing sites may also have a great influence on the morphology of induced VTs. That is the reason why, in addition to the two pacing sites previously tested in the real EP study (*epi#1* and *endo#1*), we added point

---

[42] **Video S13.** Negative VT induction on model *#5* (ER+00fib) from pacing site *endo#1*, due to bidirectional functional propagation block. https://youtu.be/xtdoWtn-DGs

epi#2 aiming to assess the feasibility of generating propagation blocks at the upper side of the CC, rather than at the lower one. Actually, despite the need of a third premature stimulus (S4 phase), pacing from point *epi#2* did manage to create functional propagation block at the upper terminal end of the epicardial CC on model *#5* (ER+00fib). However, it could not trigger VT because there was a collision at the lower side of CC that prevented from the onset of reentrant activity (see Video S10[43]). Anyhow, assuming that in some case propagation block at the upper side of the CC had been able to effectively trigger the onset of sustained reentry, the resulting monomorphic VT would have shown a different morphology. In such a case, the induced VT would have exhibited an anticlockwise macroreentrant propagation pattern, instead of the clockwise pattern described by the VT actually induced in the *in-silico* tests. Hence, it is evident that such a different propagation pattern would have significantly altered the morphology of the ECG associated with that VT episode.

Impact of MI geometry on VT inducibility

Besides the location of pacing sites, the geometry of the MI also plays an essential role in the mechanisms related to the initiation of reentrant VTs, especially the geometrical features of CCs crossing the infarct scar with the capability of acting as structural substrates for reentrant activity. In the case of our ventricular model, for instance, the particular geometry of epicardial CC was the main factor for which such structure was much more prone to generate functional propagation blocks at its lower side than at the upper one. The lower end of the epicardial CC presented a narrow funnel shape, notably narrower than the upper side (for more details of CC geometry see Chapter 5, section 5.1.6). Furthermore, source-sink mismatches due to abrupt changes in the geometry of excitable tissue are widely considered as a really important factor in promoting functional propagation blocks (Ciaccio et al., 2018; Connolly et al., 2015; Fast and Kleber, 1995). Therefore, due to its narrower section width giving rise to more abrupt changes in its geometry, it is very likely that the lower end of the epicardial CC was subject to a considerably more intense impact on

---

[43] **Video S10.** Negative VT induction on model *#5* (ER+00fib) from pacing site *epi#2*.
https://youtu.be/XWC9MMWigh0

propagation than the wider upper side, as a result of those source-sink mismatches. Both sides of the epicardial CC were affected to a similar extent by the reduction in CVs, large APD gradients mainly caused by electrical remodelling and partial tissue inactivation resulting in additional slowing-down of conduction due to fibrosis. Consequently, we finally concluded that the particular geometry of the epicardial CC appears to be the key element underlying the mechanisms by which unidirectional propagating blocks triggering self-sustained reentry, always happened at the lower side of the channel, thus determining the morphology of the monomorphic infarct-related VT, both in the clinic and in our simulation case study.

This highlights the great influence of the geometrical characteristics of both infarct scar and BZ on VT mechanisms, as discussed in a very recent computational study aimed at assessing the impact on arrhythmogenicity of the 3D architecture of viable tissue surrounding infarct scars (Pashakhanloo et al., 2018).

Chapter 8

Discussion

In this chapter we will discuss in detail all the elements involved in the pipeline of personalized computational simulation of cardiac electrophysiology (EP) proposed in this work, including the clinical data, the methods used to carry out the main tasks related to the development of the 3D models and all the decisions made in order to computationally model the EP behaviour of the different regions included in the 3D ventricular model. In addition, we will comprehensively review the results obtained from the retrospective personalized *in-silico* EP study that we performed, as well as the conclusions derived from those results. Finally, we will deal with the major limitations associated with this work.

Although presented here in a considerably further extended fashion, it must be noted that part of the content of this chapter was already included in a research article entitled "*Personalized cardiac computational models: from clinical data to simulation of infarct-related ventricular tachycardia*", which was recently published in the indexed international journal *Frontiers in Physiology* in May 2019 (Lopez-Perez et al., 2019).

8.1. Clinical data

Since it is currently the gold-standard technique for *in-vivo* assessment of myocardial ischaemic injury in clinical environments (Jamiel et al., 2017; Mahida et al., 2017; Patel et al., 2017), cardiac DE-MRI is a routine imaging test for infarcted patients referred for RFA procedures (Al-Khatib et al., 2018; Pedersen et al., 2014; Priori et al., 2015). Therefore, the use of such image modality satisfies our requisite of exclusively using non-invasive clinical data aiming to enable the feasibility of performing prospective *in-silico* EP studies prior to RFA procedures.

It is important to note that the accurate reconstruction of the 3D geometry of CCs is a critical element in generating 3D computational models of infarcted ventricles able to virtually reproduce clinical VTs (Deng et al., 2018; Pashakhanloo et al., 2018; Ukwatta et al., 2016), thus providing precise prediction of reentrant pathways to be ablated. Evidently, this is hardly possible by using low-resolution images, so achieving accurate 3D reconstructions requires image datasets of high resolution (Deng et al., 2015). In our particular case, we used a DE-MRI stack with isotropic voxel of 1.4 mm^3, that is, with in-plane resolution of 1.4×1.4 mm and spacing of 1.4 mm between consecutive slices. It is a relatively high resolution for *in-vivo* cardiac DE-MRI images, as they are usually acquired in the clinical environment with good in-plane resolution but showing gaps of 8-10 mm between slices. Nonetheless, cardiac DE-MRI with spatial resolution high enough to allow proper reconstructions of the 3D structure of CCs are clinically feasible, as it actually was in the case used in this work.

Regarding the EAMs provided by CARTO® system, it must be highlighted that we did not use them for constructing or personalizing the 3D ventricular model of cardiac EP, but for testing and validation purposes only. Note that the stabilization of 3D ventricular models in sinus rhythm, which we carried out by using the CARTO®-derived sinus activation sequence, is not a necessary step prior to conducting *in-silico* tests of VT inducibility. In fact, among the previous simulation studies aimed at RFA planning for infarct-mediated reentrant VTs, none of them included a similar stabilization stage. Thus, we did not perform

the sinus activation simulations aiming for model stabilization itself, but for assessing the capability of the set formed by patient-specific 3D ventricular model and 3D torso model to reproduce patient's ECG.

On the other hand, in those RFA procedures aimed at terminating infarct-related VTs, the myocardium affected by the MI (infarct scar and BZ) is the most thoroughly mapped region in order to find CCs across the scar as potential substrates for reentry (Baldinger et al., 2016; Pokorney et al., 2016; Soejima et al., 2002). In that region, most of EGMs show low amplitudes and/or very fractionated signals (Aliot et al., 2009; Bogun et al., 2005; Gardner et al., 1985), thus leading to a high uncertainty degree in LATs measurement. That is why we had to exclude such a large amount of CARTO® points: 462 points were removed out of a total amount of 847 included in the original CARTO® data. Nevertheless, the EAMs used in this work were recorded by the *NaviStar® ThermoCool®* catheter, which only enables point-by-point mapping process. Currently, there are catheters including multielectrode arrays with smaller electrodes (mini-electrodes), such as the *PentaRay®* for CARTO® 3 System (Biosense Webster, Inc., Diamond Bar, CA, USA) or the *IntellaMap Orion*™ for Rhythmia HDx™ System (Boston Scientific, Marlborough, MA, USA) (Mantziari et al., 2015). Those multielectrode catheters allow acquiring much larger amounts of points (denser maps) and more precise EGM signal recordings (less noisy) due to their smaller sensing areas, thereby resulting in more accurate measurements of unipolar and bipolar voltages, LATs, activation patterns, etc. (Acosta et al., 2018; Josephson and Anter, 2015).

8.2. Patient-specific ventricular model

This section addresses a number of issues related to the development of the patient-specific 3D ventricular model, specially focusing on the different features included in the model, such as the high level of detail in the reconstructed cardiac anatomy, the incorporation of cardiac fibre orientation, the method used to generate the personalized 3D geometry of the MI, including the infarct scar and the BZ, and the strategies employed to include patchy fibrosis within the BZ.

8.2.1. Detailed endocardial anatomy

From the anatomical point of view, we built a highly detailed patient-specific 3D ventricular model. Unlike ours, most of the 3D models of human ventricles used in other works do not include papillary muscles and endocardial trabeculations, especially when they are based on *in-vivo* images. Subtlety and high inter-subject variability of endocardial structures add difficulty to the already challenging task of segmenting *in-vivo* cardiac imaging datasets. Lange *et al.*, for instance, studied the impact on activation patterns of hearts suffering from left bundle branch block (LBBB) caused by endocardial details, including papillary muscles and false tendons. However, such structures were not segmented from images but synthetically added to a population of 3D human ventricular models derived from a statistical cardiac atlas (Lange et al., 2016).

In our particular case, neither papillary muscles nor trabeculations appeared to have any significant effect on VT mechanisms. However, considerable influence on activation patterns of some endocardial structures, such as the moderator band in RV, has been observed both experimentally (Durrer et al., 1970) and by computational simulation (Bishop et al., 2010), as well as its potential role in VT settings (Bogun et al., 2008; Kim et al., 1999b; Walton et al., 2018). Hence, further investigations with large cohorts of patients would be required to assess the convenience of systematically including endocardial details in patient-specific models oriented to infarct-related VT simulations, as well as to evaluate to what extent it would be worth the effort.

8.2.2. Cardiac fibre orientation

In our pipeline, cardiac fibre orientation defining myocardial architecture was generated and included in the 3D ventricular model by means of a rule-based approach based on population data, as explained in Chapter 6 (see section 6.2.3). Currently, the only option able to provide personalized information about myocardial structure is the use of diffusion tensor imaging (DTI). This is a MRI modality capable of measuring the diffusion of water molecules within biological tissues non-invasively, with the ability of revealing the direction of the longitudinal axis of myocytes within the myocardium (Holmes et al., 2000; Hsu

et al., 1998; Scollan et al., 1998). In fact, DTI-derived fibre orientation was used in various simulation studies aiming for infarct-related VTs performed with ventricular models built from *ex-vivo* images of different animal species (Arevalo et al., 2008, 2013; McDowell et al., 2011; Pashakhanloo et al., 2018; Pop et al., 2011a, 2011b). Unfortunately, despite several recent promising advances (McGill et al., 2015b, 2015a; Nguyen et al., 2016; Nielles-Vallespin et al., 2017; Stoeck et al., 2017), *in-vivo* cardiac DTI remains highly challenging due to the artefacts caused by cardiac motion. Indeed, even in *ex-vivo* settings, the acquisition of cardiac DTI sequences at a spatial resolution high enough to provide complete information about myocardial structure may take several tens of hours (Huang et al., 2019; Pashakhanloo et al., 2017, 2018). Nonetheless, an approach was proposed to estimate patient's LV fibre orientation from a few 2D slices of *in-vivo* cardiac DTI (Toussaint et al., 2013) making use of a statistical atlas based on *ex-vivo* DTI from canine hearts (Peyrat et al., 2007).

Anyhow, currently *in-vivo* cardiac DTI cannot be acquired with sufficient spatial resolution to provide full patient-specific fibre orientation and, furthermore, this technique is not clinically available, what is a requisite of our work. Moreover, some studies have compared simulation results performed on 3D ventricular models using fibre orientation derived from both rule-based methods and *ex-vivo* DTI (Bayer et al., 2012; Bishop et al., 2009; Pop et al., 2011b). In all cases, the minor differences found in electrical propagation patterns at global level were considered not significant, what confirms the validity and robustness of rule-based approaches based on experimental data for simulation studies of cardiac EP.

An alternative to rule-based approaches is the use of atlases of cardiac fibre orientation generated from high-resolution *ex-vivo* DTI images (Lombaert et al., 2012; Peyrat et al., 2007; Vadakkumpadan et al., 2012). In such a case, the atlas is registered to the 3D geometry of a particular patient-specific ventricular model by means of transformation algorithms, with the final aim to map the fibre orientation into a target model (Ringenberg et al., 2014). Nevertheless, such approach is much more computationally expensive than rule-based strategies. Furthermore, as in the case of DTI-derived fibre orientation, the use of those atlases do not seem to provide any significant improvement to the

simulation results compared to validated rule-based methods, as discussed in a recent review on infarct-related VT simulation by Trayanova and colleagues (Trayanova et al., 2017).

For the region of MI, we did not consider fibre orientation in the infarct scar because it was modelled as non-excitable tissue, so myocardial architecture in that region would have caused no impact on simulated propagation patterns. Concerning the BZ, both *ex-vivo* DTI (Winklhofer et al., 2014; Wu et al., 2006) and histological preparations (Rutherford et al., 2012; Tschabrunn et al., 2016) have revealed cardiac fibre disarray within the BZ, what would necessarily result in alterations of tissue anisotropy. Conversely, a recent study based on very high-resolution DTI observed good preservation of normal fibre orientation patterns in chronically infarcted regions, both in porcine and in human hearts (Pashakhanloo et al., 2017). Hence, there is no consensus about the preservation degree of cardiac fibre orientation within the BZ of healed infarctions. On the other hand, the study of the relation between fibre orientation within infarcted regions and ventricular arrhythmias has begun very recently (León et al., 2019), so that the potential role of the specific organization (or disorganization) of cardiac fibres in the BZ on infarct-related VT mechanisms or inducibility is still to be properly determined. Furthermore, none of those simulation studies using 3D models with myocardial architecture derived from *ex-vivo* DTI images has reported any significant influence on infarct-related VT mechanisms caused by such image-based fibre orientation patterns (Arevalo et al., 2008, 2013; McDowell et al., 2011; Pashakhanloo et al., 2018; Pop et al., 2011a, 2011b). Therefore, because of the current uncertainty on this issue, we decided to keep in the BZ the physiological fibre orientation pattern provided by the rule-based method used in our pipeline, as recommended in the above-mentioned review article (Trayanova et al., 2017).

8.2.3. Myocardial infarction segmentation

We used the well-known *SD method* (Kim et al., 1999a) to perform the segmentation of the infarcted region from cardiac DE-MRI images aiming to generate 3D reconstructions of the patient-specific geometry of the infarct scar

and BZ, as described in Chapter 5 (see section 5.1.3). The SD method is a state-of-the-art algorithm, which is based on a quite simple semi-automatic segmentation strategy based on thresholding. In fact, it involves a significant degree of previous interaction, usually performed manually, since it requires prior delineation of the LV myocardium, as well as the definition of two distinct ROIs (*remote* and *infarcted*) on every DE-MRI slice containing an infarcted area.

However, while *in-vivo* cardiac DE-MRI is widely considered as the current gold-standard test to evaluate myocardial ischaemic damage non-invasively (Jamiel et al., 2017; Mahida et al., 2017; Patel et al., 2017), there is a lack of consensus on the proper non-manual algorithm and thresholds for the delineation of MI contours from such image modality (Mesubi et al., 2015; Varga-Szemes et al., 2016). Consequently, in the two last decades a considerable amount of alternative methods have been developed aiming to segment the MI from cardiac DE-MRI datasets (see (Karim et al., 2016; McAlindon et al., 2015; Mesubi et al., 2015; Varga-Szemes et al., 2016) for a review on this topic), although it must be highlighted that many of them are variations of the original SD method. Nevertheless, full automated segmentation of MI from *in-vivo* cardiac DE-MRI is still an open challenge, while semi-automatic thresholding methods based on SD currently remain the most widely used strategies in clinical environments (Varga-Szemes et al., 2016).

A few computational studies on 3D simulations of infarct-related VTs have assessed the impact on VT inducibility and features derived from the use of different methods and/or thresholds for the 3D reconstruction of MI from DE-MRI images (Deng et al., 2018; Ng et al., 2012; Ukwatta et al., 2016). Those studies showed that defective 3D geometries resulting from inaccuracies in MI segmentation can significantly affect the inducibility and characteristics of simulated VTs. However, as an overall conclusion, the use of adequate threshold values appears to be a notably more influential factor than the choice of a particular segmentation method. Indeed, SD-based methods and even simpler thresholding algorithms, such as variations of the full-width-at-half-maximum (FWHM) strategy, remain commonly used in works aiming to study infarct-related VTs by means of computational simulation with 3D models derived from

in-vivo cardiac DE-MRI datasets (Arevalo et al., 2016; Ashikaga et al., 2013; Chen et al., 2016; Deng et al., 2016; Prakosa et al., 2018).

Importantly, evaluating the impact on simulation outcomes caused by the use of a certain segmentation algorithm was not included among the aims of this work, and neither the comparison between different methods. This, together with lack of consensus on a reference segmentation technique, finally led us to opt for the most standard approach for the segmentation of the infarcted region from DE-MRI images. Hence, we chose the original SD method (Kim et al., 1999a), as it currently remains the most used technique (Varga-Szemes et al., 2016). Such algorithm is simple and, thus, straightforward to implement. In addition, it allows to easily discriminate between infarct scar and BZ by applying distinct thresholds. Furthermore, as commented above, its use remains widely spread both in clinical environments and in the computational cardiology field.

Concerning the chosen thresholds, we used 3×SD and 2×SD above mean value for the infarct scar and the whole MI (enclosing both infarct core and BZ), respectively. Remember again that we did not aim to assess the influence of any segmentation parameter on the simulation results, so those thresholds were selected based on the related literature. Despite there is a considerable variability in the SD-based thresholds proposed in a large number of works, those values (3×SD and 2×SD) are widely used in experimental studies, likely being the most common ones for SD method ((Fieno et al., 2000; Hsu et al., 2006; Kim et al., 1999a; Kolipaka et al., 2005; Mesubi et al., 2015; Perez-David et al., 2011; Yan, 2006), just to cite a sample of works using those values).

8.2.4. Fibrosis in the border zone

A few previous simulation studies focused on mechanisms associated with infarct-related VTs have also included fibrosis within the BZ. Some authors incorporated random diffuse fibrosis modelled as electrically passive pieces of tissue (fibroblasts) in a 3D model of rabbit ventricles (McDowell et al., 2011) or micro-regions (patches) of non-conducting scarred tissue in a 3D canine model

(Arevalo et al., 2013). Similarly, a very recent work included randomly generated patterns of non-conducting fibrotic tissue within the BZ in a 3D model of infarcted rabbit ventricles (Campos et al., 2018). Another work faithfully reproduced the distribution of fibrosis in the BZ by means of highly detailed 3D models of wedge samples resulting from the reconstruction of high-resolution histological sections from two infarcted rat hearts, considering it as non-conducting dense fibrotic tissue (collagen) intermingled with healthy myocardial tissue in the BZ (Rutherford et al., 2012).

However, for obvious reasons, histological studies are not an option to personalize fibrosis patterns in image-based 3D cardiac models aiming to reproduce the cardiac EP of alive individuals. As commented above (see section 8.1), DE-MRI is currently the gold-standard modality for the assessment of cardiac fibrosis from *in-vivo* images. Hence, *in-vivo* DE-MRI is at present the most reliable data source for the generation of personalized fibrosis patterns in 3D cardiac models, as in the case of our image-based approach for patchy fibrosis within the BZ. Indeed, using an image-based approach similar to ours, a recent work included realistic patterns of fibrosis based on DE-MRI images, although in that case the aim was to assess the impact on atrial fibrillation dynamics derived from different computational strategies to model the fibrotic tissue by means of a simulation study with a 3D model of the human left atrium (Roney et al., 2016).

Nevertheless, in spite of being the reference technique, it is important to note that the gadolinium-based contrast agent used in DE-MRI studies is known to be non-specific for fibrosis, which indeed is an extracellular tracer (Saeed et al., 2001; Weinmann et al., 1984). Despite the underlying physiological mechanisms still remain to be fully elucidated (Kwong and Farzaneh-Far, 2011), gadolinium chelates are unable to cross the membrane of intact cells (Weinmann et al., 1984), so the hyperenhancement of signal intensity in DE-MRI images is commonly assumed to result from the diffusion of contrast agent through extracellular space (Mewton et al., 2011; Moon et al., 2004), which is expanded in the chronic fibrotic regions resulting from the MI healing process (Daskalopoulos et al., 2012; Hein and Schaper, 2001; Seidel et al., 2016). Moreover, each voxel of DE-MRI images is known to comprise thousands of cells of different types because of the limited spatial resolution of MRI techniques,

which is much larger than the size of cardiac cells, especially in *in-vivo* acquisitions (Hsu et al., 2006), thus leading to the so-called partial volume averaging effect (Varga-Szemes et al., 2016). Therefore, in accordance with histological observations, it is widely assumed that voxels showing intermediate intensity levels in DE-MRI images (usually classified as BZ) correspond to a mixture of myocytes and fibrotic tissue at microscopic scale (Hsu et al., 2006; Schuleri et al., 2009; Varga-Szemes et al., 2016). Then, regardless of the method used for MI segmentation, it seems reasonable to consider that those voxels identified as BZ showing the highest intensity levels within that region in DE-MRI images, probably correspond to pieces of myocardium composed of a mixture of tissue types where the percentage of fibrotic tissue is considerably high. Consequently, classifying those brightest voxels as fibrotic elements appears to be a suitable approach to define patient-specific fibrosis distributions in the BZ based on *in-vivo* DE-MRI images.

On the other hand, we must remember that the intensity level of each DE-MRI voxel was assigned (mapped) to a cluster comprising several elements of the volume mesh of 3D model (up to 64 elements) due to the large size of voxels (1.4 mm^3) relative to the size of hexahedral elements (about 0.4 mm^3). This circumstance, along with the fact that those brightest voxels in the BZ are commonly surrounded by others with similar intensities, leads our image-based method to generate scattered fibrotic patches within the BZ, giving rise to patterns of patchy fibrosis similar to those observed in histological examinations (Rutherford et al., 2012; Schuleri et al., 2009).

8.3. Electrophysiological modelling

In this section we discuss all the assumptions and decisions that we made in order to computationally model the EP behaviour of the different tissues and regions included in our patient-specific 3D model of the infarcted ventricles, comprising the EP features assigned to healthy ventricular myocardium, infarct scar and BZ. Moreover, we deal with the implications and consequences resulting from those assumptions and decisions related to the EP modelling.

8.3.1. Healthy myocardium. Transmural heterogeneity

As explained in Chapter 6 (see section 6.1.1), we considered the transmural EP heterogeneity of ventricular myocytes in our 3D model by defining three discrete layers for endocardial, mid-myocardial and epicardial cells, which encompassed 17%, 41% and 42% of myocardial wall thickness, respectively. Nevertheless, the actual distribution of those three different kinds of ventricular myocytes remains controversial, as well as the existence of M cells itself (Opthof et al., 2009, 2016). Moreover, a recent experimental study showed significant inter-subject variability in repolarization patterns (Opthof et al., 2017), which are supposed to be determined by the distinct APDs associated with the different cell types.

Anyhow, as a general rule, it is widely assumed that the repolarization starts at the epicardium and then proceeds to endocardium in human ventricles. The transmural EP heterogeneity in the ventricles (i.e., APD variation between neighbour layers) is usually considered to be the most likely responsible for that behaviour resulting in the T wave in ECG signals (Franz et al., 1987; Patel et al., 2009). In fact, according to several computational studies, to reproduce positive T waves on precordial leads by simulation, the transmural heterogeneity (including M cells) must be considered in order to create a transmural repolarization gradient leading to repolarization patterns starting at epicardium (Hurtado and Kuhl, 2014; Okada et al., 2011; Perotti et al., 2015). Then, the correct polarity of T waves in the precordial leads of simulated ECGs resulting from our sinus activation simulations (shown in Chapter 7), indicates that the distribution that we chose for transmural layers seems to be a suitable approximation to computationally reproduce the physiological EP heterogeneity of human ventricular myocardium. Furthermore, the same percentages were used in previous simulation studies, also resulting in realistic positive T waves in the precordial leads of simulated pseudo-ECGs (Dux-Santoy et al., 2011, 2013).

8.3.2. Infarct scar

Despite it is not an entirely acellular tissue (Rog-Zielinska et al., 2016; Sun et al., 2002), the region of infarct scar mostly correspond to extracellular matrix

composed of collagen (Cleutjens et al., 1999; Daskalopoulos et al., 2012; van den Borne et al., 2010). Nonetheless, a recent experimental study observed electrical conduction across the infarct scar due to its electrotonic properties, which were mainly attributed to the presence of fibroblasts in that region (Mahoney et al., 2016a), thus demonstrating that the scarred tissue is not completely electrically inactive.

When the bidomain model is used, the infarct scar is usually modelled as a bath representing the extracellular space, which can exert a slight electrotonic effect over the surrounding tissue that depends on the conductivity values assigned to the scarred tissue (Connolly et al., 2015). However, we used the monodomain model, in which extracellular space is not represented. In such a case, a passive model at the cellular level combined with low conductivity values at tissue level could be used to account for the electrotonic load caused by the infarct scar (Deng et al., 2015; Ringenberg et al., 2014). In this regard, we performed some tests assigning the MacCannell model for cardiac fibroblast to the scar region, as previously done by others (McDowell et al., 2011). Nevertheless, the use of an ionic model, even being a passive one, necessarily involves the definition of a resting potential, which is about –49 mV for MacCannell model. As a consequence, when we computed the ECG, the resulting signals showed considerable distortion because of the presence of such a large region (infarct scar comprised 16% of LV myocardium in our model) that practically remained at resting potential at every moment along the simulation, thus producing a remarkable gradient that was captured by the ECG. Hence, this circumstance affected the cardiac dipole significantly at the organ level, giving rise to an important distortion in simulated ECG signals at the body level.

That unwanted "*side effect*" would be critical for this work, since obtaining faithful simulations of the ECG is one of our main goals to be able to compare the simulation results with the patient's non-invasive recordings, that is, with the clinical standard ECG. That is the main reason why we finally decided to disregard the subtle electrotonic effect of the infarct scar. Hence, we modelled the scar as a pure insulator by imposing no-flux boundary condition at the interface between scar and surrounding tissue, as previously done in many

other computational studies on infarct-related VTs (Arevalo et al., 2013, 2016; Ashikaga et al., 2013; Deng et al., 2018; Pashakhanloo et al., 2018; Prakosa et al., 2018; Rantner et al., 2012; Relan et al., 2011).

8.3.3. Infarct border zone

With respect to the electrical remodelling in the BZ, it must be noted that all changes affecting the ionic channels that we considered in this regard, are based on experiments with cells harvested from epicardial BZs of canine hearts (Dun et al., 2004; Jiang et al., 2000; Pu and Boyden, 1997). As recently discussed elsewhere (Connolly and Bishop, 2016), it is unclear to what extent those data are representative of the electrical remodelling in the BZ of human hearts. The presence of epicardial collateral circulation in canine hearts, not present in humans, is known to influence the formation of the epicardial BZ in dogs (Schaper et al., 1988; Ursell et al., 1985), what could give rise to functional differences with respect to the surviving myocytes in human BZs.

Moreover, those studies reporting experimental evidence of the electrical remodelling in canine BZs (Dun et al., 2004; Jiang et al., 2000; Pu and Boyden, 1997) were all performed a few days after the coronary occlusion, that is, still in the healing phase of MI rather than in its chronic stage. Indeed, results from other experimental studies suggest that the surviving myocytes in the BZ tend to progressively recover normal EP properties along the MI healing process, such that in the chronic stage of MI those myocytes may even exhibit AP features similar to those of the healthy tissue, as discussed in a very recent review article (Mendonca Costa et al., 2018). Despite this, those data have been widely used in previous computational studies (Arevalo et al., 2013, 2016; Ashikaga et al., 2013; Deng et al., 2015, 2018; Hill et al., 2016; McDowell et al., 2011; Pashakhanloo et al., 2018; Prakosa et al., 2018; Rantner et al., 2012; Ringenberg et al., 2014), due to the lack of experimental data on the ionic (electrical) remodelling in the BZ of chronically infarcted human hearts.

On the other hand, the slowed conduction across the BZ is widely considered as a key factor in promoting reentry through CCs crossing the infarct

scar, as it allows the working myocardium at the other side to recover its excitability before the arrival of the wavefront coming from inside the channel (de Bakker et al., 1993; Lazzara and Scherlag, 1984; Nguyen et al., 2014). However, the underlying mechanisms of this reduction in CVs are not totally clear yet. Several studies mainly blame this reduction on the presence of dense fibrosis (collagen) scattered within the BZ, as it forces the propagation wavefront to take tortuous pathways resulting in substantial conduction delays (de Bakker et al., 1993; Engelman et al., 2010; Rutherford et al., 2012). To reproduce such slowed propagation in the BZ computationally, some authors drastically reduced only the transverse CV (Arevalo et al., 2013, 2016; Deng et al., 2015, 2018; McDowell et al., 2011; Prakosa et al., 2018). This could represent the severe reduction measured in gap junctional conductance in canine BZs only in the transverse direction (Yao et al., 2003) and/or the loss of side-to-side coupling between adjacent layers of myocytes due to the isolating effect of infiltrated fibrotic tissue (Spach and Boineau, 1997). Downregulation and lateralization of connexin 43 (Cx43), the main protein constituting gap junctions in human ventricular myocytes, have been also experimentally reported in the BZ (Severs et al., 2008; Smith et al., 1991). Downregulation of Cx43 might result in an isotropic reduction of CVs and its lateralization would exacerbate this effect in the longitudinal direction, while keeping or even increasing the transverse CV. Nonetheless, part of those lateralized gap junctions in the remodelled cardiomyocytes of the BZ are thought to be non-functional (Matsushita et al., 1999). Moreover, disorganization of cardiac fibres in the BZ might importantly affect the electrical propagation across that region, as the ratio between CVs in the different directions is determined by the specific arrangement of cardiomyocytes composing the ventricular myocardium. Thus, any remodelling in the organization of cardiac fibres would consequently alter the electrical anisotropy of myocardial tissue. However, the existence of cardiac fibre disarray within the BZ is also controversial, since there are different experimental studies reporting contradictory results in relation to this issue, as discussed above (see section 8.2.2).

In conclusion, the slowed conduction in the BZ seems to be the result of a really complex combination of structural, electrical, gap junction and cardiac fibre remodelling that is not well understood yet (de Bakker, 2017). Hence,

currently there is a lack of consensus on the proper way to model the BZ in order to reproduce such CVs reduction by replicating its underlying mechanisms in the computational cardiac models. In our particular case, in addition to the image-based patchy fibrosis, we imposed an isotropic reduction of CVs in the BZ (both longitudinal and transverse CVs were reduced to 25% [CVsBZ-25%]), aiming to reproduce macroscopically the global effect of all those diverse factors affecting the propagation and promoting the reentrant activity, as previously done in other computational studies (Hill et al., 2016; Ringenberg et al., 2014).

Regarding myocyte-fibroblast coupling, there is experimental evidence of the existence of this kind of heterocellular connection via gap junctions (connexins) in the remodelled myocardium resulting from MI (Camelliti et al., 2004; Mahoney et al., 2016b; Schwab et al., 2013), as well as by tunnelling nanotubes (Quinn et al., 2016). However, the myocyte-fibroblast coupling in the BZ of chronic MIs has not been properly characterized by experimental studies in terms of density and distribution of functional gap junctions connecting both cell types (Ongstad and Kohl, 2016). Therefore, the magnitude and the anisotropy of the electrotonic load resulting from myocyte-fibroblast couplings in the BZ remain undetermined. Despite this, we considered this possible influence by modelling the fibrosis within the BZ using a passive fibroblast model (MacCannell et al., 2007) at the cellular level, as already done in (McDowell et al., 2011) and, more recently, in a simulation study using a detailed 3D atrial model (Godoy et al., 2018). Furthermore, we defined an isotropic low conductivity at tissue level for fibrotic patches, such that this conductivity value mainly affected the coupling between adjacent myocytes and fibroblasts within the BZ by modulating the magnitude of their electrotonic interaction.

8.4. Computational simulation of cardiac EP

Regarding the computational simulation, below we comment on several concerns linked to the performance of our simulations of cardiac EP from the mathematical and computational points of view. After that, we present a thorough discussion about the simulation results obtained from the retrospective personalized *in-silico* EP study that we carried out in this work.

Furthermore, this discussion also addresses the conclusions derived from those simulations results in relation to the infarct-related VT mechanisms.

8.4.1. Numerical considerations

The monodomain model is a widely used mathematical approach to simulate the propagation of electrical activation wavefronts across cardiac tissue. However, it derives from a simplification of the bidomain model, which is more physiologically realistic, although significantly more computationally demanding, as explained in Chapter 6 (see section 6.2.1). A computational study specifically aimed at this issue only found insignificant discrepancies between the activation patterns in simulations at the organ level derived from both bidomain and monodomain models (Potse et al., 2006). Consequently, the monodomain model is widely accepted as a valid approach for propagation studies, while the bidomain model is considered to be strictly necessary only for simulations in which external electric fields are applied, such as studies related to defibrillation shocks (Potse, 2012; Trayanova, 2011; Vigmond et al., 2009). In fact, the monodomain model has been used in numerous studies performing computational simulations of cardiac EP similar to ours (Arevalo et al., 2016; Ashikaga et al., 2013; Deng et al., 2015, 2018; McDowell et al., 2011; Pashakhanloo et al., 2018; Prakosa et al., 2018; Ringenberg et al., 2014).

Concerning the spatial mesh resolution, recommended values for 3D simulations of cardiac EP based on FEM method are usually around 0.25 mm (Plank et al., 2008). Nonetheless, the developers of ELVIRA, the FEM solver used for our 3D simulations (Heidenreich et al., 2010a), performed several tests in 3D models with different spatial resolutions using the same AP model as we have used in this work (ten Tusscher and Panfilov, 2006b). They demonstrated that a spatial discretization of 0.4 mm (and even greater, up to 0.5 mm) is a suitable trade-off that ensures the stability of numerical solution, thereby allowing a substantial reduction in the number of degrees of freedom and, consequently, in the computational burden associated with the cardiac EP problem (Heidenreich et al., 2010a).

On the other hand, the use of a hexahedra-based mesh for the ventricular model provided a restricted variability of edges length, which tend to be wider in the case of tetrahedra-based meshes. In our 3D ventricular model, most of the volume elements nearly preserved the shape of a regular hexahedron (i.e., a perfect cube), since only the elements closest to the external boundaries were deformed in order to fit the smooth surface that faithfully represented the patient-specific anatomy, as shown in Chapter 5 (see figures in section 5.1.2.1). A reduced variability in element size is a critical feature of FEM meshes for cardiac EP problems in order to avoid unexpected and uncontrolled variations in CVs, which might lead to numerical artefacts or even propagation blocks, especially when the average edge length is relatively large (Prassl et al., 2009).

Regarding the integration time step (*dt*), we used a value of 0.02 ms, which is widely used in the field of computational cardiac EP in combination with the ten Tusscher model. Furthermore, this value was tested and validated by both the ELVIRA developers (Heidenreich et al., 2010a) and the authors of the AP model used in this work for human ventricular myocytes (ten Tusscher and Panfilov, 2006b).

8.4.2. Personalized *in-silico* EP study

As demonstrated by the results analysed in Chapter 7, our approach was able to reproduce the clinical infarct-related VT of a particular patient by means of computational simulation of cardiac EP performed with the patient-specific 3D model of ventricles constructed from clinical DE-MRI. Furthermore, we managed to replicate patient's ECG, both in sinus rhythm and during a clinical VT episode. In the latter case, the ECG was reproduced with enough accuracy to undoubtedly identify the simulated VT as the same as the VT spontaneously suffered by the patient. In this work, we carried out a retrospective *in-silico* EP study aiming to test the ability of our approach to predict reentrant circuits through infarct scars as optimal ablation targets. Nonetheless, the design of our pipeline is completely based on non-invasively recorded data, basically high-resolution clinical DE-MRI and standard ECG recordings, while EAMs provided

by CARTO® system were exploited exclusively for testing and validation purposes. Therefore, it might be perfectly used to perform prospective *in-silico* EP studies aiming to identify reentrant pathways, thus helping electrophysiologists in choosing optimal ablation sites prior to actual RFA procedures. Hence, we believe that the approach proposed in this work is capable of becoming a helpful tool for planning of RFA procedures aimed at eliminating infarct-related VTs. At least in this particular case, which has served as a proof-of-concept study, we can state that our pipeline would have been of great help in RFA planning. In such a case, electrophysiologists would have known the epicardial location of the structural substrate supporting the reentry responsible for the clinical VT prior to RFA procedure, instead of spending long hours mapping both endocardial and epicardial surfaces of the LV in the EP laboratory seeking for that epicardial CC.

Nevertheless, as we have done in this work, the ability to reproduce infarct-related VTs by means of computational simulation using image-based 3D cardiac models has already been demonstrated in a number of previous studies. The first work in this regard, which appeared a decade ago, managed to induce infarct-related VTs by computational simulation on a 3D model of infarcted canine ventricles constructed from high-resolution *ex-vivo* images (Arevalo et al., 2008). In fact, many of those works rely on animal experiments and 3D ventricular models constructed from *ex-vivo* images of species such as swine (Deng et al., 2015, 2018; Pashakhanloo et al., 2018; Pop et al., 2011a), rabbit (McDowell et al., 2011) or dog (Arevalo et al., 2013). Much less common are those studies using *in-vivo* images from animal subjects (Ng et al., 2012). With respect to those works based on 3D models of human infarcted ventricles built from *in-vivo* images, most of them are retrospective studies (Ashikaga et al., 2013; Cedilnik et al., 2018; Chen et al., 2016; Deng et al., 2016; Relan et al., 2011; Ringenberg et al., 2014), one of them performed on a quite considerable large cohort of 41 patients aiming for arrhythmia risk stratification rather than RFA planning (Arevalo et al., 2016). To our knowledge, currently only a very recent work has shown a prospective computational study performed with five human patients from two different hospitals, further supported by several retrospective studies with both human (21 patients) and animal (5 pigs) 3D models of infarcted ventricles (Prakosa et al., 2018).

Among those studies using human data, in addition to the number of patients ranging from only one (Relan et al., 2011) to 41 subjects (Arevalo et al., 2016), such works mainly differ in the strategies used for modelling the EP behaviour of human ventricles, especially in the region affected by the chronic ischaemic heart disease comprising both infarct scar and BZ. Some of those works, seeking for a fast performance in computational simulations, benefit from simplified EP approaches such as the Eikonal propagation model (Cedilnik et al., 2018), even making a special effort to personalize human cardiac EP as much as possible by adjusting the parameters of simplified AP models (Chen et al., 2016; Relan et al., 2011). However, as in our case, many of those studies (Arevalo et al., 2016; Ashikaga et al., 2013; Deng et al., 2016; Prakosa et al., 2018; Ringenberg et al., 2014) based their EP modelling strategies on ten Tusscher models of human ventricular AP (ten Tusscher et al., 2004; ten Tusscher and Panfilov, 2006b, 2006a), since it is a quite complete and validated ionic model capable of reproducing the complex EP phenomena underlying the mechanisms responsible for reentrant VTs, such as unidirectional propagation blocks. Thus, the major differences between these works are mainly related to the EP representation of the MI. Among them, the most usual way of modelling the MI region relies on considering the infarct scar as non-excitable tissue (i.e., an electrical insulator), including only electrical remodelling along with reduced conductivities in the BZ, with both regions segmented from *in-vivo* DE-MRI in all cases (Arevalo et al., 2016; Ashikaga et al., 2013; Deng et al., 2016; Prakosa et al., 2018). Note that those four works come from the same research team, the Trayanova's Computational Cardiology Laboratory from Johns Hopkins University (Baltimore, Maryland, USA), which is by far the most active research group worldwide in this regard. Instead, in spite of using a very similar approach for BZ, Ringenberg *et al.* modelled the infarct scar as a passive resistor-capacitor tissue with very low conductivity values in order to account for a subtle electrotonic load exerted by the scarred tissue on surrounding viable myocardium (Ringenberg et al., 2014).

Regarding the incorporation of fibrosis within the BZ, so far, no previous work using human data has considered such possibility in the context of RFA planning aimed at infarct-related VTs. Just a few studies performed on 3D models derived from *ex-vivo* images of animal infarcted hearts have previously

explored the arrhythmogenic effects of the presence of fibrosis within the BZ (Arevalo et al., 2013; McDowell et al., 2011). A 3D model of rabbit ventricles was used to study the arrhythmogenic impact of including diffuse and random arrangements of fibroblasts in the BZ (McDowell et al., 2011). Later, Arevalo *et al.* assessed the influence on arrhythmogenicity and induced VTs features derived from the presence of distinct densities of necrotic patches (non-excitable tissue) randomly organized within the BZ of a 3D model of canine infarcted ventricles (Arevalo et al., 2013). The authors observed an increasing slowing-down of propagation across BZ depending on fibrosis level, thus leading to longer CLs for induced VTs and even preventing them at fibrosis levels higher than 60%. However, they finally concluded that such kind of fibrotic representation in the BZ was not a necessary element to reproduce real VT morphologies by means of computational simulation, as long as electrical remodelling and reduced conductivities are included in the BZ.

Hence, our approach of including image-based fibrosis, leading to the generation of patient-specific fibrosis patterns within the BZ resulting in a patchy distribution modelled as fibroblasts clusters, is a novel contribution to the field of computational cardiology aimed at studying the mechanisms related to VTs in chronically infarcted human hearts. A recent work also used an image-based method to define realistic patchy fibrotic patterns in a 3D cardiac model, but in a very different context related to a simulation study on persistent atrial fibrillation (Roney et al., 2016). On the other hand, as thoroughly discussed in Chapter 7 (see sections 7.5.3 and 7.6.2), the results of our *in-silico* tests of VT inducibility suggests a pro-arrhythmogenic effect linked to the presence in the BZ of intermediate densities (10%, 20%) of imaged-based fibrosis (fibroblasts clusters). Importantly, this is further consistent with the conclusions reached by McDowell *et al.*, whose work was specifically aimed at assessing the susceptibility to infarct-related VT as a function of the degree of random diffuse fibrosis in the BZ (McDowell et al., 2011), also represented by MacCannell model of human ventricular fibroblast (MacCannell et al., 2007).

The other strongly distinguishing feature of our work relates to the simulation of ECGs derived from the VTs induced in *in-silico* tests, which were computed by means of a 3D torso model. Evidently, this is not the first study in

providing simulated ECGs using a 3D torso model (see (Cardone-Noott et al., 2016; Carpio et al., 2019; Sánchez et al., 2018), just for a few recent examples). Nevertheless, in the context of simulation studies aimed at RFA planning for infarct-related VTs, no previous work has provided simulated ECGs before, as we have done in an attempt to reproduce the patient's ECG associated with the clinical VT that is expected to be eliminated by a RFA procedure.

A reduced number of studies, focused on assessing the impact of various modelling approaches on infarct-related VT mechanisms and features, did obtain simulated pseudo-ECGs resulting from 3D models of animal infarcted ventricles (Arevalo et al., 2013; Deng et al., 2015; Pashakhanloo et al., 2018) and also of human hearts (Ukwatta et al., 2016). In all cases, extracellular potentials were calculated by considering the heart immersed in an isotropic and homogeneous conductive medium, rather than embedded in a 3D heterogeneous torso model. However, all of them simply showed simulated signals for a unique bipolar lead computed from two virtual electrodes arbitrarily placed around the ventricular model at a certain distance from the epicardial surface. In those cases, the aim was to analyse the morphologies of the various VTs induced on a same 3D ventricular model, or those of the same VT induced on different model versions (with distinct representations for scar and/or BZ, for instance) by comparing the resulting pseudo-ECGs. Therefore, in contrast to our pipeline, none of those works provided simulated signals suitable to be compared against patient's ECG recordings.

Among the previous computational studies aimed at replicating real infarct-related VTs, either clinical or experimentally induced, a subset of them were retrospective studies that made use of EAMs invasively recorded during the actual EP study in order to assess the correspondence between real and simulated VTs, using EP datasets from both swines (Deng et al., 2015, 2018; Ng et al., 2012) and human subjects (Cedilnik et al., 2018; Chen et al., 2016). In such cases, researchers directly compared the real activation patterns (LATs) obtained via mapping systems (CARTO®, Rhythmia™, EnSite™), recorded from endocardial and/or epicardial surfaces during the arrhythmic events induced in the EP laboratory, with those patterns resulting from VTs induced on image-based 3D models by computational simulation. This kind of comparison,

performed qualitatively in all of those works, basically allowed the authors to evaluate the spatial closeness between the organizing centres of real and simulated VTs, as well as the direction in which the propagation flowed around such centres. Nevertheless, besides being unfeasible for prospective studies due to the need of using data from real EP studies, this methodology must deal with an important drawback even in retrospective cases. Frequently, VTs induced *in-vivo* in the EP laboratory cannot be properly mapped (unmappable VTs) due to several reasons (Alzand et al., 2011; Fernández-Armenta et al., 2015), such as the spontaneous ending of reentrant activity (non-sustained VT) that hinders the mapping process, the need of reverting the patient to sinus rhythm because of haemodynamic instability and the resulting perfusion compromise during the VT episode (non-tolerated VT), or simply the failure in inducing the clinical VT in the actual EP study. Therefore, in many cases the direct comparison between activation patterns from real and *in-silico* induced VTs would not be a feasible option, as usually EAMs cannot be suitably recorded during *in-vivo* induced VT episodes, if inducible.

In conclusion, our approach is (to our knowledge) the first one in providing a method to evaluate the correlation between clinical and simulated infarct-related VTs that is entirely based on non-invasive clinical standard ECG recordings, instead of needing EAMs invasively registered during the actual EP study, what furthermore would severely restrict the predictive capability of prospective *in-silico* EP studies for planning RFA procedures. Thus, in the case of monomorphic VTs typically associated with reentrant activities through the scar of chronically infarcted hearts (de Bakker et al., 1988), our approach would allow the electrophysiologists to compare the morphologies of simulated and real ECGs in order to discern whether an *in-silico* induced VT matches a particular clinical VT. Thereby, in the case of positive match, electrophysiologists would receive precise information about the location of the reentrant circuit to be ablated, before taking the patient to the EP laboratory. Evidently, such kind of information would enable a better planning of the RFA procedure in advance. It would be of great help to target a restricted area to be mapped, to decide whether the case requires an endocardial or epicardial approach (or both) and to select appropriate pacing sites before the intervention. Consequently, such an accurate pre-procedure planning might likely translate into a considerable

shortening of procedure duration, a decrease of the risk of intra-operative complications and, mainly, a significant improvement in success rate of RFA procedures aimed at eliminating infarct-related VTs, thus leading to the subsequent reduction in the number of successive reinterventions (Aliot et al., 2009; Baldinger et al., 2016; Gerstenfeld, 2013; Yokokawa et al., 2013).

8.4.3. Infarct-related VT mechanisms

In this section we will focus on the mechanisms associated with the initiation and maintenance of infarct-related reentrant monomorphic VTs. According to our EP study by computational simulation, in presence of CCs traversing the scar in chronically infarcted ventricles, the most influential factors in VT promotion are the reduction in CVs and the repolarization dispersion (APD heterogeneity) within the BZ that surrounds the fibrotic core (i.e., the infarct-scar), along with the geometrical features of the CC comprising the structural substrate for reentrant activity. Furthermore, although based on a single MI geometry, the conclusions derived from our simulation results are in agreement with most of the previously published observations in both experimental and computational studies, as comprehensively discussed in Chapter 7 (see section 7.6.2).

Besides contributing to the self-sustenance of reentrant activity through CCs because of slowed conduction across them, thus enabling tissue repolarization at the other side, our results showed that the reduction in the CVs of BZ may also have a significant impact on VT inducibility and VT features, as seen in the *in-silico* tests performed on model *#6* (ER+10fib) with three different value sets for CVs in the BZ. When we used CVsBZ-75% (i.e., conduction across BZ was 25% slower than in healthy myocardium), *in-silico* tests failed to induce VT. In contrast, model *#6* (ER+10fib) with CVsBZ-50% did provide positive VT induction. However, it required a more stressful pacing protocol than the case of CVsBZ-25%, also giving rise to notable alterations in the morphology of simulated ECGs and, consequently, resulting in a lower resemblance between simulated and clinical VT.

Regarding the two main factors creating repolarization dispersion around the infarct scar, our results suggest that the APD increase associated with electrical remodelling in the BZ has a notably more pro-arrhythmogenic effect than the APD shortening induced by infiltrated fibroblasts. Among the four versions of our patient-specific ventricular model providing positive VT induction (models *#4-7*), only model *#4* (noER+30fib) lacked electrical remodelling in the BZ, requiring the highest fibrosis level (30%) and more stressful pacing protocols to give rise to the functional propagation block triggering reentrant VT. On the contrary, models *#5* (ER+00fib)*, #6* (ER+10fib)*, #7* (ER+20fib), all of them including electrical remodelling, presented larger APD gradients at both CC ends, thereby facilitating the formation of functional unidirectional propagation blocks leading to VT onset. Nonetheless, the combination of electrical remodelling and intermediate densities (10%, 20%) of fibroblasts infiltration within the BZ, arranged as a function of our image-based approach, showed a synergic impact on arrhythmogenicity. That is the main reason why models *#6* (ER+10fib) and *#7* (ER+20fib) were revealed as the two most arrhythmogenic configurations.

On the other hand, the APD reduction resulting from the presence of patchy fibrosis in the BZ, modelled as fibroblasts clusters, enabled the propagation of premature stimuli (S2-S3) at shorter CIs from pacing sites located within the region subject to fibrosis influence, thus allowing the application of more stressful PES protocols. In fact, this was the mechanism that enabled the VT onset on model *#4* (noER+30fib) when it was paced from point *epi#1*.

The considerable impact of pacing sites location on VT inducibility was also observed in our simulation study. The absolute failure of pacing site *epi#2*, together with the different results yielded by *in-silico* VT tests with PES protocols released from sites *epi#1* and *endo#1*, confirmed the key importance of pacing sites location. Indeed, one of the major advantages of *in-silico* EP studies compared to real ones relates to the feasibility of conducting VT inducibility tests from a large number of pacing sites in an absolutely harmless scenario (Arevalo et al., 2016; Prakosa et al., 2018). Obviously, a simulation study does not involve the considerable risk of intra-procedural complications that might arise from an extensive pacing approach in the EP laboratory.

Lastly, in spite of carrying it out on a unique MI geometry with a single CC, our simulation study allowed us to witness the crucial relevance of the geometrical characteristics (shape and size) of the CC supporting the reentrant activity responsible for an infarct-related VT. In our particular case, the generation of marked APD gradients at both terminal ends of the epicardial CC was the mechanism that ultimately led to unidirectional functional propagation blocks and, consequently, to the reentrant VT initiation. In addition to APD increase associated with electrical remodelling, the source-sink mismatches due to steep changes in the geometry of excitable tissue were strongly related to the genesis of such a pro-arrhythmic effect specifically located at the two CC ends. Furthermore, there existed a severe narrowing in the viable tissue at the lower (apical) end of the epicardial CC, so that tissue expansion was even more abrupt there than in upper side, thus leading to a deeper impact of structurally induced source-sink mismatches on the propagation through the lower side of the CC. That is the reason why the propensity to functional propagation blocks was much higher at the lower end of the epicardial CC compared to its upper side. Hence, these results corroborate the great influence on VT inducibility and VT morphology derived from the geometry of the viable (i.e., excitable) tissue surrounding infarct scar, as also observed in a number of previous simulation studies on infarct-related VT mechanisms (Arevalo et al., 2013; Deng et al., 2018; Pashakhanloo et al., 2018; Ringenberg et al., 2014; Ukwatta et al., 2016).

8.5. Limitations

Undoubtedly, the major limitation of this work corresponds to the fact that it is based on only one case (one patient) and, hence, on a unique MI geometry that, in addition, presented a sole CC (epicardial isthmus) giving rise to a single VT morphology. Importantly, the main goal of this project was to develop a pipeline able to reproduce patient's VTs by computational simulation of cardiac EP, not only at the organ level (simulation on 3D ventricular model) as others have previously done, but also at the body level by replicating patient's ECGs recorded during clinical VT episodes. Then, according to the results shown in Chapter 7 and discussed in sections above, we can state that the feasibility of

reproducing patient's ECGs by means of our computational simulation approach with enough accuracy to be compared against actual patient's recordings, especially those corresponding to clinical VTs, has been assessed and proved thanks to this single case. Nevertheless, a single-case study like this must be considered as a proof-of-concept study showing results that, although promising, are still preliminary. There is no doubt about the compulsory need of conducting further retrospective studies including a large number of cases (patients) in order to improve and validate our pipeline. Those studies should also consolidate (or modulate) our conclusions concerning the relation between the mechanisms triggering infarct-related VTs and the factors influencing them, as well as the decisions made about the proper cardiac EP modelling for this particular kind of *in-silico* studies.

Some structural features of the patient-specific 3D ventricular model could not be personalized. That is the case, for instance, of cardiac fibre orientation defining myocardium architecture, which were generated by means of a rule-based method derived from population data. However, it does not appear to have a significant impact on simulation studies on cardiac EP like this one, as discussed in section 8.2.2.

On the other hand, currently the electrical propagation through ventricular myocardium is known to be characterized by three distinct conductivities in longitudinal, transverse (within myocardial sheets) and normal (along transmural direction) axes (Caldwell et al., 2009; Hooks, 2007). Recent computational studies have shown the impact on propagation patterns that might result from considering such full electrical anisotropy, both in simulations at the organ level in healthy ventricles (Cardone-Noott et al., 2016; Johnston et al., 2016) and in simplified models of cardiac tissue under diseased conditions (Johnston et al., 2018). Instead, we considered a unique conductivity for all directions perpendicular to myocyte longitudinal axis, as it has been commonly assumed in most of the 3D computational studies of cardiac EP so far. Hence, the incorporation of full anisotropy to the cardiac EP modelling of our pipeline might be one of the future improvements, as well as the study of its influence on infarct-related VT inducibility.

Another limiting factor in our approach is the absolute lack of personalization of cardiac EP. A few simulation studies aimed at infarct-related VTs have already included personalization methods relying on EP data provided by EAMs invasively recorded in real EP studies (Chen et al., 2016; Pop et al., 2011a; Relan et al., 2011). However, such strategies clash with our requisite of exclusively using non-invasive data, thus becoming incompatible with the feasibility of performing prospective *in-silico* EP studies. Nonetheless, a coarse personalization process of cardiac EP based on non-invasive data might likely improve the performance of our approach by leading to better correlation between real and simulated ECGs and, consequently, to an enhanced potential to predict reentrant pathways as optimal ablation targets, as already addressed in Chapter 7 (see section 7.6.2). Such cardiac EP personalization step could rely on the recent paradigm of population of models (Britton et al., 2013; Lawson et al., 2018; Muszkiewicz et al., 2016), just choosing, among the various versions of a certain ionic model, the most suitable one for each case. Some preliminary results from an interesting ongoing work in this regard have been very recently published, which proposes a workflow for patient-specific parameterization of ventricular models of cardiac EP using non-invasive standard ECG recordings (Gillette et al., 2017, 2018).

Concerning the cardiac conduction system, we did not even consider the presence of His-Purkinje network within the patient-specific 3D ventricular model. It is known that His-Purkinje system may participate in the mechanisms responsible for various modalities of ventricular arrhythmias (Haissaguerre et al., 2016; Nogami, 2011), even in infarct-related VTs giving rise to a particular sort of monomorphic VT with relatively narrow QRS complexes (Bogun et al., 2006). However, such subtype of VTs with reentrant circuits necessarily mediated by a portion of His-Purkinje network in chronically infarcted ventricles is not so common, probably as a consequence of the longer APD of Purkinje cells and the conduction delays at Purkinje-myocardial junctions. Thus, the inclusion of a model of His-Purkinje system in the ventricular model was not expected to have a significant impact on the infarct-related VT mechanisms that we aim to reproduce by our simulation approach. Anyhow, currently there is no *in-vivo* imaging modality capable of providing information about the patient-specific geometry of His-Purkinje network. There are a few recent works proposing

approaches to infer models of His-Purkinje system from the early activated regions automatically located on endocardial EAMs (Barber et al., 2017, 2018; Palamara et al., 2015; Vergara et al., 2014). It is important to note that such methods are based on an inverse problem that is inherently ill-posed, so that the degree of correspondence between the inferred model and the real structure of patient's His-Purkinje network is uncertain. Furthermore, the use of any of those approaches would be in conflict with our requirement of only using non-invasive clinical data collected prior to the RFA procedure. Then, the only alternative available to account for the cardiac conduction system in our pipeline would be to include a fully synthetic His-Purkinje model coupled to the 3D ventricular model. Nevertheless, in such a case the extent to what the impact on simulation results derived from such artificial His-Purkinje network (if any) would be faithfully replicating the influence of the patient's cardiac conduction system in such scenario, could not be determined.

A limitation not intrinsically associated with our pipeline but affecting in the particular case of the retrospective *in-silico* EP study presented here, was the poor quality of the whole-torso anatomical MRI stack. The low resolution of such image dataset hampered the construction of a fully patient-specific 3D torso model, thus leading to the need of adapting a previously built torso model, as shown in Chapter 5 (see section 5.2). Apart from the loss of specific anatomical details of the particular patient being subject of our *in-silico* EP study, the major drawbacks might relate to the inaccurate position and orientation of the ventricles into the 3D torso model. As discussed in Chapter 7 (see section 7.6.1), a considerable distortion of the simulated ECG signals registered at the external surface of torso model could arise from such deviations in the 3D geometrical position of ventricular model with respect to the torso. However, according to the acceptable results obtained from the simulations at the body level (i.e., simulated ECGs) shown in Chapter 7, especially in the case of simulated VTs exhibiting a morphology very similar to that of clinical VT, those possible geometrical inaccuracies did not seem to cause a significant impact on simulation results in this particular case.

Finally, besides requiring several improvements and further validation by means of larger retrospective studies, the integration of the pipeline proposed

in this thesis into the clinical workflow is still far from being feasible. Once a patient suffering from infarct-related VT is referred for RFA, the DE-MRI is usually acquired just a couple of days prior to the procedure. Unfortunately, the manual processing of MRI datasets required to build patient-specific 3D computational models of infarcted ventricles and torso is a very time-consuming task, which in addition requires expertise. Furthermore, the performance of realistic simulations of human cardiac EP at both organ and torso level involves a heavy computational burden, because of the need of using detailed ionic models capable of reproducing the complex EP phenomena underlying the mechanisms responsible for infarct-related VTs onset. Therefore, conducting a prospective *in-silico* EP study aimed at planning a RFA procedure within a clinically assumable time frame, would require highly proficient staff working hard with HPC (high-performance computing) resources, all of which are not commonly available in current clinical environments.

Chapter 9

Conclusions and Perspectives

In this final chapter, we present the conclusions drawn from this work, which proposes a full pipeline for computational simulation of cardiac electrophysiology (EP) aiming to perform personalized *in-silico* EP studies on infarct-related ventricular tachycardias (VT) by means of image-based 3D models. We also discuss the possible perspectives regarding the future evolution of the proposed methodology, as well as the improvements that should be included in order to enhance the performance and reliability of this approach, aiming to evolve towards the feasibility of its introduction into clinical environments.

9.1. Conclusions and contributions of the thesis

The main general aim of this doctoral thesis was to assess the feasibility of building 3D models (ventricles and torso) capable of supporting personalized *in-silico* EP studies aiming to plan radiofrequency ablation (RFA) procedures for

infarct-related VTs, with the restriction of exclusively using non-invasive data registered prior to the therapeutic intervention. To evaluate this, first we developed a full pipeline to construct patient-specific 3D models of infarcted ventricles based only on high-resolution clinical DE-MRI images. From those images we generated personalized computational 3D reconstructions of the cardiac anatomy and of the chronic myocardial infarction (MI) geometry, even including personalized image-based fibrosis patterns within the border zone (BZ), as described in Chapter 5. Secondly, we designed an approach to computationally model the cardiac EP aiming to reproduce, as faithfully as possible, the EP behaviour of chronically infarcted ventricles by computational simulation, considering both the infarct scar and the BZ, as shown in Chapter 6. After that, we performed a single-case feasibility study in order to test the developed methodology. We carried out a retrospective *in-silico* EP study consisting of applying by computational simulation the same pacing protocols employed by the specialists in the EP laboratory for testing the inducibility of infarct-related VTs. As part of the simulation-based EP study, we moreover computed the simulated ECGs resulting from the *in-silico* induced VTs making use of a 3D torso model. This allowed to compare the simulated ECGs against the patient's clinical recordings as a method to evaluate the degree of similarity between real and simulated VTs. Additionally, we assessed several strategies for the EP modelling of the BZ, incorporating electrical remodelling and different levels of structural remodelling (in the form of image-based fibrosis) to that region, aiming to study the arrhythmogenic impact of those distinct BZ configurations.

According to our results, shown in Chapter 7 and discussed in Chapter 8, the pipeline proposed in this work was able to induce the clinical VT suffered by the patient in the *in-silico* inducibility tests performed in our single-case study. In addition, our approach was also able to reproduce the morphology of the monomorphic VT in the simulated ECGs computed by means of the 3D torso model, such that the simulated VT was unequivocally identified as the same as the clinical one, thereby providing the accurate location of the conducting channel (CC) that should be ablated to terminate the VT. Indeed, the location within the 3D ventricular model of the epicardial CC, responsible for the reentrant activity leading the infarct-related VT, highly correlated with the

ablation sites chosen by the electrophysiologists in the actual RFA procedure, who successfully removed VT inducibility from the patient by ablating in regions corresponding to the two terminal ends of the epicardial isthmus.

Therefore, the single-case retrospective study performed in this work has given a proof of the feasibility of developing patient-specific 3D computational models from non-invasive clinical data aimed at simulation of the patient's EP by means of the proposed pipeline. Hence, it seems to have the potential to become a powerful tool for therapy planning in the near future. This approach could help to improve the success rate of RFA procedures aiming for infarct-related VTs, which currently remains relatively low, since it is estimated that up to 50% of patients continue suffering from VT after the procedure. Therefore, the prospective and personalized *in-silico* EP studies might help in reducing the usual need of successive re-interventions, as well as to reduce the procedure duration and, consequently, the risk to the patient of intra- and post-procedural complications.

Concerning the overall performance of our pipeline, it was able to reproduce the patient's ECG both in sinus rhythm and in clinical VT with acceptable fidelity, considering the lack of personalization of the myocardial architecture (i.e., cardiac fibre orientation) and mainly of the cardiac EP, which was entirely based on population data. When pacing protocols give rise to positive VT induction in the EP laboratory, electrophysiologists usually compare the resulting ECG to that registered during clinical VT episodes as a method to discern whether both VTs match or not, which in turn is part of the process of selecting the optimal ablation targets. Hence, our pipeline completely based on non-invasive clinical data has the potential to replicate such process *in-silico*, thus further endorsing the idea that it might become a helpful tool in therapy planning prior to RFA procedures aimed at finishing infarct-related VTs.

Certainly, in the case of the *in-silico* EP study presented in this work, we used the EP data provided by CARTO® system, which were invasively recorded during the *in-vivo* EP study conducted immediately before the real RFA procedure. Nonetheless, as already highlighted in previous chapters, we used those datasets solely for testing and validation purposes. Indeed, the stage of

ventricular model stabilization in sinus rhythm might be removed from our simulation pipeline with no significant consequences, since it is not necessary at all for performing the subsequent stage of *in-silico* tests of VT inducibility. Thus, even omitting such simulation step, our approach could be used in prospective personalized *in-silico* EP studies aiming to predict the CC supporting the clinical VTs in order to help in finding the optimal ablation sites. In such a case, the proposed pipeline would only require the following non-invasive clinical data: (1) high-resolution clinical DE-MRI for building the patient-specific 3D model of infarcted ventricles, (2) clinical structural MRI to construct the personalized 3D torso model, and (3) patient's ECG recorded during clinical VT episodes. Then, it might be seamlessly applied prior to the actual EP study for aiding in therapy planning, that is, for planning the RFA procedure, not only by revealing the exact location of those CCs responsible for the clinical VTs that must be eliminated, but also by providing really useful information for deciding whether the approach should be endocardial, epicardial or both.

Regarding the EP mechanisms underlying the onset of reentrant infarct-related VTs, we assessed the arrhythmogenic potential derived from the incorporation of different kinds and degrees of remodelling within the BZ. However, from the functional perspective, the computational modelling of the BZ remains a challenging task because of the lack of reliable data from experimental studies on chronically infarcted human hearts, especially in relation to the electrical remodelling and the myocyte-fibroblast electrotonic interactions. In our *in-silico* case study, in addition to the reduction of CVs resulting in slowed propagation across the BZ, the most pro-arrhythmogenic factor was the repolarization dispersion around the infarct scar, that is, the APD heterogeneity within the BZ. In spite of causing opposite effects, both types of remodelling increased the repolarization dispersion in the BZ, since the electrical remodelling led to APD prolongations while patchy fibrosis, modelled as electrically passive fibroblasts, gave rise to density-dependent APD shortenings. In our case study, both remodelling types enabled by itself the formation of unidirectional functional propagations blocks triggering the infarct-related VT. However, in the absence of electrical remodelling, the ventricular model required a high fibrosis density in the BZ (30% image-based patchy fibrosis) to enable the VT induction by means of pacing protocols. Indeed, the most pro-

arrhythmogenic BZ configurations were those including the conjunction of both factors, combining the electrical remodelling with intermediate fibrosis levels (10% and 20%) in the BZ. In those 3D ventricular model versions including such BZ configurations, both kinds of remodelling interact synergistically leading to an important dispersion in the repolarization patterns around the infarct scar, thus increasing the arrhythmogenic potential in that key region. Furthermore, they gave rise to APD gradients that were especially large in the vicinity of both extremes of the epicardial CC, thereby making those critical sites more prone to the formation of functional unidirectional propagation blocks. As a consequence, those model versions experienced a significant increase in their susceptibility to the onset of reentries through the epicardial CC, thus triggering the reentrant monomorphic VTs typically suffered by chronically infarcted patients.

On the other hand, it is essential to highlight the cardinal importance of the precise and personalized 3D reconstruction of both ventricular anatomy and MI geometry from *in-vivo* high-resolution images in order to accurately predict the reentry pathways responsible for the clinical VTs as ablation targets by means of *in-silico* EP studies. Although relying on a unique MI geometry, our simulation case study allowed to observe the significant relevance in reentrant VT scenarios of the source-sink mismatches related to sudden changes in the geometry of excitable tissue. Therefore, the 3D structural features (geometry, shape, size, etc.) of the CCs crossing the infarct scar play a key role in the susceptibility to the onset of reentrant VTs. Thus, besides the appropriate EP modelling, an accurate and personalized reconstruction of the 3D structure of the MI is also required, including the complicated interpenetration between the infarct scar and the surrounding viable tissue giving rise to the formation of CCs. Such a precise reconstruction of the MI geometry is crucial for faithfully reproducing by computational simulation the patient's cardiac EP mechanisms leading to the onset of the infarct-related clinical VTs.

In recent years, there have been promising advances in the field of computational cardiology, especially in relation to the computational cardiac EP. Unfortunately, there remain several challenging issues that continue hampering the incorporation into the common clinical workflow of the image-based 3D

cardiac models aiming for personalized *in-silico* EP studies as a useful tool for diagnosis and therapy planning. There is a lack of precise and easy-to-use tools for fully automated generation of cardiac computational models including accurate 3D reconstructions of the patient-specific anatomy and MI geometry from *in-vivo* high-resolution image datasets, especially from MRI modalities such as cardiac DE-MRI. Indeed, currently this is a time-consuming task that, in addition, requires expertise in cardiac image processing. Nonetheless, future improvements in the quality and resolution (both spatial and temporal) of *in-vivo* cardiac imaging techniques, as well as the standardization of their acquisition protocols, are expected to be of great help in overcoming this important challenge.

Another major drawback is the current high computational cost of 3D simulations of cardiac EP at the organ and body (torso) levels. A prospective *in-silico* EP study aiming to thoroughly test VT inducibility from a patient-specific 3D model of infarcted ventricles involves a considerable number of multi-scale simulations of cardiac EP. Moreover, such simulations must account for a high degree of biophysical detail aiming to reproduce the complex EP mechanisms underlying the onset of infarct-related VTs. As a result, those biophysically realistic simulations of cardiac EP require long computing times on high-performance computing (HPC) resources, which furthermore must be managed by proficient computer scientists with expertise in computational cardiac EP. Nevertheless, as in the case of the automated methods for generating 3D models from *in-vivo* cardiac images, the expected evolution and optimization of (1) computing architectures, such as those based on graphical processing units (GPUs), (2) numerical techniques and (3) mathematical approaches for cardiac EP modelling, will likely aid in increasingly reducing the computational burden of such simulations and, thereby, speeding them up, as well as in expanding their accessibility to personnel with little experience in computational cardiac EP.

Consequently, in spite of the upcoming clinical advances that the field of computational cardiac EP seems to promise, the feasibility of performing prospective personalized *in-silico* EP studies aiming for therapy planning within the narrow time frame usually elapsed between the diagnosis and the therapeutic intervention in patients undergoing life-threatening cardiac

disorders, remains nowadays extremely challenging in the current clinical environments due to the high demands of such studies, in terms of long simulation times, cutting-edge computing technology and degree of interaction by expert operators.

9.2. Future perspectives

Despite its promising preliminary results, our approach is still far from being ready for its application in clinical environments aiming to perform prospective *in-silico* EP studies for planning RFA procedures oriented at eliminating infarct-related VTs. In addition to the limiting factors inherently linked to the field of computational cardiac EP discussed above, our pipeline evidently needs further improvements and validation.

The ability of the proposed approach to replicate infarct-related clinical VTs by computational simulation, including the ECG morphology, should be exhaustively assessed and validated by means of further retrospective studies with large patient cohorts. Moreover, such retrospective studies might be really useful not only for evaluating the overall performance of our methodology, but also as a testing bench for increasingly calibrating our pipeline by defining the best modelling strategy for each aspect. For instance, they would be of great help in revealing which is the most appropriate EP modelling scheme for the BZ, in terms of conduction velocities (CV) reduction, level of imaged-based patchy fibrosis, magnitude of myocyte-fibroblast electrotonic interaction, etc. Additionally, we might even test other alternatives for fibrosis within the BZ, such as considering it as dense necrotic patches modelled as non-conducting pieces of tissue. Those studies would also allow clarifying whether it is worth making the additional effort needed to include the papillary muscles and endocardial trabeculations in the patient-specific 3D ventricular models in order to predict reentrant pathways.

On the other hand, in its current state, our pipeline demands a high degree of manual interaction. Therefore, despite the lack of fully automated methods commented above, we should explore semi-automatic segmentation

approaches in order to decrease the necessary interaction, thus accelerating the building process of 3D models (infarcted ventricles and torso) and, in the case of MI segmentation, reducing or even removing the potential inter-operator variability resulting from the manual pre-processing required by the standard-deviation (SD) method. In this regard, our approach might benefit from the very recently appeared strategies for advanced image processing applied to cardiac MRI datasets based on the deep learning paradigm.

As already discussed in previous chapters, we strongly think that the performance of our approach might really benefit from the incorporation of some kind of strategy aiming to coarsely personalize the cardiac EP. However, such personalization strategy should necessarily rely on non-invasive EP data, such as standard clinical ECG recordings or, maybe, the emerging technique of ECG imaging (ECGi), which has recently shown promising advances in representing the activation maps at the organ level by reconstructing them from body surface potential maps (BSPM). Otherwise, in the case of methodologies based on invasive data such as electro-anatomical maps (EAM), they could not be applied for prospective *in-silico* EP studies aimed at RFA planning prior to the actual procedure.

Another important feature that we think we should include in the pipeline is the integration of an automated methodology to generate extensive pacing schemes. One of the main advantages of the personalized *in-silico* EP studies is the absolute absence of risk to the patient, what consequently brings the possibility of implementing comprehensive VT testing strategies by delivering programmed electrical stimulation (PES) protocols from a large amount of pacing sites. As discussed in Chapters 7 and 8, the location of the pacing sites may significantly influence the final result of VT inducibility tests. Indeed, one of the issues leading to the relatively poor success rates of RFA procedures in the context of infarct-related VTs is the frequent inability to induce the clinical VTs during the real EP study, thereby complicating the election of the optimal ablation targets aiming to terminate those clinical VTs. Hence, the computational EP studies might help to considerably diminish the probability of failing to induce the clinical VTs because of the improper choice of the few pacing sites that are usually tested in the *in-vivo* EP studies for safety

reasons. Therefore, the generation of a large set of pacing sites by means of an automatic algorithm, strategically placing points all over the surface of the patient-specific 3D ventricular model regardless of the location and extension of the MI, would be a really advantageous strategy in order to maximize the probability of success of our approach in the personalized *in-silico* EP studies.

Furthermore, the application of such an extensive pacing schemes could be highly beneficial not only for therapy planning, but also for risk stratification in chronically infarcted patients with no prior history of spontaneous infarct-related VTs. Since the pipeline proposed in this work just require non-invasive data (high-resolution clinical MRI scans and standard ECG recordings), our approach might be used to assess the probability of developing all possible reentrant VTs that could potentially derive from the specific MI geometry of a particular subject, with no kind of risk, trouble or serious discomfort for the patient.

PUBLICATIONS

List of Publications

Journal Articles

Main contributions derived from the thesis

1. **Lopez-Perez, A.**, Sebastian, R., Izquierdo, M., Ruiz, R., Bishop, M., and Ferrero, J.M. (2019). **Personalized cardiac computational models: from clinical data to simulation of infarct-related ventricular tachycardia**. *Frontiers in Physiology*, Vol. 10, May, Article 580.
   https://doi.org/10.3389/fphys.2019.00580

2. **Lopez-Perez, A.**, Sebastian, R., and Ferrero, J.M. (2015). **Three-dimensional cardiac computational modelling: methods, features and applications**. *BioMedical Engineering OnLine*, Vol. 14, April, Article 35.
   https://doi.org/10.1186/s12938-015-0033-5

Other contributions

3. Carpio, E., Gómez, J.F., Sebastian, R., **Lopez-Perez, A.**, Castellanos, E., Almendral, J., Ferrero, J.M., and Trenor, B. (2019). **Optimization of Lead Placement in the Right Ventricle During Cardiac Resynchronization Therapy. A Simulation Study**. *Frontiers in Physiology*, Vol. 10, February, Article 74.   https://doi.org/10.3389/fphys.2019.00074

Conference Communications

Main contributions derived from the thesis

1. **Lopez-Perez, A.D.**, Andreu, D., Berruezo, A., Sebastian, R., and Ferrero, J.M. (2014). **Methods for image-based three-dimensional reconstruction of infarct-derived scars to locate conducting channels as radiofrequency ablation targets**. *European Society of Cardiology Congress* (ESC 2014, Barcelona, Spain). *European Heart Journal*, Vol. 35, Suppl. 1 (Abstract supplement), pp. 1136. Oxford University Press.
   http://spo.escardio.org/abstract-book/presentation.aspx?id=128857

Other contributions

2. Rocher, S., **López, A.**, Ferrer, A., Martínez, L., Sánchez, D., and Saiz, J. (2019). **A Highly-Detailed 3D Model of the Human Atria**. *World Congress on Medical Physics and Biomedical Engineering 2018* (Prague, Czech Republic). *IFMBE Proceedings*, Vol. 68/1, pp. 649-653. Springer, Singapore. https://doi.org/10.1007/978-981-10-9035-6_121

3. Rocher, S., **López, A.**, Ferrer, A., Martínez, L., Sánchez-Quintana, D., Saiz, J. (2017). **A "true" 3D model of the human atria for atrial fibrillation studies**. *Atrial fibrillation: from Mechanisms to Population Science*, CNIC Conference 2017 (Madrid, Spain). Book of abstracts of CNIC Conference 2017, pp. 50-51.
   https://cnic-conference.com/wp-content/uploads/2018/03/Abstracts_CNIC17.pdf

4. Rocher, S., **López, A.**, Ferrer, A., Martínez, L., Sánchez-Quintana, D., Saiz, J. (2017). **Desarrollo de un modelo 3D de la aurícula humana para el estudio de la propagación tisular durante la fibrilación auricular crónica**. *XXXV Congreso Anual de la Sociedad Española de Ingeniería Biomédica* (CASEIB 2017, Bilbao, Spain). Libro de actas CASEIB 2017, pp. 495-498, ISBN: 978-84-9082-797-0. https://caseib17.github.io/154.html
   http://seib.org.es/publicaciones-cientificas-caseib/

5. Guardiola, M., Pashaei, A., Sebastián, R., **López, A.**, Acosta, J., Andreu, D., Berruezo, A., and Cámara, O. (2015). **Computational electrophysiology for prediction of the outflow tract origin in idiopathic ventricular tachycardia**. *Cardiac Physiome Workshop 2015* (Auckland, New Zealand).

    https://www.cardiacphysiome.org/meetings/2015-meeting/
    https://drive.google.com/file/d/0B1z8hBzdwOyBRFNUSmNqWFIxUTQ/view

6. Pashaei, A., Sebastian, R., **Lopez, A.**, Soto-Iglesias, D., Ferrero, J.M., Andreu, D., Acosta, J., Fernandez-Armenta, J., Berruezo, A., and Camara-Rey, O. (2014). **Determining the origin of the ectopic beat in idiopathic ventricular arrhythmias with a computational model**. *European Society of Cardiology Congress* (ESC 2014, Barcelona, Spain). *European Heart Journal*, Vol. 35, Suppl. 1 (Abstract supplement), pp. 599-600. Oxford University Press.

    http://spo.escardio.org/abstract-book/presentation.aspx?id=126823

REFERENCES

References

Abboud, S., Berenfeld, O., and Sadeh, D. (1991). Simulation of high-resolution QRS complex using a ventricular model with a fractal conduction system. Effects of ischemia on high-frequency QRS potentials. *Circ. Res.* 68, 1751–1760. doi:10.1161/01.RES.68.6.1751.

Abdelwahab, A., and Sapp, J. L. (2007). NaviStar ThermoCool catheter for ventricular tachycardia. *Expert Rev. Med. Devices* 4, 307–314. doi:10.1586/17434440.4.3.307.

Abubakar, I. I., Tillmann, T., and Banerjee, A. (2015). Global, regional, and national age–sex specific all-cause and cause-specific mortality for 240 causes of death, 1990–2013: a systematic analysis for the Global Burden of Disease Study 2013. *Lancet* 385, 117–171. doi:10.1016/S0140-6736(14)61682-2.

Acosta, J., Penela, D., Andreu, D., Cabrera, M., Carlosena, A., Vassanelli, F., et al. (2018). Multielectrode vs. point-by-point mapping for ventricular tachycardia substrate ablation: a randomized study. *EP Eur.* 20, 512–519. doi:10.1093/europace/euw406.

Al-Khatib, S. M., Stevenson, W. G., Ackerman, M. J., Bryant, W. J., Callans, D. J., Curtis, A. B., et al. (2018). 2017 AHA/ACC/HRS Guideline for Management of Patients With Ventricular Arrhythmias and the Prevention of Sudden Cardiac Death. *J. Am. Coll. Cardiol.* 72, e91–e220. doi:10.1016/j.jacc.2017.10.054.

Aliev, R. R., and Panfilov, A. V (1996). Modeling of heart excitation patterns caused by a local inhomogeneity. *J. Theor. Biol.* 181, 33–40. doi:10.1006/jtbi.1996.0112.

Aliot, E. M., Stevenson, W. G., Almendral-Garrote, J. M., Bogun, F., Calkins, C. H., Delacretaz, E., et al. (2009). EHRA/HRS Expert Consensus on Catheter Ablation of Ventricular Arrhythmias: Developed in a partnership with the European Heart Rhythm Association (EHRA), a Registered Branch of the European Society of Cardiology (ESC), and the Heart Rhythm Society (HRS); i. *Europace* 11, 771–817. doi:10.1093/europace/eup098.

Alzand, B. S. N., Timmermans, C. C. M. M., Wellens, H. J. J., Dennert, R., Philippens, S. A. M., Portegijs, P. J. M., et al. (2011). Unmappable ventricular tachycardia after an old myocardial infarction. Long-term results of substrate modification in patients with an implantable cardioverter defibrillator. *J. Interv. Card. Electrophysiol.* 31, 149–156. doi:10.1007/s10840-011-9549-1.

Amado, L. C., Gerber, B. L., Gupta, S. N., Rettmann, D. W., Szarf, G., Schock, R., et al. (2004). Accurate and objective infarct sizing by contrast-enhanced magnetic resonance imaging in a canine myocardial infarction model. *J. Am. Coll. Cardiol.* 44, 2383–2389. doi:10.1016/j.jacc.2004.09.020.

Anderson, R. H., Smerup, M., Sanchez-Quintana, D., Loukas, M., and Lunkenheimer, P. P. (2009). The three-dimensional arrangement of the myocytes in the ventricular walls. *Clin. Anat.* 22, 64–76. doi:10.1002/ca.20645.

Andreu, D., Berruezo, A., Ortiz-Pérez, J. T., Silva, E., Mont, L., Borràs, R., et al. (2011). Integration of 3D electroanatomic maps and magnetic resonance scar characterization into the navigation system to guide ventricular tachycardia ablation. *Circ. Arrhythmia Electrophysiol.* 4, 674–683. doi:10.1161/CIRCEP.111.961946.

Andreu, D., Ortiz-Pérez, J. T., Fernández-Armenta, J., Guiu, E., Acosta, J., Prat-González, S., et al. (2015). 3D delayed-enhanced magnetic resonance sequences improve conducting channel delineation prior to ventricular tachycardia ablation. *EP Eur.* 17, 938–945. doi:10.1093/europace/euu310.

Andreu, D., Penela, D., Acosta, J., Fernández-Armenta, J., Perea, R. J., Soto-Iglesias, D., et al. (2017). Cardiac magnetic resonance–aided scar dechanneling: Influence on acute and long-term outcomes. *Hear. Rhythm* 14, 1121–1128. doi:10.1016/j.hrthm.2017.05.018.

Antzelevitch, C., and Burashnikov, A. (2011). Overview of Basic Mechanisms of Cardiac Arrhythmia. *Card. Electrophysiol. Clin.* 3, 23–45. doi:10.1016/j.ccep.2010.10.012.

Antzelevitch, C., Shimizu, W., Yan, G. X., Sicouri, S., Weissenburger, J., Nesterenko, V. V, et al. (1999). The M cell: its contribution to the ECG and to normal and abnormal electrical function of the heart. *J. Cardiovasc. Electrophysiol.* 10, 1124–52. doi:10.1111/j.1540-8167.1999.tb00287.x.

Aoki, M., Okamoto, Y., Musha, T., and Harumi, K. I. (1987). Three-dimensional simulation of the ventricular depolarization and repolarization processes and body surface potentials: normal heart and bundle branch block. *IEEE Trans. Biomed. Eng.* 34, 454–462. Available at: http://www.ncbi.nlm.nih.gov/pubmed/3610193.

Appleton, B., Wei, Q., Liu, N., Xia, L., Crozier, S., Liu, F., et al. (2006). An electrical heart model incorporating real geometry and motion. in *27th Annual International Conference of the Engineering in Medicine and Biology Society (IEEE-EMBS 2005)* (Shanghai, China: IEEE), 345–348. doi:10.1109/IEMBS.2005.1616415.

Arai, A. E. (2015). Healing After Myocardial Infarction. *JACC Cardiovasc. Imaging* 8, 680–683. doi:10.1016/j.jcmg.2015.02.012.

Arevalo, H. J., Helm, P. A., and Trayanova, N. A. (2008). Development of a model of the infarcted canine heart that predicts arrhythmia generation from specific cardiac geometry and scar distribution. in *2008 Computers in Cardiology* (Bologna, Italy: IEEE), 497–500. doi:10.1109/CIC.2008.4749087.

Arevalo, H. J., Vadakkumpadan, F., Guallar, E., Jebb, A., Malamas, P., Wu, K. C., et al. (2016). Arrhythmia risk stratification of patients after myocardial infarction using personalized heart models. *Nat. Commun.* 7, 11437. doi:10.1038/ncomms11437.

Arevalo, H., Plank, G., Helm, P., Halperin, H., and Trayanova, N. (2013). Tachycardia in Post-Infarction Hearts: Insights from 3D Image-Based Ventricular Models. *PLoS One* 8, e68872. doi:10.1371/journal.pone.0068872.

Arora, R., and Kadish, A. (1996). "Fundamentals of Intracardiac Mapping," in *Catheter Ablation of Cardiac Arrhythmias* (Elsevier), 107–134. doi:10.1016/B978-1-4160-0312-0.50013-X.

Ashikaga, H., Arevalo, H., Vadakkumpadan, F., Blake, R. C., Bayer, J. D., Nazarian, S., et al. (2013). Feasibility of image-based simulation to estimate ablation target in human ventricular arrhythmia. *Hear. Rhythm* 10, 1109–1116. doi:10.1016/j.hrthm.2013.04.015.

Ashikaga, H., Sasano, T., Dong, J., Zviman, M. M., Evers, R., Hopenfeld, B., et al. (2007). Magnetic Resonance Based Anatomical Analysis of Scar-Related Ventricular Tachycardia: Implications for Catheter Ablation. *Circ. Res.* 101, 939–947. doi:10.1161/CIRCRESAHA.107.158980.

Aslanidi, O. V, Nikolaidou, T., Zhao, J., Smaill, B. H., Gilbert, S. H., Holden, A. V, et al. (2013). Application of micro-computed tomography with iodine staining to cardiac imaging, segmentation, and computational model development. *IEEE Trans. Med. Imaging* 32, 8–17. doi:10.1109/TMI.2012.2209183.

Azzouzi, A., Coudière, Y., Turpault, R., and Zemzemi, N. (2011). A mathematical model of the Purkinje-muscle junctions. *Math. Biosci. Eng. - MBE* 8, 915–930.

Baldinger, S. H., Stevenson, W. G., and John, R. M. (2016). Ablation of ischemic ventricular tachycardia: evidence, techniques, results, and future directions. *Curr. Opin. Cardiol.* 31, 29–36. doi:10.1097/HCO.0000000000000237.

Barber, F., García-Fernández, I., Lozano, M., and Sebastian, R. (2018). Automatic estimation of Purkinje-Myocardial junction hot-spots from noisy endocardial

samples: A simulation study. *Int. j. numer. method. biomed. eng.* 34, e2988. doi:10.1002/cnm.2988.

Barber, F., Lozano, M., García-Fernández, I., and Sebastián, R. (2017). Inverse estimation of terminal connections in the cardiac conduction system. *Math. Methods Appl. Sci.* doi:10.1002/mma.4280.

Baritussio, A., Scatteia, A., and Bucciarelli-Ducci, C. (2018). Role of cardiovascular magnetic resonance in acute and chronic ischemic heart disease. *Int. J. Cardiovasc. Imaging* 34, 67–80. doi:10.1007/s10554-017-1116-0.

Bayer, J. D., Blake, R. C., Plank, G., and Trayanova, N. A. (2012). A Novel Rule-Based Algorithm for Assigning Myocardial Fiber Orientation to Computational Heart Models. *Ann. Biomed. Eng.* 40, 2243–2254. doi:10.1007/s10439-012-0593-5.

Behradfar, E., Nygren, A., and Vigmond, E. J. (2014). The Role of Purkinje-Myocardial Coupling during Ventricular Arrhythmia: A Modeling Study. *PLoS One* 9, e88000. doi:10.1371/journal.pone.0088000.

Ben-Haim, S. a, Osadchy, D., Scnuster, I., Gepstein, L., Hayam, G., and Josephson, M. E. (1996). Nonfluoroscopic, in vivo navigation and mapping technology. *Nat. Med.* 2, 1393–1395. doi:10.1038/nm1296-1393.

Benito, B., and Josephson, M. E. (2012). Ventricular Tachycardia in Coronary Artery Disease. *Rev. Española Cardiol. (English Ed.* 65, 939–955. doi:10.1016/j.rec.2012.03.022.

Berenfeld, O., and Jalife, J. (1998). Purkinje-Muscle reentry as a mechanism of polymorphic ventricular arrhythmias in a 3-dimensional model of the ventricles. *Circ. Res.* 82, 1063–1077. doi:10.1161/01.RES.82.10.1063.

Bernard, O., Lalande, A., Zotti, C., Cervenansky, F., Yang, X., Heng, P.-A., et al. (2018). Deep Learning Techniques for Automatic MRI Cardiac Multi-Structures Segmentation and Diagnosis: Is the Problem Solved? *IEEE Trans. Med. Imaging* 37, 2514–2525. doi:10.1109/TMI.2018.2837502.

Berruezo, A., Fernandez-Armenta, J., Andreu, D., Penela, D., Herczku, C., Evertz, R., et al. (2015). Scar Dechanneling: New Method for Scar-Related Left Ventricular Tachycardia Substrate Ablation. *Circ. Arrhythmia Electrophysiol.* 8, 326–336. doi:10.1161/CIRCEP.114.002386.

Besl, P. J., and McKay, N. D. (1992). A method for registration of 3-D shapes. *IEEE Trans. Pattern Anal. Mach. Intell.* 14, 239–256. doi:10.1109/34.121791.

Beuckelmann, D. J., Näbauer, M., and Erdmann, E. (1992). Intracellular calcium handling in isolated ventricular myocytes from patients with terminal heart failure. *Circulation* 85, 1046–1055. doi:10.1161/01.CIR.85.3.1046.

Bishop, M. J., Hales, P., Plank, G., Gavaghan, D. J., Scheider, J., and Grau, V. (2009). "Comparison of Rule-Based and DTMRI-Derived Fibre Architecture in a Whole Rat Ventricular Computational Model," in *Functional Imaging and Modeling of the Heart-FIMH 2009, LNCS 5528*, eds. N. Ayache, H. Delingette, and M. Sermesant (Nice, France: Springer, Berlin, Heidelberg), 87–96. doi:10.1007/978-3-642-01932-6_10.

Bishop, M. J., Plank, G., Burton, R. A. B., Schneider, J. E., Gavaghan, D. J., Grau, V., et al. (2010). Development of an anatomically detailed MRI-derived rabbit ventricular model and assessment of its impact on simulations of electrophysiological function. *Am. J. Physiol. Heart Circ. Physiol.* 298, H699–H718. doi:10.1152/ajpheart.00606.2009.

Blanc, O., Virag, N., Vesin, J. M., and Kappenberger, L. (2001). A computer model of human atria with reasonable computation load and realistic anatomical properties. *IEEE Trans. Biomed. Eng.* 48, 1229–1237. doi:10.1109/10.959315.

Bodin, O. N., and Kuz'min, A. V (2006). Synthesis of a realistic model of the surface of the heart. *Biomed. Eng. (NY).* 40, 280–283. Available at: http://www.ncbi.nlm.nih.gov/pubmed/17290920 [Accessed July 16, 2014].

Bogun, F., Desjardins, B., Crawford, T., Good, E., Jongnarangsin, K., Oral, H., et al. (2008). Post-Infarction Ventricular Arrhythmias Originating in Papillary Muscles. *J. Am. Coll. Cardiol.* 51, 1794–1802. doi:10.1016/j.jacc.2008.01.046.

Bogun, F., Good, E., Reich, S., Elmouchi, D., Igic, P., Tschopp, D., et al. (2006). Role of Purkinje Fibers in Post-Infarction Ventricular Tachycardia. *J. Am. Coll. Cardiol.* 48, 2500–2507. doi:10.1016/j.jacc.2006.07.062.

Bogun, F., Krishnan, S., Siddiqui, M., Good, E., Marine, J. E., Schuger, C., et al. (2005). Electrogram Characteristics in Postinfarction Ventricular Tachycardia: Effect of Infarct Age. *J. Am. Coll. Cardiol.* 46, 667–674. doi:10.1016/j.jacc.2005.01.064.

Bordas, R., Gillow, K., Lou, Q., Efimov, I. R., Gavaghan, D., Kohl, P., et al. (2011). Rabbit-specific ventricular model of cardiac electrophysiological function including specialized conduction system. *Prog. Biophys. Mol. Biol.* 107, 90–100. doi:10.1016/j.pbiomolbio.2011.05.002.

Boyle, P. M., Deo, M., Plank, G., and Vigmond, E. J. (2010). Purkinje-mediated effects in the response of quiescent ventricles to defibrillation shocks. *Ann. Biomed. Eng.*

38, 456–468. doi:10.1007/s10439-009-9829-4.

Bradley, C. P., Pullan, A. J., and Hunter, P. J. (2000). Effects of Material Properties and Geometry on Electrocardiographic Forward Simulations. *Ann. Biomed. Eng.* 28, 721–741. doi:10.1114/1.1289467.

Bressler, S. L., and Ding, M. (2006). "Event-Related Potentials," in *Wiley Encyclopedia of Biomedical Engineering*, ed. M. Akay (Hoboken, NJ, USA: John Wiley & Sons, Inc.), 1–8. doi:10.1002/9780471740360.ebs0455.

Britton, O. J., Bueno-Orovio, A., Van Ammel, K., Lu, H. R., Towart, R., Gallacher, D. J., et al. (2013). Experimentally calibrated population of models predicts and explains intersubject variability in cardiac cellular electrophysiology. *Proc. Natl. Acad. Sci.* 110, E2098–E2105. doi:10.1073/pnas.1304382110.

Brugada, J., Berruezo, A., Cuesta, A., Osca, J., Chueca, E., Fosch, X., et al. (2003). Nonsurgical transthoracic epicardial radiofrequency ablation. *J. Am. Coll. Cardiol.* 41, 2036–2043. doi:10.1016/S0735-1097(03)00398-X.

Bueno-Orovio, A., Cherry, E. M., and Fenton, F. H. (2008). Minimal model for human ventricular action potentials in tissue. *J. Theor. Biol.* 253, 544–560. doi:10.1016/j.jtbi.2008.03.029.

Burton, R. A. B., Lee, P., Casero, R., Garny, A., Siedlecka, U., Schneider, J. E., et al. (2014). Three-dimensional histology: tools and application to quantitative assessment of cell-type distribution in rabbit heart. *Europace* 16, iv86–iv95. doi:10.1093/europace/euu234.

Burton, R. A. B., Plank, G., Schneider, J. E., Grau, V., Ahammer, H., Keeling, S. L., et al. (2006). Three-dimensional models of individual cardiac histoanatomy: tools and challenges. *Ann. N. Y. Acad. Sci.* 1080, 301–319. Available at: http://onlinelibrary.wiley.com/doi/10.1196/annals.1380.023/full [Accessed July 16, 2014].

Cabo, C., and Boyden, P. A. (2003). Electrical remodeling of the epicardial border zone in the canine infarcted heart: a computational analysis. *Am. J. Physiol. - Hear. Circ. Physiol.* 284, H372–H384. doi:10.1152/ajpheart.00512.2002.

Caldwell, B. J., Trew, M. L., Sands, G. B., Hooks, D. A., LeGrice, I. J., and Smaill, B. H. (2009). Three Distinct Directions of Intramural Activation Reveal Nonuniform Side-to-Side Electrical Coupling of Ventricular Myocytes. *Circ. Arrhythmia Electrophysiol.* 2, 433–440. doi:10.1161/CIRCEP.108.830133.

Calkins, H., Kuck, K. H., Cappato, R., Brugada, J., Camm, A. J., Chen, S.-A., et al. (2012).

2012 HRS/EHRA/ECAS Expert Consensus Statement on Catheter and Surgical Ablation of Atrial Fibrillation: Recommendations for Patient Selection, Procedural Techniques, Patient Management and Follow-up, Definitions, Endpoints, and Research Trial Design: A re. *Europace* 14, 528–606. doi:10.1093/europace/eus027.

Camara, O., Sermesant, M., Lamata, P., Wang, L., Pop, M., Relan, J., et al. (2011). Inter-model consistency and complementarity: Learning from ex-vivo imaging and electrophysiological data towards an integrated understanding of cardiac physiology. *Prog. Biophys. Mol. Biol.* 107, 122–133. doi:10.1016/j.pbiomolbio.2011.07.007.

Camelliti, P., Devlin, G. P., Matthews, K. G., Kohl, P., and Green, C. R. (2004). Spatially and temporally distinct expression of fibroblast connexins after sheep ventricular infarction. *Cardiovasc. Res.* 62, 415–425. doi:10.1016/j.cardiores.2004.01.027.

Campos, F. O., Shiferaw, Y., Weber dos Santos, R., Plank, G., and Bishop, M. J. (2018). Microscopic Isthmuses and Fibrosis Within the Border Zone of Infarcted Hearts Promote Calcium-Mediated Ectopy and Conduction Block. *Front. Phys.* 6, 1–14. doi:10.3389/fphy.2018.00057.

Cardenes, R., Sebastian, R., Berruezo, A., and Camara, O. (2014). Inverse estimation of ventricular Purkinje tree pathways from sequences of depolarization. in *Computing in Cardiology* (Cambridge, Massachusetts (USA): IEEE), 677–680.

Cardone-Noott, L., Bueno-Orovio, A., Mincholé, A., Zemzemi, N., and Rodriguez, B. (2016). Human ventricular activation sequence and the simulation of the electrocardiographic QRS complex and its variability in healthy and intraventricular block conditions. *EP Eur.* 18, iv4–iv15. doi:10.1093/europace/euw346.

Carpio, E. F., Gomez, J. F., Sebastian, R., Lopez-Perez, A., Castellanos, E., Almendral, J., et al. (2019). Optimization of Lead Placement in the Right Ventricle During Cardiac Resynchronization Therapy. A Simulation Study. *Front. Physiol.* 10, Article 74. doi:10.3389/fphys.2019.00074.

Cedilnik, N., Duchateau, J., Dubois, R., Sacher, F., Jaïs, P., Cochet, H., et al. (2018). Fast personalized electrophysiological models from computed tomography images for ventricular tachycardia ablation planning. *EP Eur.* 20, iii94–iii101. doi:10.1093/europace/euy228.

Chen, Z., Cabrera-Lozoya, R., Relan, J., Sohal, M., Shetty, A., Karim, R., et al. (2016). Biophysical Modeling Predicts Ventricular Tachycardia Inducibility and Circuit Morphology: A Combined Clinical Validation and Computer Modeling Approach.

J. Cardiovasc. Electrophysiol. 27, 851–860. doi:10.1111/jce.12991.

Chinchapatnam, P., Rhode, K. S., Ginks, M., Mansi, T., Peyrat, J. M., Lambiase, P., et al. (2009). Estimation of volumetric myocardial apparent conductivity from endocardial electro-anatomical mapping. in *31st Annual International Conference of the IEEE Engineering in Medicine and Biology Society (EMBC 2009)* (Minneapolis, MN (USA): IEEE), 2907–2910. doi:10.1109/IEMBS.2009.5334441.

Chinchapatnam, P., Rhode, K. S., Ginks, M., Rinaldi, C. A., Lambiase, P., Razavi, R., et al. (2008). Model-Based Imaging of Cardiac Apparent Conductivity and Local Conduction Velocity for Diagnosis and Planning of Therapy. *IEEE Trans. Med. Imaging* 27, 1631–1642. doi:10.1109/TMI.2008.2004644.

Ciaccio, E. J., Coromilas, J., Wit, A. L., Peters, N. S., and Garan, H. (2018). Source-Sink Mismatch Causing Functional Conduction Block in Re-Entrant Ventricular Tachycardia. *JACC Clin. Electrophysiol.* 4, 1–16. doi:10.1016/j.jacep.2017.08.019.

Clancy, C. E., and Rudy, Y. (2001). Cellular consequences of HERG mutations in the long QT syndrome: precursors to sudden cardiac death. *Cardiovasc. Res.* 50, 301–313. Available at: http://www.ncbi.nlm.nih.gov/pubmed/11334834.

Clerc, L. (1976). Directional differences of impulse spread in trabecular muscle from mammalian heart. *J. Physiol.* 255, 335–346. Available at: http://jp.physoc.org/content/255/2/335.short [Accessed July 17, 2014].

Cleutjens, J. P., Blankesteijn, W. M., Daemen, M. J., and Smits, J. F. (1999). The infarcted myocardium: simply dead tissue, or a lively target for therapeutic interventions. *Cardiovasc. Res.* 44, 232–41. doi:10.1016/S0008-6363(99)00212-6.

Colli Franzone, P., Guerri, L., Pennacchio, M., and Taccardi, B. (1998). Spread of excitation in 3-D models of the anisotropic cardiac tissue. II. Effects of fiber architecture and ventricular geometry. *Math. Biosci.* 147, 131–171. Available at: http://www.ncbi.nlm.nih.gov/pubmed/9433061.

Colli Franzone, P., Guerri, L., and Rovida, S. (1990). Wavefront propagation in an activation model of the anisotropic cardiac tissue: asymptotic analysis and numerical simulations. *J. Math. Biol.* 28, 121–176. doi:10.1007/BF00163143.

Connolly, A. J., and Bishop, M. J. (2016). Computational Representations of Myocardial Infarct Scars and Implications for Arrhythmogenesis. *Clin. Med. Insights Cardiol.* 10, 27. doi:10.4137/CMC.S39708.

Connolly, A., Trew, M. L., Smaill, B. H., Plank, G., and Bishop, M. J. (2015). Local Gradients in Electrotonic Loading Modulate the Local Effective Refractory Period:

Implications for Arrhythmogenesis in the Infarct Border Zone. *IEEE Trans. Biomed. Eng.* 62, 2251–2259. doi:10.1109/TBME.2015.2421296.

Constantine, G., Shan, K., Flamm, S. D., and Sivananthan, M. U. (2004). Role of MRI in clinical cardiology. *Lancet* 363, 2162–2171. doi:10.1016/S0140-6736(04)16509-4.

Courtemanche, M., Ramirez, R. J., and Nattel, S. (1998). Ionic mechanisms underlying human atrial action potential properties: insights from a mathematical model. *Am. J. Physiol. Circ. Physiol.* 275, H301–H321. doi:10.1152/ajpheart.1998.275.1.H301.

Craelius, W., Chen, V., and El-Sherif, N. (1988). Stretch activated ion channels in ventricular myocytes. *Biosci. Rep.* 8, 407–414. doi:10.1007/BF01121637.

Creswell, L. L., Wyers, S. G., Pirolo, J. S., Perman, W. H., Vannier, M. W., and Pasque, M. K. (1992). Mathematical modeling of the heart using magnetic resonance imaging. *IEEE Trans. Med. Imaging* 11, 581–589. Available at: http://ieeexplore.ieee.org/xpls/abs_all.jsp?arnumber=192695 [Accessed July 16, 2014].

Daskalopoulos, E. P., Janssen, B. J. a., and Blankesteijn, W. M. (2012). Myofibroblasts in the Infarct Area: Concepts and Challenges. *Microsc. Microanal.* 18, 35–49. doi:10.1017/S143192761101227X.

Dass, S., Suttie, J. J., Piechnik, S. K., Ferreira, V. M., Holloway, C. J., Banerjee, R., et al. (2012). Myocardial tissue characterization using magnetic resonance noncontrast T1 mapping in hypertrophic and dilated cardiomyopathy. *Circ. Cardiovasc. Imaging* 5, 726–733. doi:10.1161/CIRCIMAGING.112.976738.

de Bakker, J. M. T. (2017). Do Myofibroblasts Represent a Hidden Factor for Impaired Conduction and Tachyarrhythmia in Post-Myocardial Infarction? *JACC Clin. Electrophysiol.* 3, 715–717. doi:10.1016/j.jacep.2017.01.007.

de Bakker, J. M. T., Stein, M., and van Rijen, H. V. M. (2005). Three-dimensional anatomic structure as substrate for ventricular tachycardia/ventricular fibrillation. *Hear. Rhythm* 2, 777–779. doi:10.1016/j.hrthm.2005.03.022.

de Bakker, J. M., van Capelle, F. J., Janse, M. J., Tasseron, S., Vermeulen, J. T., de Jonge, N., et al. (1993). Slow conduction in the infarcted human heart. "Zigzag" course of activation. *Circulation* 88, 915–926. doi:10.1161/01.CIR.88.3.915.

de Bakker, J. M., van Capelle, F. J., Janse, M. J., Wilde, A. A., Coronel, R., Becker, A. E., et al. (1988). Reentry as a cause of ventricular tachycardia in patients with chronic ischemic heart disease: electrophysiologic and anatomic correlation.

Circulation 77, 589–606. doi:10.1161/01.CIR.77.3.589.

de Chillou, C., Lacroix, D., Klug, D., Magnin-Poull, I., Marquié, C., Messier, M., et al. (2002). Isthmus Characteristics of Reentrant Ventricular Tachycardia After Myocardial Infarction. *Circulation* 105, 726–731. doi:10.1161/hc0602.103675.

de Jong, S., van Veen, T. a B., van Rijen, H. V. M., and de Bakker, J. M. T. (2011). Fibrosis and Cardiac Arrhythmias. *J. Cardiovasc. Pharmacol.* 57, 630–638. doi:10.1097/FJC.0b013e318207a35f.

Deng, D., Arevalo, H. J., Prakosa, A., Callans, D. J., and Trayanova, N. A. (2016). A feasibility study of arrhythmia risk prediction in patients with myocardial infarction and preserved ejection fraction. *Europace* 18, iv60–iv66. doi:10.1093/europace/euw351.

Deng, D., Arevalo, H., Pashakhanloo, F., Prakosa, A., Ashikaga, H., McVeigh, E., et al. (2015). Accuracy of prediction of infarct-related arrhythmic circuits from image-based models reconstructed from low and high resolution MRI. *Front. Physiol.* 6, 1–12. doi:10.3389/fphys.2015.00282.

Deng, D., Jiao, P., Ye, X., and Xia, L. (2012). An Image-Based Model of the Whole Human Heart with Detailed Anatomical Structure and Fiber Orientation. *Comput. Math. Methods Med.* 2012, 1–16. doi:10.1155/2012/891070.

Deng, D., Nikolov, P., Arevalo, H. J., and Trayanova, N. A. (2018). Optimal contrast-enhanced MRI image thresholding for accurate prediction of ventricular tachycardia using ex-vivo high resolution models. *Comput. Biol. Med.* 102, 426–432. doi:10.1016/j.compbiomed.2018.09.031.

Dhanjal, T. S., Lellouche, N., von Ruhland, C. J., Abehsira, G., Edwards, D. H., Dubois-Randé, J.-L., et al. (2017). Massive Accumulation of Myofibroblasts in the Critical Isthmus Is Associated With Ventricular Tachycardia Inducibility in Post-Infarct Swine Heart. *JACC Clin. Electrophysiol.* 3, 703–714. doi:10.1016/j.jacep.2016.11.010.

DiFrancesco, D., and Noble, D. (1985). A Model of Cardiac Electrical Activity Incorporating Ionic Pumps and Concentration Changes. *Philos. Trans. R. Soc. B Biol. Sci.* 307, 353–398. doi:10.1098/rstb.1985.0001.

Dobrzynski, H., Anderson, R. H., Atkinson, A., Borbas, Z., D'Souza, A., Fraser, J. F., et al. (2013). Structure, function and clinical relevance of the cardiac conduction system, including the atrioventricular ring and outflow tract tissues. *Pharmacol. Ther.* 139, 260–288. doi:10.1016/j.pharmthera.2013.04.010.

Doltra, A., Amundsen, B., Gebker, R., Fleck, E., and Kelle, S. (2013). Emerging Concepts for Myocardial Late Gadolinium Enhancement MRI. *Curr. Cardiol. Rev.* 9, 185–190. doi:10.2174/1573403X113099990030.

Drouin, E., Charpentier, F., Gauthier, C., Laurent, K., and Le Marec, H. (1995). Electrophysiologic characteristics of cells spanning the left ventricular wall of human heart: Evidence for presence of M cells. *J. Am. Coll. Cardiol.* 26, 185–192. doi:10.1016/0735-1097(95)00167-X.

Dun, W., Baba, S., Yagi, T., and Boyden, P. A. (2004). Dynamic remodeling of K+ and Ca2+ currents in cells that survived in the epicardial border zone of canine healed infarcted heart. *AJP Hear. Circ. Physiol.* 287, H1046–H1054. doi:10.1152/ajpheart.00082.2004.

Durrer, D., Van Dam, R. T., Freud, G. E., Janse, M. J., Meijler, F. L., and Arzbaecher, R. C. (1970). Total Excitation of the Isolated Human Heart. *Circulation* 41, 899–912. doi:10.1161/01.CIR.41.6.899.

Dux-Santoy, L., Sebastian, R., Felix-Rodriguez, J., Ferrero, J. M., and Saiz, J. (2011). Interaction of specialized cardiac conduction system with antiarrhythmic drugs: a simulation study. *IEEE Trans. Biomed. Eng.* 58, 3475–3478. doi:10.1109/TBME.2011.2165213.

Dux-Santoy, L., Sebastian, R., Rodriguez, J. F., and Ferrero, J. M. (2013). Modeling the different sections of the cardiac conduction system to obtain realistic electrocardiograms. in *2013 35th Annual International Conference of the IEEE Engineering in Medicine and Biology Society (EMBC)* (Osaka, Japan: IEEE), 6846–6849. doi:10.1109/EMBC.2013.6611130.

Ecabert, O., Peters, J., Schramm, H., Lorenz, C., von Berg, J., Walker, M. J., et al. (2008). Automatic model-based segmentation of the heart in CT images. *IEEE Trans. Med. Imaging* 27, 1189–201. doi:10.1109/TMI.2008.918330.

Ecabert, O., Peters, J., Walker, M. J., Ivanc, T., Lorenz, C., von Berg, J., et al. (2011). Segmentation of the heart and great vessels in CT images using a model-based adaptation framework. *Med. Image Anal.* 15, 863–876. doi:10.1016/j.media.2011.06.004.

Engelman, Z. J., Trew, M. L., and Smaill, B. H. (2010). Structural Heterogeneity Alone Is a Sufficient Substrate for Dynamic Instability and Altered Restitution. *Circ. Arrhythmia Electrophysiol.* 3, 195–203. doi:10.1161/CIRCEP.109.890459.

Ertl, G., and Frantz, S. (2005). Healing after myocardial infarction. *Cardiovasc. Res.* 66, 22–32. doi:10.1016/j.cardiores.2005.01.011.

Fast, V. G., and Kleber, A. G. (1995). Block of impulse propagation at an abrupt tissue expansion: evaluation of the critical strand diameter in 2- and 3-dimensional computer models. *Cardiovasc. Res.* 30, 449–459. doi:10.1016/S0008-6363(95)00071-2.

Fenton, F., and Karma, A. (1998). Vortex dynamics in three-dimensional continuous myocardium with fiber rotation: filament instability and fibrillation. *Chaos* 8, 20–47. doi:10.1063/1.166374.

Fernández-Armenta, J., Berruezo, A., Andreu, D., Camara, O., Silva, E., Serra, L., et al. (2013). Three-dimensional architecture of scar and conducting channels based on high resolution ce-CMR: Insights for ventricular tachycardia ablation. *Circ. Arrhythmia Electrophysiol.* 6, 528–537. doi:10.1161/CIRCEP.113.000264.

Fernández-Armenta, J., Penela, D., Acosta, J., Andreu, D., and Berruezo, A. (2015). Approach to Ablation of Unmappable Ventricular Arrhythmias. *Card. Electrophysiol. Clin.* 7, 527–537. doi:10.1016/j.ccep.2015.05.011.

Ferrer-Albero, A., Godoy, E. J., Lozano, M., Martínez-Mateu, L., Atienza, F., Saiz, J., et al. (2017). Non-invasive localization of atrial ectopic beats by using simulated body surface P-wave integral maps. *PLoS One* 12, e0181263. doi:10.1371/journal.pone.0181263.

Ferrer, A., Sebastián, R., Sánchez-Quintana, D., Rodríguez, J. F., Godoy, E. J., Martínez, L., et al. (2015a). Detailed Anatomical and Electrophysiological Models of Human Atria and Torso for the Simulation of Atrial Activation. *PLoS One* 10, e0141573. doi:10.1371/journal.pone.0141573.

Ferrer, A., Sebastian, R., Sánchez-Quintana, D., Rodríguez, J., and Saíz, J. (2015b). Anatomical and electrophysiological detailed models of human atria and torso for the simulation of atrial activation [UNDER REVIEW]. *Med. Image Anal.*

Ferrero, J. M., Saiz, J., Ferrero, J. M., and Thakor, N. V. (1996). Simulation of Action Potentials From Metabolically Impaired Cardiac Myocytes: Role of ATP-Sensitive K+ Current. *Circ. Res.* 79, 208–221. doi:10.1161/01.RES.79.2.208.

Ferrero, J. M., Trénor, B., Rodríguez, B., and Sáiz, J. (2003). Electrical activity and reentry during acute regional myocardial ischemia: insights from simulations. *Int. J. Bifurc. Chaos* 13, 3703–3715. doi:10.1142/S0218127403008806.

Ferrero, J. M., Trenor, B., and Romero, L. (2014). Multiscale computational analysis of the bioelectric consequences of myocardial ischaemia and infarction. *Europace* 16, 405–415. doi:10.1093/europace/eut405.

Fieno, D. S., Kim, R. J., Chen, E., Lomasney, J. W., Klocke, F. J., and Judd, R. M. (2000). Contrast-enhanced magnetic resonance imaging of myocardium at risk: Distinction between reversible and irreversible injury throughout infarct healing. *J. Am. Coll. Cardiol.* 36, 1985–1991. doi:10.1016/S0735-1097(00)00958-X.

Fink, M., Niederer, S. A., Cherry, E. M., Fenton, F. H., Koivumäki, J. T., Seemann, G., et al. (2011). Cardiac cell modelling: Observations from the heart of the cardiac physiome project. *Prog. Biophys. Mol. Biol.* 104, 2–21. doi:10.1016/j.pbiomolbio.2010.03.002.

FitzHugh, R. (1961). Impulses and physiological states in theoretical models of nerve membrane. *Biophys. J.* 1, 445–466. doi:10.1016/S0006-3495(61)86902-6.

Fonseca, C. G., Backhaus, M., Bluemke, D. A., Britten, R. D., Chung, J. Do, Cowan, B. R., et al. (2011). The Cardiac Atlas Project--an imaging database for computational modeling and statistical atlases of the heart. *Bioinformatics* 27, 2288–2295. doi:10.1093/bioinformatics/btr360.

Forbes, M. S., and Sperelakis, N. (1984). "Ultrastructure of Mammalian Cardiac Muscle," in *Physiology and Pathophysiology of the Heart*, 3–42. doi:10.1007/978-1-4757-1171-4_1.

Frangi, A. F., Niessen, W. J., and Viergever, M. A. (2001). Three-dimensional modeling for functional analysis of cardiac images: a review. *IEEE Trans. Med. Imaging* 20, 2–25. doi:10.1109/42.906421.

Frangi, A. F., Rueckert, D., Schnabel, J. A., and Niessen, W. J. (2002). Automatic construction of multiple-object three-dimensional statistical shape models: application to cardiac modeling. *IEEE Trans. Med. Imaging* 21, 1151–1166. doi:10.1109/TMI.2002.804426.

Franz, M. R., Bargheer, K., Rafflenbeul, W., Haverich, A., and Lichtlen, P. R. (1987). Monophasic action potential mapping in human subjects with normal electrocardiograms: direct evidence for the genesis of the T wave. *Circulation* 75, 379–386. doi:10.1161/01.CIR.75.2.379.

Freudenberg, J., Schiemann, T., Tiede, U., and Höhne, K. H. (2000). Simulation of cardiac excitation patterns in a three-dimensional anatomical heart atlas. *Comput. Biol. Med.* 30, 191–205. Available at: http://www.ncbi.nlm.nih.gov/pubmed/10821938.

Gabriel, S., Lau, R. W., and Gabriel, C. (1996). The dielectric properties of biological tissues: II. Measurements in the frequency range 10 Hz to 20 GHz. *Phys. Med. Biol.* 41, 2251–2269. doi:10.1088/0031-9155/41/11/002.

Garcia-Bustos, V., Sebastian, R., Izquierdo, M., Molina, P., Chorro, F. J., and Ruiz-Sauri, A. (2017). A quantitative structural and morphometric analysis of the Purkinje network and the Purkinje-myocardial junctions in pig hearts. *J. Anat.* 230, 664–678. doi:10.1111/joa.12594.

Garcia-Bustos, V., Sebastian, R., Izquierdo, M., Rios-Navarro, C., Bodí, V., Chorro, F. J., et al. (2019). Changes in the spatial distribution of the Purkinje network after acute myocardial infarction in the pig. *PLoS One* 14, e0212096. doi:10.1371/journal.pone.0212096.

Gardner, P. I., Ursell, P. C., Fenoglio, J. J., and Wit, a L. (1985). Electrophysiologic and anatomic basis for fractionated electrograms recorded from healed myocardial infarcts. *Circulation* 72, 596–611. doi:10.1161/01.CIR.72.3.596.

Gepstein, L., Hayam, G., and Ben-Haim, S. A. (1997). A Novel Method for Nonfluoroscopic Catheter-Based Electroanatomical Mapping of the Heart : In Vitro and In Vivo Accuracy Results. *Circulation* 95, 1611–1622. doi:10.1161/01.CIR.95.6.1611.

Gerstenfeld, E. P. (2013). Recurrent Ventricular Tachycardia After Catheter Ablation in Post-Infarct Cardiomyopathy. *J. Am. Coll. Cardiol.* 61, 74–76. doi:10.1016/j.jacc.2012.07.057.

Geselowitz, D. B., and Miller, W. T. (1983). A bidomain model for anisotropic cardiac muscle. *Ann. Biomed. Eng.* 11, 191–206. doi:10.1007/BF02363286.

Geuzaine, C., and Remacle, J.-F. (2009). Gmsh: A 3-D finite element mesh generator with built-in pre- and post-processing facilities. *Int. J. Numer. Methods Eng.* 79, 1309–1331. doi:10.1002/nme.2579.

Ghista, D., and Sandler, H. (1969). An analytic elastic-viscoelastic model for the shape and the forces in the left ventricle. *J. Biomech.* 2, 35–47. Available at: http://www.sciencedirect.com/science/article/pii/0021929069900402 [Accessed July 16, 2014].

Gibb, M., Bishop, M., Burton, R., Kohl, P., Grau, V., Plank, G., et al. (2009). The role of blood vessels in rabbit propagation dynamics and cardiac arrhythmias. in *Functional Imaging and Modeling of the Heart - FIMH 2009, LNCS 5528* (Springer-Verlag Berlin Heidelberg), 268–276.

Gibb, M., Burton, R. A. B., Bollensdorff, C., Afonso, C., Mansoori, T., Schotten, U., et al. (2012). "Resolving the three-dimensional histology of the heart," in *Computational Methods in Systems Biology - Lecture Notes in Computer Science 7605* (Springer-Verlag Berlin Heidelberg), 2–16.

Gillette, K., Prassl, A., Bayer, J., Vigmond, E., Neic, A., and Plank, G. (2017). Patient-specific Parameterization of Left-ventricular Model of Cardiac Electrophysiology using Electrocardiographic Recordings. in *Computing in Cardiology*, 1–4. doi:10.22489/CinC.2017.229-112.

Gillette, K., Prassl, A., Bayer, J., Vigmond, E., Neic, A., and Plank, G. (2018). Automatic Generation of Bi-Ventricular Models of Cardiac Electrophysiology for Patient Specific Personalization Using Non-Invasive Recordings. in *Computing in Cardiology*, 2–5. doi:10.22489/CinC.2018.265.

Godoy, E. J., Lozano, M., García-Fernández, I., Ferrer-Albero, A., MacLeod, R., Saiz, J., et al. (2018). Atrial Fibrosis Hampers Non-invasive Localization of Atrial Ectopic Foci From Multi-Electrode Signals: A 3D Simulation Study. *Front. Physiol.* 9. doi:10.3389/fphys.2018.00404.

Goodall, C. (1991). Procrustes methods in the statistical analysis of shape. *J. R. Stat. Soc. Ser. B. Stat. Methodol.* 53, 285–339. Available at: http://www.jstor.org/stable/2345744.

Gower, J. C. (1975). Generalized procrustes analysis. *Psychometrika* 40, 33–51. doi:10.1007/BF02291478.

Grandi, E., Pandit, S. V., Voigt, N., Workman, A. J., Dobrev, D., Jalife, J., et al. (2011). Human Atrial Action Potential and Ca2+ Model: Sinus Rhythm and Chronic Atrial Fibrillation. *Circ. Res.* 109, 1055–1066. doi:10.1161/CIRCRESAHA.111.253955.

Grandi, E., Pasqualini, F. S., and Bers, D. M. (2010). A novel computational model of the human ventricular action potential and Ca transient. *J. Mol. Cell. Cardiol.* 48, 112–121. doi:10.1016/j.yjmcc.2009.09.019.

Greenbaum, R. A., Ho, S. Y., Gibson, D. G., Becker, A. E., and Anderson, R. H. (1981). Left ventricular fibre architecture in man. *Heart* 45, 248–263. doi:10.1136/hrt.45.3.248.

Gurev, V., Lee, T., Constantino, J., Arevalo, H., and Trayanova, N. A. (2011). Models of cardiac electromechanics based on individual hearts imaging data. *Biomech. Model. Mechanobiol.* 10, 295–306. doi:10.1007/s10237-010-0235-5.

Haddad, R., Clarysse, P., Orkisz, M., Croisille, P., Revel, D., and Magnin, I. E. (2005). A realistic anthropomorphic numerical model of the beating heart. in *Functional Imaging and Modeling of the Heart (FIMH 2005), LNCS 3504* (Springer-Verlag Berlin Heidelberg), 384–393.

Haissaguerre, M., Vigmond, E., Stuyvers, B., Hocini, M., and Bernus, O. (2016).

Ventricular arrhythmias and the His–Purkinje system. *Nat. Rev. Cardiol.* 13, 155–166. doi:10.1038/nrcardio.2015.193.

Hansen, D. E., Craig, C. S., and Hondeghem, L. M. (1990). Stretch-induced arrhythmias in the isolated canine ventricle. Evidence for the importance of mechanoelectrical feedback. *Circulation* 81, 1094–1105. doi:10.1161/01.CIR.81.3.1094.

Harrild, D. M., and Henriquez, C. S. (2000). A computer model of normal conduction in the human atria. *Circ. Res.* 87, e25–e36. doi:10.1161/01.RES.87.7.e25.

Hegyi, B., Bossuyt, J., Griffiths, L. G., Shimkunas, R., Coulibaly, Z., Jian, Z., et al. (2018). Complex electrophysiological remodeling in postinfarction ischemic heart failure. *Proc. Natl. Acad. Sci.* 115, E3036–E3044. doi:10.1073/pnas.1718211115.

Heidenreich, E. A., Ferrero, J. M., Doblaré, M., and Rodríguez, J. F. (2010a). Adaptive Macro Finite Elements for the Numerical Solution of Monodomain Equations in Cardiac Electrophysiology. *Ann. Biomed. Eng.* 38, 2331–2345. doi:10.1007/s10439-010-9997-2.

Heidenreich, E. A., Ferrero, J. M., and Rodríguez, J. F. (2012). "Modeling the human heart under acute ischemia," in *Patient-Specific Computational Modeling* Lecture Notes in Computational Vision and Biomechanics., eds. B. Calvo Lopez and E. Peña (Dordrecht: Springer Netherlands), 81–103. doi:10.1007/978-94-007-4552-0.

Heidenreich, E. A., Gaspar, F. J., Ferrero, J. M., and Rodríguez, J. F. (2010b). Compact schemes for anisotropic reaction-diffusion equations with adaptive time step. *Int. J. Numer. Methods Eng.* 82, 1022–1043. doi:10.1002/nme.2801.

Hein, S., and Schaper, J. (2001). The extracellular matrix in normal and diseased myocardium. *J. Nucl. Cardiol.* 8, 188–196. doi:10.1067/mnc.2001.113331.

Helm, P. A., Tseng, H. J., Younes, L., McVeigh, E. R., and Winslow, R. L. (2005). Ex vivo 3D diffusion tensor imaging and quantification of cardiac laminar structure. *Magn. Reson. Med.* 54, 850–859. doi:10.1002/mrm.20622.

Hill, Y. R., Child, N., Hanson, B., Wallman, M., Coronel, R., Plank, G., et al. (2016). Investigating a novel activation-repolarisation time metric to predict localised Vulnerability to reentry using computational modelling. *PLoS One* 11, 1–22. doi:10.1371/journal.pone.0149342.

Hodgkin, A. L., and Huxley, A. F. (1952). A quantitative description of membrane current and its application to conduction and excitation in nerve. *J. Physiol.* 117,

500–544. Available at: http://www.ncbi.nlm.nih.gov/pmc/articles/pmc1392413/ [Accessed July 16, 2014].

Hoekema, R., Uijen, G. J. H., and van Oosterom, A. (2001). Geometrical aspects of the interindividual variability of multilead ECG recordings. *IEEE Trans. Biomed. Eng.* 48, 551–559. doi:10.1109/10.918594.

Holmes, A. A., Scollan, D. F., and Winslow, R. L. (2000). Direct histological validation of diffusion tensor MRI in formaldehyde-fixed myocardium. *Magn. Reson. Med.* 44, 157–161. doi:10.1002/1522-2594(200007)44:1<157::AID-MRM22>3.0.CO;2-F.

Hoogendoorn, C., Duchateau, N., Sanchez-Quintana, D., Whitmarsh, T., Sukno, F. M., De Craene, M., et al. (2013). A high-resolution atlas and statistical model of the human heart from multislice CT. *IEEE Trans. Med. Imaging* 32, 28–44. doi:10.1109/TMI.2012.2230015.

Hooks, D. a (2007). Myocardial segment-specific model generation for simulating the electrical action of the heart. *Biomed. Eng. Online* 6, 21. doi:10.1186/1475-925X-6-21.

Horan, L. G., Hand, R. C., Johnson, J. C., Sridharan, M. R., Rankin, T. B., and Flowers, N. C. (1978). A theoretical examination of ventricular repolarization and the secondary T wave. *Circ. Res.* 42, 750–757. doi:10.1161/01.RES.42.6.750.

Hsu, E. W., Muzikant, A. L., Matulevicius, S. A., Penland, R. C., and Henriquez, C. S. (1998). Magnetic resonance myocardial fiber-orientation mapping with direct histological correlation. *AJP Hear. Circ. Physiol.* 274, H1627–H1634. Available at: http://www.ncbi.nlm.nih.gov/pubmed/9612373.

Hsu, L.-Y., Natanzon, A., Kellman, P., Hirsch, G. a, Aletras, A. H., and Arai, A. E. (2006). Quantitative myocardial infarction on delayed enhancement MRI. Part I: Animal validation of an automated feature analysis and combined thresholding infarct sizing algorithm. *J. Magn. Reson. Imaging* 23, 298–308. doi:10.1002/jmri.20496.

Huang, J., Wang, L., Chu, C., Liu, W., and Zhu, Y. (2019). Accelerating cardiac diffusion tensor imaging combining local low-rank and 3D TV constraint. *Magn. Reson. Mater. Physics, Biol. Med.* doi:10.1007/s10334-019-00747-1.

Hundley, W. G., Bluemke, D. a, Finn, J. P., Flamm, S. D., Fogel, M. a, Friedrich, M. G., et al. (2010). ACCF/ACR/AHA/NASCI/SCMR 2010 expert consensus document on cardiovascular magnetic resonance: a report of the American College of Cardiology Foundation Task Force on Expert Consensus Documents. *J. Am. Coll. Cardiol.* 55, 2614–62. doi:10.1016/j.jacc.2009.11.011.

Hurtado, D. E., and Kuhl, E. (2014). Computational modelling of electrocardiograms: repolarisation and T-wave polarity in the human heart. *Comput. Methods Biomech. Biomed. Engin.* 17, 986–996. doi:10.1080/10255842.2012.729582.

Issa, Z. F., Miller, J. M., and Zipes, D. P. (2012). "Post-Infarction Sustained Monomorphic Ventricular Tachycardia," in *Clinical Arrhythmology and Electrophysiology: A Companion to Braunwald's Heart Disease* (Elsevier), 512–561. doi:10.1016/B978-1-4557-1274-8.00022-1.

Jafri, M. S. (2012). "Models of excitation-contraction coupling in cardiac ventricular myocytes," in *Bioinformatics and Drug Discovery, Methods in Molecular Biology* (New York: Springer Science+Business Media), 309–335. doi:10.1007/978-1-61779-965-5.

Jamiel, A., Ebid, M., Ahmed, A. M., Ahmed, D., and Al-Mallah, M. H. (2017). The role of myocardial viability in contemporary cardiac practice. *Heart Fail. Rev.* 22, 401–413. doi:10.1007/s10741-017-9626-3.

Janse, M. J., and Kleber, A. G. (1981). Electrophysiological changes and ventricular arrhythmias in the early phase of regional myocardial ischemia. *Circ. Res.* 49, 1069–1081. doi:10.1161/01.RES.49.5.1069.

Janse, M. J., and Wit, A. L. (1989). Electrophysiological mechanisms of ventricular arrhythmias resulting from myocardial ischemia and infarction. *Physiol. Rev.* 69, 1049–1169. doi:10.1152/physrev.1989.69.4.1049.

Janz, R. F., and Grimm, A. F. (1972). Finite-Element Model for the Mechanical Behavior of the Left Ventricle: prediction of deformation in the potassium-arrested rat heart. *Circ. Res.* 30, 244–252. doi:10.1161/01.RES.30.2.244.

Jiang, M., Cabo, C., Yao, J.-A., Boyden, P. A., and Tseng, G.-N. (2000). Delayed rectifier K currents have reduced amplitudes and altered kinetics in myocytes from infarcted canine ventricle. *Cardiovasc. Res.* 48, 34–43. doi:10.1016/S0008-6363(00)00159-0.

Johnston, B., Barnes, J., and Johnston, P. (2016). The Effect of Conductivity Values on Activation Times and Defibrillation Thresholds. in *Computing in Cardiology (CinC)*, 10–13. doi:10.22489/CinC.2016.050-233.

Johnston, B. M. (2016). Six Conductivity Values to Use in the Bidomain Model of Cardiac Tissue. *IEEE Trans. Biomed. Eng.* 63, 1525–1531. doi:10.1109/TBME.2015.2498144.

Johnston, B. M., Coveney, S., Chang, E. T. Y., Johnston, P. R., and Clayton, R. H. (2018).

Quantifying the effect of uncertainty in input parameters in a simplified bidomain model of partial thickness ischaemia. *Med. Biol. Eng. Comput.* 56, 761–780. doi:10.1007/s11517-017-1714-y.

Josephson, M. E., and Anter, E. (2015). Substrate Mapping for Ventricular Tachycardia: Assumptions and Misconceptions. *JACC Clin. Electrophysiol.* 1, 341–352. doi:10.1016/j.jacep.2015.09.001.

Kania, M., Rix, H., Fereniec, M., Zavala-Fernandez, H., Janusek, D., Mroczka, T., et al. (2014). The effect of precordial lead displacement on ECG morphology. *Med. Biol. Eng. Comput.* 52, 109–119. doi:10.1007/s11517-013-1115-9.

Kaplinsky, E., Ogawa, S., Michelson, E. L., and Dreifus, L. S. (1981). Instantaneous and delayed ventricular arrhythmias after reperfusion of acutely ischemic myocardium: evidence for multiple mechanisms. *Circulation* 63, 333–340. doi:10.1161/01.CIR.63.2.333.

Karim, R., Bhagirath, P., Claus, P., James Housden, R., Chen, Z., Karimaghaloo, Z., et al. (2016). Evaluation of state-of-the-art segmentation algorithms for left ventricle infarct from late Gadolinium enhancement MR images. *Med. Image Anal.* 30, 95–107. doi:10.1016/j.media.2016.01.004.

Katritsis, D. G., Boriani, G., Cosio, F. G., Hindricks, G., Jaïs, P., Josephson, M. E., et al. (2017). European Heart Rhythm Association (EHRA) consensus document on the management of supraventricular arrhythmias, endorsed by Heart Rhythm Society (HRS), Asia-Pacific Heart Rhythm Society (APHRS), and Sociedad Latinoamericana de Estimulación Cardiaca y Elect. *EP Eur.* 19, 465–511. doi:10.1093/europace/euw301.

Keener, J. P. (1991). An eikonal-curvature equation for action potential propagation in myocardium. *J. Math. Biol.* 29, 629–651. doi:10.1007/BF00163916.

Keener, J. P., and Bogar, K. (1998). A numerical method for the solution of the bidomain equations in cardiac tissue. *Chaos An Interdiscip. J. Nonlinear Sci.* 8, 234–241. doi:10.1063/1.166300.

Keller, D. U. J., Weber, F. M., Seemann, G., and Dössel, O. (2010). Ranking the Influence of Tissue Conductivities on Forward-Calculated ECGs. *IEEE Trans. Biomed. Eng.* 57, 1568–1576. doi:10.1109/TBME.2010.2046485.

Kerckhoffs, R. C. P., Bovendeerd, P. H. M., Kotte, J. C. S., Prinzen, F. W., Smits, K., and Arts, T. (2003). Homogeneity of cardiac contraction despite physiological asynchrony of depolarization: a model study. *Ann. Biomed. Eng.* 31, 536–547. doi:10.1114/1.1566447.

Kerckhoffs, R. C. P., Campbell, S. G., Flaim, S. N., Howard, E. J., Sierra-Aguado, J., Mulligan, L. J., et al. (2009). Multi-scale modeling of excitation-contraction coupling in the normal and failing heart. in *31st Annual International Conference of the IEEE Engineering in Medicine and Biology Society (EMBC 2009)* (Minneapolis, MN (USA): IEEE), 4281–4282. doi:10.1109/IEMBS.2009.5332708.Multi-Scale.

Kerckhoffs, R. C. P., Neal, M. L., Gu, Q., Bassingthwaighte, J. B., Omens, J. H., and McCulloch, A. D. (2007). Coupling of a 3D finite element model of cardiac ventricular mechanics to lumped systems models of the systemic and pulmonic circulation. *Ann. Biomed. Eng.* 35, 1–18. doi:10.1007/s10439-006-9212-7.

Kim, R. J., Fieno, D. S., Parrish, T. B., Harris, K., Chen, E. L., Simonetti, O., et al. (1999a). Relationship of MRI delayed contrast enhancement to irreversible injury, infarct age, and contractile function. *Circulation* 100, 1992–2002. doi:10.1161/01.CIR.100.19.1992.

Kim, Y.-H., Xie, F., Yashima, M., Wu, T.-J., Valderrabano, M., Lee, M.-H., et al. (1999b). Role of Papillary Muscle in the Generation and Maintenance of Reentry During Ventricular Tachycardia and Fibrillation in Isolated Swine Right Ventricle. *Circulation* 100, 1450–1459. doi:10.1161/01.CIR.100.13.1450.

Kléber, A. G., and Rudy, Y. (2004). Basic Mechanisms of Cardiac Impulse Propagation and Associated Arrhythmias. *Physiol. Rev.* 84, 431–488. doi:10.1152/physrev.00025.2003.

Klepfer, R. N., Johnson, C. R., and Macleod, R. S. (1997). The effects of inhomogeneities and anisotropies on electrocardiographic fields: a 3-D finite-element study. *IEEE Trans. Biomed. Eng.* 44, 706–719. doi:10.1109/10.605427.

Knupp, P. M. (2000). Achieving finite element mesh quality via optimization of the Jacobian matrix norm and associated quantities. Part II - A framework for volume mesh optimization and the condition number of the Jacobian matrix. *Int. J. Numer. Methods Eng.* 48, 1165–1185. doi:10.1002/(SICI)1097-0207(20000720)48:8<1165::AID-NME940>3.0.CO;2-Y.

Knupp, P. M. (2003). Algebraic mesh quality metrics for unstructured initial meshes. *Finite Elem. Anal. Des.* 39, 217–241. doi:10.1016/S0168-874X(02)00070-7.

Kohl, P., and Gourdie, R. G. (2014). Fibroblast–myocyte electrotonic coupling: Does it occur in native cardiac tissue? *J. Mol. Cell. Cardiol.* 70, 37–46. doi:10.1016/j.yjmcc.2013.12.024.

Kohl, P., Hunter, P., and Noble, D. (1999). Stretch-induced changes in heart rate and

rhythm: clinical observations, experiments and mathematical models. *Prog. Biophys. Mol. Biol.* 71, 91–138. doi:10.1016/S0079-6107(98)00038-8.

Kohl, P., Sachs, F., and Franz, M. R. (2005). *Cardiac mechano-electric feedback and arrhythmias: from pipette to patient*. Philadelphia: Elsevier Health Sciences.

Kolipaka, A., Chatzimavroudis, G. P., White, R. D., O'Donnell, T. P., and Setser, R. M. (2005). Segmentation of non-viable myocardium in delayed enhancement magnetic resonance images. *Int. J. Cardiovasc. Imaging* 21, 303–11. doi:10.1007/s10554-004-5806-z.

Konukoglu, E., Relan, J., Cilingir, U., Menze, B. H., Chinchapatnam, P., Jadidi, A., et al. (2011). Efficient probabilistic model personalization integrating uncertainty on data and parameters: Application to eikonal-diffusion models in cardiac electrophysiology. *Prog. Biophys. Mol. Biol.* 107, 134–146. doi:10.1016/j.pbiomolbio.2011.07.002.

Koushanpour, E., and Collings, W. (1966). Validation and dynamic applications of an ellipsoid model of the left ventricle. *J. Appl. Physiol.* 21, 1655–1661. Available at: http://jap.physiology.org/content/jap/21/5/1655.full.pdf [Accessed July 16, 2014].

Krueger, M. W., Schulze, W. H. W., Rhode, K. S., Razavi, R., Seemann, G., and Dössel, O. (2013a). Towards personalized clinical in-silico modeling of atrial anatomy and electrophysiology. *Med. Biol. Eng. Comput.* 51, 1251–1260. doi:10.1007/s11517-012-0970-0.

Krueger, M. W., Seemann, G., Rhode, K., Keller, D. U. J., Schilling, C., Arujuna, A., et al. (2013b). Personalization of atrial anatomy and electrophysiology as a basis for clinical modeling of radio-frequency ablation of atrial fibrillation. *IEEE Trans. Med. Imaging* 32, 73–84. doi:10.1109/TMI.2012.2201948.

Kwong, R. Y., and Farzaneh-Far, A. (2011). Measuring Myocardial Scar by CMR. *JACC Cardiovasc. Imaging* 4, 157–160. doi:10.1016/j.jcmg.2010.12.004.

Lamata, P., Niederer, S., Nordsletten, D., Barber, D. C., Roy, I., Hose, D. R., et al. (2011). An accurate, fast and robust method to generate patient-specific cubic Hermite meshes. *Med. Image Anal.* 15, 801–813. doi:10.1016/j.media.2011.06.010.

Lambiase, P., Rinaldi, A., Hauck, J., Mobb, M., Elliott, D., Mohammad, S., et al. (2004). Non-contact left ventricular endocardial mapping in cardiac resynchronisation therapy. *Heart* 90, 44–51. doi:10.1136/heart.90.1.44.

Lange, M., Di Marco, L. Y., Lekadir, K., Lassila, T., and Frangi, A. F. (2016). Protective

Role of False Tendon in Subjects with Left Bundle Branch Block: A Virtual Population Study. *PLoS One* 11, e0146477. doi:10.1371/journal.pone.0146477.

Larrabide, I., Omedas, P., Martelli, Y., Planes, X., Nieber, M., Moya, J. A., et al. (2009). GIMIAS: An open source framework for efficient development of research tools and clinical prototypes. *Lect. Notes Comput. Sci. (including Subser. Lect. Notes Artif. Intell. Lect. Notes Bioinformatics)* 5528, 417–426. doi:10.1007/978-3-642-01932-6_45.

Laurita, K. R., and Rosenbaum, D. S. (2000). Interdependence of Modulated Dispersion and Tissue Structure in the Mechanism of Unidirectional Block. *Circ. Res.* 87, 922–928. doi:10.1161/01.RES.87.10.922.

Lawson, B. A. J., Drovandi, C. C., Cusimano, N., Burrage, P., Rodriguez, B., and Burrage, K. (2018). Unlocking data sets by calibrating populations of models to data density: A study in atrial electrophysiology. *Sci. Adv.* 4, e1701676. doi:10.1126/sciadv.1701676.

Lazzara, R., and Scherlag, B. J. (1984). Electrophysiologic basis for arrhythmias in ischemic heart disease. *Am. J. Cardiol.* 53, B1–B7. doi:10.1016/0002-9149(84)90493-4.

Lazzara, R., and Scherlag, B. J. (2003). Mechanisms of monomorphic ventricular tachycardia in coronary artery disease. *J. Interv. Card. Electrophysiol.* 8, 87–92. doi:10.1023/A:1023651231389.

Lee, A. W. C., Costa, C. M., Strocchi, M., Rinaldi, C. A., and Niederer, S. A. (2018). Computational Modeling for Cardiac Resynchronization Therapy. *J. Cardiovasc. Transl. Res.* 11, 92–108. doi:10.1007/s12265-017-9779-4.

LeGrice, I. J., Smaill, B. H., Chai, L. Z., Edgar, S. G., Gavin, J. B., and Hunter, P. J. (1995). Laminar structure of the heart: ventricular myocyte arrangement and connective tissue architecture in the dog. *Am. J. Physiol. Circ. Physiol.* 269, H571–H582. doi:10.1152/ajpheart.1995.269.2.H571.

León, D. G., López-Yunta, M., Alfonso-Almazán, J. M., Marina-Breysse, M., Quintanilla, J. G., Sánchez-González, J., et al. (2019). Three-dimensional cardiac fibre disorganization as a novel parameter for ventricular arrhythmia stratification after myocardial infarction. *EP Eur.*, 1–11. doi:10.1093/europace/euy306.

Li, P., and Rudy, Y. (2011). A model of canine purkinje cell electrophysiology and Ca(2+) cycling: rate dependence, triggered activity, and comparison to ventricular myocytes. *Circ. Res.* 109, 71–79. doi:10.1161/CIRCRESAHA.111.246512.

Liehn, E. A., Postea, O., Curaj, A., and Marx, N. (2011). Repair After Myocardial Infarction, Between Fantasy and Reality. *J. Am. Coll. Cardiol.* 58, 2357–2362. doi:10.1016/j.jacc.2011.08.034.

Liu, D. W., Gintant, G. A., and Antzelevitch, C. (1993). Ionic bases for electrophysiological distinctions among epicardial, midmyocardial, and endocardial myocytes from the free wall of the canine left ventricle. *Circ. Res.* 72, 671–687. Available at: http://www.ncbi.nlm.nih.gov/pubmed/8431990.

Lombaert, H., Peyrat, J.-M., Croisille, P., Rapacchi, S., Fanton, L., Cheriet, F., et al. (2012). Human Atlas of the Cardiac Fiber Architecture: Study on a Healthy Population. *IEEE Trans. Med. Imaging* 31, 1436–1447. doi:10.1109/TMI.2012.2192743.

Lopez-Perez, A., Sebastian, R., and Ferrero, J. M. (2015). Three-dimensional cardiac computational modelling: methods, features and applications. *Biomed. Eng. Online* 14, 35. doi:10.1186/s12938-015-0033-5.

Lopez-Perez, A., Sebastian, R., Izquierdo, M., Ruiz, R., Bishop, M., and Ferrero, J. M. (2019). Personalized Cardiac Computational Models: From Clinical Data to Simulation of Infarct-Related Ventricular Tachycardia. *Front. Physiol.* 10, Article 580. doi:10.3389/fphys.2019.00580.

Lorange, M., and Gulrajani, R. M. (1993). A computer heart model incorporating anisotropic propagation: I. Model construction and simulation of normal activation. *J. Electrocardiol.* 26, 245–261.

Lorenz, C., and von Berg, J. (2006). A comprehensive shape model of the heart. *Med. Image Anal.* 10, 657–670. doi:10.1016/j.media.2006.03.004.

Lorenzo-Valdés, M., Sanchez-Ortiz, G. I., Mohiaddin, R., and Rueckert, D. (2002). Atlas-based segmentation and tracking of 3D cardiac MR images using non-rigid registration. in *Medical Image Computing and Computer Assisted Intervention (MICCAI 2002), LNCS 2488* (Springer-Verlag Berlin Heidelberg), 642–650. Available at: http://link.springer.com/chapter/10.1007/3-540-45786-0_79 [Accessed July 16, 2014].

Lötjönen, J., Kivistö, S., Koikkalainen, J., Smutek, D., and Lauerma, K. (2004). Statistical shape model of atria, ventricles and epicardium from short- and long-axis MR images. *Med. Image Anal.* 8, 371–386. doi:10.1016/j.media.2004.06.013.

MacCannell, K. A., Bazzazi, H., Chilton, L., Shibukawa, Y., Clark, R. B., and Giles, W. R. (2007). A Mathematical Model of Electrotonic Interactions between Ventricular Myocytes and Fibroblasts. *Biophys. J.* 92, 4121–4132.

doi:10.1529/biophysj.106.101410.

MacLeod, R. S., Johnson, C. R., and Ershler, P. R. (1991). Construction Of An Inhomegeneous Model Of The Human Torso For Use In Computational Electrocardiography. in *Proceedings of the Annual International Conference of the IEEE Engineering in Medicine and Biology Society Volume 13: 1991* (IEEE), 688–689. doi:10.1109/IEMBS.1991.684145.

MacLeod, R. S., Ni, Q., Punske, B., Ershler, P. R., Yilmaz, B., and Taccardi, B. (2000). Effects of heart position on the body-surface electrocardiogram. *J. Electrocardiol.* 33, 229–237. doi:10.1054/jelc.2000.20357.

Mahida, S., Sacher, F., Dubois, R., Sermesant, M., Bogun, F., Haïssaguerre, M., et al. (2017). Cardiac Imaging in Patients with Ventricular Tachycardia. *Circulation* 136, 2491–2507. doi:10.1161/CIRCULATIONAHA.117.029349.

Mahoney, V. M., Mezzano, V., Mirams, G. R., Maass, K., Li, Z., Cerrone, M., et al. (2016a). Connexin43 contributes to electrotonic conduction across scar tissue in the intact heart. *Sci. Rep.* 6, 26744. doi:10.1038/srep26744.

Mahoney, V. M., Mezzano, V., and Morley, G. E. (2016b). A review of the literature on cardiac electrical activity between fibroblasts and myocytes. *Prog. Biophys. Mol. Biol.* 120, 128–133. doi:10.1016/j.pbiomolbio.2015.12.006.

Maleckar, M. M., Greenstein, J. L., Giles, W. R., and Trayanova, N. A. (2009). K+ current changes account for the rate dependence of the action potential in the human atrial myocyte. *Am. J. Physiol. - Hear. Circ. Physiol.* 297, H1398–H1410. doi:10.1152/ajpheart.00411.2009.

Mansoori, T., Plank, G., Burton, R., Schneider, J., Khol, P., Gavaghan, D., et al. (2007). An iterative method for registration of high-resolution cardiac histoanatomical and MRI images. in *4th IEEE International Symposium on Biomedical Imaging: From Nano to Macro (ISBI 2007)* (Arlington, VA (USA): IEEE), 572–575. Available at: http://ieeexplore.ieee.org/xpls/abs_all.jsp?arnumber=4193350 [Accessed December 16, 2014].

Mantziari, L., Butcher, C., Kontogeorgis, A., Panikker, S., Roy, K., Markides, V., et al. (2015). Utility of a Novel Rapid High-Resolution Mapping System in the Catheter Ablation of Arrhythmias. *JACC Clin. Electrophysiol.* 1, 411–420. doi:10.1016/j.jacep.2015.06.002.

Marchlinski, F. E., Callans, D. J., Gottlieb, C. D., and Zado, E. (2000). Linear Ablation Lesions for Control of Unmappable Ventricular Tachycardia in Patients With Ischemic and Nonischemic Cardiomyopathy. *Circulation* 101, 1288–1296.

doi:10.1161/01.CIR.101.11.1288.

Marks, A. R. (2013). Calcium cycling proteins and heart failure: mechanisms and therapeutics. *J. Clin. Invest.* 123, 46–52. doi:10.1172/JCI62834.

Martinez-Mateu, L., Romero, L., Ferrer-Albero, A., Sebastian, R., Rodríguez Matas, J. F., Jalife, J., et al. (2018). Factors affecting basket catheter detection of real and phantom rotors in the atria: A computational study. *PLOS Comput. Biol.* 14, e1006017. doi:10.1371/journal.pcbi.1006017.

Martos, R., Baugh, J., Ledwidge, M., O'Loughlin, C., Conlon, C., Patle, A., et al. (2007). Diastolic heart failure: evidence of increased myocardial collagen turnover linked to diastolic dysfunction. *Circulation* 115, 888–895. doi:10.1161/CIRCULATIONAHA.106.638569.

Matsushita, T., Oyamada, M., Fujimoto, K., Yasuda, Y., Masuda, S., Wada, Y., et al. (1999). Remodeling of Cell-Cell and Cell-Extracellular Matrix Interactions at the Border Zone of Rat Myocardial Infarcts. *Circ. Res.* 85, 1046–1055. doi:10.1161/01.RES.85.11.1046.

McAlindon, E., Pufulete, M., Lawton, C., Angelini, G. D., and Bucciarelli-Ducci, C. (2015). Quantification of infarct size and myocardium at risk: evaluation of different techniques and its implications. *Eur. Hear. J. - Cardiovasc. Imaging* 16, 738–746. doi:10.1093/ehjci/jev001.

McDowell, K. S., Arevalo, H. J., Maleckar, M. M., and Trayanova, N. A. (2011). Susceptibility to Arrhythmia in the Infarcted Heart Depends on Myofibroblast Density. *Biophys. J.* 101, 1307–1315. doi:10.1016/j.bpj.2011.08.009.

McGill, L.-A., Scott, A. D., Ferreira, P. F., Nielles-Vallespin, S., Ismail, T., Kilner, P. J., et al. (2015a). Heterogeneity of Fractional Anisotropy and Mean Diffusivity Measurements by In Vivo Diffusion Tensor Imaging in Normal Human Hearts. *PLoS One* 10, e0132360. doi:10.1371/journal.pone.0132360.

McGill, L. A., Ferreira, P. F., Scott, A. D., Nielles-Vallespin, S., Giannakidis, A., Kilner, P. J., et al. (2015b). Relationship between cardiac diffusion tensor imaging parameters and anthropometrics in healthy volunteers. *J. Cardiovasc. Magn. Reson.* 18, 2. doi:10.1186/s12968-015-0215-0.

Mendonca Costa, C., Plank, G., Rinaldi, C. A., Niederer, S. A., and Bishop, M. J. (2018). Modeling the Electrophysiological Properties of the Infarct Border Zone. *Front. Physiol.* 9, 1–14. doi:10.3389/fphys.2018.00356.

Mesubi, O., Ego-Osuala, K., Jeudy, J., Purtilo, J., Synowski, S., Abutaleb, A., et al. (2015).

Differences in quantitative assessment of myocardial scar and gray zone by LGE-CMR imaging using established gray zone protocols. *Int. J. Cardiovasc. Imaging* 31, 359–368. doi:10.1007/s10554-014-0555-0.

Mewton, N., Liu, C. Y., Croisille, P., Bluemke, D., and Lima, J. A. C. (2011). Assessment of myocardial fibrosis with cardiovascular magnetic resonance. *J. Am. Coll. Cardiol.* 57, 891–903. doi:10.1016/j.jacc.2010.11.013.

Miller, W. T., and Geselowitz, D. B. (1978). Simulation studies of the electrocardiogram. I. The normal heart. *Circ. Res.* 43, 301–315. doi:10.1161/01.RES.43.2.301.

Miragoli, M., Gaudesius, G., and Rohr, S. (2006). Electrotonic Modulation of Cardiac Impulse Conduction by Myofibroblasts. *Circ. Res.* 98, 801–810. doi:10.1161/01.RES.0000214537.44195.a3.

Mitchell, C. C., and Schaeffer, D. G. (2003). A two-current model for the dynamics of cardiac membrane. *Bull. Math. Biol.* 65, 767–793. doi:10.1016/S0092-8240(03)00041-7.

Mitchell, S. C., Bosch, J. G., Lelieveldt, B. P. F., van der Geest, R. J., Reiber, J. H. C., and Sonka, M. (2002). 3-D active appearance models: segmentation of cardiac MR and ultrasound images. *IEEE Trans. Med. Imaging* 21, 1167–1178. doi:10.1109/TMI.2002.804425.

Mitchell, S., Lelieveldt, B., van der Geest, R., Bosch, J., Reiber, J., and Sonka, M. (2000). Segmentation of cardiac MR images: An active appearance model approach. in *Proceedings of SPIE 3979, Medical Imaging 2000: Image Processing*, ed. K. M. Hanson (San Diego, CA (USA): SPIE Digital Library), 224–234. doi:10.1117/12.387684.

Moe, G. K., Rheinboldt, W. C., and Abildskov, J. A. (1964). A computer model of atrial fibrillation. *Am. Heart J.* 67, 200–220. Available at: http://www.sciencedirect.com/science/article/pii/0002870364903710 [Accessed July 21, 2014].

Moon, J. C. ., Reed, E., Sheppard, M. N., Elkington, A. G., Ho, S., Burke, M., et al. (2004). The histologic basis of late gadolinium enhancement cardiovascular magnetic resonance in hypertrophic cardiomyopathy. *J. Am. Coll. Cardiol.* 43, 2260–2264. doi:10.1016/j.jacc.2004.03.035.

Morady, F. (1999). Radio-Frequency Ablation as Treatment for Cardiac Arrhythmias. *N. Engl. J. Med.* 340, 534–544. doi:10.1056/NEJM199902183400707.

Mullins, P. D., and Bondarenko, V. E. (2013). A mathematical model of the mouse

ventricular myocyte contraction. *PLoS One* 8, e63141.
doi:10.1371/journal.pone.0063141.

Muszkiewicz, A., Britton, O. J., Gemmell, P., Passini, E., Sánchez, C., Zhou, X., et al.
(2016). Variability in cardiac electrophysiology: Using experimentally-calibrated
populations of models to move beyond the single virtual physiological human
paradigm. *Prog. Biophys. Mol. Biol.* 120, 115–127.
doi:10.1016/j.pbiomolbio.2015.12.002.

Ng, J., Jacobson, J. T., Ng, J. K., Gordon, D., Lee, D. C., Carr, J. C., et al. (2012). Virtual
Electrophysiological Study in a 3-Dimensional Cardiac Magnetic Resonance
Imaging Model of Porcine Myocardial Infarction. *J. Am. Coll. Cardiol.* 60, 423–
430. doi:10.1016/j.jacc.2012.03.029.

Nguyen, C. T., Fan, Z., Xie, Y., Pang, J., Bi, X., Speier, P., et al. (2016). In vivo cardiac DTI
on a widely available 3T clinical scanner: an optimized M2 approach. *J.
Cardiovasc. Magn. Reson.* 18, O18. doi:10.1186/1532-429X-18-S1-O18.

Nguyen, T. P., Qu, Z., and Weiss, J. N. (2014). Cardiac fibrosis and arrhythmogenesis:
The road to repair is paved with perils. *J. Mol. Cell. Cardiol.* 70, 83–91.
doi:10.1016/j.yjmcc.2013.10.018.

Nguyên, U. C., Potse, M., Regoli, F., Caputo, M. L., Conte, G., Murzilli, R., et al. (2015).
An in-silico analysis of the effect of heart position and orientation on the ECG
morphology and vectorcardiogram parameters in patients with heart failure and
intraventricular conduction defects. *J. Electrocardiol.* 48, 617–625.
doi:10.1016/j.jelectrocard.2015.05.004.

Niederer, S. A., Kerfoot, E., Benson, A. P., Bernabeu, M. O., Bernus, O., Bradley, C., et
al. (2011). Verification of cardiac tissue electrophysiology simulators using an N-
version benchmark. *Philos. Trans. R. Soc. A. Math. Phys. Eng. Sci.* 369, 4331–
4351. doi:10.1098/rsta.2011.0139.

Niederer, S. A., Shetty, A. K., Plank, G., Bostock, J., Razavi, R., Smith, N. P., et al. (2012).
Biophysical modeling to simulate the response to multisite left ventricular
stimulation using a quadripolar pacing lead. *Pacing Clin. Electrophysiol.* 35, 204–
214. doi:10.1111/j.1540-8159.2011.03243.x.

Niederer, S., Rhode, K., Razavi, R., and Smith, N. (2009). The importance of model
parameters and boundary conditions in whole organ models of cardiac
contraction. in *Functional Imaging and Modeling of the Heart (FIMH 2009), LNCS
5528*, eds. N. Ayache, H. Delingette, and M. Sermesant (Springer-Verlag Berlin
Heidelberg), 348–356. doi:10.1007/978-3-642-01932-6_38.

Nielles-Vallespin, S., Khalique, Z., Ferreira, P. F., de Silva, R., Scott, A. D., Kilner, P., et al. (2017). Assessment of Myocardial Microstructural Dynamics by In Vivo Diffusion Tensor Cardiac Magnetic Resonance. *J. Am. Coll. Cardiol.* 69, 661–676. doi:10.1016/j.jacc.2016.11.051.

Nielsen, P. M. F., LeGrice, I. J., Smaill, B. H., and Hunter, P. J. (1991). Mathematical model of geometry and fibrous structure of the heart. *Am. J. Physiol. - Hear. Circ. Physiol.* 260, H1365–H1378. Available at: http://ajpheart.physiology.org/content/ajpheart/260/4/H1365.full.pdf [Accessed July 16, 2014].

Nogami, A. (2011). Purkinje-Related Arrhythmias Part I: Monomorphic Ventricular Tachycardias. *Pacing Clin. Electrophysiol.* 34, 624–650. doi:10.1111/j.1540-8159.2011.03044.x.

Nowbar, A. N., Howard, J. P., Finegold, J. A., Asaria, P., and Francis, D. P. (2014). 2014 Global geographic analysis of mortality from ischaemic heart disease by country, age and income: Statistics from World Health Organisation and United Nations. *Int. J. Cardiol.* 174, 293–298. doi:10.1016/j.ijcard.2014.04.096.

Nygren, A., Fiset, C., Firek, L., Clark, J. W., Lindblad, D. S., Clark, R. B., et al. (1998). Mathematical Model of an Adult Human Atrial Cell : The Role of K+ Currents in Repolarization. *Circ. Res.* 82, 63–81. doi:10.1161/01.RES.82.1.63.

O'Hara, T., Virág, L., Varró, A., and Rudy, Y. (2011). Simulation of the Undiseased Human Cardiac Ventricular Action Potential: Model Formulation and Experimental Validation. *PLoS Comput. Biol.* 7, e1002061. doi:10.1371/journal.pcbi.1002061.

Okada, J., Washio, T., Maehara, A., Momomura, S., Sugiura, S., and Hisada, T. (2011). Transmural and apicobasal gradients in repolarization contribute to T-wave genesis in human surface ECG. *Am. J. Physiol. Circ. Physiol.* 301, H200–H208. doi:10.1152/ajpheart.01241.2010.

Okada, J., Washio, T., Nakagawa, M., Watanabe, M., Kadooka, Y., Kariya, T., et al. (2017). Multi-scale, tailor-made heart simulation can predict the effect of cardiac resynchronization therapy. *J. Mol. Cell. Cardiol.* 108, 17–23. doi:10.1016/j.yjmcc.2017.05.006.

Okajima, M., Fujino, T., Kobayashi, T., and Yamada, K. (1968). Computer simulation of the propagation process in excitation of the ventricles. *Circ. Res.* 23, 203–211. doi:10.1161/01.RES.23.2.203.

Ongstad, E., and Kohl, P. (2016). Fibroblast–myocyte coupling in the heart: Potential

relevance for therapeutic interventions. *J. Mol. Cell. Cardiol.* 91, 238–246. doi:10.1016/j.yjmcc.2016.01.010.

Opthof, T., Coronel, R., and Janse, M. J. (2009). Is there a significant transmural gradient in repolarization time in the intact heart?: Repolarization Gradients in the Intact Heart. *Circ. Arrhythmia Electrophysiol.* 2, 89–96. doi:10.1161/CIRCEP.108.825356.

Opthof, T., Janse, M. J., Meijborg, V. M. F., Cinca, J., Rosen, M. R., and Coronel, R. (2016). Dispersion in ventricular repolarization in the human, canine and porcine heart. *Prog. Biophys. Mol. Biol.* 120, 222–235. doi:10.1016/j.pbiomolbio.2016.01.007.

Opthof, T., Remme, C. A., Jorge, E., Noriega, F., Wiegerinck, R. F., Tasiam, A., et al. (2017). Cardiac activation–repolarization patterns and ion channel expression mapping in intact isolated normal human hearts. *Hear. Rhythm* 14, 265–272. doi:10.1016/j.hrthm.2016.10.010.

Ordas, S., Boisrobert, L., Huguet, M., and Frangi, A. F. (2003). Active shape models with invariant optimal features (IOF-ASM) application to cardiac MRI segmentation. in *Computers in Cardiology* (Thessaloniki, Greece: IEEE), 633–636. doi:10.1109/CIC.2003.1291235.

Ordas, S., Oubel, E., Sebastian, R., and Frangi, A. F. (2007). Computational anatomy atlas of the heart. in *5th International Symposium on Image and Signal Processing and Analysis (ISPA 2007)* (Istanbul, Turkey: IEEE), 338–342. Available at: http://scholar.google.com/scholar?hl=en&btnG=Search&q=intitle:Computationa l+Anatomy+Atlas+of+the+Heart#0 [Accessed July 16, 2014].

Ortiz-Pérez, J. T., Rodríguez, J., Meyers, S. N., Lee, D. C., Davidson, C., and Wu, E. (2008). Correspondence Between the 17-Segment Model and Coronary Arterial Anatomy Using Contrast-Enhanced Cardiac Magnetic Resonance Imaging. *JACC Cardiovasc. Imaging* 1, 282–293. doi:10.1016/j.jcmg.2008.01.014.

Palamara, S., Vergara, C., Catanzariti, D., Faggiano, E., Pangrazzi, C., Centonze, M., et al. (2014). Computational generation of the Purkinje network driven by clinical measurements: The case of pathological propagations. *Int. j. numer. method. biomed. eng.* 30, 1558–1577. doi:10.1002/cnm.2689.

Palamara, S., Vergara, C., Faggiano, E., and Nobile, F. (2015). An effective algorithm for the generation of patient-specific Purkinje networks in computational electrocardiology. *J. Comput. Phys.* 283, 495–517. doi:10.1016/j.jcp.2014.11.043.

Pashakhanloo, F., Herzka, D. A., Halperin, H., McVeigh, E. R., and Trayanova, N. A. (2018). Role of 3-Dimensional Architecture of Scar and Surviving Tissue in Ventricular Tachycardia. *Circ. Arrhythmia Electrophysiol.* 11, e006131. doi:10.1161/CIRCEP.117.006131.

Pashakhanloo, F., Herzka, D. A., Mori, S., Zviman, M., Halperin, H., Gai, N., et al. (2017). Submillimeter diffusion tensor imaging and late gadolinium enhancement cardiovascular magnetic resonance of chronic myocardial infarction. *J. Cardiovasc. Magn. Reson.* 19, 9. doi:10.1186/s12968-016-0317-3.

Passini, E., Trovato, C., Tissier, A., Nagy, N., Varro, A., Severi, S., et al. (2017). A Novel In Silico Human Cardiac Purkinje Cell Model to Investigate Drug Safety and Efficacy. *J. Pharmacol. Toxicol. Methods* 88, 209. doi:10.1016/j.vascn.2017.09.134.

Patel, C., Burke, J. F., Patel, H., Gupta, P., Kowey, P. R., Antzelevitch, C., et al. (2009). Is there a significant transmural gradient in repolarization time in the intact heart? *Circ. Arrhythmia Electrophysiol.* 2, 80–88. doi:10.1161/CIRCEP.108.791830.

Patel, H., Mazur, W., Williams, K. A., and Kalra, D. K. (2017). Myocardial viability–State of the art: Is it still relevant and how to best assess it with imaging? *Trends Cardiovasc. Med.*, In press. doi:10.1016/j.tcm.2017.07.001.

Pathmanathan, P., Cooper, J., Fletcher, A., Mirams, G., Murray, P., Osborne, J., et al. (2009). A computational study of discrete mechanical tissue models. *Phys. Biol.* 6, 036001. doi:10.1088/1478-3975/6/3/036001.

Paul, T., Moak, J. P., Morris, C., and Garson, A. (1990). Epicardial Mapping: How to Measure Local Activation? *Pacing Clin. Electrophysiol.* 13, 285–292. doi:10.1111/j.1540-8159.1990.tb02042.x.

Pedersen, C. T., Kay, G. N., Kalman, J., Borggrefe, M., Della-Bella, P., Dickfeld, T., et al. (2014). EHRA/HRS/APHRS Expert Consensus on Ventricular Arrhythmias. *Hear. Rhythm* 11, e166–e196. doi:10.1016/j.hrthm.2014.07.024.

Perez-David, E., Arenal, Á., Rubio-Guivernau, J. L., del Castillo, R., Atea, L., Arbelo, E., et al. (2011). Noninvasive Identification of Ventricular Tachycardia-Related Conducting Channels Using Contrast-Enhanced Magnetic Resonance Imaging in Patients With Chronic Myocardial Infarction. *J. Am. Coll. Cardiol.* 57, 184–194. doi:10.1016/j.jacc.2010.07.043.

Perotti, L. E., Krishnamoorthi, S., Borgstrom, N. P., Ennis, D. B., and Klug, W. S. (2015). Regional segmentation of ventricular models to achieve repolarization dispersion in cardiac electrophysiology modeling. *Int. j. numer. method. biomed. eng.* 31, e02718. doi:10.1002/cnm.2718.

Perperidis, D., Mohiaddin, R., and Rueckert, D. (2005). Construction of a 4D statistical atlas of the cardiac anatomy and its use in classification. in *Medical Image Computing and Computer-Assisted Intervention—MICCAI 2005, LNCS 3750*, 402-410. Springer-Verlag Berlin Heidelberg. Available at: http://link.springer.com/chapter/10.1007/11566489_50 [Accessed July 15, 2014].

Petitjean, C., and Dacher, J. N. (2011). A review of segmentation methods in short axis cardiac MR images. *Med. Image Anal.* 15, 169–184. doi:10.1016/j.media.2010.12.004.

Peyrat, J.-M., Sermesant, M., Pennec, X., Delingette, H., Chenyang Xu, McVeigh, E. R., et al. (2007). A Computational Framework for the Statistical Analysis of Cardiac Diffusion Tensors: Application to a Small Database of Canine Hearts. *IEEE Trans. Med. Imaging* 26, 1500–1514. doi:10.1109/TMI.2007.907286.

Pfeiffer, E. R., Tangney, J. R., Omens, J. H., and McCulloch, A. D. (2014). Biomechanics of cardiac electromechanical coupling and mechanoelectric feedback. *J. Biomech. Eng.* 136, 021007-1-021007–11. doi:10.1115/1.4026221.

Plank, G., Burton, R. A. B., Hales, P., Bishop, M., Mansoori, T., Bernabeu, M. O., et al. (2009). Generation of histo-anatomically representative models of the individual heart: tools and application. *Philos. Trans. R. Soc. A. Math. Phys. Eng. Sci.* 367, 2257–2292. doi:10.1098/rsta.2009.0056.

Plank, G., Zhou, L., Greenstein, J. L., Cortassa, S., Winslow, R. L., O'Rourke, B., et al. (2008). From mitochondrial ion channels to arrhythmias in the heart: computational techniques to bridge the spatio-temporal scales. *Philos. Trans. R. Soc. A Math. Phys. Eng. Sci.* 366, 3381–3409. doi:10.1098/rsta.2008.0112.

Plotkowiak, M., Rodriguez, B., Plank, G., Schneider, J. E., Gavaghan, D., Kohl, P., et al. (2008). High performance computer simulations of cardiac electrical function based on high resolution MRI datasets. in *International Conference on Computational Science (ICCS 2008), LNCS 5101* (Berlin Heidelberg: Springer-Verlag), 571–580. Available at: http://link.springer.com/chapter/10.1007/978-3-540-69384-0_62 [Accessed July 16, 2014].

Pokorney, S. D., Friedman, D. J., Calkins, H., Callans, D. J., Daoud, E. G., Della-Bella, P., et al. (2016). Catheter ablation of ventricular tachycardia: Lessons learned from past clinical trials and implications for future clinical trials. *Hear. Rhythm* 13, 1748–1754. doi:10.1016/j.hrthm.2016.04.001.

Pollard, A. E., and Barr, R. C. (1991). Computer simulations of activation in an anatomically based model of the human ventricular conduction system. *IEEE*

Trans. Biomed. Eng. 38, 982–996. doi:10.1109/10.88444.

Pop, M., Sermesant, M., Mansi, T., Crystal, E., Ghate, S., Peyrat, J.-M., et al. (2011a). Correspondence Between Simple 3-D MRI-Based Computer Models and In-Vivo EP Measurements in Swine With Chronic Infarctions. *IEEE Trans. Biomed. Eng.* 58, 3483–3486. doi:10.1109/TBME.2011.2168395.

Pop, M., Sermesant, M., Peyrat, J.-M., Crystal, E., Ghate, S., Mansi, T., et al. (2011b). "A 3D MRI-Based Cardiac Computer Model to Study Arrhythmia and Its In-vivo Experimental Validation," in *Functional Imaging and Modeling of the Heart. FIMH 2011. Lecture Notes in Computer Science*, ed. A. L. Metaxas D.N. (Springer, Berlin, Heidelberg), 195–205. doi:10.1007/978-3-642-21028-0_25.

Potse, M. (2012). Mathematical Modeling and Simulation of Ventricular Activation Sequences: Implications for Cardiac Resynchronization Therapy. *J. Cardiovasc. Transl. Res.* 5, 146–158. doi:10.1007/s12265-011-9343-6.

Potse, M., Dube, B., Richer, J., Vinet, A., and Gulrajani, R. M. (2006). A Comparison of Monodomain and Bidomain Reaction-Diffusion Models for Action Potential Propagation in the Human Heart. *IEEE Trans. Biomed. Eng.* 53, 2425–2435. doi:10.1109/TBME.2006.880875.

Prakosa, A., Arevalo, H. J., Deng, D., Boyle, P. M., Nikolov, P. P., Ashikaga, H., et al. (2018). Personalized virtual-heart technology for guiding the ablation of infarct-related ventricular tachycardia. *Nat. Biomed. Eng.* 2, 732–740. doi:10.1038/s41551-018-0282-2.

Prassl, A. J., Kickinger, F., Ahammer, H., Grau, V., Schneider, J. E., Hofer, E., et al. (2009). Automatically Generated, Anatomically Accurate Meshes for Cardiac Electrophysiology Problems. *IEEE Trans. Biomed. Eng.* 56, 1318–1330. doi:10.1109/TBME.2009.2014243.

Priori, S. G., Aliot, E., Blomstrom-Lundqvist, C., Bossaert, L., Breithardt, G., Brugada, P., et al. (2001). Task Force on Sudden Cardiac Death of the European Society of Cardiology. *Eur. Heart J.* 22, 1374–1450. doi:10.1053/euhj.2001.2824.

Priori, S. G., Blomström-Lundqvist, C., Mazzanti, A., Blom, N., Borggrefe, M., Camm, J., et al. (2015). 2015 ESC Guidelines for the management of patients with ventricular arrhythmias and the prevention of sudden cardiac death. *Eur. Heart J.* 36, 2793–2867. doi:10.1093/eurheartj/ehv316.

Pu, J., and Boyden, P. A. (1997). Alterations of Na+ Currents in Myocytes From Epicardial Border Zone of the Infarcted Heart : A Possible Ionic Mechanism for Reduced Excitability and Postrepolarization Refractoriness. *Circ. Res.* 81, 110–

119. doi:10.1161/01.RES.81.1.110.

Quinn, T. A., Camelliti, P., Rog-Zielinska, E. A., Siedlecka, U., Poggioli, T., O'Toole, E. T., et al. (2016). Electrotonic coupling of excitable and nonexcitable cells in the heart revealed by optogenetics. *Proc. Natl. Acad. Sci.* 113, 14852–14857. doi:10.1073/pnas.1611184114.

Quinn, T. A., Kohl, P., and Ravens, U. (2014). Cardiac mechano-electric coupling research: fifty years of progress and scientific innovation. *Prog. Biophys. Mol. Biol.* 115, 71–75. doi:10.1016/j.pbiomolbio.2014.06.007.

Rantner, L. J., Arevalo, H. J., Constantino, J. L., Efimov, I. R., Plank, G., and Trayanova, N. A. (2012). Three-dimensional mechanisms of increased vulnerability to electric shocks in myocardial infarction: Altered virtual electrode polarizations and conduction delay in the peri-infarct zone. *J. Physiol.* 590, 4537–4551. doi:10.1113/jphysiol.2012.229088.

Relan, J., Chinchapatnam, P., Sermesant, M., Rhode, K., Ginks, M., Delingette, H., et al. (2011). Coupled personalization of cardiac electrophysiology models for prediction of ischaemic ventricular tachycardia. *Interface Focus* 1, 396–407. doi:10.1098/rsfs.2010.0041.

Reumann, M., Farina, D., Miri, R., Lurz, S., Osswald, B., and Dössel, O. (2007). Computer model for the optimization of AV and VV delay in cardiac resynchronization therapy. *Med. Biol. Eng. Comput.* 45, 845–854. doi:10.1007/s11517-007-0230-x.

Rice, J. J., Wang, F., Bers, D. M., and de Tombe, P. P. (2008). Approximate Model of Cooperative Activation and Crossbridge Cycling in Cardiac Muscle Using Ordinary Differential Equations. *Biophys. J.* 95, 2368–2390. doi:10.1529/biophysj.107.119487.

Ringenberg, J., Deo, M., Filgueiras-Rama, D., Pizarro, G., Ibañez, B., Peinado, R., et al. (2014). Effects of fibrosis morphology on reentrant ventricular tachycardia inducibility and simulation fidelity in patient-derived models. *Clin. Med. Insights. Cardiol.* 8, 1–13. doi:10.4137/CMC.S15712.

Roberts, B. N., Yang, P. C., Behrens, S. B., Moreno, J. D., and Clancy, C. E. (2012). Computational approaches to understand cardiac electrophysiology and arrhythmias. *Am. J. Physiol. - Hear. Circ. Physiol.* 303, H766–H783. doi:10.1152/ajpheart.01081.2011.

Rodríguez, B., Tice, B. M., Eason, J. C., Aguel, F., Ferrero Jr, J. M., and Trayanova, N. (2004). Effect of acute global ischemia on the upper limit of vulnerability: a simulation study. *Am. J. Physiol. - Hear. Circ. Physiol.* 286, H2078–H2088.

doi:10.1152/ajpheart.01175.2003.

Rog-Zielinska, E. A., Norris, R. A., Kohl, P., and Markwald, R. (2016). The Living Scar – Cardiac Fibroblasts and the Injured Heart. *Trends Mol. Med.* 22, 99–114. doi:10.1016/j.molmed.2015.12.006.

Rohmer, D., Sitek, A., and Gullberg, G. T. (2007). Reconstruction and Visualization of Fiber and Laminar Structure in the Normal Human Heart from Ex Vivo Diffusion Tensor Magnetic Resonance Imaging (DTMRI) Data. *Invest. Radiol.* 42, 777–789. doi:10.1097/RLI.0b013e3181238330.

Rohr, S. (2012). Arrhythmogenic Implications of Fibroblast-Myocyte Interactions. *Circ. Arrhythmia Electrophysiol.* 5, 442–452. doi:10.1161/CIRCEP.110.957647.

Romero, D., Sebastian, R., Bijnens, B. H., Zimmerman, V., Boyle, P. M., Vigmond, E. J., et al. (2010). Effects of the purkinje system and cardiac geometry on biventricular pacing: a model study. *Ann. Biomed. Eng.* 38, 1388–1398. doi:10.1007/s10439-010-9926-4.

Romero, L., Trénor, B., Alonso, J. M., Tobón, C., Saiz, J., and Ferrero (Jr), J. M. (2009). The relative role of refractoriness and source-sink relationship in reentry generation during simulated acute ischemia. *Ann. Biomed. Eng.* 37, 1560–1571. doi:10.1007/s10439-009-9721-2.

Roney, C. H., Bayer, J. D., Zahid, S., Meo, M., Boyle, P. M. J., Trayanova, N. A., et al. (2016). Modelling methodology of atrial fibrosis affects rotor dynamics and electrograms. *Europace* 18, 146–155. doi:10.1093/europace/euw365.

Roth, B. J. (1988). The electrical potential produced by a strand of cardiac muscle: A bidomain analysis. *Ann. Biomed. Eng.* 16, 609–637. doi:10.1007/BF02368018.

Roth, B. J. (1992). How the anisotropy of the intracellular and extracellular conductivities influences stimulation of cardiac muscle. *J. Math. Biol.* 30, 633–646. doi:10.1007/BF00948895.

Rudy, Y., and Silva, J. R. (2006). Computational biology in the study of cardiac ion channels and cell electrophysiology. *Q. Rev. Biophys.* 39, 57–116. doi:10.1017/S0033583506004227.

Ruiz-Villa, C. A., Tobón, C., Rodríguez, J. F., Ferrero, J. M., Hornero, F., and Saíz, J. (2009). Influence of atrial dilatation in the generation of re-entries caused by ectopic activity in the left atrium. in *Computers in Cardiology*, 36, 457–460. Available at: http://ieeexplore.ieee.org/xpls/abs_all.jsp?arnumber=5445370 [Accessed July 16, 2014].

Rutherford, S. L., Trew, M. L., Sands, G. B., LeGrice, I. J., and Smaill, B. H. (2012). High-Resolution 3-Dimensional Reconstruction of the Infarct Border Zone: Impact of Structural Remodeling on Electrical Activation. *Circ. Res.* 111, 301–311. doi:10.1161/CIRCRESAHA.111.260943.

Saeed, M., Lund, G., Wendland, M. F., Bremerich, J., Weinmann, H.-J., and Higgins, C. B. (2001). Magnetic Resonance Characterization of the Peri-Infarction Zone of Reperfused Myocardial Infarction With Necrosis-Specific and Extracellular Nonspecific Contrast Media. *Circulation* 103, 871–876. doi:10.1161/01.CIR.103.6.871.

Sakmann, B., and Neher, E. (1984). Patch clamp techniques for studying ionic channels in excitable membranes. *Annu. Rev. Physiol.* 41, 455–472. Available at: http://www.annualreviews.org/doi/pdf/10.1146/annurev.ph.46.030184.002323 [Accessed July 21, 2014].

Sampson, K. J., Iyer, V., Marks, A. R., and Kass, R. S. (2010). A computational model of Purkinje fibre single cell electrophysiology: implications for the long QT syndrome. *J. Physiol.* 588, 2643–2655. doi:10.1113/jphysiol.2010.187328.

Sánchez, C., D'Ambrosio, G., Maffessanti, F., Caiani, E. G., Prinzen, F. W., Krause, R., et al. (2018). Sensitivity analysis of ventricular activation and electrocardiogram in tailored models of heart-failure patients. *Med. Biol. Eng. Comput.* 56, 491–504. doi:10.1007/s11517-017-1696-9.

Schaper, W., Görge, G., Winkler, B., and Schaper, J. (1988). The collateral circulation of the heart. *Prog. Cardiovasc. Dis.* 31, 57–77. doi:10.1016/0033-0620(88)90011-4.

Schijvenaars, B. J. A., van Herpen, G., and Kors, J. A. (2008). Intraindividual variability in electrocardiograms. *J. Electrocardiol.* 41, 190–196. doi:10.1016/j.jelectrocard.2008.01.012.

Schneiders, R. (2000). Octree-based hexahedral mesh generation. *Int. J. Comput. Geom. Appl.* 10, 383–398. doi:10.1142/S021819590000022X.

Schuleri, K. H., Centola, M., George, R. T., Amado, L. C., Evers, K. S., Kitagawa, K., et al. (2009). Characterization of Peri-Infarct Zone Heterogeneity by Contrast-Enhanced Multidetector Computed Tomography. *J. Am. Coll. Cardiol.* 53, 1699–1707. doi:10.1016/j.jacc.2009.01.056.

Schulte, R. F., Sands, G. B., Sachse, F. B., Dössel, O., and Pullan, A. J. (2001). Creation of a human heart model and its customisation using ultrasound images. *Biomed. Tech. Eng.* 46, 26–28. doi:10.1515/bmte.2001.46.s2.26.

Schwab, B. C., Seemann, G., Lasher, R. A., Torres, N. S., Wulfers, E. M., Arp, M., et al. (2013). Quantitative Analysis of Cardiac Tissue Including Fibroblasts Using Three-Dimensional Confocal Microscopy and Image Reconstruction: Towards a Basis for Electrophysiological Modeling. *IEEE Trans. Med. Imaging* 32, 862–872. doi:10.1109/TMI.2013.2240693.

Scollan, D. F., Holmes, A., Winslow, R., and Forder, J. (1998). Histological validation of myocardial microstructure obtained from diffusion tensor magnetic resonance imaging. *AJP Hear. Circ. Physiol.* 275, H2308–H2318. Available at: http://www.ncbi.nlm.nih.gov/pubmed/9843833 [Accessed July 16, 2014].

Sebastian, R., Zimmerman, V., Romero, D., Sanchez-Quintana, D., and Frangi, A. F. (2013). Characterization and modeling of the peripheral cardiac conduction system. *IEEE Trans. Med. Imaging* 32, 45–55. doi:10.1109/TMI.2012.2221474.

Sebastian, R., Zimmerman, V., Sukno, F., Bijnens, B. B., and Frangi, A. F. (2009). Cardiac Modelling for Pathophysiology Research and Clinical Applications. The Need for an Automated Pipeline. in *World Congress on Medical Physics and Biomedical Engineering 2009*, eds. O. Dössel and W. C. Schlegel (Springer-Verlag Berlin Heidelberg), 2207–2210. doi:10.1007/978-3-642-03882-2_586.

Seemann, G., Höper, C., Sachse, F. B., Dössel, O., Holden, A. V, and Zhang, H. (2006). Heterogeneous three-dimensional anatomical and electrophysiological model of human atria. *Philos. Trans. R. Soc. A. Math. Phys. Eng. Sci.* 364, 1465–1481. doi:10.1098/rsta.2006.1781.

Seg3D, C. (2013). Volumetric image segmentation and visualization. *Sci. Comput. Imaging Inst.*

Seidel, T., Edelmann, J.-C., and Sachse, F. B. (2016). Analyzing Remodeling of Cardiac Tissue: A Comprehensive Approach Based on Confocal Microscopy and 3D Reconstructions. *Ann. Biomed. Eng.* 44, 1436–1448. doi:10.1007/s10439-015-1465-6.

Sermesant, M., Chabiniok, R., Chinchapatnam, P., Mansi, T., Billet, F., Moireau, P., et al. (2012). Patient-specific electromechanical models of the heart for the prediction of pacing acute effects in CRT: a preliminary clinical validation. *Med. Image Anal.* 16, 201–215. doi:10.1016/j.media.2011.07.003.

Sermesant, M., Delingette, H., and Ayache, N. (2006a). An electromechanical model of the heart for image analysis and simulation. *IEEE Trans. Med. Imaging* 25, 612–625. doi:10.1109/TMI.2006.872746.

Sermesant, M., Forest, C., Pennec, X., Delingette, H., and Ayache, N. (2003).

Deformable biomechanical models: application to 4D cardiac image analysis. *Med. Image Anal.* 7, 475–488. Available at: http://www.ncbi.nlm.nih.gov/pubmed/14561552.

Sermesant, M., Moireau, P., Camara, O., Sainte-Marie, J., Andriantsimiavona, R., Cimrman, R., et al. (2006b). Cardiac function estimation from MRI using a heart model and data assimilation: advances and difficulties. *Med. Image Anal.* 10, 642–656. doi:10.1016/j.media.2006.04.002.

Sermesant, M., Peyrat, J.-M., Chinchapatnam, P., Billet, F., Mansi, T., Rhode, K., et al. (2008). Toward patient-specific myocardial models of the heart. *Heart Fail. Clin.* 4, 289–301. doi:10.1016/j.hfc.2008.02.014.

Severs, N. J., Bruce, A. F., Dupont, E., and Rothery, S. (2008). Remodelling of gap junctions and connexin expression in diseased myocardium. *Cardiovasc. Res.* 80, 9–19. doi:10.1093/cvr/cvn133.

Shaw, R. M., and Rudy, Y. (1997). Electrophysiologic effects of acute myocardial ischemia: a theoretical study of altered cell excitability and action potential duration. *Cardiovasc. Res.* 35, 256–272. Available at: http://www.ncbi.nlm.nih.gov/pubmed/9349389.

Sheth, P. J., Danton, G. H., Siegel, Y., Kardon, R. E., Infante, J. C., Ghersin, E., et al. (2015). Cardiac Physiology for Radiologists: Review of Relevant Physiology for Interpretation of Cardiac MR Imaging and CT. *RadioGraphics* 35, 1335–1351. doi:10.1148/rg.2015140234.

Si, H., and Gärtner, K. (2005). "Meshing Piecewise Linear Complexes by Constrained Delaunay Tetrahedralizations," in *Proceedings of the 14th International Meshing Roundtable*, ed. B. W. Hanks (Berlin/Heidelberg: Springer-Verlag), 147–163. doi:10.1007/3-540-29090-7_9.

Sicouri, S., and Antzelevitch, C. (1991). A subpopulation of cells with unique electrophysiological properties in the deep subepicardium of the canine ventricle. The M cell. *Circ. Res.* 68, 1729–1741. doi:10.1161/01.RES.68.6.1729.

Sicouri, S., Fish, J., and Antzelevitch, C. (1994). Distribution of M Cells in the Canine Ventricle. *J. Cardiovasc. Electrophysiol.* 5, 824–837. doi:10.1111/j.1540-8167.1994.tb01121.x.

Siregar, P., Sinteff, J. P., Julen, N., and Le Beux, P. (1998). An interactive 3D anisotropic cellular automata model of the heart. *Comput. Biomed. Res.* 31, 323–347. Available at: http://www.ncbi.nlm.nih.gov/pubmed/9790739.

Smaill, B. H., and Hunter, P. J. (2010). *Cardiac Electrophysiology Methods and Models*. , eds. D. C. Sigg, P. A. Iaizzo, Y.-F. Xiao, and B. He Boston, MA: Springer US doi:10.1007/978-1-4419-6658-2.

Smith, J. H., Green, C. R., Peters, N. S., Rothery, S., and Severs, N. J. (1991). Altered patterns of gap junction distribution in ischemic heart disease. An immunohistochemical study of human myocardium using laser scanning confocal microscopy. *Am. J. Pathol.* 139, 801–21. Available at: /pmc/articles/PMC1886321/?report=abstract.

Smith, N., de Vecchi, A., McCormick, M., Nordsletten, D., Camara, O., Frangi, A. F., et al. (2011). euHeart: personalized and integrated cardiac care using patient-specific cardiovascular modelling. *Interface Focus* 1, 349–364. doi:10.1098/rsfs.2010.0048.

Soejima, K., Stevenson, W. G., Maisel, W. H., Sapp, J. L., and Epstein, L. M. (2002). Electrically Unexcitable Scar Mapping Based on Pacing Threshold for Identification of the Reentry Circuit Isthmus: Feasibility for Guiding Ventricular Tachycardia Ablation. *Circulation* 106, 1678–1683. doi:10.1161/01.CIR.0000030187.39852.A7.

Sosa, E., and Scanavacca, M. (2005). Epicardial Mapping and Ablation Techniques to Control Ventricular Tachycardia. *J. Cardiovasc. Electrophysiol.* 16, 449–452. doi:10.1046/j.1540-8167.2005.40710.x.

Sosa, E., Scanavacca, M., D'Avila, A., Oliveira, F., and Ramires, J. A. F. (2000). Nonsurgical transthoracic epicardial catheter ablation to treat recurrent ventricular tachycardia occurring late after myocardial infarction. *J. Am. Coll. Cardiol.* 35, 1442–1449. doi:10.1016/S0735-1097(00)00606-9.

Sosa, E., Scanavacca, M., D'Avila, A., and Pilleggi, F. (1996). A New Technique to Perform Epicardial Mapping in the Electrophysiology Laboratory. *J. Cardiovasc. Electrophysiol.* 7, 531–536. doi:10.1111/j.1540-8167.1996.tb00559.x.

Soto-Iglesias, D., Butakoff, C., Andreu, D., Fernández-Armenta, J., Berruezo, A., and Camara, O. (2016). Integration of electro-anatomical and imaging data of the left ventricle: An evaluation framework. *Med. Image Anal.* 32, 131–144. doi:10.1016/j.media.2016.03.010.

Spach, M. S., and Boineau, J. P. (1997). Microfibrosis Produces Electrical Load Variations Due to Loss of Side-to-Side Cell Connections: A Major Mechanism of Structural Heart Disease Arrhythmias. *Pacing Clin. Electrophysiol.* 20, 397–413. doi:10.1111/j.1540-8159.1997.tb06199.x.

Spach, M. S., Miller, W. T., Miller-Jones, E., Warren, R. B., and Barr, R. C. (1979). Extracellular potentials related to intracellular action potentials during impulse conduction in anisotropic canine cardiac muscle. *Circ. Res.* 45, 188–204. doi:10.1161/01.RES.45.2.188.

Sridhar, S., Vandersickel, N., and Panfilov, A. V. (2017). Effect of myocyte-fibroblast coupling on the onset of pathological dynamics in a model of ventricular tissue. *Sci. Rep.* 7, 1–12. doi:10.1038/srep40985.

Stephenson, R. S., Atkinson, A., Kottas, P., Perde, F., Jafarzadeh, F., Bateman, M., et al. (2017). High resolution 3-Dimensional imaging of the human cardiac conduction system from microanatomy to mathematical modeling. *Sci. Rep.* 7, 7188. doi:10.1038/s41598-017-07694-8.

Stephenson, R. S., Boyett, M. R., Hart, G., Nikolaidou, T., Cai, X., Corno, A. F., et al. (2012). Contrast enhanced micro-computed tomography resolves the 3-dimensional morphology of the cardiac conduction system in mammalian hearts. *PLoS One* 7, e35299. doi:10.1371/journal.pone.0035299.

Stevens, C., Remme, E., LeGrice, I., and Hunter, P. (2003). Ventricular mechanics in diastole: material parameter sensitivity. *J. Biomech.* 36, 737–748. doi:10.1016/S0021-9290(02)00452-9.

Stevenson, W. G., Khan, H., Sager, P., Saxon, L. A., Middlekauff, H. R., Natterson, P. D., et al. (1993). Identification of reentry circuit sites during catheter mapping and radiofrequency ablation of ventricular tachycardia late after myocardial infarction. *Circulation* 88, 1647–1670. doi:10.1161/01.CIR.88.4.1647.

Stevenson, W. G., and Soejima, K. (2005). Recording Techniques for Clinical Electrophysiology. *J. Cardiovasc. Electrophysiol.* 16, 1017–1022. doi:10.1111/j.1540-8167.2005.50155.x.

Stewart, P., Aslanidi, O. V, Noble, D., Noble, P. J., Boyett, M. R., and Zhang, H. (2009). Mathematical models of the electrical action potential of Purkinje fibre cells. *Philos. Trans. R. Soc. A. Math. Phys. Eng. Sci.* 367, 2225–2255. doi:10.1098/rsta.2008.0283.

Stoeck, C. T., von Deuster, C., Fleischmann, T., Lipiski, M., Cesarovic, N., and Kozerke, S. (2017). Direct comparison of in vivo versus postmortem second-order motion-compensated cardiac diffusion tensor imaging. *Magn. Reson. Med.* 00. doi:10.1002/mrm.26871.

Streeter, D. D., Spotnitz, H. M., Patel, D. P., Ross, J., and Sonnenblick, E. H. (1969). Fiber Orientation in the Canine Left Ventricle during Diastole and Systole. *Circ. Res.* 24,

339–347. doi:10.1161/01.RES.24.3.339.

Sun, Y., Kiani, M. F., Postlethwaite, A. E., and Weber, K. T. (2002). Infarct scar as living tissue. *Basic Res. Cardiol.* 97, 343–347. doi:10.1007/s00395-002-0365-8.

Sutton, M. G. S. J., and Sharpe, N. (2000). Left Ventricular Remodeling After Myocardial Infarction : Pathophysiology and Therapy. *Circulation* 101, 2981–2988. doi:10.1161/01.CIR.101.25.2981.

Szentadrassy, N., Banyasz, T., Biro, T., Szabo, G., Toth, B. I., Magyar, J., et al. (2005). Apico-basal inhomogeneity in distribution of ion channels in canine and human ventricular myocardium. *Cardiovasc. Res.* 65, 851–860. doi:10.1016/j.cardiores.2004.11.022.

Taggart, P., Sutton, P. M., Opthof, T., Coronel, R., Trimlett, R., Pugsley, W., et al. (2000). Inhomogeneous Transmural Conduction During Early Ischaemia in Patients with Coronary Artery Disease. *J. Mol. Cell. Cardiol.* 32, 621–630. doi:10.1006/jmcc.2000.1105.

Tedrow, U., and Stevenson, W. G. (2009). Strategies for Epicardial Mapping and Ablation of Ventricular Tachycardia. *J. Cardiovasc. Electrophysiol.* 20, 710–713. doi:10.1111/j.1540-8167.2008.01427.x.

ten Tusscher, K. H. W. J., Noble, D., Noble, P. J., and Panfilov, A. V (2004). A model for human ventricular tissue. *Am. J. Physiol. Hear. Circ. Physiol.* 286, H1573–H1589. doi:10.1152/ajpheart.00794.2003.

ten Tusscher, K. H. W. J., and Panfilov, A. V (2006a). Cell model for efficient simulation of wave propagation in human ventricular tissue under normal and pathological conditions. *Phys. Med. Biol.* 51, 6141–6156. doi:10.1088/0031-9155/51/23/014.

ten Tusscher, K. H. W. J., and Panfilov, A. V (2007). Influence of diffuse fibrosis on wave propagation in human ventricular tissue. *Europace* 9, vi38–vi45. doi:10.1093/europace/eum206.

ten Tusscher, K., and Panfilov, A. (2006b). Alternans and spiral breakup in a human ventricular tissue model. *AJP Hear. Circ. Physiol.* 291, H1088–H1100. doi:10.1152/ajpheart.00109.2006.

Thakor, N. V, and Eisenman, L. N. (1989). Three-dimensional computer model of the heart: fibrillation induced by extrastimulation. *Comput. Biomed. Res.* 22, 532–545. Available at: http://www.sciencedirect.com/science/article/pii/0010480989900736 [Accessed July 16, 2014].

Thygesen, K., Alpert, J. S., Jaffe, A. S., Chaitman, B. R., Bax, J. J., Morrow, D. A., et al. (2019). Fourth universal definition of myocardial infarction (2018). *Eur. Heart J.* 40, 237–269. doi:10.1093/eurheartj/ehy462.

Thygesen, K., Alpert, J. S., and White, H. D. (2007). Universal Definition of Myocardial Infarction. *J. Am. Coll. Cardiol.* 50, 2173–2195. doi:10.1016/j.jacc.2007.09.011.

Tice, B. M., Rodríguez, B., Eason, J., and Trayanova, N. (2007). Mechanistic investigation into the arrhythmogenic role of transmural heterogeneities in regional ischaemia phase 1A. *Europace* 9, vi46–vi58. doi:10.1093/europace/eum204.Mechanistic.

Toussaint, N., Sermesant, M., Stoeck, C. T., Kozerke, S., and Batchelor, P. G. (2010). "In vivo Human 3D Cardiac Fibre Architecture: Reconstruction Using Curvilinear Interpolation of Diffusion Tensor Images," in *Medical image computing and computer-assisted intervention : MICCAI ... International Conference on Medical Image Computing and Computer-Assisted Intervention*, 418–425. doi:10.1007/978-3-642-15705-9_51.

Toussaint, N., Stoeck, C. T., Schaeffter, T., Kozerke, S., Sermesant, M., and Batchelor, P. G. (2013). In vivo human cardiac fibre architecture estimation using shape-based diffusion tensor processing. *Med. Image Anal.* 17, 1243–1255. doi:10.1016/j.media.2013.02.008.

Tranum-Jensen, J., Wilde, A. A., Vermeulen, J. T., and Janse, M. J. (1991). Morphology of electrophysiologically identified junctions between Purkinje fibers and ventricular muscle in rabbit and pig hearts. *Circ. Res.* 69, 429–437. doi:10.1161/01.RES.69.2.429.

Trayanova, N. A. (2011). Whole-heart modeling: applications to cardiac electrophysiology and electromechanics. *Circ. Res.* 108, 113–128. doi:10.1161/CIRCRESAHA.110.223610.Whole.

Trayanova, N. A., Constantino, J., and Gurev, V. (2010). Models of stretch-activated ventricular arrhythmias. *J. Electrocardiol.* 43, 476–485. doi:10.1016/j.jelectrocard.2010.05.014.

Trayanova, N. A., Pashakhanloo, F., Wu, K. C., and Halperin, H. R. (2017). Imaging-Based Simulations for Predicting Sudden Death and Guiding Ventricular Tachycardia Ablation. *Circ. Arrhythmia Electrophysiol.* 10, e004743. doi:10.1161/CIRCEP.117.004743.

Trayanova, N. A., and Rice, J. J. (2011). Cardiac electromechanical models: from cell to organ. *Front. Physiol.* 2, Article 43. doi:10.3389/fphys.2011.00043.

Trayanova, N. a, and Boyle, P. M. (2013). Advances in modeling ventricular arrhythmias: from mechanisms to the clinic. *Wiley Interdiscip. Rev. Syst. Biol. Med.* 6, 209–24. doi:10.1002/wsbm.1256.

Trayanova, N. a, O'Hara, T., Bayer, J. D., Boyle, P. M., McDowell, K. S., Constantino, J., et al. (2012). Computational cardiology: how computer simulations could be used to develop new therapies and advance existing ones. *Europace* 14, v82–v89. doi:10.1093/europace/eus277.

Trayanova, N., Eason, J., and Aguel, F. (2002). Computer simulations of cardiac defibrillation: a look inside the heart. *Comput. Vis. Sci.* 4, 259–270. doi:10.1007/s00791-002-0082-8.

Trénor, B., Romero, L., Ferrero, J. M., Sáiz, J., Moltó, G., and Alonso, J. M. (2007). Vulnerability to reentry in a regionally ischemic tissue: a simulation study. *Ann. Biomed. Eng.* 35, 1756–1770. doi:10.1007/s10439-007-9353-3.

Trovato, C., Passini, E., Tissier, A., Nagy, N., Varro', A., Severi, S., et al. (2017). In silico trials in human ventricular and purkinje cell models predict safety and efficacy of 10 antiarrhythmic drugs. *EP Eur.* 19, iii116–iii116. doi:10.1093/ehjci/eux140.007.

Trunk, P., Mocnik, J., Trobec, R., and Gersak, B. (2007). 3D heart model for computer simulations in cardiac surgery. *Comput. Biol. Med.* 37, 1398–1403. doi:10.1016/j.compbiomed.2006.11.003.

Tschabrunn, C. M., Roujol, S., Nezafat, R., Faulkner-Jones, B., Buxton, A. E., Josephson, M. E., et al. (2016). A swine model of infarct-related reentrant ventricular tachycardia: Electroanatomic, magnetic resonance, and histopathological characterization. *Hear. Rhythm* 13, 262–273. doi:10.1016/j.hrthm.2015.07.030.

Tse, G. (2016). Mechanisms of cardiac arrhythmias. *J. Arrhythmia* 32, 75–81. doi:10.1016/j.joa.2015.11.003.

Ukwatta, E., Arevalo, H., Li, K., Yuan, J., Qiu, W., Malamas, P., et al. (2016). Myocardial Infarct Segmentation From Magnetic Resonance Images for Personalized Modeling of Cardiac Electrophysiology. *IEEE Trans. Med. Imaging* 35, 1408–1419. doi:10.1109/TMI.2015.2512711.

Ursell, P. C., Gardner, P. I., Albala, A., Fenoglio, J. J., and Wit, a L. (1985). Structural and electrophysiological changes in the epicardial border zone of canine myocardial infarcts during infarct healing. *Circ. Res.* 56, 436–451. doi:10.1161/01.RES.56.3.436.

Vadakkumpadan, F., Arevalo, H., Ceritoglu, C., Miller, M., and Trayanova, N. (2012).

Image-Based Estimation of Ventricular Fiber Orientations for Personalized Modeling of Cardiac Electrophysiology. *IEEE Trans. Med. Imaging* 31, 1051–1060. doi:10.1109/TMI.2012.2184799.

Vadakkumpadan, F., Rantner, L. J., Tice, B., Boyle, P., Prassl, A. J., Vigmond, E., et al. (2009). Image-based models of cardiac structure with applications in arrhythmia and defibrillation studies. *J. Electrocardiol.* 42, 157.e1-157.e10. doi:10.1016/j.jelectrocard.2008.12.003.

van den Borne, S. W. M., Diez, J., Blankesteijn, W. M., Verjans, J., Hofstra, L., and Narula, J. (2010). Myocardial remodeling after infarction: the role of myofibroblasts. *Nat. Rev. Cardiol.* 7, 30–37. doi:10.1038/nrcardio.2009.199.

Van den Broek, J. H. J. M., and Van den Broek, M. H. L. M. (1980). Application of an ellipsoidal heart model in studying left ventricular contractions. *J. Biomech.* 13, 493–503. Available at: http://www.sciencedirect.com/science/article/pii/0021929080903425 [Accessed July 15, 2014].

Varga-Szemes, A., van der Geest, R. J., Schoepf, U. J., De Cecco, C. N., Tesche, C., Fuller, S. R., et al. (2016). MRI Post-Processing Methods for Myocardial Infarct Quantification. *Curr. Radiol. Rep.* 4, 30. doi:10.1007/s40134-016-0159-7.

Vergara, C., Palamara, S., Catanzariti, D., Nobile, F., Faggiano, E., Pangrazzi, C., et al. (2014). Patient-specific generation of the Purkinje network driven by clinical measurements of a normal propagation. *Med. Biol. Eng. Comput.* 52, 813–826. doi:10.1007/s11517-014-1183-5.

Vetter, F. J., and McCulloch, A. D. (1998). Three-dimensional analysis of regional cardiac function: a model of rabbit ventricular anatomy. *Prog. Biophys. Mol. Biol.* 69, 157–183. Available at: http://www.ncbi.nlm.nih.gov/pubmed/9785937.

Vigmond, E., Vadakkumpadan, F., Gurev, V., Arevalo, H., Deo, M., Plank, G., et al. (2009). Towards predictive modelling of the electrophysiology of the heart. *Exp. Physiol.* 94, 563–577. doi:10.1113/expphysiol.2008.044073.

Virag, N., Jacquemet, V., Henriquez, C. S., Zozor, S., Blanc, O., Vesin, J. M., et al. (2002). Study of atrial arrhythmias in a computer model based on magnetic resonance images of human atria. *Chaos* 12, 754–763. doi:10.1063/1.1483935.

Volders, P. G., Sipido, K. R., Carmeliet, E., Spätjens, R. L., Wellens, H. J., and Vos, M. A. (1999). Repolarizing K+ currents ITO1 and IKs are larger in right than left canine ventricular midmyocardium. *Circulation* 99, 206–210. doi:10.1161/01.CIR.99.2.206.

Wagner, A., Mahrholdt, H., Holly, T. A., Elliott, M. D., Regenfus, M., Parker, M., et al. (2003). Contrast-enhanced MRI and routine single photon emission computed tomography (SPECT) perfusion imaging for detection of subendocardial myocardial infarcts: an imaging study. *Lancet* 361, 374–379. doi:10.1016/S0140-6736(03)12389-6.

Walton, R. D., Pashaei, A., Martinez, M. E., Constantin, M., Duchateau, J., Bear, L., et al. (2018). Compartmentalized Structure of the Moderator Band Provides a Unique Substrate for Macroreentrant Ventricular Tachycardia. *Circ. Arrhythmia Electrophysiol.* 11, e005913. doi:10.1161/CIRCEP.117.005913.

Wang, Z., Taylor, L. K., Denney, W. D., and Hansen, D. E. (1994). Initiation of ventricular extrasystoles by myocardial stretch in chronically dilated and failing canine left ventricle. *Circulation* 90, 2022–2031. doi:10.1161/01.CIR.90.4.2022.

Weese, J., Groth, A., Nickisch, H., Barschdorf, H., Weber, F. M., Velut, J., et al. (2013). Generating anatomical models of the heart and the aorta from medical images for personalized physiological simulations. *Med. Biol. Eng. Comput.* 51, 1209–1219. doi:10.1007/s11517-012-1027-0.

Weinmann, H., Brasch, R., Press, W., and Wesbey, G. (1984). Characteristics of gadolinium-DTPA complex: a potential NMR contrast agent. *Am. J. Roentgenol.* 142, 619–624. doi:10.2214/ajr.142.3.619.

Wenger, W., and Kligfield, P. (1996). Variability of precordial electrode placement during routine electrocardiography. *J. Electrocardiol.* 29, 179–184. doi:10.1016/S0022-0736(96)80080-X.

Wenk, J. F., Zhang, Z., Cheng, G., Malhotra, D., Acevedo-Bolton, G., Burger, M., et al. (2010). First finite element model of the left ventricle with mitral valve: insights into ischemic mitral regurgitation. *Ann. Thorac. Surg.* 89, 1546–1553. doi:10.1016/j.athoracsur.2010.02.036.The.

Western, D., Hanson, B., and Taggart, P. (2015). Measurement bias in activation-recovery intervals from unipolar electrograms. *Am. J. Physiol. Circ. Physiol.* 308, H331–H338. doi:10.1152/ajpheart.00478.2014.

WHO (2018). *World Health Statistics 2018: monitoring health for the SDGs, sustainable development goals*. Available at: https://www.who.int/gho/publications/world_health_statistics/2018/en/.

Wijnmaalen, A. P., van der Geest, R. J., van Huls van Taxis, C. F. B., Siebelink, H.-M. J., Kroft, L. J. M., Bax, J. J., et al. (2011). Head-to-head comparison of contrast-enhanced magnetic resonance imaging and electroanatomical voltage mapping

to assess post-infarct scar characteristics in patients with ventricular tachycardias: real-time image integration and reversed registration. *Eur. Heart J.* 32, 104–114. doi:10.1093/eurheartj/ehq345.

Wilber, D. J. (2008). Catheter ablation of ventricular tachycardia: Two decades of progress. *Hear. Rhythm* 5, S59–S63. doi:10.1016/j.hrthm.2008.02.001.

Wilkins, E., Wilson, L., Wickramasinghe, K., Bhatnagar, P., Leal, J., Luengo-Fernandez, R., et al. (2017). European Cardiovascular Disease Statistics 2017. *Eur. Hear. Network, Brussels*. doi:978-2-9537898-1-2.

Williams, G. S. B., Smith, G. D., Sobie, E. A., and Jafri, M. S. (2010). Models of cardiac excitation-contraction coupling in ventricular myocytes. *Math. Biosci.* 226, 1–15. doi:10.1016/j.mbs.2010.03.005.

Winklhofer, S., Stoeck, C. T., Berger, N., Thali, M., Manka, R., Kozerke, S., et al. (2014). Post-mortem cardiac diffusion tensor imaging: detection of myocardial infarction and remodeling of myofiber architecture. *Eur. Radiol.* 24, 2810–2818. doi:10.1007/s00330-014-3322-7.

Winslow, R. L., Scollan, D. F., Holmes, A., Yung, C. K., Zhang, J., and Jafri, M. S. (2000). Electrophysiological modeling of cardiac ventricular function: from cell to organ. *Annu. Rev. Biomed. Eng.* 2, 119–155. Available at: http://www.ncbi.nlm.nih.gov/pmc/articles/PMC1403490/ [Accessed July 15, 2014].

Wu, M.-T., Tseng, W.-Y. I., Su, M.-Y. M., Liu, C.-P., Chiou, K.-R., Wedeen, V. J., et al. (2006). Diffusion Tensor Magnetic Resonance Imaging Mapping the Fiber Architecture Remodeling in Human Myocardium After Infarction: Correlation With Viability and Wall Motion. *Circulation* 114, 1036–1045. doi:10.1161/CIRCULATIONAHA.105.545863.

Xie, Y., Garfinkel, A., Camelliti, P., Kohl, P., Weiss, J. N., and Qu, Z. (2009). Effects of fibroblast-myocyte coupling on cardiac conduction and vulnerability to reentry: A computational study. *Hear. Rhythm* 6, 1641–1649. doi:10.1016/j.hrthm.2009.08.003.

Yamada, T. (2014). Catheter ablation of epicardial ventricular tachycardia. *J. Arrhythmia* 30, 262–271. doi:10.1016/j.joa.2014.04.011.

Yamashita, S., SACHER, F., MAHIDA, S., BERTE, B., LIM, H. S., KOMATSU, Y., et al. (2016). Image Integration to Guide Catheter Ablation in Scar-Related Ventricular Tachycardia. *J. Cardiovasc. Electrophysiol.* 27, 699–708. doi:10.1111/jce.12963.

Yan, A. T. (2006). Characterization of the Peri-Infarct Zone by Contrast-Enhanced Cardiac Magnetic Resonance Imaging Is a Powerful Predictor of Post-Myocardial Infarction Mortality. *Circulation* 114, 32–39. doi:10.1161/CIRCULATIONAHA.106.613414.

Yan, G.-X., Shimizu, W., and Antzelevitch, C. (1998). Characteristics and Distribution of M Cells in Arterially Perfused Canine Left Ventricular Wedge Preparations. *Circulation* 98, 1921–1927. doi:10.1161/01.CIR.98.18.1921.

Yang, G., Toumoulin, C., Coatrieux, J. L., Shu, H., Luo, L., and Boulmier, D. (2006). A 3D static heart model from a MSCT data set. in *27th Annual International Conference of the IEEE Engineering in Medicine and Biology Society (IEEE-EMBS 2005)* (Shangai, China: IEEE), 5499–5502. doi:10.1109/IEMBS.2005.1615728.

Yao, J.-A., Hussain, W., Patel, P., Peters, N. S., Boyden, P. A., and Wit, A. L. (2003). Remodeling of Gap Junctional Channel Function in Epicardial Border Zone of Healing Canine Infarcts. *Circ. Res.* 92, 437–443. doi:10.1161/01.RES.0000059301.81035.06.

Yokokawa, M., Desjardins, B., Crawford, T., Good, E., Morady, F., and Bogun, F. (2013). Reasons for Recurrent Ventricular Tachycardia After Catheter Ablation of Post-Infarction Ventricular Tachycardia. *J. Am. Coll. Cardiol.* 61, 66–73. doi:10.1016/j.jacc.2012.07.059.

Young, A. A., and Frangi, A. F. (2009). Computational cardiac atlases: from patient to population and back. *Exp. Physiol.* 94, 578–596. doi:10.1113/expphysiol.2008.044081.

Zeigler, A. C., Richardson, W. J., Holmes, J. W., and Saucerman, J. J. (2016). Computational modeling of cardiac fibroblasts and fibrosis. *J. Mol. Cell. Cardiol.* 93, 73–83. doi:10.1016/j.yjmcc.2015.11.020.

Zemlin, C. W., Herzel, H., Ho, S. Y., and Panfilov, A. V (2001). "A realistic and efficient model of excitation propagation in the human atria," in *Computer Simulation and Experimental Assessment of Cardiac Electrophysiology*, eds. N. Virag, L. Kappenberger, and O. Blanc (Arkmonk, New York: Futura Publishing Company, Inc.), 29–34. Available at: http://www.researchgate.net/publication/46616301_A_realistic_and_efficient_model_of_excitation_propagation_in_the_human_atria/file/9fcfd50a1168a46fb0.pdf [Accessed July 16, 2014].

Zhao, J., Butters, T. D., Zhang, H., LeGrice, I. J., Sands, G. B., and Smaill, B. H. (2013). Image-based model of atrial anatomy and electrical activation: a computational platform for investigating atrial arrhythmia. *IEEE Trans. Med. Imaging* 32, 18–27.

doi:10.1109/TMI.2012.2227776.

Zlochiver, S., Muñoz, V., Vikstrom, K. L., Taffet, S. M., Berenfeld, O., and Jalife, J. (2008). Electrotonic Myofibroblast-to-Myocyte Coupling Increases Propensity to Reentrant Arrhythmias in Two-Dimensional Cardiac Monolayers. *Biophys. J.* 95, 4469–4480. doi:10.1529/biophysj.108.136473.

UNIVERSITAT
POLITÈCNICA
DE VALÈNCIA